Politechnika Wrocławska

FIELD OF SCIENCE: Engineering and Technology

DISCIPLINE OF SCIENCE: Chemical Engineering

DOCTORAL DISSERTATION

Synthesis and characterization of carbon cathode materials for secondary lithium-oxygen cells

Denis Kopiec

Supervisor:
dr hab. Krzysztof Kierzek, prof. PWr

Keywords: lithium-oxygen battery, carbon nanomaterials, energy storage, surface functionalization, carbon aerogels

WROCŁAW 2025

Firstly, I would like to thank my late Mother, Anna Kopiec, who had always supported me during my school and academic journey. She had motivated me to dedicate my efforts towards learning, which has later transformed in the interest, passion, and determination to understand how the world around us works. I will always be thankful for that.

This work could not be finished without the academic support from my supervisor, professor Krzysztof Kierzek. I appreciate every remark and suggestion during many discussion regarding research, articles, or this work. It all has helped me to develop and grow as a researcher. Also, I would like to express my gratitude to my colleagues from the Group of Carbon Materials at the Department of Process Engineering and Technology of Polymer and Carbon Materials of Wrocław University of Science and Technology. Yours support and kind words, both in laboratory and in private, have made those years whole, so special thank you to Natalia Tyszkiewicz, Bartosz Widera, Aleksander de Rosset, Izabela Walendzik, Daria Minta, Małgorzata Ulatowska, Karolina Kordek-Khalil, Katarzyna Gajewska, and Marta Posadzy.

During my PhD I had the opportunity to meet and work with exceptional researchers who allowed me to develop my scientific interests. I would like to thank the NFFA network for enabling me to conduct my research projects at the Universitat Autònoma de Barcelona and the Institut de Recerca en Energia de Catalunya in Barcelona. I would also like to express my gratitude to the Centre of Polymer Materials of the Polish Academy of Sciences for the opportunity to complete my internship and to Adam Moyseowicz for including me in the Stablebat project.

One last, but certainly not least, thank you goes to my friends and family, who have always listened – willingly – to my complaints about unsuccessful experiments, and just as eagerly joined in celebrating the small victories. Your support has meant more than you know.

Table of Contents

Table of Tables

Table of Figures

List of used abbreviations:

MAB – Metal Air Batteries

ORR – Oxygen Reduction Reactions

OER – Oxygen Evolution Reactions

ESS – Energy Storage System

SHE – Standard Hydrogen Electrode

SSA – Specific Surface Area

XPS – X-ray Photoelectron Spectroscopy

FTIR – Fourier-transform Infrared Spectroscopy

DEMS – Differential Electrochemical Mass Spectrometry

SEM – Scanning Electron Microscope

TEM – Transmission Electron Microscope

Li_2O_2 – Lithium Peroxide

LiO_2 – Lithium Superoxide

Li_2O – Lithium Oxide

LiOH – Lithium Hydroxide

NASICON – Sodium Super Ionic Conductor

LISICON – Lithium Super Ionic Conductor

PEO – Polyethylene Oxide

PAN – Polyacrylonitrile

PPO – Polypropylene Oxide

PVDF - Polyvinylidene Fluoride

PTFE - Polytetrafluoroethylene

CB – Carbon Black

AC – Activated Carbon

EDLC – Electric double-layer capacitor

CVD – Chemical Vapor Deposition

GO – Graphene Oxide

CNF – Carbon Nanofibers

CNT – Carbon Nanotubes

GCPL – Galvanostatic Cycling with Potential Limitation

1. Introduction

In recent years, the development of renewable energy and electric vehicles sectors has promoted the efforts in improving currently available energy storage systems. Nowadays, the most widely utilized systems are based on Li-ion batteries, but their low specific energy creates limitations that constrain further progress of electrification of various industries. Thus, the development of more efficient type of battery is required.

Lithium-oxygen batteries have been proposed as a potential solution to the growing demand for energy storage capacity mainly due to their extremely high theoretical specific energy, reaching around 11 430 Wh kg^{-1}, which is the most out all metal-air type of batteries and almost on par with gasoline. Such high specific energy is attributed to the oxygen reduction reactions and oxygen evolution reactions occurring during discharge and charge, respectively. However, sluggish kinetic of electrode reactions, parasitic reactions, and the insulating and insoluble nature of discharge products are the main factors limiting the development of lithium-oxygen batteries. To overcome mentioned issues, wide range of solutions have been researched and majority of them are focusing around enhancing properties of cathode materials as an effective way of improving performance of the battery.

Among various cathode materials, carbon nanomaterials have drawn attention due to their promising properties, including high electric conductivity, catalytic activity, and porosity, that can be tailored according to requirements. Additionally, wide range of available structures, synthesis routes, and relative cost-effectiveness are increasing their potential.

In this work, synthesis of wide range of carbon materials, including carbon nanofiber, activated carbons, and carbon aerogels, is carried out. The influence of synthesis process parameters on the structure and properties of obtained materials is thoroughly examined and described. An extensive study comparing *in-situ* and *ex-situ* nitrogen doping is presented. Facile approaches to prepare and utilize nickel oxalate-based catalysts in the synthesis of carbon nanofibers and carbon nanofibers/activated carbons composites are showed. Based on the synthesis and characterization of different activated carbons, the investigation on the influence of porosity on the performance of lithium-oxygen batteries is conducted. Moreover, in efforts to develop free-standing cathodes, a novel approach to the preparation of carbon aerogels is presented.

In terms of electrochemical measurements, prepared samples have been examined in the lithium-oxygen cell in order to determine their potential as cathode materials. The operation across the first discharge charge cycle has been assessed, as well as the cyclability performance.

2. Literature review

While lead-acid and lithium-ion batteries have been crucial in meeting energy storage demands, the ongoing scientific effort is focused on developing new generation of batteries that will facilitate the growing needs generated by renewable energy sources and electric vehicle (EV) sectors. To power the future in a sustainable and efficient way, the development of systems with higher energy densities and improved safety is required for electric vehicles. Simultaneously, the expanding integration of renewable energy sources should propel the advances in industrial scale energy storage solutions [1]. To better understand why the metal-air batteries (MAB) are viewed as potential solutions to the constantly growing energy storage market, the better understanding of conventional batteries (lead-acid and lithium-ion (Li-ion)) is needed.

The concept of generation of energy via electrochemical reactions is known for over two hundred years, when Volt proposed first electrochemical cell in 1800 [2]. Since then, numerous technologies, aiming at production and storage of electricity, have been developed and applied, to larger or smaller extend, in every aspect of our everyday lives. However, the first system to achieve worldwide application for several decades is the lead-acid battery. Lead based batteries are able to reach that level of success due to their reliability and cost-effectiveness, which are primarily achieved by the selection of materials. The lead battery is most commonly composed of lead dioxide (PbO_2) as a cathode, lead sponge as an anode, and sulfuric acid solution in the role of electrolyte. Materials have been precisely chosen based on their functionality, with PbO_2 facilitating the reduction-oxidation reactions during the discharge/charge cycles, lead sponge allowing the efficient conversion between lead and lead oxide during the work of the battery, and the sulfuric acid enabling the flow of ions between cathode and anode [3]. While this choice of materials is reasonable and cogent from the application point of view, it creates the main concern related to lead-acid batteries – the environmental impact of production and disposal of these batteries [4]. Despite, the environmental concerns regarding the lead toxicity, lead-acid batteries still remain as the primary energy source for starting the internal combustion engine.

The revolutionization of energy storage landscape came with the development of lithium-ion batteries. In comparison with the lead-acid batteries, the Li-ion systems are characterized by higher energy density, longer life-cycle, and lighter weight [5]. These properties have enabled Li-ion batteries becoming the backbone of various applications, where compact, efficient, and rechargeable energy storage is vital, including portable electronics and EV. In this type of battery, the cathode is most often composed of various lithium oxides, such as lithium cobalt oxide ($LiCoO_2$) [6], lithium manganese oxide ($LiMnO_2$) [7], or lithium iron phosphate ($LiFePO_4$) [8]. To increase the energy density and efficiency of Li-ion batteries, the combination of different lithium oxides is commonly used, e.g., lithium nickel cobalt aluminum oxide (NCA) [9], lithium nickel manganese cobalt oxide (NMC) [10], or lithium nickel cobalt oxide (LCO) [11]. In the case of anode, the most frequently used material is graphite, due to its ability to efficiently intercalate lithium ions during the work of the battery. Lithium salt dissolved in a mixture of organic solvent is often used as an electrolyte, with ethylene carbonate

and diethyl carbonate typically being used as a solvent [12]. Despite the widespread use of Li-ion batteries, they face several limitations that restrain their further development. Potential fire hazard and safety concerns are created due to the flammable nature of organic electrolytes and chemical instability of lithium oxides based cathode. The extraction and processing of lithium, manganese, cobalt, and nickel, combined with the difficult recycling of Li-ion batteries pose environmental challenges [13]. Additionally, the gradual degradation of capacity of lithium-ion batteries still remains an unsolved issue, as it heavily limits the overall lifespan of this batteries.

2.1. Metal-air batteries

In the search for alternative energy storage systems (ESS), that could replace currently used lead-acid and lithium-ion batteries, metal-air batteries are recognized as one of the most promising solutions. The wide variety of researched MAB technologies rises an optimistic outlook, that one of these systems could put a significant mark on the energy storage sector and that it will increase the efficiency and sustainability of systems that we will use in the future [14]. The list of the leading-edge systems includes the lithium-air (Li-air), aluminum-air (Al-air), zinc-air (Zn-air), and sodium-air (Na-air) batteries. The operating principle of all MAB is very similar and it is based on the oxygen reduction reaction (ORR) taking place during discharging, and the oxygen evolution reaction (OER) during charging. The utilization of oxygen in electrode reactions is enabled by employing the semi-open systems with three common components present in each type of metal-air battery. Similar to many battery systems, the negative electrode is composed of bulk metal serving as a fuel in the occurring reactions (e.g., lithium, sodium, aluminum, and zinc). The positive electrode is made from porous material, that facilitate the supply of oxygen from outside of the battery. Between the two electrodes, there is an electrolyte, the type of which varies significantly depending on the battery. However, its purpose remains the same: to enable the transportation of ions between the anode and cathode [1].

Incorporation of the air in the work of the battery, by shifting the architecture of the cell to include porous air cathode, is key to achieving exceptionally high theoretical energy densities in MAB. The comparison of theoretical specific energy of main metal-air batteries and gasoline is presented in the Fig. 1. Furthermore, eliminating the need to include all components necessary for carrying out electrode reactions in a closed system reduces the weight of MAB. Due to the improved energy density and lightweight of air-based batteries, their potential applications include the expanding EV and industrial energy storage sectors. Moreover, incorporating air into electrode reactions can lead to the limited usage of scarce resources, which are essential for battery preparation (mainly transition metal oxides) [15].

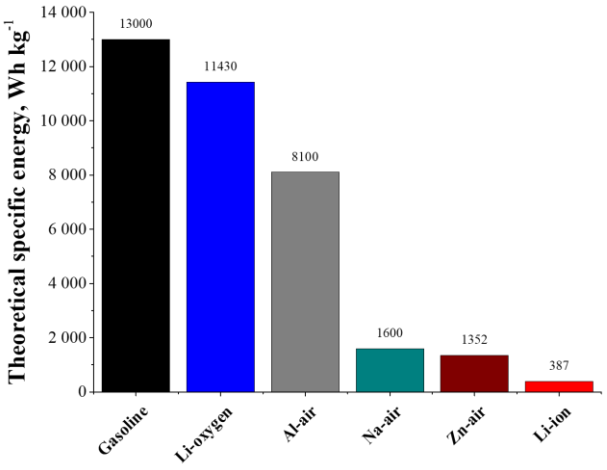

Fig. 1. Comparison of theoretical specific energy of key metal air batteries and a gasoline. All values for MAB are calculated with the exclusion of oxygen mass.

Although the term "metal-air" battery is widely used in the literature, this should be considered more as an operational label and not as a precise description. To be strict, the term metal-air batteries, assume that the oxygen required for electrode reactions originate from ambient air. Indeed such approach would be highly beneficial, as air is free and always available, but it would also generate operational issues varying between different types of systems, depending on the nature of employed electrolyte and metal anode. However, some degree of pre-treatment of supplied air is almost always required for all metal-air batteries. The removal of impurities, like carbon dioxide (CO_2) and moisture, is crucial for improving the durability of battery's components by limiting the side reactions that can degrade electrodes or electrolyte [16]. The negative influence of CO_2 on the alkaline electrolytes has been reported multiple times – carbon dioxide interacts with alkaline electrolyte and precipitate as solid carbonates in the porous electrode blocking the oxygen supply pathways [17]. On the other hand, moisture is predominantly problematic for batteries operating with anode metal reactive to even slight water content, like lithium or sodium. This put additional requirement on utilizing non-aqueous and aprotic electrolyte in these batteries [17]. Also, other air components can have negative influence on the work of the MAB, e.g., sulfur dioxide (SO_2) or nitrogen (N_2) [1]. To reduce the contamination of oxygen transferred to the battery, the semipermeable, polymeric membranes can be employed [18]. Another approach to completely cease the flow of impurities to the interior of battery is the utilization of pure oxygen. Regardless of the chosen method of air purification, this step increases the complexity of the metal-air based energy storage system and reduces it efficiency and energy density by adding weight to the battery.

In this work the term "metal-air battery" will be used, while describing different types of systems utilizing metals other that lithium (Na-air, Al-air, and Zn-air). In the part dedicated to the lithium based batteries, the discussion will be narrowed down to systems operating with the use of pure oxygen.

The MAB can be separated into two groups based on their rechargeability – primary and secondary. The primary metal-air batteries are non-rechargeable, which is the result

of the depletion of chemical components during discharging. Once the primary batteries are discharged, they could not be recharged, meaning they need to be replaced. On the other side, there are secondary batteries, that are rechargeable, which is attributed to the reversibility of chemical reactions occurring during the work of the battery. Due to the rechargeability, they can be used multiple times. The contrast in the reversibility of operation of both types of MAB, implies the further differences in other areas, such as application, construction, and cost [19].

In the case of possible application, primary batteries, due to their single-use nature, tend to be used where long shelf life and high energy density are important. At the same time, frequent replacements are acceptable or the device is not often used, e.g., emergency equipment, certain medical devices, and military application [20]. The potential use of secondary metal-air batteries is more widespread, and it includes all sectors, where frequent charging is feasible, like portable electronics, electric vehicles, and industrial energy storage systems. The different applications of primary and secondary batteries impose specific requirements in terms of materials used and the construction of each type of a battery. The secondary MAB must utilize more robust materials and have more complex construction to be able to withstand the repeating discharging/charging cycles, and the stress coming from longer use (mainly thermal and mechanical stress). The chemistry behind secondary MAB involves balancing energy density with the ability to efficiently reverse the electrochemical reactions. While primary batteries can have a simpler construction not designed to endure the same tensions as secondary batteries, the main goal of their chemistry optimization is to achieve high energy density and a long shelf life, rather than an extended cycle life [20]. From the cost-effectiveness point of view, the primary batteries can be more economical due to the lower cost of the used materials, but their single-use nature creates concerns regarding waste and environmental impact. In contrast, the secondary batteries can be potentially more expensive upfront based on their complex design, but over long-term they can turn out to be more environmentally friendly and cost-effective.

Another approach to the classification of the MAB is based on the type of applied metal, which impacts the crucial factors, such as chosen materials, energy density, and the mechanism of reactions taking place during discharging/charging. Even though that all metal-air batteries share a lot of common advantages, arising from the oxygen utilization, there are some unique characteristics creating additional opportunities and challenges for each of the mentioned metal-air technologies. The lithium based systems will be described in details in section 2.2, and the next segments will provide overview of other promising oxygen utilizing technologies.

2.1.1. Na-air

Perhaps, the closest element to lithium in terms of chemical properties is sodium. Both metals share similar electronegativity, sensitivity towards water, and lightweight, with sodium being the second lightest metal after lithium [21]. The abundance (Na is the sixth most abundant element in Earth's crust [22]) and the uniform geographical distribution of sodium are one of the main advantages of this metal, leading to its lower and less volatile price, compared to lithium. Despite, the theoretical specific energy of

Li-air cell being significantly superior than that of Na-air cell (around 1 600 Wh kg^{-1} [23, 24]) , the potential of Na-air batteries is investigated due to advantages in the field of sustainability and cost-effectiveness.

In the case of the design of Na-air batteries, two types can be distinguished: non-aqueous and hybrid batteries. Both of these systems utilize sodium metal as an anode and air-electrode, composed of porous materials. The requirements toward cathode materials include appropriate porosity (with dominant mesoporosity), catalytic activity in ORR/OER, and high electric conductivity. Few groups of materials meet those criteria and are applied in Na-air batteries. Carbon materials, such as graphene [25, 26] and carbon nanotubes [21, 27], have been investigated both in non-aqueous and hybrid systems. Additionally, the most commonly used electrocatalyst in ORR/OER, including noble metals (Pt, Au, Pd) [26, 28, 29] and transition metal oxides [30, 31], have been applied to improve the performance of sodium based air batteries.

Apart from similarities in anode and cathode materials, significant differences can be observed between non-aqueous and hybrid Na-air batteries, including the type of electrolyte, reactions taking place during discharge/charge, deposited products, and the overall architecture of the cell. The design of the non-aqueous Na-air cell is more straightforward, and usually include metal anode, porous air-electrode, and the polymer separator soaked in organic electrolyte between them. The non-aqueous electrolyte is made of aprotic, organic solvent, usually ether or carbonate, and the sodium salt [24, 32]. The primary discharge product is still investigated by the researchers and the final agreement on the ORR product has not yet been achieved, with two compounds being frequently reported as a main discharge product: sodium peroxide (Na_2O_2) [24] and sodium superoxide (NaO_2) [33].

On the other hand, the design of the hybrid Na-air battery is more complicated, because it includes two separate areas with two different electrolytes. The anode design is similar to the non-aqueous battery, with sodium as an anode and anolyte based on the organic solvent. However, the cathode space is composed of the air-electrode and aqueous catholyte. In most studies, aqueous solution of KOH or NaOH is used [34]. Due to the application of two different electrolytes, the incorporation of solid membrane that will separate both solutions and only enable the transportation of Na^+ is required. For this purpose, typically the ceramic membranes utilized in fuel cells are investigated (e.g., NASICON) [21]. The separation of anode and cathode spaces leads to the different mechanism of the discharge/charge reactions occurring during the work of the cell. This change is observable in different nature of the product of discharge reactions: in non-aqueous Na-air battery insoluble Na_2O_2 or NaO_2 can be deposited, whereas in hybrid cell the known discharge product is soluble NaOH. Due to the incorporation of the solid membrane, the growth of the dendrites is largely restricted preventing the possibility of the short circuit.

The further development of Na-air batteries is still facing major challenges. For both non-aqueous and hybrid systems, the development of efficient and cost effective

cathode materials is needed to enhance the stability of the battery. In the case of non-aqueous batteries, the determination of the mechanism of reactions taking place during discharge/charge will be crucial to better understanding the system. In the case of the hybrid Na-air battery, complex design impose specific requirements towards materials, especially the separation membrane. The further advances in this area might be vital for the development of safe and efficient hybrid batteries.

2.1.2. Zn-air

One of the few types of air batteries that have found application in the modern world is the primary Zn-air battery, which is extensively used in medical (e.g., hearing aids), military, and telecommunication applications [35]. Moreover, Zn-air batteries have gained popularity across researchers due to the abundance of zinc in the earth crust and its relative low-cost in comparison to other metals used in batteries, e.g., lithium, cobalt. Additionally, the relatively high resistance to corrosion of zinc in aqueous and alkaline solutions, enables utilization of simple electrolytes (e.g., KOH and NaOH solutions) [36]. All of the mentioned factors, combined with relatively high theoretical specific energy of Zn-air systems, reaching around 1 086 Wh kg^{-1} [37, 38], present this type of battery a promising and relatively cheap solution to growing needs in the energy storage sector.

The design of Zn-air cell, typically include the Zn powder connected by the addition of binders and other additives, to form coherent electrode. However, micro- and nanostructures of zinc have also been developed and used as an anode, including nanospheres, flakes, nanofibers, and sheets, resulting in an increased electrode surface area and improved cell performance [19]. Generally, the alkaline electrolytes in the form of KOH or NaOH aqueous solutions are employed, despite their susceptibility to CO_2 contamination from air. The KOH based electrolytes (typically 7 M or 30 wt.% solutions) present higher ionic conductivity, lower viscosity, and higher oxygen diffusion coefficient, but are more prone to the degradation due to higher solubility of CO_2 [1]. Arguably, the air electrode is the crucial factor in the development of Zn-air batteries. Cathode is usually composed of porous carbon mixed with a gas diffusion layer, to provide good activity in ORR/OER and sufficient access to oxygen. Most often, a catalyst can be added to enhance catalytical activity of cathode material, leading to the increased capacity and reversibility of the battery.

The main challenges in the development of secondary Zn-air batteries include the parasitic reactions, low cyclability, dendrites growth, and large overpotential of electrode reactions [39]. Different approaches have been proposed to solve these issues: in the anode, the attempts to slow down the degradation via alloying Zn with other metals (e.g., Bi, Sn, Pb, Mg) have been made [40, 41]; in electrolyte, the addition of organic corrosion inhibitors or the shift towards aprotic and nonaqueous electrolytes have been tried [42, 43]; in cathode, mainly the incorporation of various electrocatalyst (e.g., MnO_2, Pt, Pd, Ru) has been proposed as a possible solution [44–46]. The primary Zn-air batteries have been successfully applied in medical devices (like hearing aids), but the development of stable and rechargeable system is still ongoing challenge for researchers.

2.1.3. Al-air

The second highest theoretical specific energy across metal-air systems is showed by Al-air batteries, with the value of approximately 4 500 Wh kg^{-1} [23]. The combination of such large specific energy and favorable intrinsic properties of aluminum as the anode metal, including the abundance, non-toxicity, relatively low-cost, and ease of recycling, have placed Al-air batteries high on the list of potential replacements of Li-ion batteries [47]. Efforts towards reducing the corrosion of anode, improving the kinetics of ORR/OER, and increasing the stability of Al-air batteries have led to significant developments in all elements of the cell.

Most commonly, the aluminum metal is used as an anode in the Alair batteries, however the impurities present in the Al anode might lead to the disturbance in the work of the cell and hamper its performance. Moreover, the passivation of the aluminum, after the exposure to humidity and air, slows down the oxidation resulting in increased corrosion resistance, but limited availability for of Al for electrode reactions [48]. To reduce the limitations of the pure aluminum, alloys have been studied as a potential anode substitute in Al-air cells. In the composition of Al alloys, different elements have been considered, including Zn, Ga, Ti, In, and Sn [49, 50]. The main advantages of alloys application is the improvement of anode corrosion resistance combined with the reduction of the occurrence of parasitic reactions by increasing the hydrogen evolution potential.

In the case of the cathode in Al-air batteries, the main challenges are focused around finding the efficient catalyst for ORR/OER to improve the kinetics of electrode reactions. Noble metals (mainly Pt and Ag) and transition metal oxides have been proposed, due to their high activity, but the limiting factors are high cost and scarcity of resources [47]. The economically beneficial alternatives includes carbon materials [51, 52]. However, the most promising results have been reported for the combined application of carbon materials decorated with noble metals and transition metal oxides [53–55].

The electrolytes utilized in Al-air batteries are usually aqueous, with KOH and NaOH solution being the main choices, due to their high ionic conductivity and non-toxicity. However, the major issue with the alkaline solutions is the rapid corrosion rate of aluminum occurring in this type of electrolytes. Additionally, this class of electrolytes is sensitive to the CO_2 contamination causing the precipitation of carbonates, leading to the decline of battery's performance [56]. Some researches indicate that the corrosion of anode materials can be limited by the utilization of acidic electrolytes, such as H_2SO_4 and HCl [57, 58]. Another approach to improve the stability of aqueous electrolytes includes incorporation of additives. The aim of addition of these organic (e.g., dicarboxylic acids, 1-allyl-3-methylimidazolium bis(trifluoromethylsulfonyl)imide) [59, 60] or inorganic (e.g., ZnO, $Ce(NO_3)_3$) [61, 62] compounds is to reduce the corrosion rate of Al anode and suppressing the side reactions, like hydrogen evolution. On the other hand, the application of non-aqueous electrolytes, including aprotic electrolytes, ionic liquids, or polymer electrolytes, have

been investigated, but regardless of their great potential, those designs still require further development [47].

Despite the considerable efforts from the researchers to overcome the obstacles in the development of Al-air batteries, still major challenges remain unresolved. To achieve the viability and industrial scalability the steps towards the reduction of anode corrosion and stability of electrolyte are required. Additionally, the improvement in the ORR/OER kinetics is critical to attain the desired level of stability and cyclability of Al-air batteries.

2.2. Lithium-oxygen cells

Perhaps, the system drawing the most attention from researchers and one of the most promising solution to address the increasing demand for the energy storage capacity is lithium-oxygen (Li-O_2) cell. The main reason behind that popularity of Li-O_2 batteries is their extremely large theoretical energy density of around 11 430 Wh kg^{-1}, which is the highest out of all MAB and almost comparable to the energy density of fossil fuels (13 000 Wh kg^{-1}) [63, 64]. Although, this tremendous specific energy is the crucial factor propelling the development of the Li-O_2 batteries, it is worth to bring back the difference between "metal-air" and "metal-oxygen" terms. In the metal-air batteries, the oxygen required for the electrode reactions is sourced from the air, thus its mass is excluded from the calculation of specific energy of each system. On the other hand, when the metal-oxygen systems are discussed, the pure oxygen, needed for the operation of the cell, is supplied directly to the cell's interior. As a consequence, the oxygen mass is included in the calculation of specific energy, which leads to its decrease, for example the theoretical specific energy of lithium-air cell can reach the value of nearly 12 kWh kg^{-1}, but when the mass of oxygen is taken into consideration the theoretical specific energy of lithium-oxygen cell reduces to 3 500 Wh kg^{-1} [65, 66]. This drop might be considered as a significant, but such high specific energy is still almost 10-times higher than the theoretical specific energy of Li-ion batteries [1].

The potential of employing lithium as anode in the electrochemical energy storage system has been noticed in the 1970s, when the first concept of aqueous lithium-oxygen cell is dated. However, the research activity in this field gained momentum in the 1990s and the early twenty-first century, when the need for more efficient ESS became evident [64] and number of publications and patents regarding rechargeable Li-O_2 batteries has increased significantly. After the initial interest only from the academia, the Li-O_2 batteries also attracted the attention from the industry with IBM launching the IBM's Battery 500 Project, aiming to develop a battery system enabling the 500-miles range for the EV [64]. Nowadays, the research is focusing on solving the key issues hampering the development of Li-O_2 batteries: sluggish kinetics of ORR/OER, poor cyclability, low stability, large charge overpotential, and the detrimental influence of parasitic reactions on the performance of Li-O_2 batteries.

High theoretical energy density of Li-O_2 batteries is attributed to the energy released from the oxidation of lithium. Even though, the amount of available energy to be released remain the same, the process of oxidation can be carried out in different ways.

Depending on the type of electrolyte utilized in a battery, three main systems can be distinguished: aprotic (non-aqueous), aqueous, and solid-state lithium-oxygen batteries – the advantages, disadvantages, material requirements, and the mechanism of electrode reactions taking place will be discussed in details in the following subsections.

2.2.1. Non-aqueous lithium-oxygen cells

Arguably, the highest attention among the mentioned three types of the Li-O_2 cells has been observed for cells utilizing the non-aqueous/aprotic electrolyte. The typical configuration of such cell is presented in the Fig. 2. The main components of aprotic Li-air cell include the lithium metal anode, electrolyte, porous cathode, and a semipermeable membrane, which allows the inflow of oxygen, but blocks the access of contaminations (mainly moisture and carbon dioxide). When the design of the cell do not include the semipermeable membrane, pure oxygen needs to be supplied to the interior of the cell, hence the term Li-O_2 cell. The employment of non-aqueous electrolyte affects the overall design of the cell along with the electrode reactions taking place during discharge/charge. The variety of available electrolytes combined with their unique properties generate opportunities to increase safety and efficiency of the Li-O_2 battery, but it also creates additional operational challenges.

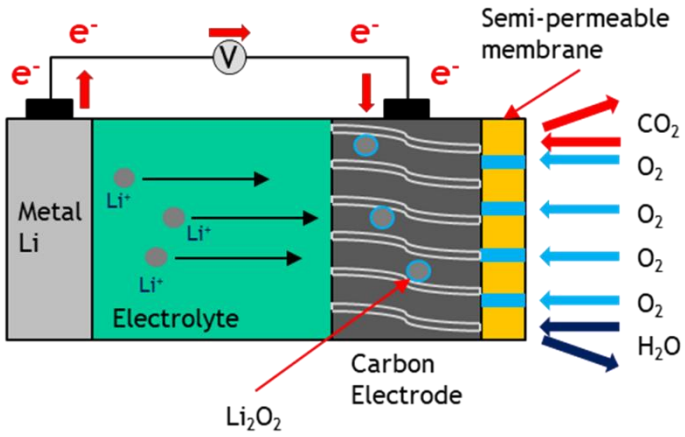

Fig. 2. The schematic configuration of the non-aqueous (aprotic) Li-air cell.

The discussion regarding the influence of the non-aqueous electrolyte on the operation of the Li-O_2 battery, should be preceded by the short explanation of the term "non-aqueous". Non-aqueous electrolytes are composed of a lithium salt dissolved in an aprotic solvents. While there is a wide range of a lithium salts that can be used (e.g., $LiPF_6$, $LiCF_3SO_3$, LiTFSI, $LiAsF_6$) [67, 68], the definition of the term "aprotic" restricts the number of available solvents. The aprotic solvents are a class of solvents lacking an acidic proton in their composition, which means that such compounds do not contain hydroxyl nor amine groups. As a result these solvents can not serve as hydrogen donors in hydrogen bonding, and can only act as proton acceptors. Many inorganic (e.g., sulfur dioxide, sulfuryl chloride fluoride, dinitrogen tetroxide) and organic (acetone, acetonitryl, dichloromethane, tetrahydrofuran) compounds are classified as aprotic solvents, but particular interest is focused on the polar aprotic solvents, as they possess the ability to dissolve salts, which is the key property when preparing the electrolyte

solution. The terms “non-aqueous” and “aprotic” will be used interchangeably in this work.

Requirements towards non-aqueous electrolytes include good stability during discharge/charge processes, high oxygen diffusivity, and low vapor pressure. Among the most frequently applied solvents in the aprotic electrolytes, two groups of organic compounds stands out – organic carbonates and ethers. Initially, carbonates, such as propylene carbonate and ethylene carbonate, have been investigated as potential solvents for aprotic electrolytes, due to their good electrical conductivity and oxygen solubility [69]. However, carbonates undergo decomposition in parasitic reactions, mainly at higher voltages (above 4.0 V). The alternative solvents for non-aqueous electrolytes are ethers. This group of organic solvents is characterized by larger stability and lower vapor pressure than carbonates. The examples of most commonly used ethers include tetraethylene glycol dimethyl ether (TEGDME), 1,2-dimethoxyethene (DME), and triethylene glycol dimethyl ether (triglyme) [70–72].

As has been previously mentioned, the operation principle of aprotic Li-O_2 cells is based on the two main reactions: ORR during discharging, and OER during charging. Initially during the development of these cells, the mechanism and final products of those reactions have been discussed and heavily researched. Different paths and mechanism have been proposed, but nowadays the common agreement is set, that ORR occurs via the path presented by the equations (1), (2), and (3). The lithium peroxide (Li_2O_2) is considered as the final product obtained via superoxide (LiO_2) intermediate [72, 73]. At the same time, the reaction yielding in the creation of lithium oxide (Li_2O) takes place (3).

$$Li^+ + O_2 + e^- \rightarrow LiO_2 \qquad (1)$$

$$LiO_2 + Li^+ + e^- \rightarrow Li_2O_2 \qquad (2)$$

$$Li_2O_2 + 2Li^+ + 2e^- \rightarrow 2\,Li_2O \qquad (3)$$

The OER occurring during discharging and yielding the evolution of gaseous oxygen can be described by equation (4) and (5).

$$Li_2O_2 \rightarrow LiO_2 + Li^+ + e^- \qquad (4)$$

$$LiO_2 \rightarrow Li^+ + O_2 + e^- \qquad (5)$$

The overall reactions taking place during the work of the aprotic Li-O_2 cell can be shortly presented by the equation (6). The theoretical standard potential of that reaction is 2.96 V, but due to the solid electrolyte interface (SEI) formation, side reactions, and other practical limitations (e.g., limited diffusion of oxygen in organic electrolyte), the actually measured potential is often much higher, which is defined as a cell’s overpotential.

$$2Li^+ + 2e^- + O_2 \leftrightarrow Li_2O_2 \qquad (6)$$

The crucial issue to overcome for the non-aqueous Li-O_2 cells is the reduction of the parasitic reactions occurring during the cell’s work. Due to the nature of used

materials – carbon containing electrolytes (e.g., carbonates) and the application of carbon materials in the cathode – the main challenge is to limit the interaction of those components with discharge products leading to the formation of by-products. Those by-products later decompose during charging, which result in the evolution of CO_2, instead or jointly with the evolution of O_2. The main by-products of those parasitic reactions are Li_2CO_3 and $LiRCO_3$ (R=alkyl group). While the precise mechanism of the formation and decomposition of those compound is still under consideration, many researches have proposed similar explanation that revolves around the interaction of carbon-containing components of the cell with discharge products, leading to the degradation of the prior [73–75]. The proposed approach indicates that reactions on the carbon-Li_2O_2 interface, leading to the formation of Li_2CO_3, are based on the equations (7) and (8). Similarly, the $LiRCO_3$ can be produced as a result of side reactions during discharging. However, the alkyl group (presented as R) derives from the decomposition of electrolyte.

$$Li_2O_2 + C + \frac{1}{2}O_2 \rightarrow Li_2CO_3 \qquad (7)$$

$$2Li_2O_2 + C \rightarrow Li_2O + Li_2CO_3 \qquad (8)$$

The described mechanism indicate that the nature of parasitic reactions can be either chemical or electrochemical. In the assessment of which process is dominant, multiple techniques, such as XPS, FTIR, and DEMS, have been implemented [75, 76]. From these measurements methods, the quantitative differential electrochemical mass spectrometry (DEMS), seems to provide the most valuable information – number of electrons per O_2 consumed during discharging or produced during charging (e^-/O_2 ratio). From the equation (6), the stoichiometric value for the e^-/O_2 ratio can be established at 2.000 – in the production/consumption of every molecule of O_2 two electrons are utilized. The analysis of DEMS measurements, enables the evaluation, whether the nature of parasitic reactions is rather electrochemical (e^-/O_2 ratio larger than 2.000) or chemical (e^-/O_2 close to 2.000). The determination of e^-/O_2 ratio is one of more precise method to verify the nature of parasitic reactions.

Multiple research works propose similar path for the creation of lithium carbonates, depending on cell's voltage and phase of the operation (discharge/charge) [75–77]. During discharge, the Li_2O_2 is formed as the main product, but the degradation of carbon cathode leads to the deposition of Li_2CO_3 at the C-Li_2O_2 interface. At the same time, the $LiRCO_3$ species, created from the decomposition of electrolyte, can be dispersed in the deposited layer of Li_2O_2. The value of e^-/O_2 ratio for this route is close to 2.000, suggesting the chemical nature. During charging the potential range has significant role on the occurring reactions. In the range of around 3 – 4 V vs Li, mostly lithium peroxide is decomposed and small amount of CO_2 is produced from the decay of electrolyte. Simultaneously, the lithium carbonates are accumulating on the Li_2O_2-electrolyte interface. After this phase, when the charging continues above 4 V vs Li, the full decomposition of the Li_2O_2 layer happens, which significantly increases the OER overpotential. The oxidation of carbonates, formed due to cathode degradation and electrolyte decomposition, takes place with higher intensity.

As a result, the majority of CO_2 evolved during charging is created at this phase. The considerable rise in the charge overpotential suggest the electrochemical character of these processes. The deposition of carbonates layer on the Li_2O_2 interface is so detrimental, that it is stated that even formation of one monolayer of the carbonates limits the charge transport and can lead to the 10-100-folds reduction of the exchanged current density [77].

The origin of parasitic reactions still remain the subject of research, with the superoxide activity being mentioned as the key factor promoting the formation of by-products during discharging [75, 76]. This theory is supported by the strong nucleophilic and base character of superoxide, and the fact that according to the equations (1) and (2), the LiO_2 serve as the intermediate in the Li_2O_2 formation. Moreover, the deviation of only couple of percent from the stoichiometric value of 2.000 in the DEMS measurements supports the thesis of superoxide's origin of parasitic reactions. While superoxide and peroxide activity in the side reactions is notable, it could not provide an explanation on why, during charging, additional solid side products are formed. The significant variations of DEMS measurements, by more than 10%, for charging, suggest the involvement of additional processes in the parasitic reactions occurring during charging [77]. The hypothesis regarding the creation of the singleton oxygen ($^1O_2$) has been proposed as a plausible explanation for the mentioned phenomenon and has later been proven by the experimental measurements [78]. Additionally, it has been observed that even trace amount of water can increase the creation of singleton oxygen, furtherly worsening the stability of the Li-O_2 cell. However, once the influence of $^1O_2$ production on the formation of the solid state by-products has been proven, new approached to improve the performance of the Li-O_2 cells has been proposed – $^1O_2$ traps and quenchers have been presented as a way to limit the creation of singleton oxygen, leading to the reduction of carbonates formation [78].

2.2.2. Aqueous lithium-oxygen cells

As a contrast to aprotic systems, the aqueous Li-O_2 cells utilize lithium salts solutions in water as the electrolyte (e.g., 1 M LiCl aqueous solution [79]), which proposes advantages not achievable for non-aqueous cells, but it also poses significant challenges for applied materials and the overall design of the cell. The schematic configuration of the aqueous Li-O_2 cell is presented in the Fig. 3. The utilization of aqueous electrolytes enables the limitation of used semipermeable membranes – only membrane blocking the inflow of CO_2 is required, as the carbon dioxide can take part in the parasitic reactions leading to the formation of carbonates. Additional advantage of aqueous electrolyte is their better cost-effectiveness, larger oxygen diffusivity, and higher ionic conductivity in comparison to aprotic electrolytes [80].

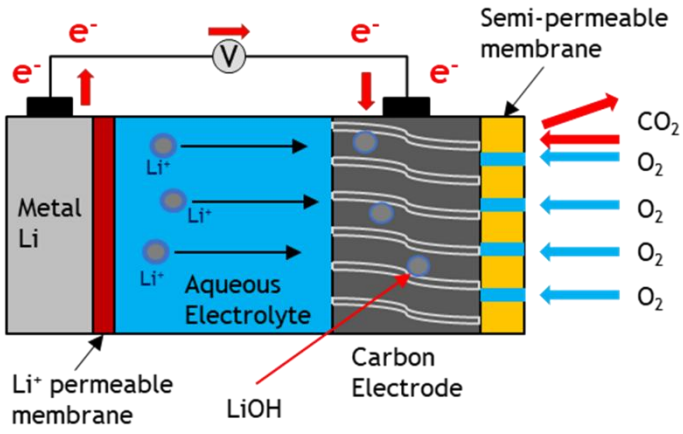

Fig. 3. The schematic configuration of the aqueous Li-air cell.

However, the main challenge in the application of water-based electrolytes is observed at the lithium metal anode-electrolyte interface – lithium vigorously reacts with water, creating a lot of heat, which can lead to the ignition. Potential high flammability is a significant risk, heavily impacting safety of aqueous lithium-oxygen batteries. To protect the lithium anode from reacting with water additional semipermeable membrane needs to be implemented between anode and electrolyte. Such membrane needs to act as an artificial SEI to prevent any contact between lithium and water, but, at the same time, it needs to allow the transportation of Li^+, so the electrode reaction could take place [81]. The development of effective, semipermeable membrane to protect Li-anode is still limiting further progress of the aqueous Li-O_2 cells. In most cases, polymer-based or ceramic-based interfaces are applied, with materials like lithium phosphorous nitride (LiPON) or PEO_{18}LiTFSI -1.44PP13TFSI being tested [79, 81, 82].

The mechanism of electrode reactions is another crucial difference between aprotic and aqueous Li-O_2 cells, but there is a general agreement that work of the aqueous system is based on the reversible reaction presented by the equation (9). On the cathode, oxygen reduction/evolution reactions take place, while on the anode Li/Li^+ redox reaction occurs.

$$2Li + \frac{1}{2}O_2 + 2H_2O \leftrightarrow 2LiOH \qquad (9)$$

The additional advantage of described electrode reactions, is the nature of the main discharge product – lithium hydroxide (LiOH) – as it is soluble in aqueous electrolyte. Due to that property of LiOH, the limitation of aprotic cells, like blockage of cathode's porosity, electrical conductivity issues, and volume expansion, are largely eliminated [64].

2.2.3. Solid state lithium-oxygen cells

One of the most interesting type of design for Li-O_2 cells are offered by the application of the solid state electrolyte. The architecture of such cell is presented in the Fig. 4. and it is similar to the design of aprotic Li-O_2 cell (Fig. 2.), with the main difference laying in the physical state of an electrolyte. The key advantages of

utilization of solid electrolyte are improved safety during the cell's operation, due to the lack of flammable and volatile solvents, and higher durability (solid electrolyte can not dry out). Additionally, the solid state Li-O_2 cells can operate in the elevated temperatures, as opposed to the aprotic or aqueous cells. However, the solid state electrolytes suffer from issues that substantially hamper their development and wide use, mainly low lithium ion and electrical conductivity, combined with providing insufficient contact surface area between electrodes and gaseous oxygen [81].

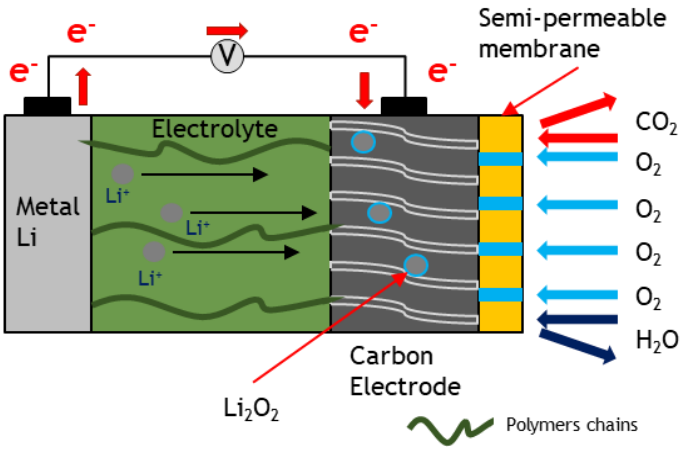

Fig. 4. The schematic configuration of the Li-air cell with solid state electrolyte.

To effectively take advantage of opportunities presented by the solid electrolytes, materials proposed as such electrolytes needs to meet specific requirements in terms of their properties, sustainability, and fabrication methods. The solid state electrolytes should be available in the form of thin and mechanically robust membranes, that can guarantee a high lithium ions conductivity and an efficient oxygen diffusivity. Moreover, materials for solid state electrolytes should be chemically and electrochemically stable in contact with lithium metal anode, air electrode, and discharge products. In order to attract attention from the industrial development perspective, proposed materials should also offer the ease of fabrication, non-toxicity, and low-cost [83]. Based on the utilized materials, solid state electrolytes can be divide into two main groups: organic (mainly polymer-based) and inorganic (e.g., ceramic based electrolytes, perovskites, and garnet-type lithium ions conducting oxides) [81].

Due to their chemical and thermal stability, good mechanical strength, and relative ease of manufacturing, the glass-ceramics compounds are arguably the most promising solutions for inorganic solid state electrolytes. Two main groups of the ceramic-based solid electrolytes include the NASICON-type and LISICON-type materials. NASICON stand for the Sodium Super Ionic Conductor and were firstly obtained by Hong and Goodenough *et al.* in 1976 [84]. The firstly obtained and characterized NASICON-type materials could be described by the general formula of $Na_{1+x}Zr_2(Si_xP_{3-x})O_{12}$ ($0 \leq x \leq 3$). Since then, this class of inorganic compound have been intensively studied and used in energy storage applications, including Li-O_2 cells [85, 86]. Similar family of materials are LISICONs (Lithium Super Ionic Conductors), with the general formula of $Li_{2+2x}Zn_{1-x}GeO_4$. Both of these groups are

characterized by relatively good ionic conductivity at a room temperature, which, in some cases, can be increased after the temperature elevation [81]. Even though, the ceramic-based electrolytes are noted as chemically and mechanically resistant, they are prone to react with lithium metal. The contact of NASICON or LISICON type solid electrolyte with Li anode, combined with the pressure usually applied to the cell, required to maintain the connection between components of the cell, can cause cracks in the ceramic membranes [87]. Another challenge in the utilization of ceramic-based electrolyte is poor surface area of connection on the interface of Li anode-ceramic electrolyte-cathode.

Another class of inorganic solid state electrolytes are perovskites. The extensive investigation of their applications in Li-O_2 is attributed to their high lithium ion conductivity at the room temperatures. The crystal structure of perovskite utilized as solid state electrolytes can be presented with a general formula of ABO_3, with A = Ca, Sr, La, and B = Al, Ti [88, 89]. The example of perovskite that has been widely utilized in Li-O_2 cells is lithium lanthanum titanate (LTO or LLTO) [90]. High Li^+-ion conductivity of perovskites is related to the concentration of A type site vacancies, which enable the transportation of lithium ions between the A-sites. Moreover, due to the stability of perovskites in aqueous solutions, they have been proposed as the artificial protective SEI interfaces for aqueous and hybrid Li-O_2 cells, leading to the improvement in their performance [91, 92]. The development of perovskite as solid state electrolytes, or protective layers, is severely limited by their tendency to interact with lithium metal anode and high grain boundary resistance. The instability of perovskites in contact with Li metal is caused by the reduction of Ti^{4+} to Ti, as observed in LLTO, which lower ionic conductivity of the material [88]. The efforts to reduce the effect of the high grain-boundary resistance by the modification of perovskites structure have been proposed, with nitrogen doping increasing the boundary conductivity [93].

High lithium ions conductivity, good thermal stability, combined with the stability in contact with lithium metal, led to the world-wide interest in garnet-type materials as solid state electrolytes and artificial SEI layer in the aqueous Li-O_2 cells [81, 94, 95]. Since the synthesis by Murugan *et al.* in 2007 of highly conductive at room temperature $Li_7La_3Zr_3O_{12}$ the interest in garnet-based materials has grown significantly [95, 96]. However, the garnet-type electrolytes are sensitive for even a trace amounts of moisture or CO_2, which block they potential application as an artificial SEI for aqueous Li-O_2 cells. Also, the high cost of mass production of garnet-based materials limits their possible utilization at industrial scale [90].

In organic solid state electrolytes, polymers-based solutions have been the most frequently researched, due to their less complex synthesis routes and wide range of available compounds. Additionally, it has been proven that the Li-O_2 cell with the solid state polymer electrolyte can operate at elevated temperature (80°C) and still present low overpotential and satisfactory discharge capacity [97]. Although, the temperature range of operation of polymer-based electrolytes is significantly lower than the range for ceramic, but it is still higher than for aprotic or aqueous electrolytes. The polymer-based solid electrolytes are usually composed of polyethylene oxide (PEO), as it

provides excellent interface between cell's components and can be easily formed. However, other polymers have also been proposed as a potential solid state electrolytes, including polyacrylonitrile (PAN), polypropylene oxide (PPO) or copolymer of polyvinylidene fluoride and hexafluoropropylene (PVDF-HFP) [90, 98, 99]. Although, the polymers are perceived as promising solid state electrolytes the insufficient ionic conductivity and potential decomposition of polymer matrixes under the operating conditions in the Li-O_2 cells are still hindering the development of this type of electrolytes.

Despite significant differences between electrolytes in aprotic and solid state Li-O_2 cells, it is commonly accepted that electrode reactions taking place during discharging and charging in solid state cells follow the same mechanism as the ones described for aprotic Li-O_2 cells [90]. The same routes for the ORR/OER are proposed for cells operating with the organic or inorganic solid state electrolytes, which can be presented by equations (1-5) and summarized by the equation (6).

The advantages of solid state Li-O_2 cells are a promising perspective for the development of lithium-oxygen batteries that could be applied at a larger scale. The increased safety and longer cycle life, resulting from the application of inflammable and non-volatile electrolyte, are crucial for future development of Li-O_2 batteries. However, the still unsatisfactory ionic conductivity, the proneness to react with lithium, and insufficient contact area between cell's components are the main challenges to overcome for the advancement of solid state electrolytes.

2.3. Cathode materials of lithium-oxygen cells

The cathode is a key component of a Li-O_2 cell as it catalyzes ORR/OER, stores discharge products, facilitates oxygen diffusion and ions transportation. The typical cathode for lithium-oxygen cell consists of three main parts – current collector, binder, and cathode material. The current collector is usually made of nickel foam, stainless steel mesh, or carbon paper [100–102], and is used to create a connection between the active cathode material and the external electrical circuit to transmit electrons between them. In addition, current collectors improve the mechanical stability of cathode. Binder is mixed with a cathode material and as obtained slurry is placed onto current collector‘s surface. The main role of binder is to help adhere the active cathode materials to current collector and maintain the structural integrity of the electrode. Typically polymers, such as polyvinylidene fluoride (PVDF) and polytetrafluoroethylene (PTFE), are applied as binders and their content in the slurry composition usually is around a couple of mass percentage (~10% wt. %) [103]. A cathode material is the main active component, which influences the cell performance. Because of the functionality of this component, cathode materials are required to meet a vast list of requirements.

The appropriate porous structure of cathode materials is one of the crucial characteristic of cathode materials. In order to enable sufficient level of oxygen diffusivity and to offer large storage capacity for discharge products, cathode materials should have dominant mesoporosity and relatively large specific surface area

(SSA) [104]. Furthermore, materials that are considered to work as cathodes in Li-O_2 cells must present good electrical conductivity and catalytic activity in ORR/OER. The good electrical conductivity of the material improves electron transfer, which, combined with high catalytic activity, lead to a decrease in charge overpotential, improving the cell's performance [105]. Additionally, the cathode material must have good mechanical and chemical stability, which will enable good and consistent performance of Li-O_2 battery without the risk of the decomposition of materials. The chemical resistance during the operation of the cell, combined with the selectivity of catalytic activity toward the ORR/OER lead to the limitation of parasitic reactions occurring during the work of the cell.

Apart from the intrinsic properties of cathode materials, other aspects are also included in the assessment process. Examples of such factors include material sustainability, ease of manufacturing, scalability of production, and cost. The material suitable for the large-scale application as the cathode in lithium-oxygen cells needs to be environmentally friendly and cost-effective [105]. Additionally, its production should be scalable and relatively straightforward.

Among the cathode materials, three main groups can be distinguished: carbon materials, non-carbon materials, and catalyst. Each of the mentioned groups will be discussed in a separate section.

2.3.1. Carbon materials

Carbon materials are a broad class of solids composed primarily of carbon at different hybridizations – sp, sp^2, sp^3, or mixed hybridizations that create the C-C bonding. This class includes a wide range of structures that vary in properties, from materials such as diamonds, graphite, activated carbons, or carbon blacks to nanomaterials, including graphene, fullerenes, graphene oxides (GO), carbon nanotubes (CNT), and carbon nanofibers (CNF). This variety of carbon materials results in their application in many industries, for example, activated carbons are used as a support material for catalysts and as an absorbent in medicine and in industrial gasses purification. The additional advantage of this group is the diversity of synthesis methods and raw materials that can be utilized in their production. Depending on the requirements, bottom-up or top-down techniques can be employed in the preparation of various carbon materials.

As has been previously emphasized, high porosity, large specific surface area, catalytic activity in ORR/OER, and good electrical conductivity are necessary qualities of cathode material for the application in Li-O_2 batteries. Many carbon materials have been proposed and investigated in this role, including carbon blacks, activated carbons, GO, CNT, and CNF, because of their ability to meet the mentioned requirements. The overview of the synthesis routes, characteristics, and performance as cathode materials of selected carbon materials is presented in the following subsections (2.3.1.1 – 2.3.1.5).

2.3.1.1. Carbon black

Carbon black (CB) is one of the most abundantly produced carbon materials. It is manufactured by the thermal decomposition of carbon rich substrate at high

temperature under precisely controlled oxygen-depleted (partial combustion) or inert (pyrolysis) atmosphere. The majority of CBs produced worldwide is utilized as pigments or as fillers in rubber and plastics. In recent years, carbon black has reclaimed the interest due to research regarding its potential applications in the carbon capture technologies, energy storage (batteries) and production (fuel cells) sectors. The great interest in CBs is closely related to their economical attractiveness, wide range of production methods, and the tunability of properties according to the requirements [106].

Based on the production method, three main groups of carbon blacks can be distinguished – furnace blacks, thermal blacks, and acetylene blacks. The other groups of CBs, such as impingement, gas, channel, or lamp blacks, have been gradually phased out of the large scale production due to the lower environmental friendliness and economic viability of their manufacturing processes [107].

Depending on the used raw materials and manufacturing process, the composition and structure of carbon black can vary significantly. Carbon blacks are mainly composed of carbon, with thermal and acetylene blacks consisting of more than 99% carbon. Other CBs grades can consist of considerable amounts of hydrogen, oxygen, nitrogen, and sulfur. Nitrogen and sulfur are usually integrated with the aromatic structures, while hydrogen is mostly present in C-H bonds at the edges of the carbon layers. Different oxygen groups, such as -OH, -COOH, and C=O, can be found on the surface of carbon black depending on the amount of oxygen used during the manufacturing process [106].

In terms of structure, carbon blacks are aggregates of spheroidal nanoparticles, with the diameters of around 10-100 nm. Each nanoparticle is composed of graphene-like domains, made of 3-4 turbostratically stacked polyaromatic sheets, surrounding an amorphous core, the described structure is schematically presented in the Fig. 5. The graphene-like domains typically arrange themselves in a concentric pattern around the amorphous core, forming disordered onion-like structures, and are commonly referred to as the basic structural unit (BSU) [108]. The structure of an aggregate is determined by the size and number of BSU. Low structure carbon blacks have aggregates made of less but larger BSU, which results in coarse structure. On the contrary, high structure carbon blacks consist larger number of smaller aggregates creating fine structure.

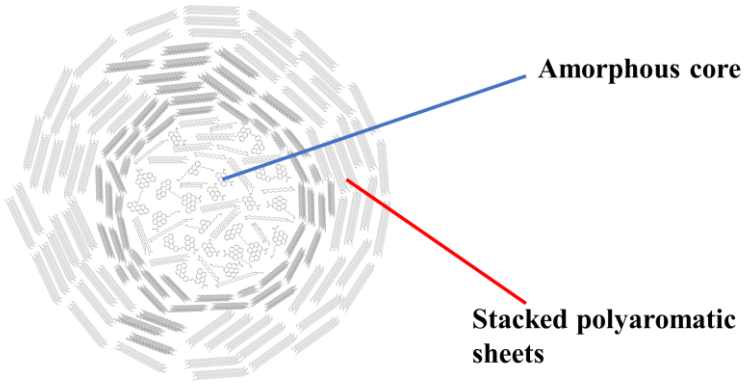

Fig. 5. Schematic representation of structure of carbon blacks.

One of the most relevant properties of carbon blacks for application as cathode materials in batteries is their electric conductivity. Due to the described structure of CBs, their mechanism of electrical conductivity is a combination of intra- and inter-particle charge transport. The intraparticle mechanism of electrical conduction within graphene-like domains is based on holes as primary charge carriers [109]. For the interparticle conduction, the mechanism is primarily governed by electron tunneling, which facilitates the transfer of electrons across the aggregates. As a result, electrical properties of CBs are dependent on the contact between BSUs, which relies on the size and separation distance of aggregates. Additionally, the number of impurities and heteroatoms also affects the electric conductivity of CBs. Thus, thermal treatment is proposed as one of the solutions to increase the graphitization level and to remove heteroatoms from carbon black, consequently leading to the improvement of electrical properties of the material. In addition, mechanical compression has been proven to be an effective way to increase contact between aggregates and increase electrical conductivity [110].

Apart from the good electrical conductivity, the possibility of obtaining carbon blacks with relatively large specific surface area is advantageous for their application as cathode materials. Typically, CBs have a specific surface area of around 20 to 150 m^2g^{-1}, but, depending on raw materials and production methods, the SSA can be increased even to 1500 m^2g^{-1} [111]. In addition, carbon blacks can be easily modified or functionalized, enabling further tailoring of their properties to enhance their potential as cathodes [106]. The main factor hampering utilization of CBs as cathode materials in Li-O_2 batteries is their insufficient catalytic activity in ORR/OER.

2.3.1.2. Activated carbon

The application of activated carbons (ACs) as cathode materials in Li-O_2 batteries is mainly attributed to their extremely well-developed porosity and high specific surface area. Moreover, porosity and SSA can be designed precisely according to the requirements by adjusting the production method, process parameters, and type of carbon precursors. The production of activated carbon is economically attractive and can easily be expanded to the industrial scale. Additionally, the mechanical and chemical resistivity, combined with good electrical conductivity promoted application

of activated carbons in various energy storage systems – not only as cathode materials in lithium-oxygen cells, but also as an electrode materials in electric double-layer capacitors (EDLCs) or as an adsorbent in hydrogen and methane storage [112, 113].

Even though activated carbons are widely considered in the energy storage sector, they are predominantly utilized as an adsorptive materials in different end-use – from the medical and waste management sectors to the purification of industrial gasses [114]. Apart from the application as adsorbents, activated carbons are also considered as support materials for catalyst or in drug delivery systems [115].

In order to obtain material with high specific surface area and porosity, a material needs to undergo a process to develop existing porous structures or generate a new porosity. This treatment is called 'activation' and can be divided into two groups, physical activation and chemical activation. The goal of both of these processes is the same, but there are significant differences in the mechanism, utilized resources, and properties of the final product. The physical activation is usually a two-step process that is often used at the industrial scale. During the first phase, precarbonization of the raw material occurs as a result of a thermal treatment in an inert conditions (around 600-900°C). In the second stage, activation, or gasification, occurs (around 800-1000°C) and the porosity of final product is increased. Among activation agents, carbon dioxide, steam, and air are the most widely used. On the other hand, the chemical activation is based on a one-step process that consist of cocarbonization of a raw material with an activation agent, in this case solid or liquid chemical. The wide range of potential agents can be applied in chemical activation, but the most commonly used are potassium hydroxide, phosphoric acid, and zinc chloride. The activated carbons obtained via chemical activation are usually characterized by higher specific surface area, which can exceed 3000 m^2g^{-1} in the case of processes utilizing KOH as activation agent. The structure and porosity of activated carbons depend not only on the preparation method and process parameters, but also on the nature of the raw materials used for their production. One of the many advantages of ACs is the broad range of precursors that can be utilized in their synthesis – almost any carbon containing material can be used for this purpose. However, the source material selected for the production process will have fundamental impact on properties of the final product, thus, the precursor must meet the specific requirements, changing according to the application of the obtained material. In most cases, high carbon content and low inorganic matter content are beneficial, because they lead to high carbonization yield [112]. The low mineral content is especially important for the production of activated carbons that will be applied as electrode materials. Mechanical properties also strongly depend on the nature of carbon precursors, e.g., the utilization of some types of waste biomass, such as coconut shells, yields in ACs with high mechanical durability [116]. Additionally, carbon source should be low cost, that is why many waste materials are utilized in the manufacturing of activated carbons. Among raw materials used for the production of activated carbons, three main groups can be distinguished: 1) wood and waste biomass (including lignocellulosic materials) [112]; 2) polymeric wastes (e.g., polystyrene, poly(ethylene terephthalate), phenol-formaldehyde resins) [117–119]; 3) coals.

Depending on the availability of raw materials and the desired properties of the final product, different types or mixtures of a few groups of precursors can be utilized in the production of activated carbons.

The structure of activated carbons is composed of graphene crystallites oriented randomly, cross-linked by disordered carbon, which creates open pore spaces – the schematic structure of activated carbons is presented in the Fig. 6.1. ACs are classified as a non-graphitizable carbons, which indicates that this group of materials can not form a three-dimensional graphitic structure under high-temperature treatment (up to 3000°C) in an inert atmosphere [112] – as presented in the Fig. 6.2. The well-developed porosity of activated carbons is attributed to their specific structure, resembling wood shavings. Micropores are open spaces, usually slit-shaped, present in the ACs structure, while mesopores and macropores are a consequence of hollow voids between aggregates.

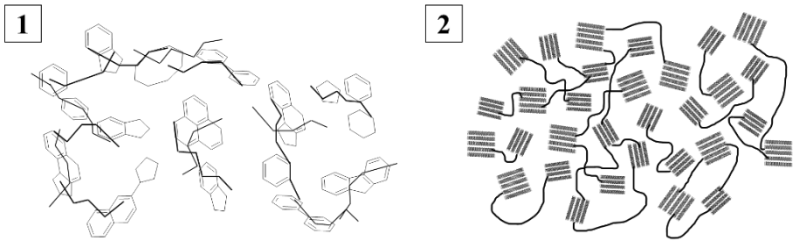

Fig. 6. Schematic presentation of the carbon structure of: 1) activated carbons; 2) non-graphitizable carbons.

The main composition element of activated carbons is carbon, but its content can vary significantly from 70 to 95 wt.%. Similar fluctuations are observed for the oxygen content, which can be in the range of 5-25 wt.%. In the case of heteroatoms, mainly nitrogen, sulfur, and phosphor are found in ACs, and their content can change. The final composition of activated carbon is closely related to the activation method and the type of carbon precursor chosen for the production process. Moreover, in some cases, a raw material with high nitrogen content can be selected as a method of functionalization of the produced material to enhance its electrochemical activity [114].

2.3.1.3. Carbon nanofibers

Carbon nanofibers are cylindrical nanostructures classified as one-dimensional (1D) nanomaterials with sp^2 carbon atoms as a main building element. The stacked graphene layers, building the nanofibers, can be arranged in the form of cones, plates, or cups. The orientation of the graphene layers has a dominant impact on the properties of the CNF, especially the mechanical properties. Three types of CNF can be distinguished depending on the position of the graphene layers – platelet, tubular, and fishbone, as it is presented in the Fig. 7.

Generally, carbon nanofibers display good thermal and electrical conductivity, low weight, high surface-to-volume ratio, relatively well-developed SSA and porosity. Due to their unique characteristics, CNF have been proposed in the broad range of applications – from utilization in the medical sector, e.g., as carriers in drug delivery systems (predominantly CNT are proposed for this application, but CNF are also investigated), biosensors or tissue engineering, to the huge interest in the energy storage

systems [120]. In the field of ESS, carbon nanofibers are considered in the utilization in batteries, supercapacitors, and hydrogen storage.

The final characteristics of produced carbon nanofibers and as a result their potential end-use is to a large extend dependent on the synthesis method, raw materials, and conditions of the manufacturing process. Among many available processes, the most commonly utilized are chemical vapor deposition (CVD) and electrospinning, with other methods such as arc-discharge and templating being less frequently applied [121].

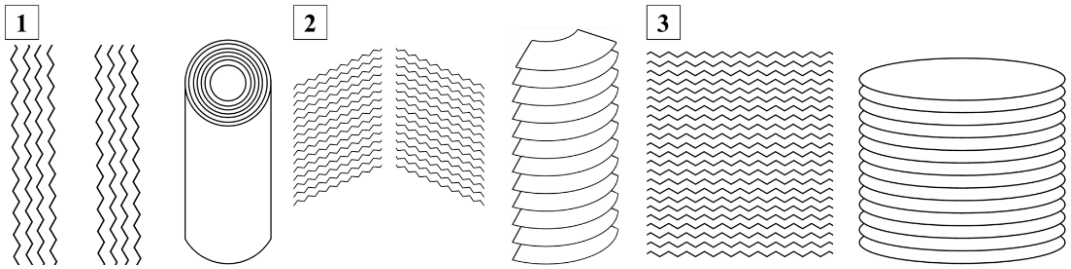

Fig. 7. Schematic presentation of the three types of carbon nanofibers structure: 1) tubular type; 2) fishbone type; 3) platelet type.

The electrospinning method includes two steps – fabrication of polymer nanofiber and subsequent thermal treatment. In the first phase, nanofiber is electrospun from a polymer solution by applying a strong electrostatic field to a capillary attached to a container with the solution. In the second step, the obtained nanofibers are thermally treated in an inert atmosphere, leading to the synthesis of carbon nanofibers that can have various dimensions, from a couple of nanometers to micrometers in length [121]. This method is characterized by its relatively low cost, simplicity, and the opportunity to tailor the morphology of the produced CNF by controlling the process parameters. In the case of the electrospinning phase, the main parameters include the spinning voltage, concentration of the polymer solution, feeding rate, and working distance. Among the variety of polymer precursors that can be potentially applied, the three most commonly used are polyacrylonitrile, pitch, or cellulose, with PAN being the most widespread due to its flexibility and high carbon yield [122]. Other polymers, such as poly(vinyl alcohol), phenolic resin, and poly(vinyl fluoride), have also been investigated as precursors in electrospinning for the production of CNF, but they did not receive similar attention within researchers. In terms of solvent, a wide range of compounds are applied, for example, acetone, toluene, dimethylformamide, toluene or even water [123]. The main parameter related to the second phase of the CNF synthesis is the temperature of thermal treatment. Once more, the selection of the process temperature has a definitive impact on the morphology of the product, and that influence changes depending on the composition of the feeding solution. The range of applied temperature is vast, from around 600°C to 1200°C, but in general with higher temperatures of the thermal treatment, thinner CNF are obtained [121].

Chemical vapor deposition, either thermally or plasma assisted, is the dominant method of production of carbon nanofibers. This process is based on the decomposition of the gaseous carbon precursor at high temperatures. The presence of catalyst particles

is required for the decomposition of a carbon source and the subsequent growth of CNF. The CVD process can be relatively easily scaled-up, which favors its utilization in the commercial production of carbon nanofibers. Furthermore, by optimizing process parameters, such as type of carbon precursor, type of catalyst, and temperature of the process, the morphology of produced nanofibers can be tailored according to the requirements [120]. Usually, simple gaseous hydrocarbons, such as methane, ethane, propane, or ethylene, are used as a carbon precursor because of their availability and low cost. Among the utilized catalysts, transition-metal particles are commonly employed, with nickel, iron, and cobalt being the most frequently used. However, other transition metals, such as chromium, molybdenum, and vanadium, are also being investigated [124]. Alternatively, noble metals, including platinum and palladium, can be used, but due to scarcity and high cost, they are less commonly used as a catalyst [125]. Various combinations of the three mentioned parameters (catalyst, carbon source, and temperature) can lead to the synthesis of different morphologies of CNF, from platelet through fishbone to tubular, with the combination of different morphologies obtained during one process also being possible. Arguably the most prevalent catalyst in the CNF synthesis is nickel, its utilization at lower temperatures (around 450°C-550°C) generally favors the growth of the platelet CNF, while the moderate range of temperatures (around 550°C to 700°C) yields in the production of fishbone CNF, and above this range usually the tubular CNF are produced [126–128]. This versatility of design opportunities in the CVD process is particularly important for the synthesis of CNF for specific applications, like cathode materials for lithium-oxygen batteries.

2.3.1.4. Carbon nanotubes

Carbon nanotubes can be depicted as 1D nanomaterials composed of a two-dimensional graphene sheet rolled up to create a hollow cylinder. Generally, carbon nanotubes exhibit exceptional properties, especially in terms of exceptional tensile strength and excellent electrical and thermal conductivity [129, 130]. However, the specific characteristics of CNT are heavily dependent on their structure. Based on the number of sheets forming a CNT structure, two main types can be distinguished – single walled CNT (SWCNT) and multiwalled CNT (MWCNT). Moreover, carbon nanotubes can be separated into three groups based on the configuration of the carbon rings, zigzag, chiral and armchair CNT, as schematically presented in the Fig. 8. Described parameters of the carbon structure have fundamental influence mainly on the electrical properties. Depending on electrical conductivity, CNT can be divided into two categories: metallic nanotubes (with conductivity pathway similar to those observed in metals, such as gold or aluminum) and semiconducting nanotubes (way of conduct similar to silicon) [131]. Even a slight difference in the diameter of the nanotubes can shift the conductivity from the semiconducting to the metallic state.

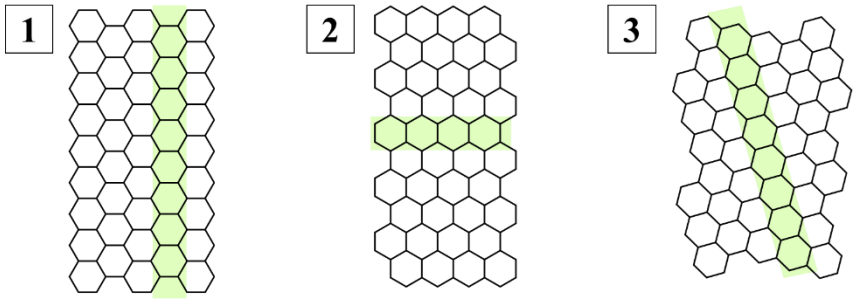

Fig. 8. Schematic representation of types of CNT based on the possible configurations of carbon rings: 1) armchair; 2) zigzag; 3) chiral.

Most of potential applications of carbon nanotubes are attributed to their unique electrical properties, due to which they are considered in various end-uses – as electrode materials in fuel cells and in energy storage systems (supercapacitors and batteries) [132–134]. In addition, because of the hollow space inside the CNT, they have been investigated as potential carriers in drug delivery systems. However, one of the most widespread commercial applications include their use in composite materials. CNT are added to various polymers to improve their thermal, electrical, and mechanical properties – such solution is used in the automotive, aerospace, or sport equipment industries [135].

Carbon nanotubes can be considered as an unique subtype of carbon nanofibers, thus their synthesis methods are very similar, and can be divided into two groups – a high temperature treatment of a carbon precursor (mostly graphite) and a chemical vapor deposition. The first group is characterized by extremally high temperatures (around 4000°C) required to obtain CNT and short times of the actual formation of nanostructures (from microseconds to milliseconds). The thermal requirements for these methods require the use of arc or plasma, so the main techniques utilized are arc discharge and laser ablation [135]. For both methods, parameters that can be controlled, which directly impact the characteristics of obtained CNT. Composition of the carbon precursor (usually the metal-impregnated graphite target), atmosphere (inert or vacuum), and the process temperature can be tailored according to the required properties of the final product. In terms of mechanism and principles, arc discharge and laser ablation are similar, but the main difference is the source of energy – electric discharge and laser, respectively. Both techniques yield in the mix of carbon nanostructures (e.g., fullerenes), which requires the purification step after synthesis, but product of laser ablation consist of around 70-90% of CNT, which is significantly higher than for the product of arc discharge [136]. However, from the financial standpoint the laser ablation is more expensive than the arc discharge technique, limiting its commercial application.

The most commonly used method for producing CNT is chemical vapor deposition, because of its relative simplicity, wide range of available carbon precursors, and lower cost of production. Another advantage in favor of CVD over arc discharge or laser ablation techniques is the range of temperatures used in CVD technique (500-1100°C), but the specific process temperature will rely on the applied raw material,

catalyst, and the required characteristics of produced CNT. As already described in the CNF section (2.3.1.3), all parameters of the CVD process can be tailored according to the desired properties of the obtained nanomaterial. In the case of CNT, another morphology parameter that can be designed is the number of walls in prepared CNT. Generally, carbon nanotubes are obtained on the iron-based catalyst, but, depending on the size of the catalyst particles size SWCNT or MWCNT can be synthesized – on smaller particles of catalyst will yield in the fabrication of SWCNT, and larger will lead to the preparation of MWCNT. CNT can also be produced on a nickel or cobalt-based catalyst, but this requires optimization in terms of other process parameters [135].

2.3.1.5. Carbon aerogels

All of the previously described carbon materials are usually used as cathode materials in the form of a slurry that is deposited on the surface of current collector. Such processing can severely reduce the porous structure and catalytic activity of carbon materials. The opportunity to limit the detrimental effect of material processing is presented by the preparation of a freestanding cathode. Although they do not represent an independent group of carbon materials, carbon aerogels are considered as a potential standalone cathode for lithium-oxygen batteries, due to their unique characteristics, including their lightweight nature, three-dimensional porous structure, and good mechanical and electrochemical stability [137]. Three main categories of carbon aerogels can be distinguished based on the type of carbon precursor utilized – phenolic resin derived aerogels, biomass derived carbon aerogels, and carbon nanomaterials derived aerogels (mostly CNT and graphene oxide based). Each of the aforementioned groups is produced by slightly different synthesis routes.

In the fabrication of phenolic resin-based aerogels, five basic steps can be distinguished: 1) sol formation at ambient temperature; 2) gelation at slightly increased temperature (25-90°C); 3) solvent exchange; 4) drying via various available methods (supercritical, room-temperature, or freeze-drying); 5) carbonization [138]. In the case of biomass-derived aerogels, their preparation is based on the condensation and cross-linking of organic polymers, such as chitin, cellulose, or lignin [138–140]. The gelation of biomass derived aerogels is governed by the intra- and intermolecular interactions of hydrogen bonds from the hydroxyl groups in polymer's chains, which limits the need to use additional cross-linking agents [141], but usually, strongly basic or acidic conditions are required to enable the dissolution of organic polymers. The formation of aerogels is preceded by freeze-drying combined with carbonization. Carbon aerogels that are derived from carbon nanomaterials are fabricated via initial preparation of a hydrogel, combined with subsequent drying or freeze-drying to form an aerogel. The preparation of hydrogel is a crucial step in the fabrication of carbon nanomaterials based aerogels, and it consists of a creation of an aqueous dispersion of nanomaterials, followed by a hydrothermal or chemical reduction. In the case of graphene oxides based aerogels, the aqueous dispersion is relatively straightforward to obtain (due to high content of oxygen groups in GO), but for CNT this step usually requires the addition of surfactant (like sodium dodecylbenzene sulfonate) or prior functionalization of CNT, due to their rather hydrophobic nature [142, 143].

The aforementioned properties of carbon aerogels have drawn the attention of researchers and resulted in the investigation of this class of materials in various applications in energy storage. The potential use of carbon aerogels as cathode in secondary batteries, including lithium-ion and lithium-sulfur batteries, has been extensively researched [144, 145]. However, utilization in lithium-oxygen batteries is still relatively new, with few papers examining this field [146, 147]. Mostly, graphene oxides aerogels have been implemented as a cathode in Li-O_2 batteries, but also CNT based aerogels are reported [137]. The combination of the easily accessible porosity of the aerogel with the catalytic activity and electrical conductivity of the carbon precursor allows good performance of a Li-O_2 battery equipped with such cathode.

2.3.2. Non-carbon materials

Although carbon materials have been widely used as cathode materials, due to their excellent properties, their application faces significant drawbacks. In the highly oxidizing environment of the lithium-oxygen cell, carbon based materials show a tendency to decompose during electrode reactions. The occurring parasitic reactions lead to the formation of side products, which can result in the increase of overpotential and cathode passivation, significantly limiting the battery life. Moreover, binders, commonly used in the preparation of carbon cathode slurry, generally have a nonconductive nature, furtherly reducing charge transfer, which hampers performance of the cell [148].

One of the strategy to overcome issues, related to the use of carbon materials, is the utilization of non-carbon cathode materials, like noble metals, transition metal oxides, metal-organic frameworks (MOFs), or perovskites. Most often these materials are added as catalysts to a carbon material-based slurry, to improve its properties, but their application as a standalone cathode material has also been investigated [149].

Among the reported solutions, porous gold has been proposed as a cathode material and tested in the Li-O_2 cell, which resulted in the decrease in charge overpotential in comparison to the carbon-based cathode [150]. Another approach presented the synthesis Co_3O_4 nanorods directly on the nickel foam carried out by chemical deposition reaction and utilization of as prepared free-standing cathode in lithium-oxygen cell [151]. The application of cobalt oxide nanorods, as the only material in cathode composition, resulted in achieving discharge and charge voltages close to the theoretical values. The main factors limiting the use of noble metals and transition metal oxides as sole cathode materials are their high price and scarcity. The utilization of MOFs and perovskites as standalone cathode materials is still relatively rarely investigated due to the more complex synthesis methods of those materials [152].

Even though, the utilization of non-carbon based cathode materials could lead to the improvement in the performance of the Li-O_2 batteries, the main research effort is still focused on the application of carbon containing materials. The outstanding characteristics and wide range of available carbon materials, combined with their low cost and tunability of performance, still tip the balance in favor of carbon. However, the potential of non-carbon materials is utilized by their use as catalysts.

2.3.3. Catalyst

The main goal of the application of catalyst is to enhance the properties of cathode materials, leading to the improvement in the performance of the Li-O_2 cell. To achieve enhanced electric conductivity and catalytic activity, precious metals, transition metal oxides, or heteroatoms can be incorporated into the structure of carbon materials. All of the mentioned types of structure functionalization offer specific advantages, face different drawbacks, and can be conducted via various methods.

2.3.3.1. Precious metals

Among the investigated precious metals, Au, Pt, Pd, and Ru have been the most frequently investigated, due to their extraordinary catalytic activity in the oxygen evolution reaction combined with good electric conductivity. Precious metals are most commonly incorporated in the carbon material in the form of nanoparticles deposited on their surface. Additionally, for CNT, endohedral encapsulation of noble metal nanoparticles is also achievable. Characteristic of the material is dependent on the preparation method, size of nanoparticles, and type of utilized approach [153].

Wet impregnation is one of the most frequently used techniques to conduct precious metal decoration of carbon materials. Impregnation is usually followed by thermal annealing that leads to the reduction and creation of precious metal's nanoparticles. The size of deposited nanoparticles can be controlled by manipulating the process parameters, e.g., type of chemical compounds, their concentration, temperature or the environment of thermal annealing. This relatively simple procedure can be used to deposit Ru, Pt, Pd, or Au nanoparticles on the carbon surface [154–156].

Another approach available for material modification is endohedral encapsulation of precious metal nanoparticles, and because of their structure this type of functionalization is accessible only for carbon nanotubes. To achieve encapsulation, the closed structure of CNT needs to be open via, for example, ball milling, and subsequent wet impregnation and thermal annealing can be performed [157]. Such change in the localization of precious metal nanoparticles significantly alternate the catalysis and conductivity mechanisms.

The noticeable growth in capacity and decrease in charge overpotential for the lithium-oxygen cells utilizing precious metal decorated carbon cathode can be attributed to the modified electronic state of cathode material's surface. Due to the high catalytic activity of precious metal nanoparticles in the oxygen evolution reaction, they promote the decomposition of Li_2O_2 during charging. However, the deposited nanoparticles can also participate in the ORR and formation of lithium peroxide during discharging. The inclusion of precious metal nanoparticles in the deposited Li_2O_2 can slightly increase its conductive properties, enabling easier decomposition during charging [153]. Moreover, some types of noble metal nanoparticles, e.g., gold, can even facilitate the decomposition of side reaction products, which can furtherly improve the performance of the Li-O_2 cell [154].

The coating conducted by the conventional wet impregnation leads to the formation of localized agglomerations of precious metal nanoparticles on the surface of

carbon material – active seeds, that display significantly higher catalytic activity than a pristine carbon material. The creation of active seeds leads to the formation of local enrichments of deposited Li_2O_2 on nanoparticle agglomerates, which results in an uneven coverage of cathode material. Agglomerates of non-conductive lithium peroxide formed on active seeds do not have a direct contact with the conductive surface of cathode material, which significantly worsen the decomposition of discharge products and eventually leads to electrode polarization. However, the creation of localized agglomerates of highly active seeds can be omitted by the encapsulation of precious metal nanoparticles inside CNT. These encapsulated nanoparticles affect the formation of discharge products on the surface of cathode materials by providing uniform electron distribution on the surface, resulting in a more evenly distributed layer of Li_2O_2 that decomposes more easily during charging.

However, the enhanced reactivity of precious metal containing cathode material can have undesirable impact on the performance of the Li-O_2 cell. Promotion of parasitic reactions can be caused by lowering the oxidation potentials for the evolution of carbon dioxide or increasing the oxygen reactivity toward the decomposition of an electrolyte. Such deteriorating activity of electrocatalyst has been reported for Pt, Ru, Au, and MnO_2 [158].

The final impact of precious metal doping on the performance of lithium-oxygen battery will vary, depending on the type of metal, chosen synthesis route, and the parameters of testing, such as current density or cathode support material. However, in the case of all precious metals, usually substantial improvement of performance can be observed. The utilization of Ru nanoparticles can lead to the increase of the first discharge capacity by 77% with the simultaneous decrease in charge and discharge overpotential, by 0.07 V and 0.55 V, respectively [156]. Similarly high increases in the first cycle discharge capacities by 42% and 67% have been observed, when Pd and Au nanoparticles, respectively, have been incorporated in the structure of carbon materials [154, 155].

In general, the use of precious metals is considered as an effective way of enhancing the properties of carbon-based cathode materials. The level of achievable improvement is substantial in comparison to that of unmodified carbon materials, but the broader application of this type of catalyst is constrained by its high price and scarcity. The large-scale production of lithium-oxygen batteries utilizing the precious metal containing cathode materials could be seen as not financially favorable, thus their application is limited to the laboratory scale.

2.3.3.2. Transition metal oxides

Apart from precious metals, transition metal oxides have been one of the first compounds investigated in the role of catalyst for cathode materials in lithium-oxygen cells. The variety of available transition metal oxides and functionalization methods, combined with thoroughly researched electrochemical properties have brought the attention of researchers to this class of catalysts. Moreover, the application of transition metal oxides is more economically viable than the use of precious metals. Transition

metal oxides improve the performance of Li-O_2 cells by increasing cyclability and lowering overpotential due to their high catalytic activity in ORR and OER, acceptable electric conductivity, and in most cases good corrosion resistance [153].

Among many transition metal oxides tested in the role of catalyst, manganese dioxide (MnO_2) is one of the most extensively investigated. Incorporation of MnO_2 into the structure of the carbon material can be carried out by various techniques, including wet impregnation followed by thermal annealing, hydrothermal method, or electrochemical deposition [159–161]. The appropriate adaptation of the functionalization process parameters allows to control the characteristic of the created MnO_2 layer, such as the mass loading of catalysts on the carbon material, the uniformity of the deposited layer, and the type of crystal structure (depending on the pH and temperature, α, β, or mixture of polymorphic crystal structures can be deposited from the $KMnO_4$ solution).

Another frequently explored catalyst of this class is cobalt and its oxides. Similarly to manganese dioxide, the feasibility of tailoring of synthesis techniques and significant improvements of Li-O_2 cell's performance are the main factors favoring the application of cobalt oxides. The majority of functionalization methods are based on wet impregnation of cobalt salts solution with subsequent thermal annealing [162, 163]. However, other techniques, including electrochemical deposition and the hydrothermal method, are also used for the incorporation of cobalt oxides into the carbon structure [163, 164].

Other transition metal oxides have been proposed as catalysts for cathode materials, but much less emphasis has been placed on them compared to manganese or cobalt oxides – iron and titanium oxides have been often researched. In the case of the functionalization of carbon materials with titanium oxide (TiO_2), predominantly the corrosion resistance of cathode material is enhanced, which directly improve the stability of cathode and cyclability of the cell. The coating of carbon material can be performed employing the atomic laser deposition technique (ALD), which allows relatively uniform coverage of carbon material with TiO_2 and precise control of thickness of the deposited layer [165]. On the other hand, the utilization of iron oxides as catalyst is a more cost-effective alternative to the previously described transition metal oxides. At the same time, high catalytic activity of iron oxides provides a sufficient improvement of Li-O_2 cell performance. The synthesis routes for the functionalization with iron oxides vary from straightforward wet impregnation and subsequent thermal treatment to electrospinning combined with calcination [166, 167].

The incorporation of transition metal oxides into the structure of carbon materials leads to the significant improvements in both discharge capacity and cyclability in comparison to unmodified cathode materials. The rise of discharge capacity varies, depending on the type of transition metal oxides included – from 13% increase observed for the CNT coated with CoO/Co [162], up to 77% growth in the first cycle discharge capacity, when the CNT/$TiO_{(2-x)}$ composite is applied as cathode material [165]. Even for the same transition metal oxides, the improvement of

performance of Li-O_2 cell can vary, as can be observed in the case of the application of MnO_2 as catalyst. Typically, an increase of couple of dozens percents in the first cycle discharge capacity is achievable, as presented in the work of Kavaki *et al.* (when the growth of 53% has been reported) [168]. However, substantial enhancements in the performance of the battery are also achievable, as reported by Li *et al.*, when the increase of 339% in the first cycle discharge capacity has been observed [159]. Additionally, the cyclability of the lithium-oxygen battery is also improved, as observed in the work of Yang *et al.* – when with the restricted discharge capacity at 500 mAh g^{-1}, the number of cycles have grown from 50 to 90 cycles after the functionalization of CNT with $TiO_{(2-x)}$ [165].

Different factors limit the application of transition metal oxides as a widespread catalyst for cathode materials for lithium-oxygen cells. Although the cost of transition metal oxides based catalyst is lower than precious metals based, they suffer from lower catalytic activity and poorer conductivity. Additionally, the environmental risks and geopolitical tensions related to the mining of some of those metals (e.g., cobalt) would need to be solved before the large-scale utilization in lithium-oxygen batteries [169, 170].

2.3.3.3. Heteroatoms

Despite the offered improvement in the Li-O_2 cell's performance , the utilization of precious metals and transition metals oxides as catalyst leads to a sustainability concern and increases the cost of cathode materials. The opportunity to eliminate these issues, while still enhancing the properties of cathode materials, is presented by the heteroatom doping. This method of functionalization is one of the most promising approaches for improving the characteristics of carbon materials, because of the extremely wide range of modification techniques available, great economic effectiveness, and tunability of the carbon structure. Moreover, the incorporation of different heteroatoms has been proven to impact the properties of carbon materials in a beneficial way, which only increases the attractiveness of this type of structure modification.

Oxygen

Apart from carbon and hydrogen, one of the main element in the composition of carbon materials is oxygen. The incorporation of oxygen into the carbon structure can occur unintentionally during synthesis or processing of carbon materials, or can be carried out deliberately to shift the properties of material. Chemical oxidation in acids (e.g., H_2SO_4 or HNO_3) or in hydrogen peroxide are one of the most frequently used methods to incorporate additional oxygen atoms into carbon structure. Oxygen is present in carbon structure in the form of various functional groups, the main oxygen groups appearing in the carbon materials are presented in the Fig. 9.

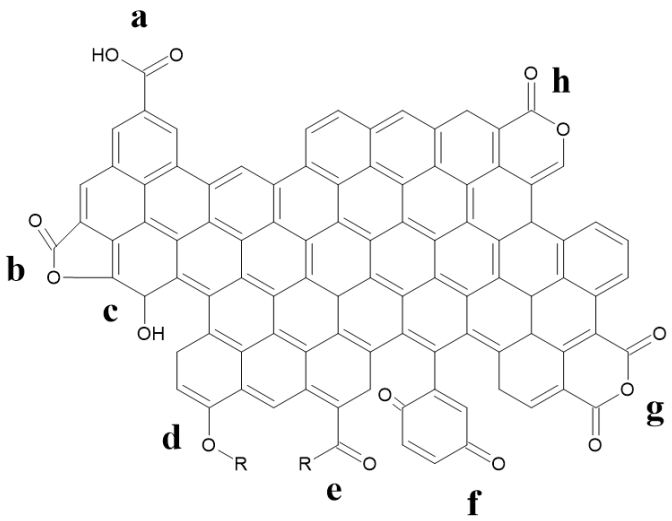

Fig. 9. Schematic presentation of main types of oxygen functional groups: a) carboxyl, b) lactone, c) hydroxyl, d) ether, e) carbonyl, f) quinone, g) acid anhydride, h) pyrone.

Generally, the oxidation of carbon materials changes their nature from hydrophobic to hydrophilic, which improves the wetting process of the cathode (in the case of polar electrolytes) and the diffusion of the electrolyte. Furthermore, the incorporation of oxygen functional groups in the cathode material changes the structure of discharge products by decreasing the size of the deposited Li_2O_2 crystallites (from around 2 μm to approximately 700 nm for unmodified and oxidized electrode, respectively), thus facilitating their easier decomposition during charging [171]. However, the increased content of oxygen groups can also have a detrimental influence on the working of lithium-oxygen cell. The interaction between oxygen groups and electrolyte can promote the decomposition of carbon cathode and electrolyte, resulting in a decrease in cyclability [172].

Nitrogen

Incorporation of nitrogen atoms as a catalyst has been investigated in various applications, including fuel cells, lithium-ion batteries, or EDLC [173]. The abundance of nitrogen-containing compounds, variety of functionalization methods, and different ways in which N atoms can influence the work of an electrochemical system are main reasons for the intense research on that element.

Methods of nitrogen doping can be separated into two groups – *in-situ* and *ex-situ* approach. The fundamental difference between these two groups is the phase of synthesis during which nitrogen atoms are built into the carbon structure. For the *in-situ* methods, N atoms are incorporated directly into carbon structure during the synthesis, which provide the opportunity to obtain N-doped carbon materials via relatively straightforward routes. Additional compounds, which act as nitrogen donors, can be introduced to the feed of raw materials. Alternatively, a carbon source can be replaced with a different chemical compound containing nitrogen and carbon, which will act as a carbon and nitrogen donor simultaneously. Due to the ease of modifying raw materials' feed, simplicity of technique, and its low cost, chemical vapor deposition is

frequently used for conducting the *in-situ* N-doping. Wide range of compounds can be utilized as nitrogen or nitrogen and carbon donors, including ammonia, melamine, or acetonitrile, which enables relatively simple design of N-doped materials. On the other hand, *ex-situ* approach require two-steps route – firstly, the carbon materials are synthesized via conventional techniques, and the subsequent treatment is conducted to incorporate nitrogen atoms into material's structure. In this case, the N-doping is usually conducted via wet treatment or hydrothermal method, where the carbon material reacts with nitrogen donor. This is a facile approach, due to the abundance of chemical compounds consisting of N atoms that can serve as a donor – from inorganic acids to organic solvents [153].

The broad range of available functionalization methods and the reactivity of carbon and nitrogen atoms leads to the multitude of nitrogen containing functional groups, which are presented in the Fig. 10. Although, there is vast number of configurations in which nitrogen can create bonds with other atoms to form various functional groups, the two key groups in terms of improving the properties of cathode materials in Li-O_2 cells are pyridinic and pyrrolic groups [100, 174–176]. Pyridinic nitrogen is bonded to sp^2 carbon atoms and is depicted as N atom located at the edge of carbon layers or as defect formed inside the carbon planes. Pyrrolic nitrogen is incorporated into the carbon framework by substituting carbon atoms. It is bonded to sp^3 hybridized carbon within a five-membered ring. Additionally, the graphitic (quaternary) nitrogen, which substitutes the carbon atom in a six-membered ring in the graphene basal plane, can improve the electrical conductivity of carbon material (by contributing two electrons to the π-π system), thus improving the performance of cathode material in lithium-oxygen battery. Nitrogen can influence the performance of the lithium-oxygen cell via different mechanisms.

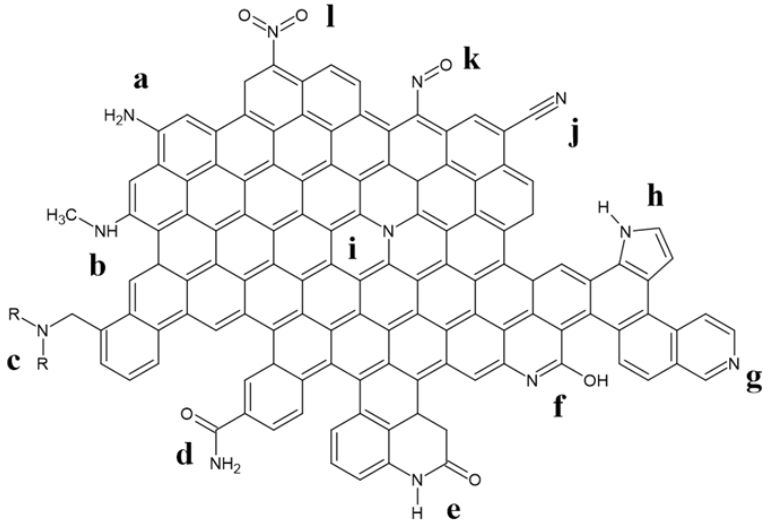

Fig. 10. Schematic presentation of types of nitrogen functional groups: a) primary amine, b) secondary amine, c) tertiary amine, d) amide, e) lactam, f) pyridone, g) pyridinic, h) pyrrolic, i) graphitic (quaternary), j) nitrile, k) nitroso, l) nitro.

Comparable amount of nitrogen atoms can be incorporated into the structure of carbon materials via *in-situ* and *ex-situ* functionalization methods. However, the final

composition and structure of N-doped carbon material will depend on process parameters, type of nitrogen donor, and reactivity of the carbon material itself, which is especially important for the *ex-situ* functionalization. Typically, around few percent (either wt. % or at. %) of nitrogen can be built into the structure of carbon materials in relatively mild conditions [174, 177–180]. However, the final influence of incorporated nitrogen on the performance of lithium-oxygen battery is heavily reliant on the settings and aperture used during the electrochemical measurements, e.g. type of cell, type of electrolyte, applied current density, and composition of cathode. For instance, in works from Ionescu *et al.* [177] and Mi *et al.* [178], similar amounts of nitrogen at 4.0 at. % and 3.92 at. %, respectively, have been built into the structure of cathode materials via *in-situ* functionalization, but the observed changes in the performance of Li-O_2 battery have been different. For the prior research by Ionescu *et al.*, increase by 18% of the first cycle discharge capacity have been observed, as compared to the unmodified material, while in the research by Mi *et al.* growth by 44% has been reported. Similar incoherent findings have been reported for cathode materials, that have undergone N-doping via *ex-situ* techniques. In the research by Zhang *et al.* [180] and Li *et al.* [174], comparable amount of N atoms have been introduced to the structure of cathode materials, respectively 2.98 at. % and 2.8 at. %. Comparable increases, to the ones mentioned above, of the first cycle discharge capacity by 22% and 40%, respectively, have been reported.

In general, nitrogen can be described as an n-type carbon dopant, which donates electrons into the graphene domain and assists in the formation of defected carbon nanostructures, which can facilitate the ORR. During the oxygen reduction reaction, additional electrons from nitrogen's lone pair can increase the binding energy between the carbon, nitrogen, and oxygen, leading to the enhanced oxygen molecule adsorption on the functionalized material's surface. Moreover, the N-doping can improve the electrochemical properties of carbon materials by the interaction of the nitrogen's electrons lone pair and graphene's π-electrons. The introduction of nitrogen into the carbon structure leads to the formation of a large number of active sites and a more irregular morphology. An increased number of nucleation sites results in the formation of more uniformly distributed layer of discharge products, which favors lower polarization and leads to the superior performance of the cell. The increased conductivity of modified surface and more evenly distributed layer of discharge products, promote the decomposition of Li_2O_2 during charging, improving the catalytic activity of N-doped materials in OER [153].

Other heteroatoms

Apart from the already described catalyst, other heteroatoms are also used in this role for cathode materials in lithium-oxygen cells. However, in comparison to nitrogen, oxygen, precious metals, or transition metal oxides, their application is much less frequently investigated. Amongst other heteroatoms applied as catalyst, boron, silicon, and phosphorus are one of the mostly tested.

In the case of functionalization of carbon materials with boron, such functionalization can be conducted by the wet impregnation in boron alcoholic suspension followed by thermal annealing [181]. The implementation of boron into the carbon structure yielded in exceptionally high capacity combined with good stability, which has been attributed to formation of the large number of nucleation sites, promoting the deposition of uniform layer of discharge products and their easier decomposition during charging.

The improvement of a Li-O_2 cell performance is also observed for the Si-enriched CNT, prepared via magnetic sputtering [182]. The as prepared Si-coated cathode material promoted the formation of smaller Li_2O_2 particles, leading to their more facile decomposition during charging, which significantly decreased the charge overpotential and increased discharge capacity.

Phosphorus doping has been reported as an effective way to improve the electrocatalytic properties of carbon materials, mainly by improving their activity in ORR [183]. However, the application of P-doped carbon materials as cathodes in lithium-oxygen cells is rarely investigated field. Although, the use of phosphorus doped Co_3O_4 particles, as cathode material, has been proven to improve the performance of the LiO_2 cell in comparison to unmodified material [184].

The preparation of efficient cathode material is still a crucial challenge for the development of Li-O_2 cells, but the availability of various catalysts and different functionalization methods is promising. Significant improvements in the work of the cells are observed after the modification with precious metal, transition metal oxides, or heteroatoms doping. Achieving suitable performance in a cost-efficient way is the key for the future of lithium-oxygen cells.

3. Goals

The main goal of the presented research is to develop or improve a synthesis method of new cathode materials and optimize their properties to achieve the best performance of lithium-oxygen batteries. However, each section is targeted to investigate slightly different parameters of synthesis that influence the structure of obtained materials and, as a result, the operation of the Li-O_2 battery.

Based on the conducted research, the correlation between synthesis temperature of carbon nanofibers via CVD method and their performance as cathode materials for lithium-oxygen battery will be investigated and the optimal temperature will be determined. In the case of surface modifications, multiple functionalization techniques, both *in-situ* and *ex-situ*, are explored in order to determine the influence of nitrogen and oxygen contents on the electrochemical performance of tested materials. Based on obtained results, the functionalization method that leads to the most significant improvement of performance of Li-O_2 battery will be selected.

Furthermore, the research regarding the influence of porosity of cathode material on the performance of lithium-oxygen battery is carried out to test the beneficial impact of dominant mesoporosity in activated carbons. The activated carbon enabling the best

performance of the Li-O_2 battery will be selected as a support material for the development of cathode materials composed of carbon nanofibers synthesized on the AC and nickel oxalate based catalyst. The influence of composition of the catalyst on the electrochemical properties of obtained materials will be investigated.

Lastly, new method of preparation of carbon aerogels is proposed and the potential application of obtained aerogels as free-standing cathodes is researched.

4. Scope of research

Firstly, the research regarding the synthesis of carbon nanofibers on the catalyst composed of nickel deposited on alumina oxide is presented. It is aimed to investigate the influence of the temperature of CVD synthesis on the properties of obtained CNF and how the observed changes impact the work of the battery. Based on the findings in this part, the temperature for the *in-situ* nitrogen doping is chosen. Additionally, achieved results serve as a reference point in the further development of nickel oxalate-based catalyst.

In the section regarding the nitrogen functionalization, the main goal is to compare the *in-situ* and *ex-situ* doping and decide, which method is more effective in terms of incorporation of nitrogen atoms into the carbon structure of CNF, resulting in the most significant impact on the battery performance. Moreover, extensive research regarding the type of nitrogen source on the amount of nitrogen build-into the CNF structure via *in-situ* method has been conducted – during CVD process different dopants (ammonia, acetonitrile, melamine) and their combinations have been added to the feeding stream. In the case of *ex-situ* modifications, two techniques have been chosen – hydrothermal treatment and subsequent ammonization in the tube furnace. The influence of wide range of parameters, including temperature, mass ratios of reactants, and pH, have been investigated for hydrothermal treatment. For subsequent ammonization, type of starting material and thermal procedure of the process have been selected as researched variables. For all samples, the amounts of incorporated nitrogen and oxygen atoms have been measured and for selected samples, types of incorporated nitrogen functional groups have also been analyzed.

Next section is aimed at the preparation of standalone nickel oxalate-based catalyst, that will enable synthesis of CNF via CVD process. Due to the precipitation of nickel oxalate from aqueous solutions, the need for support materials is eliminated. The goal of preparing standalone catalyst is to simplify the process of catalyst's formulation and to eliminate the need for its removal after synthesis. The influence of the process temperature is also investigated and the obtained results are compared with the standard catalyst.

Different activated carbons have been prepared via chemical activation techniques, which enables the comparison of two activation agents (H_3PO_4 and KOH) on the porosity of prepared materials. Analysis on the influence of process parameters (type of raw materials and the mass ratios between reactants) on the properties of AC obtained via KOH activation is also carried out. Moreover, the investigation on the post-

treatment of AC obtained via activation with H_3PO_4 is conducted. The impact of all the abovementioned factors on the operation of lithium-oxygen battery is also presented. The study regarding properties of activated carbons has been conducted in order to determine optimal raw materials and conditions of synthesis of material for the application as a support material in CNF/AC composite preparations. In order to maximize the performance of the Li-O_2 battery, carbon nanofibers and activated carbon based composite materials have been prepared. To achieve that, the relatively facile method of catalyst preparation has been developed and as obtained catalysts have been utilized in the conventional CVD synthesis. The influence of catalyst composition on the properties of CNF/AC composites has been tested.

Lastly, the facile method of preparation of CNT carbon aerogels has been developed. Due to the properties of obtained aerogels, their application as free-standing cathodes in the Li-O_2 batteries has been proposed. The influence of CNT concentration of initial mixture used in the preparation of aerogels on the porosity and structure of aerogels is comprehensively analyzed. The goal of proposing free-standing cathode is to simplify the construction of cathode and to limit the impact of side reactions by eliminating the number of components.

The influence of parameters of synthesis, chosen method, and/or type of raw materials on the porosity, morphology, composition, and structure of prepared materials is investigated via various techniques, including SEM, N_2 adsorption/desorption isotherm at 77 K, Raman spectroscopy, and for selected samples additional techniques have been utilized, such as XRD spectroscopy, elemental analysis, and XPS spectroscopy. In terms of electrochemical measurements, for all of the samples the GCPL measurements have been conducted, aimed to research the performance of the Li-O_2 battery across the first discharge-charge cycle, but also the cyclability across the 50 discharge cycles (for all samples, apart from carbon aerogels). Moreover, for CNF/AC composites the investigation regarding the influence of the current density on the first cycle performance has been carried out, as well as the influence of the restricting of discharge capacity on the cyclability.

5. Methodology

5.1. Preparation of cathode materials

5.1.1. Synthesis of carbon nanofibers

Two types of catalysts have been utilized in order to synthesize CNF by catalytic chemical vapor deposition. Firstly alumina based catalyst, which will be later noted as “standard”, has been prepared by the wet impregnation technique using 1.0 M aqueous solution of $Ni(NO_3)_2 \cdot 6H_2O$ (POCH, 99%). In order to obtain final catalyst with the Ni content of 14 wt. %, the appropriate amounts of alumina powder (Sigma Aldrich, particles size <50 nm) and Ni precursor have been mixed. The as prepared sample has been left to dry overnight in 110ºC and has been later calcinated in 350ºC in air for 4 h. Synthesis of carbon nanofibers has been carried out in a quartz tube of diameter of 32 mm in a horizontal furnace (Czylok). For each synthesis, 0.2 g of the catalyst has been spread in the bottom of the quartz boat, which has been later placed in the middle

of the quartz tube. Before the growth of CNF, the catalyst has been heated to 700ºC with heating rate of 5ºC/min in a nitrogen flow of 9 dm^3h^{-1} and subsequently reduced in a flow of hydrogen (9 dm^3h^{-1}) for 2 h. After the reduction, furnace has been cooled down in the flow of nitrogen and hydrogen (1:1, v/v, 9 dm^3h^{-1} each) to the actual temperature of synthesis, see Tab. 1. The growth of CNF has been carried out in a flow of C_3H_8 and H_2 (1:1, v/v, 9 dm^3h^{-1}) for 1 h. After that step, the furnace has been cooled down to the room temperature in the flow of N_2 (9 dm^3h^{-1}). To collect sufficient amount of samples, each synthesis has been performed multiple times. As collected CNF have been purified by leaching via sonification in Teflon-made container in concentrated hydrofluoric acid for 1 h. After removing the alumina support, CNF have been washed and filtered with distilled water until the pH of filtrate reached neutral level. The final product has been dried overnight at 100ºC and has been stored in desiccator.

The second catalyst for CVD synthesis is based on the free-standing nickel oxalate. The nickel oxalate has been prepared by precipitation of the salt from the 1.0 M aqueous solutions of $Ni(NO_3)_2$ (POCH, 99%) and 1.0 M aqueous solutions of $(COOH)_2$ ($(COOH)_2$•$5H_2O$, POCH, 99%). The oxalic acid solution has been slowly added to the nickel nitrate solution. The drop-wise titration has been conducted with simultaneous intense mixing (450 rpm) of the nickel nitrate solution, to enable formation of small crystallites of nickel oxalate. After the precipitation, the obtained catalyst has been washed and filtered with distilled water until the pH of filtrate has reached neutral level. As collected material has been dried overnight at 100ºC and has been stored in desiccator. The process of CNF growth has been conducted similarly to the process carried out on the standard catalyst, however, due to the properties of nickel oxalate, the step of catalyst reduction could be omitted. Therefore, after nickel oxalate has been spread in the bottom of the quartz boat and placed in the middle of the quartz tube. The furnace has been heated at a rate of 5ºC in the flow of nitrogen (9 dm^3h^{-1}) to the synthesis temperature, see Tab. 1. Then, CNF growth has been carried out in the flow of C_3H_8 and hydrogen (1:1, v/v, 9 dm^3h^{-1} each) for 1 h. After that step, the furnace has been cooled down to the room temperature in the flow of N_2 (9 dm^3h^{-1}). To collect sufficient amount of samples, each synthesis has been performed multiple times.

Tab. 1. List of the CNF samples obtained via CVD.

Sample name	Type of catalyst	Temperature of synthesis	Reduction details
CNF450	Ni deposited on alumina support	450ºC	For 2 h at 700ºC in hydrogen atmosphere
CNF500		500 ºC	
CNF550		550 ºC	
CNF600		600 ºC	
CNF450-NiOx	Nickel oxalate	450 ºC	None
CNF500-NiOx		500 ºC	
CNF550-NiOx		550 ºC	
CNF600-NiOx		600 ºC	

5.1.2. Nitrogen functionalization

5.1.2.1. In-situ methods

The synthesis of nitrogen-doped CNF via *in-situ* techniques has been conducted similarly to the procedure described in the section 5.1.1. – dedicated for the CVD synthesis on the standard catalyst. The alumina-supported catalyst has been firstly reduced at 700ºC in H_2 atmosphere and after the furnace has been cooled down to 500ºC the growth of N-doped CNF has been carried out. However, nitrogen precursors have been added to propane in the stream of raw materials. Various nitrogen precursors have been investigated, including ammonia, acetonitrile, melamine, and their combination, see full list of samples in the Tab. 2. Gaseous ammonia has been added to the flow of C_3H_8 and H_2 as the third stream, with the proportion between the three gasses in the ratio of 1:1:1, v/v (9 dm^3h^{-1} each). Acetonitrile has been introduced to the stream of raw materials by carrying out the bubbling of the liquid acetonitrile by the flow of C_3H_8 (9 dm^3h^{-1}), which transported fumes of acetonitrile to the quartz tube to the zone of CNF growth. The mass of introduced acetonitrile has been estimated to be around 3.0 g. Melamine (1.0 g), in the form of powder, has been placed in a smaller quartz boat and has been held in the quartz tube outside of the heating zone. Once the furnace has reached target temperature of 500ºC, boat with melamine has been transported to the area of the tube with the temperature of around 350ºC, which has enabled the sublimation of the powder. The created melamine in the gas form has been transferred to the growth zone of CNF by the flow of propane and hydrogen (1:1, v/v, 9 dm^3h^{-1} each). In the cases, where two or more nitrogen precursors have been utilized, the procedure is based on the combination of abovementioned methods.

Tab. 2. List of samples obtained during the in-situ functionalization of CNF grown on the standard catalyst at 500ºC.

Sample name	**Nitrogen precursor**
CNF500-Am	Ammonia
CNF500-Ac	Acetonitrile
CNF500-Me	Melamine
CNF500-Am-Ac	Ammonia + Acetonitrile
CNF500-Am-Me	Ammonia + Melamine
CNF500-Ac-Me	Acetonitrile + Melamine
CNF500-Am-Ac-Me	Ammonia + Acetonitrile + Melamine

The yield of each synthesis conducted via CVD process has been calculated based on the catalyst weight increase after the process using the equation (10):

$$Y = \frac{m_t - m_{cat}}{m_{cat}} \qquad (10)$$

Where Y is the yield of CNF synthesis expressed in the mass of CNF produced during the CVD per mass of catalyst [$g_{CNF}g_{cat}^{-1}$], m_t is the combined mass of deposited carbon material after the reaction and the mass of catalyst, and m_{cat} is the initial mass of catalyst. Additionally, the yield of synthesis conducted on the standard catalyst

expressed in the mass of CNF per mass of nickel contained in the catalyst (Y_{Ni} [$g_{CNF}g_{Ni}^{-1}$]) is also calculated using the equation (11):

$$Y_{Ni} = \frac{m_t - m_{cat}}{0.14 \cdot m_{cat}} \qquad (11)$$

Where the fraction of 0.14 is related to the nickel content in the standard catalyst (14 wt. %). The yield of CVD synthesis conducted on the nickel oxalate based catalyst expressed in mass of CNF per mass of nickel (Y_{Ni}) has been calculated according to the equation (12) for synthesis of carbon nanofibers on the nickel oxalate based catalyst. Slightly different formula results from different content of nickel in the initial catalyst – nickel oxalate contains 39.5 wt. % of Ni.

$$Y_{Ni} = \frac{m_t - m_{cat}}{0.395 \cdot m_{cat}} \qquad (12)$$

5.1.2.2. Ex-situ methods

The investigation on the influence of the functionalization via *ex-situ* methods on the amount and type of incorporated nitrogen atoms has been carried out for the CNF500 sample.

Hydrothermal treatment

Functionalization of CNF sample via hydrothermal technique has been conducted in the pressur reactor equipped with the stainless steel vessel (4590 Micro Stirred Reactor, Parr Instrument Company), mechanical stirrer and thermocouple, the utilized setup is presented in the Fig. 11. The CNF500 and ammonia solution have been mixed together in appropriate proportions to achieve the desired mass ratio of CNF to nitrogen donor. For processes requiring the pH adjustments, the appropriate volume of concentrated acetic acid (99.5 wt. % solution) has been added. The distilled water has been added in each case to achieve total volume of the reaction mixture of 100 cm^3. After the setup has been assembled, the stirring speed set at 200 rpm and the heating have been switched on. Wide range of parameters have been tested, including different ratios of CNF to dopant and temperature, detail list is presented in the Tab. 3.

Fig. 11. Image of utilized Parr reactor for the hydrothermal functionalization of CNF [185].

Tab. 3. List of nitrogen doped samples prepared via hydrothermal treatment.

Sample name	**Mass ratio of CNF500 to ammonia**	**Temperature**	**pH**
CNF500/HT-N25/160	1:25	160°C	Not adjusted
CNF500/HT-N25/180		180°C	Not adjusted
CNF500/HT-N25/180/pH7			7
CNF500/HT-N25/180/pH5			5
CNF500/HT-N25/200		200°C	Not adjusted
CNF500/HT-N25/220		220°C	Not adjusted
CNF500/HT-N50/180	1:50	180°C	Not adjusted
CNF500/HT-N100/180	1:100		Not adjusted
CNF500/HT-N200/180	1:200		Not adjusted

Subsequent ammonization

Functionalization via subsequent ammonization has been carried out in the same horizontal furnace as CVD processes. For each process, 0.2 g of CNF sample has been spread in the bottom of the quartz boat, which has been later placed in the middle of the quartz tube. The furnace has been heated to 500ºC with a heating rate of 10ºC/min in a nitrogen flow of 9 dm^3h^{-1}. The ammonization has been conducted in the flow of nitrogen and ammonia (1:1, v/v, 9 dm^3h^{-1} each) for 4 h. After that step, the furnace has been cooled down to the room temperature in the flow of N_2 (9 dm^3h^{-1}).

Three variations of this doping procedure have been carried out: 1) sample of CNF500 has been subjected to the aforementioned procedure and the obtained sample is later noted as CNF500-Am-ex; 2) CNF500 has been oxidized before ammonization. The oxidation step has been conducted in a flask, where 0.6 g of CNF500 has been mixed with 100 cm^3 of concentrated nitric acid. The mixture has been stirred (200 rpm) and heated (100ºC) under reflux condenser for 24 h. Next, as-collected CNF have been washed and filtered with distilled water until the pH of filtrate reached neutral level. The final product has been dried overnight at 100ºC and later noted as CNF500-OX. The subsequent ammonization has been conducted according to the procedure described

earlier and the obtained sample is later noted as CNF500-OX-Am-ex1; 3) Additionally, the ammonization of CNF500-OX, where the whole process (heating and the actual ammonization) is carried out in the flow of nitrogen and ammonia (1:1, v/v, 9 dm^3h^{-1} each). The as obtained sample is later noted as CNF500-OX-Am-ex2. The list of samples obtained via subsequent ammonization is presented in the Tab. 4.

Tab. 4. List of samples prepared via subsequent ammonization.

Sample name	Raw material	Procedure
CNF500-Am-ex	CNF500	Heating in the flow of N_2 at rate 10ºC/min. Ammonization in the flow of N_2 and NH_3 at 500ºC for 4 h. Cooling down in the flow of N_2.
CNF500-OX-Am-ex1	CNF500-OX	
CNF500-OX-Am-ex2	CNF500-OX	Heating (10ºC/min) and ammonization (at 500ºC for 4 h) in the flow of N_2 and NH_3. Cooling down in the flow of N_2.

5.1.3. Preparation of activated carbons

Wide range of activated carbons has been prepared by carbonization and chemical activation of organic precursors. Activation with potassium hydroxide and phosphoric acid have been employed to obtain ACs with different porosity.

The process of preparation of activated carbons from coal-tar pitch (CP) begins from the synthesis of two semi-cokes by the pyrolysis of CP at 520°C and 600°C. The pyrolysis of coal pitch has been carried out in a vertical glass retort, where a 50-60 g of raw material has been heated at a rate of 5ºC/min to 520ºC and has been held for 2 hours in an inert atmosphere of nitrogen. The grains of as collected material have been grinded to the size from 0.1 to 0.63 mm, and as prepared sample is noted as CP520. Furtherly, thermal treatment of the semicoke obtained from coal pitch has been conducted in a horizontal tube furnace, where 12 g of CP520 have been spread in the bottom of the quartz boat and placed in the middle of the quartz tube. Later, the furnace has been heated at the rate of 10ºC/min to 600ºC in the flow of nitrogen (9 dm^3h^{-1}) and held for 1 h. The as prepared material is noted as CP600.

The preparation of activated carbons via chemical activation with KOH has been conducted in a quartz tubular reactor with a diameter of 36 mm. The reaction mixture, weighing approximately 30 g consisting flakes potassium hydroxide and carbonized coal pitch in a mass ratio of 3:1 and 4:1, has been placed in a nickel boat. Heating has been carried out to a final temperature of 800ºC at a rate of 10ºC/min. Activation has been conducted for 1 h in the atmosphere of nitrogen flowing through the reactor at a rate of 30 dm^3h^{-1}. After heating, the furnace is cooled down to the room temperature. The obtained sinter of activated carbon and potassium hydroxide decomposition products is washed from the nickel boat with a stream of distilled water. After filtering off the excess of alkaline solution, the activated carbon suspension is poured with 5% HCl and placed in an ultrasonic bath at 50°C for approximately 15 minutes, then filtered under vacuum using a Büchner funnel. The carbonaceous material remaining on the filter is washed with hot distilled water until the filtrate contains no chloride ions. The

activated carbon is dried in air at 110°C until the constant weight is achieved and then it is stored in a desiccator. Three activated carbons have been prepared via described process, and details regarding the obtained materials are presented in the Tab. 5.

Tab. 5. List of activated carbons prepared via chemical activation with potassium hydroxide.

Sample name	Carbonaceous raw material	Mass ratio of KOH to carbonaceous raw material
AC/CP520/3KOH	CP520	3:1
AC/CP600/3KOH	CP600	3:1
AC/CP600/4KOH	CP600	4:1

The process of chemical activation with concentrated phosphoric acid has been conducted via two-step procedure, that includes wet impregnation of pine wood followed by pyrolysis. Wood shavings are initially impregnated with concentrated H_3PO_4 at 1:3 biomass/acid mass ratio. This mixture is then heated in an oven at 120ºC for 24 hours. After the impregnation, the pyrolysis of carbonaceous material is conducted in a horizontal tube furnace. The sample has been spread in the bottom of quartz boat and placed in the middle of the quartz tube. Heating has been carried out to a final temperature of 800ºC at a rate of 10ºC/min. The activation process has been conducted for 1 h in an atmosphere of nitrogen flowing through the reactor at a rate of 30 dm^3h^{-1}. The prepared carbonaceous material is washed with hot distilled water in a Soxhlet extractor for 24 h to remove any residuals of phosphoric acid. The activated carbon is dried in air at the temperature of 110°C until the constant weight is achieved and then it is stored in a desiccator. The as prepared material is noted as AC/H_3PO_4. Additionally, the as obtained activated carbon has been reduced at 500°C with a heating rate of 10°C/min for 1h in a flow of hydrogen and nitrogen (1:1, v/v, 9 dm^3h^{-1} each). The as prepared material is noted as AC/H_3PO_4/RED.

The yield of each activation process, defined as a loss of mass after the process, has been calculated based on the decrease of weight of material after the process using the equation (13):

$$Y_{AC} = \frac{m_{raw} - m_{AC}}{m_{raw}} \cdot 100\% \qquad (13)$$

Where Y_{AC} is the yield of activation expressed in loss of the mass of raw material after activation, m_{raw} is the mass of raw material before the process, and m_{AC} is the mass of obtained activated carbon after washing and drying to constant mass.

5.1.4. Synthesis of carbon nanofibers and activated carbon composites

Firstly, catalysts have been prepared by physical mixing of appropriate amounts of nickel oxalate powder (prepared according to the procedure described in the section 5.1.1.) and AC/H_3PO_4 in an agate mortar. Components of the catalyst have been ground together until the homogenous powder has been obtained. The amount of nickel oxalate has been adjusted, so that the nickel content in a catalyst has reached the value of 10, 20, and 50 wt. %, and catalysts are noted as AC/H_3PO_4/10, AC/H_3PO_4/20, and AC/H_3PO_4/50, respectively. Carbon nanofibers and activated carbon based composites

have been synthesized via CVD technique and the procedure previously described in section 5.1.1. (subsection dedicated to the synthesis of CNF on the nickel oxalate) is used. In the bottom of the quartz boat, the 0.2 g of each of the prepared catalysts has been spread and then the furnace has been heated to the temperature of 500ºC at a rate of 5ºC in the flow of nitrogen (9 dm^3h^{-1}). The CNF growth has been carried out in the flow of C_3H_8 and hydrogen (1:1, v/v, 9 dm^3h^1 each) for 1 h. After that step, the furnace has been cooled down to the room temperature in the flow of N_2 (9 dm^3h^{-1}). To collect sufficient amount of sample, each synthesis has been performed multiple times. The composites synthesized on the appropriate catalyst are noted as CNF500/AC/H_3PO_4/10, CNF500/AC/H_3PO_4/20, and CNF500/AC/H_3PO_4/50.

The yield of each synthesis of CNF (Y) has been calculated according to the equation (10). However, in order to calculated yield of reaction expressed in the mass of CNF per mass of nickel (Y_{Ni}) for synthesis of CNF500/AC/H_3PO_4/10, CNF500/AC/H_3PO_4/20, and CNF500/AC/H_3PO_4/50 equation (12) required readjustment to include the actual content of nickel oxalate in each of utilized catalysts – equation (14):

$$Y_{Ni} = \frac{m_t - m_{cat}}{X \cdot 0.395 \cdot m_{cat}} \qquad (14)$$

Where X expresses the content of nickel oxalate in the initial catalyst, other symbols represent the same values as for the equation (10).

5.1.5. Preparation of carbon aerogels

Carbon aerogels have been prepared from commercially available CNT purchased from Sigma-Aldrich (Cat. number of 724 769). CNT are dispersed in 4 ml of deionized water using an ultrasonic stirrer for 1 h, followed by the addition of 60 µl of concentrated aqueous ammonia and further mixing using an ultrasonication bath for 1 h. TETA (0.1 mmol) is added after the dispersing process and then the mixture is heated in a sealed bottle in an oil bath at 95°C for 24 h. The obtained hydrogels have been subsequently flash-frozen in liquid nitrogen and freeze-dried for 24 h. The aerogels with the concentration of CNT in the initial dispersion set at 3.0, 4.5, 6.0 and 7.5 mg_{CNT} ml^{-1} are prepared, and the samples are noted as Aero_3.0, Aero_4.5, Aero_6.0 and Aero_7.5, respectively.

5.2. Materials characterization

5.2.1. Specific surface area and porosity

The characterization of the porous structure of all samples has been carried out by nitrogen gas adsorption at 77K (ASAP 2020, Micrometrics). This technique allows to characterize pores of sizes in the range of 0.7 and 50 nm (generally micro- and mesopores). Before measurements, all samples have been degassed to remove absorbed species. The temperatures of degassing have been adjusted appropriately to the properties of each sample. After the initial degassing, materials with expected high specific surface area and large share of microporosity (activated carbons and CNF/AC composites), have been subsequently dried to remove any residual of adsorbed contaminations (300°C, 12 h, <0.01 µmHg). Total pore volume (V_T), specific surface

area (S_{QSDFT}), and pores size distribution (PSD) have been calculated according to the QSDFT equilibrium model for slit pores for the data for adsorption and desorption of nitrogen at 77 K.

5.2.2. SEM

The surface morphology of materials has been investigated by scanning electron microscopy. Two different microscopes have been employed to conduct observations:

- FE SEM, Zeis Merlin, for the characterization of CNF, activated carbons, and CNF/AC composites
- FEI Company, Quanta 250 FEG for the characterization of CNT and carbon aerogels

For both of microscopes and for each measurement, the observation parameters (such as lens type and accelerating voltage) have been individually adjusted to enable obtaining the best achievable quality of SEM images.

5.2.3. Raman spectroscopy

Raman spectroscopy has been performed using an Xplora Nano (HORIBA) spectrometer with a 100x objective (numerical aperture 0.9, Olympus) with a 532 nm green laser at a laser power of ~2 mW to analyze the surface of the prepared materials (CNF, AC, CNF/AC composites). The measurements have been conducted with static mode centered at 1500 cm^{-1} (which corresponds to acquisition window from 0 to 3500 cm^{-1}) with 100 accumulations and integration time of 2 s. Two main bands can be distinguished during the analysis of Raman spectra of carbon nanomaterials:

- G-band – positioned at around ~1600 cm^{-1} and related to the in-plane vibrations of sp^2 carbon atoms in a graphitic structure
- D-band – positioned at around ~1300 cm^{-1} and associated with disorders, defects, or edges of carbon layers

For both of the above bands the intensity and position have been analyzed in order to provide valuable information regarding the structural characteristics of synthesized materials. Additionally, the intensity ratio of D and G bands (I_D/I_G) is also calculated, as it informs us about the degree of structural imperfection of the material.

5.2.4. Elemental analysis

The elemental analysis of the bulk content of nitrogen and oxygen in selected samples has been conducted at the Centre of Molecular and Macromolecular Studies at Polish Academy of Science in Łódź, Poland with the use of EuroVector model 3018 analyzer.

5.2.5. XPS

XPS measurements have been carried out at the AGH University of Cracow according to the following methodology. XPS analysis have been performed with a PHI VersaProbeII (ULVAC-PHI, Chigasaki, Japan) using focused, monochromatic X-ray radiation of the Al Kα line (1486.6 eV). The beam has been focused to a 100 µm spot and scanned a 400 µm x 400 µm area on the sample surface. For each measurement location, one wide-range spectrum (0-1200 eV) with low resolution (0.5 eV) and high-

resolution spectra (0.1 eV) have been measured in the regions of the C 1s, O 1s, N 1s and Ni 2p lines. During the measurements, surface charge neutralization has been used by irradiating the surface with a beam of low-energy electrons (1 eV) and ions (7 eV Ar+) to ensure a constant surface potential despite the emitted photoelectrons. The vacuum value in the analytical chamber has been set at around 2×10^{-9} mbar. The spectral line fitting has been performed using the PHI Multipak program (v.9.9.3) by subtracting the background using the Shirley method [186].

The spectra in the C 1s region have been fitted with eight lines, of which line 1 with an energy of 284.4 eV represents a C=C (sp^2) bond, line 2 with an energy of 285.0 eV is responsible for the presence of a C-C (sp^3) bond, line 3 with an energy of 286.1 eV corresponds to the presence of C-O-C and/or C-OH and/or C=N bonds in the aromatic structure, line 4 with an energy of 287.1 eV corresponds to C=O and/or O-C-O and/or N-C-O bonds, line 5 with an energy of 288.4 eV corresponds to O-C=O and/or N-C=O bonds, line 6 with an energy of 289.5 eV corresponding to O-(C=O)-O bonds, and lines 7 and 8 located at the binding energy of 290.9 eV and 293.3 eV, respectively, associated with the shake-up excitation [187, 188]. The shake-up excitation originates from sp^2 carbon and its aromatic forms and is an additional parameter confirming the presence of this type of groups.

Spectra in the oxygen O 1s region have been fitted with two lines, where the first line located at the binding energy of 531.5 eV indicates the presence of both O=C bonds and organic species of the $-NO_2$ (nitro) type and metal oxides such as Ni-O [189]. The second line at the energy of 533.1 eV indicates the presence of O-C and/or –OH bonds [190]. The N 1s spectra were fitted with two lines (for samples CNF500-Am-Me, CNF500-Am-Ac-Me, CNF500/HT-N25/180, and CNF500-OX-Am-ex2), the first line at the binding energy of 398.8 eV, which indicates the presence of amides and/or C=N bonds in aromatic systems, that can correspond to either graphitic, pyrrolic or pyridinic nitrogen. The second line at the energy of 400.6 eV, indicating the presence of O-C-N and/or NC=O bonds and/or ammonium groups [188, 189]. For CNF500-OX, the N 1s spectrum has been fitted with a single line at the energy of 405.6 eV, which indicates the presence of nitro groups $–NO_2$ [188].

5.2.6. XRD

XRD measurements have been conducted at the Faculty of Mechanical Engineering at Wrocław University of Science and Technology according to the following description. XRD measurements have been carried out using the Rigaku Ultima IV diffractometer with Kα1 monochromatic beam from Cu anode. All measurements have been performed in air with 0.02° step size in the 10-100° scanning range and the time of measurement of 3 minutes per degree.

5.3. Electrochemical measurements

5.3.1. Materials and cell's component

All of electrochemical measurements have been conducted in the ECC-Air test cell purchased from EL-Cell Company, Germany. The utilized electrolyte for each test was the 1.0 M solution of $LiCF_3SO_4$ dissolved in TEGDME, both purchased from

Sigma Aldrich. Prior to the preparation of electrolyte solution, the lithium trifluoromethanesulfonate ($LiCF_3SO_4$) (99 wt.%) and tetraethylene glycol dimethyl ether (TEGDME) (99 wt.%) have been dried. The salt has been dried at 100°C for 24 h under vacuum and TEGDME has been dried using molecular sieves 5A for 24 h. For the electrochemical measurements glass fibre separators have been purchased from Whatman (GF/F). A Li metal disk (MTI Corp., thickness of 0.38 mm, diameter was cut to 10 mm) is used as the anode.

If not stated otherwise, all cathodes have been prepared in a similar manner. Cathodes have been prepared by pressing the appropriate amount of cathode material slurry, which contains 10 wt. % of the PTFE binder, into Ni foam pieces with a diameter of 10 mm and a thickness of ~1.6 mm. Only exceptions from the above described procedure are aerogels, which have been utilized as a free-standing cathodes.

All of the cell components have been dried under vacuum at 90°C for 24 h before placing them into the glove box, where they have been stored in an Ar atmosphere.

5.3.2. Measurements setup and conditions

The assembly of all of the Li-O_2 cells have taken place in the glove box in an Ar atmosphere. The anode, in the form of lithium disc, is pressed on the stainless steel surface of ECC-Air test cell. On the anode, glass fibre separator is placed and appropriate amount of electrolyte is added dropwise. The cathode, either in the form of Ni foam supported disc or free-standing, is placed on the GF separator. After that the rest of the cell test is being assembled, and as prepared setup is removed from the glove box.

Wide range of electrochemical assessments is carried out using the BioLogic VSP potentiostat:

- Galvanostatic cycling with potential limitation (GCPL) – the maximum discharge and charge capacity is measured by performing the tests between 2.0 V and 4.5 V vs. Li at a constant current density of 0.4 mA cm^{-2}. Simultaneously, the cyclability of battery is assessed across 50 discharge and charge cycles – for each of the electrochemically analyzed samples, except aerogels.
- The investigation of the influence of the current density on the performance of the Li-O_2 cell – for the selected sample.
- The investigation of the influence of the discharge and charge capacities on the cyclability of the Li-O_2 cell – for the selected sample.
- The EIS analysis of new, discharged, and recharged Li-O_2 cell – for the selected sample.

In this work, all of the presented gravimetric values (e.g., discharge capacity) are calculated based on the active cathode mass. In the case of Ni foam supported cathodes, active mass is defined as mass of carbon material and the PTFE binder on an individual cathode. In the case of aerogels, active mass is defined as the mass of carbon material

and TETA binder. Additionally, if not stated otherwise, the overpotential is defined as difference between plateau of discharge or charge curve, for discharge or charge overpotential respectively, and the theoretical potential of OER/ORR (2.96 V). The first cycle reversibility is defined as the ratio of the capacity retained during the first charging to the capacity measured during the first discharge. Moreover, any variations from the above described tests (e.g., different current density or different range of potential) are precisely highlighted during the analysis of results.

6. Results and discussion

6.1. Influence of process temperature on the properties of CNF synthesized on the reference catalyst

6.1.1. Synthesis

At all of the tested temperatures of CVD process, proposed combination of synthesis technique and applied catalyst have led to the synthesis of CNF. In the Tab. 6 yields of synthesis conducted on the standard catalyst at the temperature ranging from 450°C to 600°C are presented.

The synthesis yields of CVD process conducted on the standard catalyst have increased with the growing process temperature in the range from 450°C to 550°C. The lowest synthesis yield of 1.2 $g_{CNF}g_{cat}^{-1}$ has been reported at the 450°C and it has increased significantly to 7.1 $g_{CNF}g_{cat}^{-1}$ with the rise in the process temperature up to 500°C. Additionally, almost two-fold increase of synthesis yield up to 13.5 $g_{CNF}g_{cat}^{-1}$ has been observed after another rise in the temperature to 550°C. However, further increase in process temperature to 600°C did not resulted in an increase in synthesis yield, on contrary the yield has decreased to 11.6 $g_{CNF}g_{cat}^{-1}$.

The expected increase in synthesis yield in the temperature range of 450-550°C can be explained by the more efficient decomposition of propane at higher temperatures and the improved diffusion of nickel nanoparticles onto the surface of the catalyst's support. However, excessive temperatures may lead to the aggregation of catalyst particles resulting in the formation of large nanoparticles that promotes the growth of CNF less efficiently. The described change of kinetics of the CNF growth could explain the decrease of synthesis yield at 600°C [191].

Achieved values of synthesis yields can be considered as relatively high, especially after the consideration that the active component of the standard catalyst, which are nickel nanoparticles, represents only around 14 wt. % of the total mass of the catalyst. Taking that into account and utilizing formula described in equation (11), synthesis yields of all CVD processes have grown significantly to 8.3, 50.8, 96.5, and 82.5 $g_{CNF}g_{Ni}^{-1}$ for CNF450, CNF500, CNF550, and CNF600 samples, respectively. In literature, comparable values of Y and Y_{Ni} have been reported by Miniach *et al.* by the utilization of similar CVD technique and temperature range yields ranging from 3.9 to 5.9 $g_{CNF}g_{cat}^{-1}$, which corresponds to 27.6 to 42.5 $g_{CNF}g_{Ni}^{-1}$ have been achieved [191]. In another research study, Śliwak *et al.* reported the yield of 5 $g_{CNF}g_{cat}^{-1}$ for CNF synthesis via CVD method using the Ni/Al_2O_3 based catalyst [192]. In both of the

mentioned works, methane is used as carbon source and due to its higher stability, the slightly lower yields of synthesis are reported, as compared to yields achieved in this study.

The reported high synthesis yields, especially for temperatures of 500°C and above, can also be attributed to the presence of hydrogen in the feeding stream. The presence of hydrogen in the raw materials stream can either accelerate or hamper the formation of carbon nanostructures [193]. Although, not applicable in the case of this research, the suppressing effect of hydrogen on CNF formation is linked to surface hydrogenation reactions and hydrogasification of deposited carbon leading to the formation of methane. On the other hand, the accelerating influence of hydrogen on the CNF formation can be attributed to one of the two possible interpretations. One of them suggests, that during the CVD process hydrogen reacts with inactive metal carbides resulting in their decomposition and maintaining the catalytically active surface of metals. According to the second possible explanation, hydrogen supports the removal of graphite overlayer, which suppress the catalytic activity of metals [193]. In this research, hydrogen definitely enables maintaining the high catalytic activity of nickel nanoparticles and helps achieving high synthesis yield.

Tab. 6. Yields of synthesis of CNF on standard catalyst via CVD process at different temperatures.

Sample	**Synthesis yield, Y ($g_{CNF}g_{cat}^{-1}$)**	**Synthesis yield, Y_{Ni} ($g_{CNF}g_{Ni}^{-1}$)**
CNF450	1.2	8.3
CNF500	7.1	50.8
CNF550	13.5	96.5
CNF600	11.6	82.5

6.1.2. Materials characterization

As can be observed on the SEM images in the Fig. 12.1, 12.4, 12.7, and 12.10, the macroscopic structure of all of the compared samples is relatively similar and consists relatively large agglomerates of very entangled carbon nanofibers. Furtherly, the SEM images obtained with higher magnification (Fig. 12.2, 12.5, 12.8, and 12.11) depict a dense and entangled network of carbon nanofibers. The presented curled and interconnected morphology of CNF is typical for carbon nanofibers grown by the CVD technique. Moreover, the high degree of entanglement, suggesting morphological uniformity in micrometers scale of produced CNF, is characteristic for nanofibers obtained on nickel-based catalyst [194]. That type of morphology is often desired for applications in energy storage, as it indicates good development of specific surface area, which is desired in cathode materials for Li-O_2 batteries.

Parameters of porous structure presented in the Tab. 7 along with the N_2 adsorption/desorption isotherms and PSD shown in the Fig. 13 are utilized for the characterization of porosity of CNF prepared on the standard catalyst. Total pore volume, mesopores volume, and specific surface area are key parameters of materials that are considered for application in lithium-oxygen batteries.

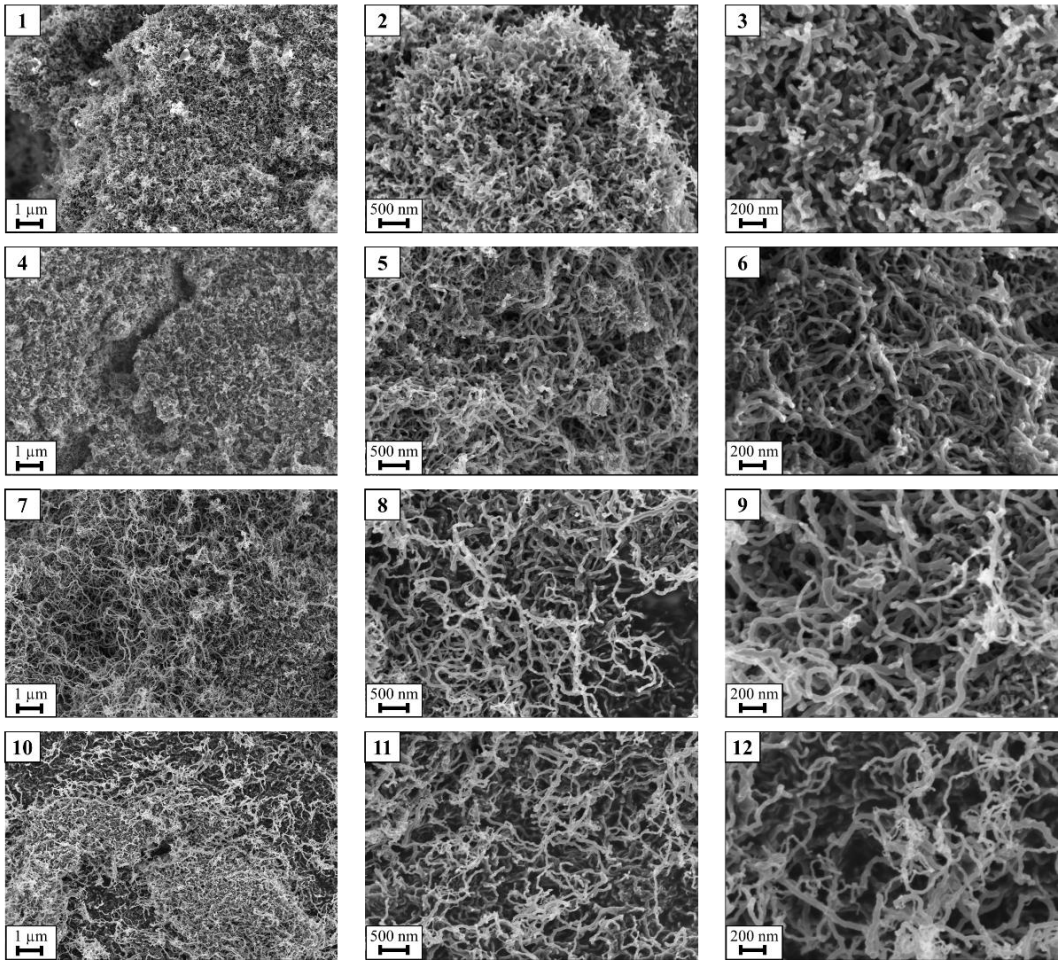

Fig. 12. SEM images of CNF synthesized on the standard catalyst via CVD process at different temperatures: 1, 2, 3 - CNF450; 4, 5, 6 - CNF500; 7, 8, 9 - CNF550; 10, 11, 12 - CNF600.

Based on the presented data, continuous growth of specific surface area with the increase of synthesis temperature can be noticed. The lowest SSA of at 96 m^2g^{-1} has been observed for CNF450. The specific surface area rises to 123 m^2g^{-1} for CNF500 and to 143 m^2g^{-1} for CNF550, but the highest value at 151 m^2g^{-1} is reported for CNF600. The lowest V_T and V_{meso} of 0.176 cm^3g^{-1} and 0.144 cm^3g^{-1} are observed for CNF450. Initially, total pore volume and mesopores volume follow similar pattern in terms of growth with the increasing temperature of synthesis, which result in the rise of V_T and V_{meso} to 0.294 cm^3g^{-1} and 0.258 cm^3g^{-1} for CNF500, and to 0.343 cm^3g^{-1} and 0.306 cm^3g^{-1} for CNF550. However, further increase of CVD temperature to 600°C has led to the decrease of both total pore and mesopores volumes to 0.308 cm^3g^{-1} and 0.270 cm^3g^{-1}, respectively. Another, useful parameter to assess the potential of material to its application as cathode materials in Li-O_2 battery is the ratio of V_{meso}/V_T that indicates what share of total pore volume is represented by mesopores. In the case of CNF obtained on the standard catalyst, the lowest V_{meso}/V_T ratio of 0.82 is observed for CNF450 and for other materials the ratio is at similar value – 0.88 for CNF500 and CNF600, and slightly higher at 0.89 for CNF550.

Tab. 7. Parameters of the porous structure of CNF synthesized on the standard catalyst via CVD process.

Sample	**Specific surface area, S_{QSDFT} (m^2g^{-1})**	**Total pore volume, V_T (cm^3g^{-1})**	**Mesopores volume, V_{meso} (cm^3g^{-1})**	**V_{meso}/V_T**
CNF450	96	0.176	0.144	0.82
CNF500	123	0.294	0.258	0.88
CNF550	143	0.343	0.306	0.89
CNF600	151	0.308	0.270	0.88

The above described characteristics of porosity indicates, that obtained carbon nanofibers present dominant mesoporous nature. The dominant mesoporosity of all samples is related to the shape of N_2 adsorption/desorption isotherms (Fig. 13.1, 13.3, 13.5, and 13.7), which all can be assigned to the type IV of adsorption/desorption isotherm according to the IUPAC methodology [195]. Small hysteresis loop is visible in the graph for the CNF450 (Fig. 13.1) and it continuously increase its size for samples obtained at higher temperatures. Another confirmation of mesoporous character of discussed CNF is shown in PSD graphs, presented in Fig. 13.2, 13.4, 13.6 and 13.8. On all graphs, minimal share of micropores volume and the dominant share of mesoporous volume is observed. Pores with the highest volume can be distinguished for CNF550 and CNF600, at the range of 11-13 nm and 8-10 nm, respectively. However, for CNF450 and CNF500 the selection of pores with specific diameter that have distinctly larger share than others is less obvious, as no evident peak is PSD graph is visible for either of samples.

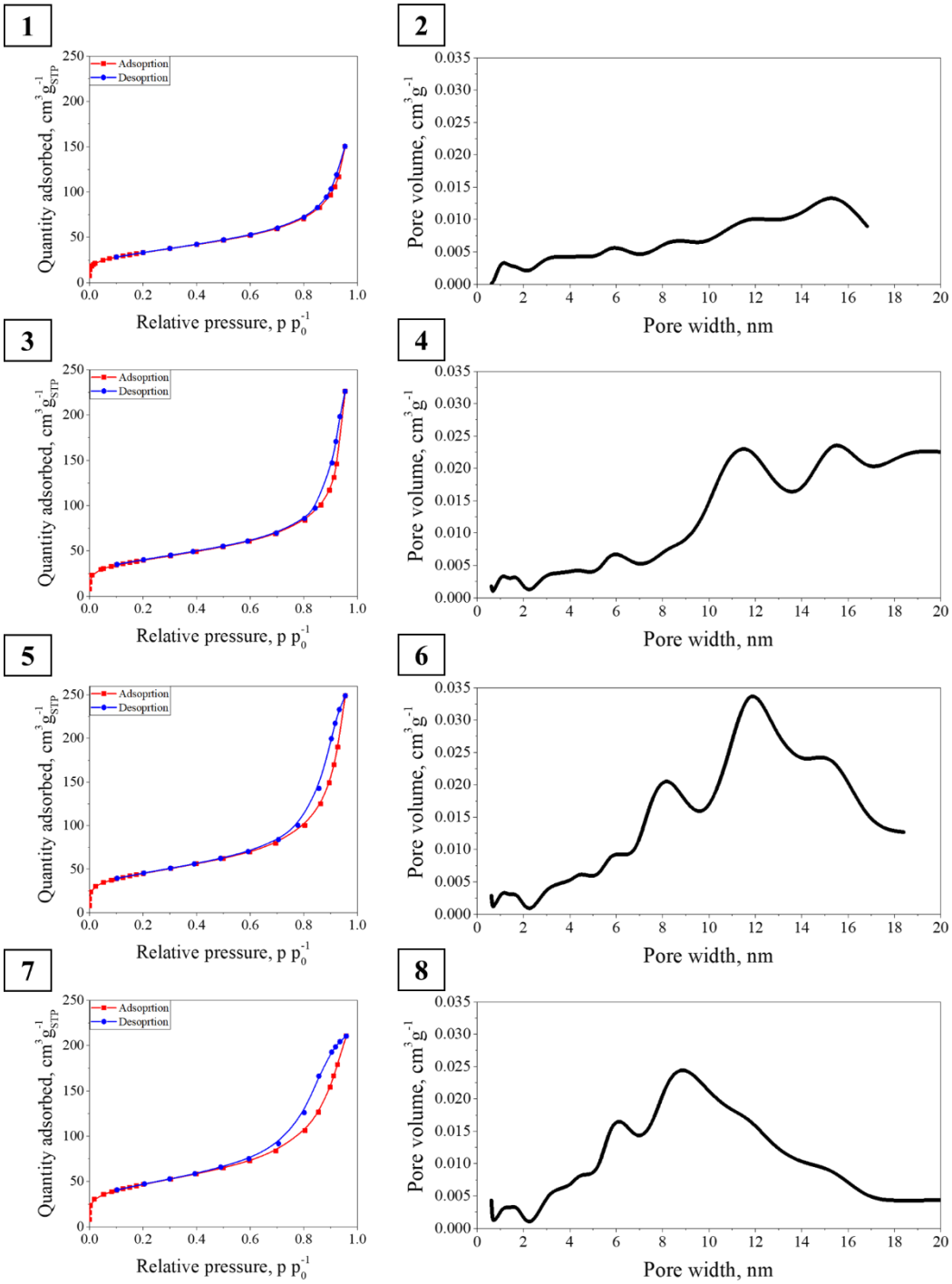

Fig. 13. The N_2 adsorption/desorption isotherms and PSD of the CNF synthesized on the standard catalyst via CVD process: 1, 2 - CNF450; 3, 4 - CNF500; 5, 6 - CNF550; 7, 8 - CNF600.

The similarity of carbon structure of compared CNF is additionally confirmed by their Raman spectra presented in the Fig. 14. The I_D/I_G ratio for all of analyzed samples is higher than 1, which is typical for materials with high disorder level. However, fluctuations of the mentioned factor are observed with CNF450 and CNF500 having similar I_D/I_G ratios of 1.38 and 1.34, respectively, and CNF550 and CNF600 having higher, but even closer ratios of 1.67 and 1.66. Substantially higher values of I_D/I_G ratio

for CNF550 and CNF600 indicate that their structure contains more defects and display lower graphitization level than CNF450 and CNF500.

Tab. 8. Comparison of key parameters of Raman spectra of carbon nanofibers synthesized on the standard catalyst via CVD at different temperatures.

Sample	**D-band peak position, cm^{-1}**	**G-band peak position, cm^{-1}**	**I_D/I_G ratio**
CNF450	1 351	1 586	1.38
CNF500	1 348	1 586	1.34
CNF550	1 339	1 579	1.67
CNF600	1 347	1 583	1.66

In terms of position and shape of D-band and G-band peaks, high level of similarity is observed for all samples with relatively narrow and separated peaks being presented in Raman spectra, which implies rather high crystallinity and low share of amorphous carbon in these materials. Moreover, position of peaks of D-band and G-band shift by marginal values between each samples – peaks of D-band are positioned at the range between 1 339 to 1 351 cm^{-1} and G-band peaks are located at the range between 1 579 to 1 586 cm^{-1}, detailed positions of peaks for each material are presented in the Tab. 8.

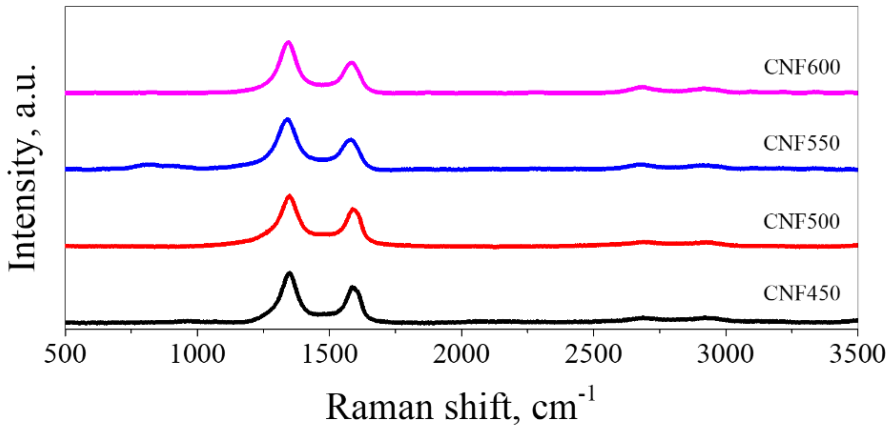

Fig. 14. Comparison of Raman spectra of CNF synthesized on the standard catalyst via CVD process.

6.1.3. Performance of Li-O_2 cells

The summary of the electrochemical performance of the Li-O_2 batteries utilizing carbon nanofiber synthesized on the standard catalyst as a cathode materials is presented in the Tab. 9. The highest first cycle discharge capacity of 815 mAh g^{-1} has been noted for the battery employing CNF500 as the cathode material. A significant decrease in capacity for the first cycle has been registered for the rest of the CNF samples, with batteries utilizing CNF450 and CNF550 reaching the capacity of 521 mAh g^{-1} and 548 mAh g^{-1}, respectively. Further drop to 299 mAh g^{-1} in the first cycle discharge capacity is observed when CNF600 is used as cathode material.

Tab. 9. Summary of electrochemical performance of Li-O_2 batteries with CNF synthesized on the standard catalyst as cathode materials during the first discharge-charge cycle.

Sample	**1st cycle discharge capacity, mAh g^{-1}**	**1st cycle charge capacity, mAh g^{-1}**	**1st cycle reversibility**
CNF450	521	212	41%
CNF500	815	456	56%
CNF550	548	84	15%
CNF600	299	232	78%

On the other hand, the largest reversibility of the first cycle at 78% is observed for CNF600. While for other samples reversibility reaches 56%, 41%, and 15% for CNF500, CNF450, and CNF550, respectively. The charging plateau at around 4.4 V can be observed for CNF500 (Fig. 15.2), which corresponds to OER overpotential around 1.4 V. In contrast, no distinct charging plateaus can be distinguished for the rest of CNF prepared on the standard catalyst (Fig. 15.1, 15.3, and 15.4).

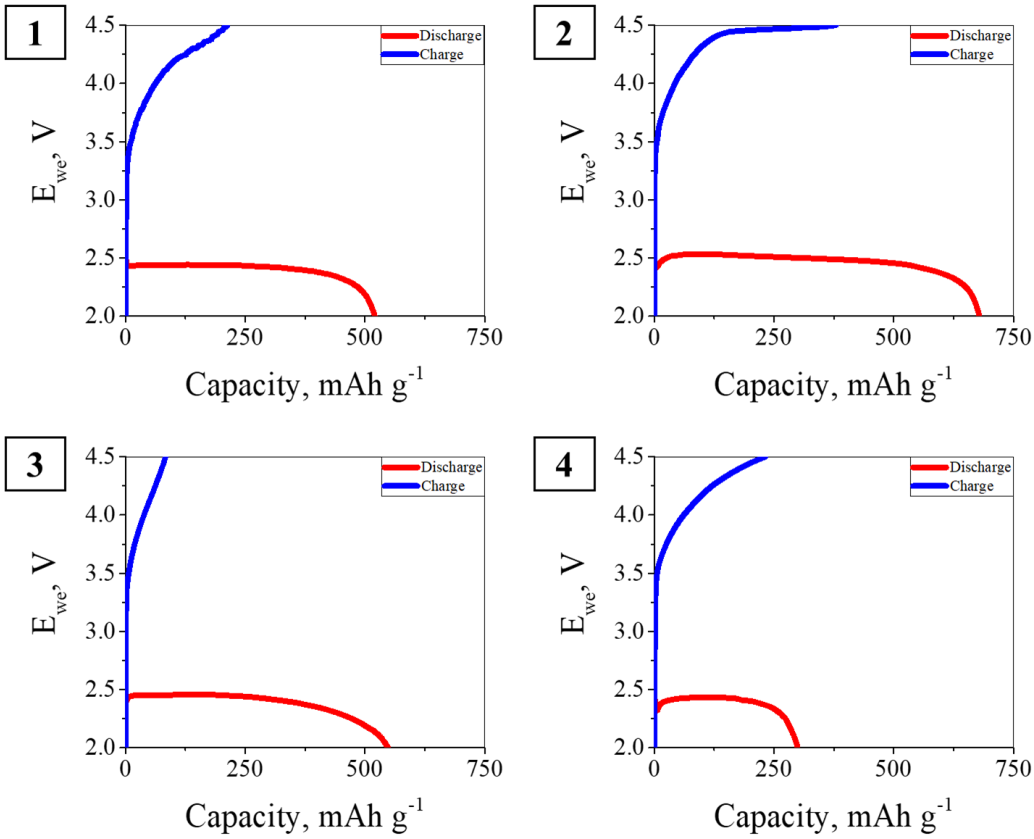

Fig. 15. Comparison of GCPL measurements for the first discharge-charge cycle conducted at current density of 0.4 mA cm^{-2} with CNF synthesized on the standard catalyst via CVD process as a cathode materials: 1 - CNF450; 2- CNF500; 3 - CNF550; 4 - CNF600.

Another important aspect in the assessment of performance of cathode materials for lithium-oxygen batteries is the achievable cyclability. In the Fig. 16, discharge capacities across 50 discharge-charge cycles for CNF prepared on the standard catalyst

are shown. The biggest differences between all four samples can be noticed up to around 10th cycle – up to this point the substantially higher capacities are observed for CNF500 with values over 50 mAh g^{-1} being reported for couple of the first cycles. For the rest of CNF samples the capacity reported since 2nd cycle does not exceed 50 mAh g^{-1}. Moreover, CNF500 displays higher capacities than CNF450 and CNF550 for the approximately 15 cycles, but after around 20th cycle the capacity observed for the mentioned three samples is very similar and is reaching around 20-25 mAh g^{-1}. The most stable cyclability is displayed by the CNF600 sample, which presents the capacity of around 35-45 mAh g^{-1} for the initial 10 cycles. Later, the discharge capacity remains at the same level of around 30 mAh g^{-1}, which is almost two-times higher than the capacity observed for other samples after the 40th cycle.

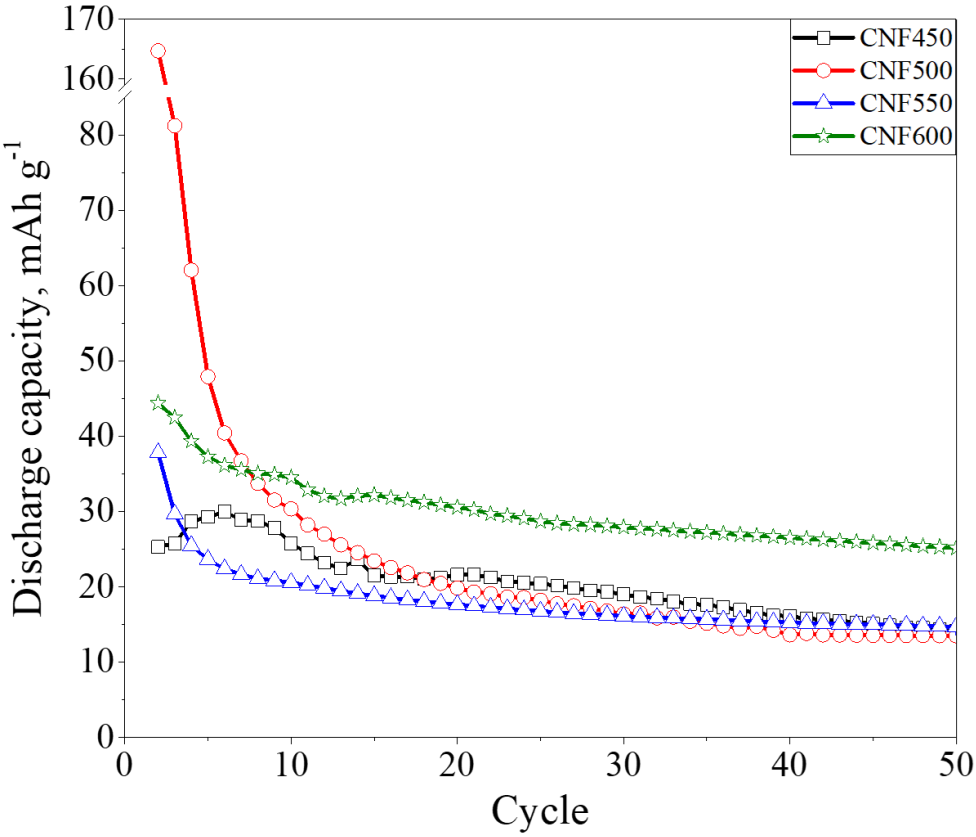

Fig. 16. Comparison of cyclability performance of CNF synthesized on the standard catalyst via CVD process as cathode materials during the GCPL measurements at 0.4 mA cm^{-2}, the first discharge cycle is excluded.

Unfortunately, based on the presented results no straightforward correlation between measured properties of CNF and their electrochemical performance can be drawn. Even though, the influence of the temperature of synthesis on specific surface area, porosity and disorder level have been described above, there is no direct connection between these properties and the observed electrochemical performance. The material that has enabled reaching the highest discharge capacity, combined with satisfactory reversibility and cyclability, CNF500, is not characterized by the highest share of mesoporosity or SSA. These findings do not align with multiple studies that

highlighted the advantage of mesoporous materials with large specific surface area in the application as cathodes in the Li-O_2 batteries [104, 137, 196]. The only parameter that CNF500 excelled in is the lowest disorder level, which surprisingly is not the quality necessarily desired for cathode materials, which will be detailly described in later sections.

The explanation of such contradicting observation is challenging and presented hypothesis is highly speculatory, but based on the finding in literature. Widely perceived as important factor in the assessment of cathode material's suitability is electric conductivity. In the case of carbon nanofibers, electric conductivity heavily depends on the position of graphene layers – based on that three types of CNF can be distinguished platelet, tubular, and fishbone. Although, the influence of temperature on the type of produced CNF have not been investigated in this research, it has been proven in previous studies that for nickel-based catalyst and propane as carbon source, in 450°C platelet CNF can be created, in 500°C and 550°C combination of fishbone and platelet CNF can be obtained, and in 600°C the growth of fishbone CNF is dominant [197, 198]. However, best to my knowledge, no specific work discussing the explicit influence of the type of carbon nanofibers on the performance of lithium-oxygen battery has been published.

6.2. Influence of the nitrogen doping on the properties of CNF500

As have been mentioned earlier in this work, the research on impact of different methods of nitrogen functionalization on the content and type of nitrogen incorporated into the structure of carbon nanofibers has been carried out. For the *in-situ* method, various nitrogen sources have been added to the raw materials stream to investigate the influence of type of dopant on the final content of nitrogen in CNF. However, in the case of *ex-situ* techniques, ammonia has been selected as the nitrogen source and the emphasis of the research has been placed on parameters of the process.

The temperature of 500°C has been chosen for synthesis with *in-situ* functionalization due to the superior performance of lithium-oxygen cell utilizing CNF500 as cathode material in comparison to other carbon nanofibers prepared on the standard catalyst. Accordingly, CNF500 has been chosen for the *ex-situ* functionalization due to the same reasoning.

6.2.1. Synthesis

Synthesis yields of CNF obtained on the standard catalyst with the *in-situ* nitrogen doping at 500°C are presented in the Tab. 10. It is worth reminding that for the same process, but without any source of nitrogen in the feeding stream, the synthesis yield is 7.1 $g_{CNF}g_{cat}^{-1}$ (as stated in Tab. 6). The yields of almost all processes, that included *in-situ* nitrogen doping, have been lower than for the unmodified synthesis. The most significant decreases in synthesis yields are observed, when gaseous ammonia is added to the feeding stream, either as the individual nitrogen source (CNF500-Am) or in combination with acetonitrile (CNF500-Am-Ac), melamine (CNF500-Am-Me), or both (CNF500-Am-Ac-Me). The lowest yields of 2.8 and 2.5 $g_{CNF}g_{cat}^{-1}$ are noted for CNF500-Am and CNF500-Am-Me, respectively. Slightly higher yields are observed for

CNF500-Am-Ac-Me and CNF500-Am-Ac, with 3.2 and 3.6 $g_{CNF}g_{cat}^{-1}$, respectively. The drop of yields of synthesis utilizing melamine as a nitrogen source (CNF500-Me), and the combination of melamine and acetonitrile (CNF500-Ac-Me) is less notable, with yields reaching similar values of 6.4 and 6.1 $g_{CNF}g_{cat}^{-1}$, correspondingly. The only increase of yield of synthesis for *in-situ* functionalization, in comparison to the unmodified process, is observed for the preparation of CNF500-Ac sample, when the acetonitrile has been added to the feeding stream, and the yield has risen up to 8.1 $g_{CNF}g_{cat}^{-1}$. The same dependencies are observed, when the yields of synthesis are recalculated to be expressed in $g_{CNF}g_{Ni}^{-1}$.

The decrease in yield of processes utilizing ammonia has been expected, as it supports the creation of highly dense nucleation sites on the catalyst for CNF synthesis and prevents the passivation of catalyst by removing amorphous carbon, especially in the initial stages of synthesis [199]. Similar decrease of synthesis yields has been observed in previous studies, due to the beneficial effects of ammonia as the dopant that can potentially increase the organization of obtained carbon nanofibers and reduce the amount of amorphous carbon deposited during the synthesis [200]. As a result the overall synthesis yields decreases, but the structure ordering of obtained CNF should be improved. At high temperature melamine decomposes to the wide range of compounds, including ammonia and as a result of above described mechanism of synthesis yield reduction by ammonia is also accurate for melamine [201]. On the other hand, high temperature treatment of acetonitrile leads to the formation of reactive cyano (-CN) and hydrocarbons radicals, thus the formation of carbon nanofibers is less impacted [202].

Tab. 10. Influence of nitrogen doping via *in-situ* technique on the yield of synthesis of CNF on standard catalyst via CVD process at 500°C.

Sample	**Synthesis yield, Y** $(g_{CNF}g_{cat}^{-1})$	**Synthesis yield,** Y_{Ni} $(g_{CNF}g_{Ni}^{-1})$
CNF500-Am	2.8	19.8
CNF500-Ac	8.1	57.6
CNF500-Me	6.4	45.6
CNF500-Am-Ac	3.6	25.8
CNF500-Am-Me	2.5	17.9
CNF500-Ac-Me	6.1	43.8
CNF500-Am-Ac-Me	3.2	22.6

In the case of the nitrogen doping conducted via *ex-situ* methods, the synthesis yield could not be straightforwardly measured. Change of mass due to doping via *ex-situ* methods, either by hydrothermal method or subsequent ammonization technique, is hardly detectable with the use of the analytical balance, thus the yields of *ex-situ* processes can not be estimated in the same way as have been done for the *in-situ* methods – only the amount of nitrogen incorporated to the structure of CNF is measured by elemental analysis and XPS measurements.

6.2.2. Materials characterization

The key parameter for materials analyzed in this chapter is the content of nitrogen that has been incorporated to the structure of carbon nanofibers via various methods. Two main measures of the amount of incorporated nitrogen can be used in such comparison – bulk and surface nitrogen. The bulk form of nitrogen includes all types of nitrogen atoms contained in the material, both internal and surface atoms, and it is measured by elemental analysis. More relevant for the analysis of the impact of nitrogen on the electrochemical performance of cathode materials, is the amount of nitrogen on the surface of material assessed by the XPS measurements. XPS technique provides the data regarding the N content in the top 5-10 nm layer of material. Firstly, the bulk content of nitrogen is compared for all samples and later more in-depth analysis of the surface nitrogen has been carried out for selected samples. Additionally, the bulk oxygen contents for all of the analyzed samples are included, as it also provides insights regarding changes in the material's structure occurring during functionalization.

Utilization of *in-situ* methods via the addition of different nitrogen sources to the stream of raw materials has enabled the incorporation of different amounts of bulk nitrogen in the structure of carbon nanofibers, as presented in the Tab. 11. However, even the pristine CNF500 contains trace amounts of nitrogen and oxygen, 0.65 and 1.02 wt. % respectively. The origin of trace amounts of bulk nitrogen and oxygen is ambiguous, as it may arise from either contaminations during synthesis or purification, or impurities introduced during the measurement.

For processes utilizing only one source of nitrogen, the largest content of incorporated nitrogen of 2.42 wt. % is achieved when ammonia is used. Slightly lower amounts of nitrogen have been built-in with the use of melamine (2.27 wt. %) and acetonitrile (1.35 wt. %) as dopants. When a combination of two or more dopants is used, in most cases the resulting bulk nitrogen content in CNF is higher in comparison to using a single nitrogen source. The only exception is observed for CNF500-Ac-Me, for which the achieved N content of 1.82 wt. % is lower than when only melamine has been used, but it is still slightly higher than for acetonitrile. The amount of nitrogen incorporated into CNF by two or more dopants is not a simple sum of amounts of nitrogen incorporated by these compounds, when used as single dopants. Interestingly, the highest bulk nitrogen content has been achieved not for the combination of all of the tested dopants, but when the combination of ammonia and melamine has been used as nitrogen sources. However, the difference between the bulk nitrogen content in both samples is slight, with 3.90 wt. % and 3.69 wt. % noted respectively for CNF500-Am-Me and CNF500-Am-Ac-Me.

Based on the presented results, the application of ammonia and melamine, as individual dopants, has led to the synthesis of N-doped carbon nanofibers with relatively high content of bulk nitrogen. The beneficial impact on functionalization is amplified, when both of these compounds are used as nitrogen sources at the same time. However, the addition of acetonitrile to melamine in the stream of raw materials leads to the partial reduction of building-in the N atoms to the carbon structure, which is indicated by lower N content in CNF500-Ac-Me and CNF500-Am-Ac-Me. On the other

hand, when the acetonitrile is used in the combination with ammonia, such effect is not observed.

Tab. 11. The comparison of bulk nitrogen and oxygen content in CNF obtained via *in-situ* functionalization.

Sample name	Nitrogen content, wt. %	Oxygen content, wt. %
CNF500	0.65	1.02
CNF500-Am	2.42	1.84
CNF500-Ac	1.35	1.33
CNF500-Me	2.27	1.21
CNF500-Am-Ac	3.28	2.52
CNF500-Am-Me	3.90	1.95
CNF500-Ac-Me	1.82	1.72
CNF500-Am-Ac-Me	3.69	3.02

During the analysis of the of the data in the Tab. 12, the correlation between the bulk nitrogen content and three main parameters of hydrothermal synthesis can be observed. Firstly, with increasing mass ratio of CNF500 to ammonia, the amount of nitrogen incorporated into the carbon structure decreases. When the process is conducted with the smallest excess of ammonia in the mass ratio of 1:25 (CNF500/HT-N25/180), the largest amount of nitrogen of 2.12 wt. % is built into the CNF structure. Conducting hydrothermal processes with increasing excess of ammonia in the initial mixture, in mass ratios of 1:50, 1:100, and 1:200, has led to the gradual decrease in the nitrogen content to 1.39, 1.15, and 0.95 wt. %, respectively. Similar results have been reported in the literature, when with the increasing content of nitrogen source in the initial mixture the content of nitrogen in the final material has decreased. In the work by Zhang *et al.* [203], the amount of nitrogen incorporated into the GO structure has stabilized after exceeding certain mass ratio of GO to urea. Moreover, in the work by Sun *et al.* [204], exceeding certain excess of urea in the initial mixture has led to the decrease in the amount of nitrogen content in the obtained materials.

Secondly, with decreasing pH of the initial mixture the N content in the obtained CNF decreases. The initial alkaline pH of the mixture enables achieving the highest content of nitrogen in the modified carbon nanofibers – 2.12 wt. % for CNF500/HT-N25/180. When the pH is adjusted to 7 and 5, the content of bulk nitrogen in the prepared CNF has dropped to 1.78 and 1.68 wt. %, respectively. The pH of solution influences the chemical state of ammonia, as well as the oxygen functional groups. In an acidic conditions, oxygen functional groups are protonated, and ammonia can act as a nucleophile attacking carbonyls. However, full protonation of oxygen groups reduces their electrophilicity, which makes them less reactive. Moreover, the stability of dispersion of CNF in water is lowered due to aggregation occurring at low pH. In the neutral condition, partial deprotonation of oxygen groups occurs, which slightly increases their reactivity and the stability of water dispersion is also improved. Fully deprotonated oxygen functional groups in the high range of pH are more prone to interact with ammonia, which may lead to nucleophilic substitution or condensation.

In the case of the influence of the temperature of the process on the amount of nitrogen incorporated into the structure of CNF, the correlation is not as straightforward as for pH or the mass ratio between reactants. Initial increase in the process temperature from 160°C to 180°C has resulted in the increase in N content from 1.20 wt. % to 2.12 wt. %. However, the additional increases in the temperature up to 200°C and 220°C have led to the decrease in bulk nitrogen content to 0.92 and 0.86 wt. %.

Tab. 12. The comparison of bulk nitrogen and oxygen content in CNF obtained via *ex-situ* functionalization by hydrothermal method.

Sample name	Nitrogen content, wt. %	Oxygen content, wt. %
CNF500/HT-N25/180	2.12	2.64
CNF500/HT-N25/160	1.20	1.56
CNF500/HT-N25/200	0.92	1.30
CNF500/HT-N25/220	0.86	1.33
CNF500/HT-N25/180/pH7	1.78	1.20
CNF500/HT-N25/180/pH5	1.68	1.23
CNF500/HT-N200/180	0.95	1.67
CNF500/HT-N100/180	1.15	1.53
CNF500/HT-N50/180	1.39	1.89

The subsequent ammonization in the stream of gaseous ammonia in the CVD tube reactor has been selected as the additional *ex-situ* functionalization technique. After the ammonization of pristine CNF500, only marginal increase of bulk nitrogen content up to 1.05 wt. % has been observed, see Tab. 13. The stable structure of carbon nanofibers with moderate susceptibility to modification could be the reason for such insignificant growth of bulk nitrogen content. To investigate this hypothesis, the CNF500 has been oxidized to increase the number of defects in the carbon structure to create additional active sites in carbon nanofibers structure. The as obtained CNF500-OX have significantly higher oxygen content – 7.38 wt. % vs 1.02 wt. % for CNF500 – indicating the rise in number of active sites in the form of oxygen functional groups present on the surface of material. The ammonization of the oxidized material has led to obtaining the material with more than twice the nitrogen content compared to the process carried out on previously unmodified material – 2.43 wt. % for CNF500-OX-Am-ex1. At the same time, the oxygen content in the obtained CNF has dropped to 2.08 wt. %, indicating that oxygen functional groups in the CNF500-OX have reacted with the ammonia and oxygen atoms have been replaced by nitrogen, at least to some extent.

Although, the oxidation of carbon nanofibers seems to be an effective way of making material more prone to the ammonization, the nature of oxygen functional groups suggests that more optimization in the process parameters could be done to maximize the nitrogen content in the final material. Oxygen functional groups in carbon nanomaterials display tendency to decompose during heating in the inert atmosphere. The first signs of the degradation of oxygen functional groups can be noticed already at around 300°C [205]. In the already described process, such degradation of oxygen

functional groups would suggest that when the ammonia is added to the atmosphere of CVD process, majority of the functional groups is already decomposed, which reduces the number of active sites for potential incorporation of nitrogen atoms. Thus, for the preparation of CNF500-OX-Am-ex2 ammonia has been added to the stream of gases from the beginning of the process enabling the reaction of ammonia with oxygen functional groups before they could decompose in higher temperatures. As a result, the obtained material contains higher amount of bulk nitrogen (2.89 wt. %) than the previously prepared CNF. At the same time, lower content of oxygen in CNF500-OX1N-ex2 suggests that the additional nitrogen atoms have replaced oxygen atoms in the structure of the final material.

Tab. 13. The comparison of bulk nitrogen and oxygen content in CNF obtained via *ex-situ* functionalization by subsequent ammonization.

Sample name	Nitrogen content, wt. %	Oxygen content, wt. %
CNF500-Am-ex	1.05	0.59
CNF500-OX	1.85	7.38
CNF500-OX-Am-ex1	2.43	2.08
CNF500-OX-Am-ex2	2.89	1.89

To furtherly investigate the influence of N-doping on the structure of carbon nanofibers, several CNF have been chosen for the XPS measurements. The deconvolution of C 1s peaks has been conducted for CNF500 and CNF500-OX samples to assess the impact of oxidation on carbon structure of CNF. Additionally, the deconvolution of O 1s and N 1s peaks has been conducted for selected samples to analyze the types and amounts of oxygen and nitrogen functional groups that have been introduced to the surface of CNF. The calculated atomic composition and high-resolution XPS spectra of CNF500 and CNF500-OX are presented in the Tab. 14 and Fig. 17.

Tab. 14. Types and amounts (at. %) of carbon atoms according to the deconvolution of C 1s peak from XPS spectra.

	C 1s peak deconvolution							
	C=C sp^2	C–C sp^3	C–O C=N	C–O–C C–NH N–C–O	C=O O–C–O N–C=O	O–C=O	Shake-up	Shake-up
Binding energy, eV	284.4	285.0	286.1	287.1	288.4	289.5	290.9	293.3
CNF500	59.6	13.1	6.5	4.6	3.3	2.2	6.0	2.2
CNF500-OX	51.8	12.4	7.0	4.5	4.3	2.2	5.8	2.4

The summarized data regarding types and amounts of nitrogen and oxygen functional groups, combined with the high-resolution spectra is presented in the Tab. 15 and Fig. 17. Additional trace amounts of Ni have been detected in the XPS spectra for

CNF500-Am-Me and CNF500-Am-Ac-Me. However, due to the marginal atomic concentrations of nickel in these materials, which are actually at the detection limit of the XPS method, and the resulting low signal/noise ratio, their influence on the structure and properties of the mentioned samples is negligible.

Tab. 15. Types and amounts (at. %) of nitrogen and oxygen functional groups based on the deconvolution of N 1s and O 1s peaks from XPS spectra.

	N 1s peak deconvolution			**O 1s peak deconvolution**	
	C=N(Ar) C-NH	O–C–N O=C–N NH_4^+	$-NO_2$	O=C O-Ni N–O	O–C –OH
Binding energy, eV	398.8	400.6	405.6	531.5	533.1
CNF500	-	-	-	0.4	2.2
CNF500-OX	-	-	0.5	3.5	5.7
CNF500-Am-Me	1.8	1.5	-	2.2	0.9
CNF500-Am-Ac-Me	1.3	1.1	-	1.2	1.5
CNF500/HT-N25/180	2.9	2	-	0.9	4.8
CNF500-OX-Am-ex2	1.1	1.1	-	0.7	1.7

From the presented XPS data for CNF500 and CNF500-OX, the dominant share of C=C sp^2 carbon bonds related to the graphitic carbon is visible. However, the share of graphitic carbon in composition is reduced from 59.6 at. % for CNF500 to 51.8 at. % for CNF500-OX, suggesting that the introduction of oxygen functional groups occurs at the expense of sp^2 carbons. The disruption of graphitic structure is also noticeable in the slight changes in the shake-up signals. The effectiveness of the proposed oxidation method is visible in the notable increase in the overall surface oxygen content from 2.6 at. % for CNF500 to 9.2 at. % for CNF500-OX. The introduction of oxygen in the form of carbonyl (C=O), hydroxyl (-OH), and carboxyl (-COOH) groups is visible in the increasing proportion of peaks corresponding to these groups, especially at 531.5 eV and 533.1 eV in O 1s spectra and at 288.4 eV in C 1s. Moreover, the treatment with nitric acid has introduced minimal amount (0.5 at. %) of nitrogen in the form of nitro groups ($-NO_2$), but the absence of other nitrogen-related peaks in the spectra of CNF500-OX indicate, that the significant N-doping did not occur in this process.

The *in-situ* nitrogen doping via CVD process has led to the incorporation of moderate amounts of nitrogen atoms on the surface of carbon nanofibers, but in comparison to the CNF500 (0.0 at. % of N according to the Tab. 15) the observed increase to 3.3 and 2.4 at. % for CNF500-Am-Me and CNF500-Am-Ac-Me, respectively, is substantial. Moreover, the balance between the types of incorporated functional groups is visible for both *in-situ* modified samples, as presented in the Fig. 18. 1 and 18.3.

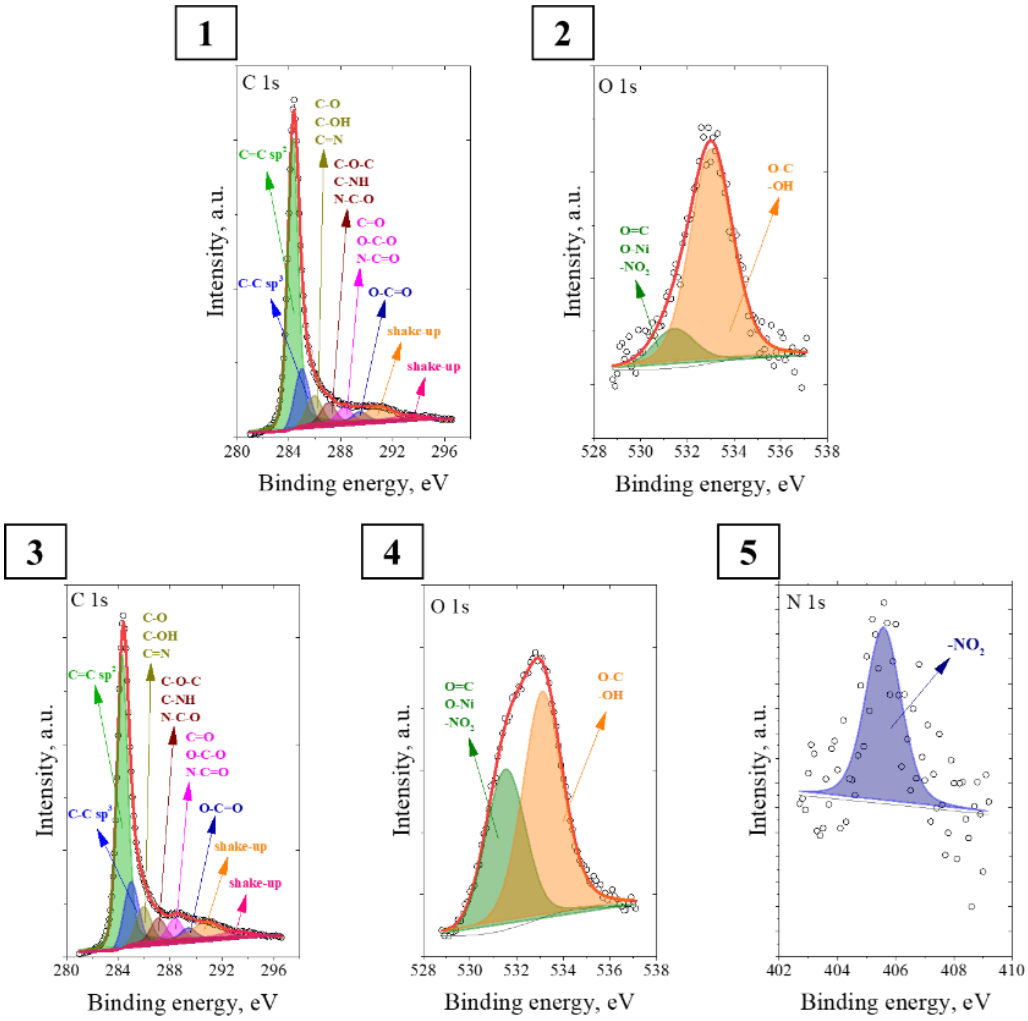

Fig. 17. High-resolution XPS spectra results for: 1, 2 - CNF500; 3, 4, 5 - CNF500-OX.

The reduction in amount of N atoms, that have been built-into the CNF structure after the addition of acetonitrile to the stream of raw materials, can originate from the properties of acetonitrile itself and potential competition with other nitrogen sources (ammonia and melamine). Acetonitrile role, as a both nitrogen and carbon source, can limit its potential in incorporating N atoms to the carbon structure. The thermal decomposition of acetonitrile leads to the formation of reactive cyano (-CN) and hydrocarbons radicals. While hydrocarbons radicals may effectively contribute to the formation of carbon nanofibers, the -CN radicals can form highly volatile HCN, which could potentially leave the reactor, leading to the loss of nitrogen as gaseous side product [206]. Such explanation is furtherly supported by lower content of bulk nitrogen incorporated in carbon nanofibers during the process, when acetonitrile has been used as an only dopant (1.35% for CNF500-Ac), in comparison to nanofibers obtained via synthesis utilizing ammonia or melamine as individual dopants (2.42% for CNF500-Am and 2.27% for CNF500-Am-Me). Additionally, for the synthesis of CNF500-Am-Ac-Me, acetonitrile competes as N-donor with ammonia and melamine, which are more effective dopants as their decomposition leads to the generation of

amine, pyridinic, and pyrrolic species, that can be more easily built into the CNF [207–209].

In terms of *ex-situ* techniques, subsequent ammonization of CNF500-OX in the stream of gaseous ammonia has led to the introduction of lower amount of nitrogen atoms as compared to the *in-situ*. The -NO_2 groups that have been introduced during the oxidation have been reduced and additional nitrogen atoms have been incorporated in the form of amides and/or C=N bonds in aromatic systems (1.1 at. %) and O-C-N and/or N-C=O bonds and/or ammonium groups (1.1 at. %). Moreover, the overall reduction of carbon nanofibers has occurred during this process, which is visible in the substantial decrease of oxygen functional groups content in material before and after ammonization – from 9.2 at. % for CNF500-OX to 2.4 at. % for CNF500-OX-Am-ex2. The observed reduction could be expected as ammonia in the gaseous form can interact with oxygen functional groups replacing them in the carbon structure – such reaction can occur at temperatures as low as 300°C [205]. Thus, the addition of the gaseous ammonia to the stream of raw materials at the beginning of ammonization has a beneficial effect on the amount of incorporated nitrogen, as demonstrated by the data in the Tab. 13 (2.43% of N for CNF500-OX-Am-ex1 vs 2.89% of N for CNF500-OX-Am-ex2).

On the other hand, the second technique of *ex-situ* functionalization – hydrothermal method – has resulted in the highest content of surface nitrogen amongst compared samples – 4.9 at. % for CNF500-HT-N25/180. However, high oxygen content of 5.7 at. % seems slightly counterintuitive given the presence of ammonia (reducing agent) and overall reducing environment of the process. The observed retention of oxygen content can originate from the combination of stabilizing influence of aqueous environment on the oxygen functional groups, incomplete reduction of existing oxygen functional groups and the formation of mixed nitrogen-oxygen functional groups. The aqueous environment in hydrothermal synthesis can stabilize oxygen functional groups, making them less susceptible to reduction or removal [210]. Additionally, the relatively low temperature might not be sufficient to fully reduce oxygen-containing groups [211]. Lastly, rather than fully removing oxygen groups from the material's surface, ammonia in hydrothermal conditions can react with some oxygen-containing functional groups leading to the formation of mixed nitrogen-oxygen groups [212].

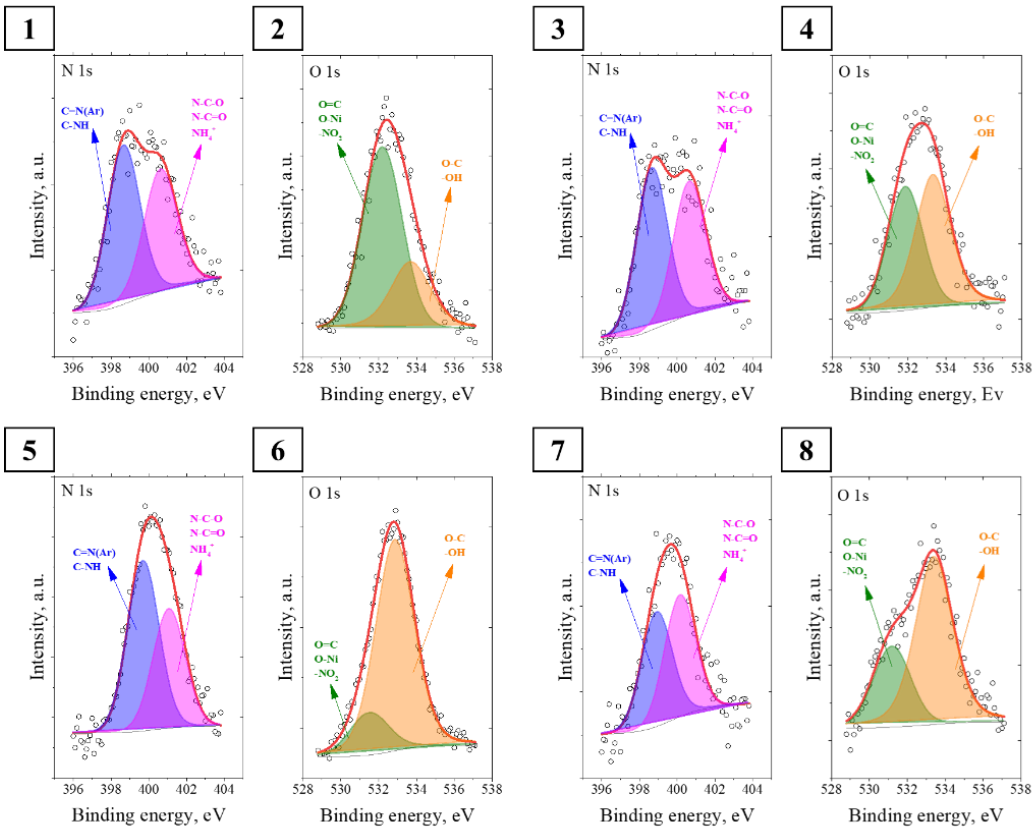

Fig. 18. High-resolution XPS spectra of N 1s and O 1s of selected N-doped samples: 1, 2 - CNF500-Am-Me; 3, 4 - CNF500-Am-Ac-Me; 5, 6 - CNF500/HT-N25/180; 7, 8 – CNF500-OX-Am-ex2.

In terms of comparing the amounts of surface nitrogen and bulk nitrogen introduced into the carbon structure by each of the analyzed processes, higher bulk nitrogen content is visible in most materials. For the functionalization via *in-situ* method and subsequent ammonization, higher content of bulk nitrogen could be expected due to the higher temperature of these processes. During high-temperature processes, like the discussed CVD-based ammonization, nitrogen atoms incorporate into the carbon structure may migrate into the bulk regions of material, rather than remaining at the surface. Additionally, in the case of *in-situ* functionalization, nitrogen is build-into the carbon matrix directly during the growth of carbon nanofibers. Thus, nitrogen atoms that are introduced to the bulk regions of CNF are not detectable during the surface analysis via XPS measurements. The only exception is the sample obtained as a result of the hydrothermal process, for which a higher surface nitrogen content is noticeable – such result could be related with the previously discussed effects of surface modifications (due to the formation of mixed nitrogen-oxygen functional groups) and stabilization of functional groups at the surface of material in the aqueous environment.

In the case of susceptibility of carbon nanofibers to the ammonization via compared *ex-situ* techniques, interesting observations can be made. For the hydrothermal process, pre-treatment is not required to achieve relatively high content of incorporated nitrogen atoms. On the other hand, when raw material for the subsequent ammonization has not been oxidated before the process, the amount of incorporated

nitrogen atoms have been over two times lower than for the oxidized raw materials (see Tab. 13). The observed results, indicate that prepared carbon nanofibers (CNF500) are relatively stable at high temperatures and resistant to the ammonization by gaseous ammonia. However, in the aqueous environment and high pressure, but significantly lower temperature utilized in the hydrothermal process, the same carbon nanofibers display tendency to react with ammonia, which leads to the introduction of N atoms to their surface.

In general, all of the proposed functionalization methods have resulted in the preparation of carbon nanofibers with comparable content of nitrogen, but optimization of process parameters plays a key role. Also, the type of incorporated nitrogen varies between each techniques, with *in-situ* functionalization introducing higher content of bulk nitrogen than surface nitrogen, whereas hydrothermal treatment is leading to higher content of surface nitrogen. In the case of subsequent ammonization, oxidation of material is required to achieve similar amounts of nitrogen atoms as in *in-situ* or hydrothermal modification. In the case of types of incorporated nitrogen functional groups, for the *in-situ* doping and subsequent ammonization, the obtained materials display balanced share between C=N(Ar), C-NH, and O-C-N, O=C-N, NH_4^+ groups. For sample prepared via hydrothermal treatment, slight excess of C=N(Ar), CNH groups is observed.

Apart from the composition, nitrogen doping has influence on other parameters of the structure of carbon nanofibers, including morphology, porosity, and level of structural organization. However, when the SEM images of unmodified CNF500, shown in the Fig. 12, are compared with the SEM images of selected carbon nanofibers after functionalization, shown in the Fig. 19, no evident differences in the morphology of the presented materials are visible. Morphology of all of the presented materials is rather similar, with individual nanofibers having comparable dimensions (diameters and length) and materials displaying heavily entangled macroscopic structure. The bright elements visible in the Fig. 19.1 should be identified as residuals of nickel nanoparticles that have not been fully removed from the material after synthesis. The presence of Ni residuals is in agreement with the XPS measurements, that have indicated such observations.

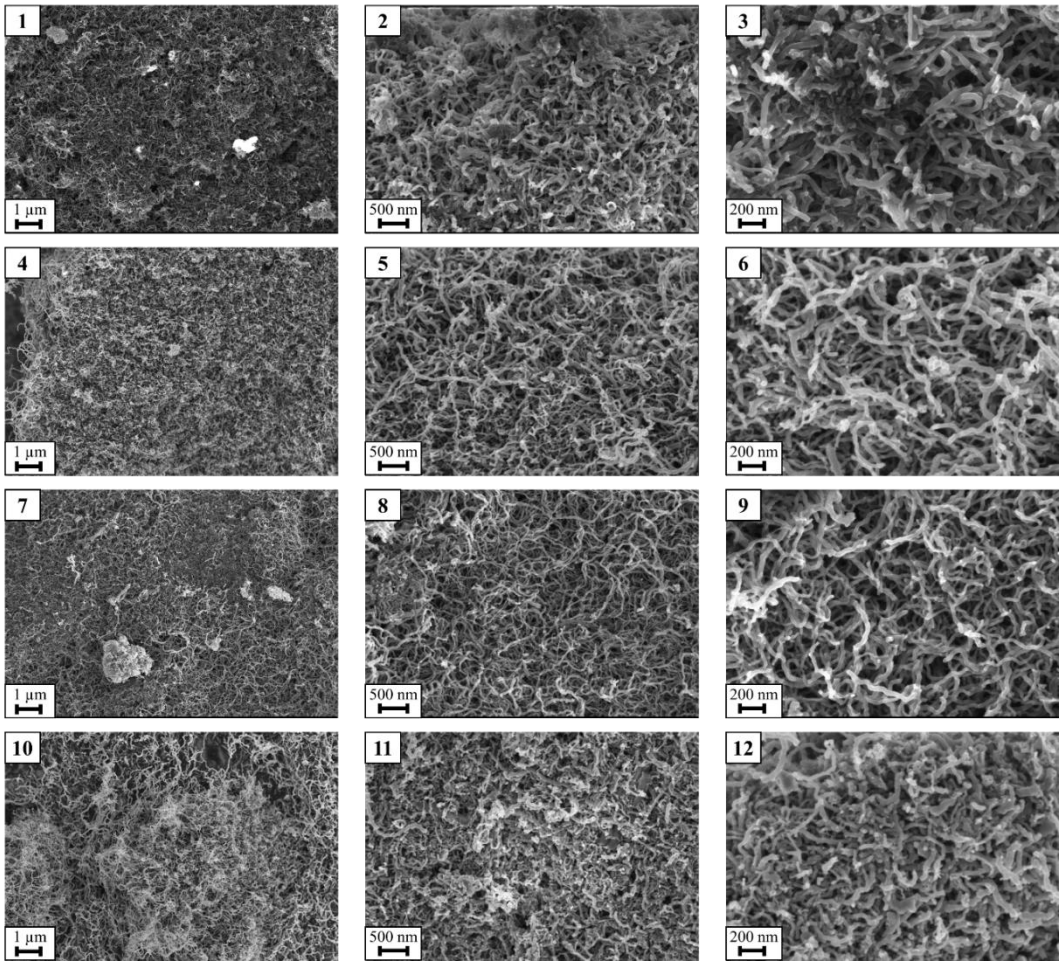

Fig. 19. Comparison of SEM images of N-doped carbon nanofibers: 1, 2, 3 - CNF500-Am-Me; 4, 5, 6 - CNF500-OX; 7, 8, 9 - CNF500-OX-Am-ex2; 10, 11, 12 - CNF500/HT-N25/180.

According to the parameters of porosity of nitrogen doped CNF presented in Tab. 16, specific surface area of all of the functionalized samples have increased in comparison to the unmodified CNF500. When only one nitrogen source is utilized as a dopant, the smallest change in the SSA is observed for CNF obtained with ammonia in the raw materials stream (CNF500-Am), for which the specific surface area has grown only to 135 m^2g^{-1}. More significant changes of SSA are noticed for CNF500-Ac and CNF500-Me, so for the addition of acetonitrile and melamine into the raw materials stream, for which the surface area has increased up to 183 and 211 m^2g^{-1}, respectively. If the combination of two nitrogen sources has been used in the preparation of CNF, the observed growth has been more significant. In these cases, the specific surface area has risen to 211, 223, and 191 m^2g^{-1} for CNF500-Am-Ac, CNF500-Am-Me, and CNF500-Ac-Me, correspondingly. However, the most substantial increase in specific surface area to 284 m^2g^{-1}, which is over 2-times higher than for unmodified sample, has been noticed for the CNF500-Am-Ac-Me sample.

Tab. 16. Influence of nitrogen doping via *in-situ* technique on the parameters of porous structure of CNF on standard catalyst via CVD process at 500°C.

Sample	Specific surface area, S_{QSDFT} (m^2g^{-1})	Total pore volume, V_T (cm^3g^{-1})	Mesopores volume, V_{meso} (cm^3g^{-1})	V_{meso}/V_T
CNF500	123	0.294	0.258	0.88
CNF500-Am	135	0.242	0.201	0.83
CNF500-Ac	183	0.402	0.352	0.88
CNF500-Me	211	0.479	0.419	0.88
CNF500-Am-Ac	223	0.310	0.247	0.80
CNF500-Am-Me	225	0.438	0.379	0.86
CNF500-Ac-Me	191	0.339	0.285	0.84
CNF500-Am-Ac-Me	284	0.372	0.291	0.78

In the case of total pore and mesopores volume, the straightforward correlation between the utilization of different nitrogen sources in *in-situ* doping processes can not be drawn. In general, the V_T of nitrogen doped CNF has risen as compared to CNF500, with the exception of CNF500-Am for which the total pore volume decreased to 0.242 cm^3g^{-1}. Similarly, the V_{meso} of almost all nitrogen functionalized samples has risen with the exception of CNF500-Am and CNF500-Am-Ac samples, for which mesopores volumes have dropped to 0.201 cm^3g^{-1} and 0.247 cm^3g^{-1}, respectively. However, all of carbon nanofibers synthesized with the utilization of *in-situ* functionalization techniques have maintained their dominant mesoporous characteristics, which is proven by high V_{meso}/V_T ratio, between 0.78-0.90 (see Tab. 16), and type IV of adsorption/desorption isotherm with typical hysteresis loop visible in each of N_2 adsorption/desorption graphs (Fig. 20.1, 20.3, 20.5, 20.7, 20.9, 20.11, and 20.13). Moreover, the PSD graphs (Fig. 20.2, 20.4, 20.6, 20.8, 20.10, 20.12, and 20.14) clearly show that pores with diameter above 2 nm majorly contribute to the total pore volume of each material, which furtherly indicate the dominant mesoporous character of CNF synthesized during *in-situ* functionalization.

As can be observed in the Tab. 17, the influence of *ex-situ* modifications on the porosity of carbon nanofibers is less significant than the *in-situ* functionalization. The oxidation of pristine carbon nanofibers in concentrated nitric acid has led to the slight increase of SSA and V_T to 135 m^2g^{-1} and 0.375 cm^3g^{-1} in comparison to the CNF500. The subsequent ammonization of as obtained material has led to further increase of SSA to 155 m^2g^{-1} and marginal rise in V_T to 0.377 cm^3g^{-1}. The observed development of porous structure in the mentioned samples is related to the introduction of nitrogen and oxygen containing functional groups, which increases number of defect sites enhancing the porosity.

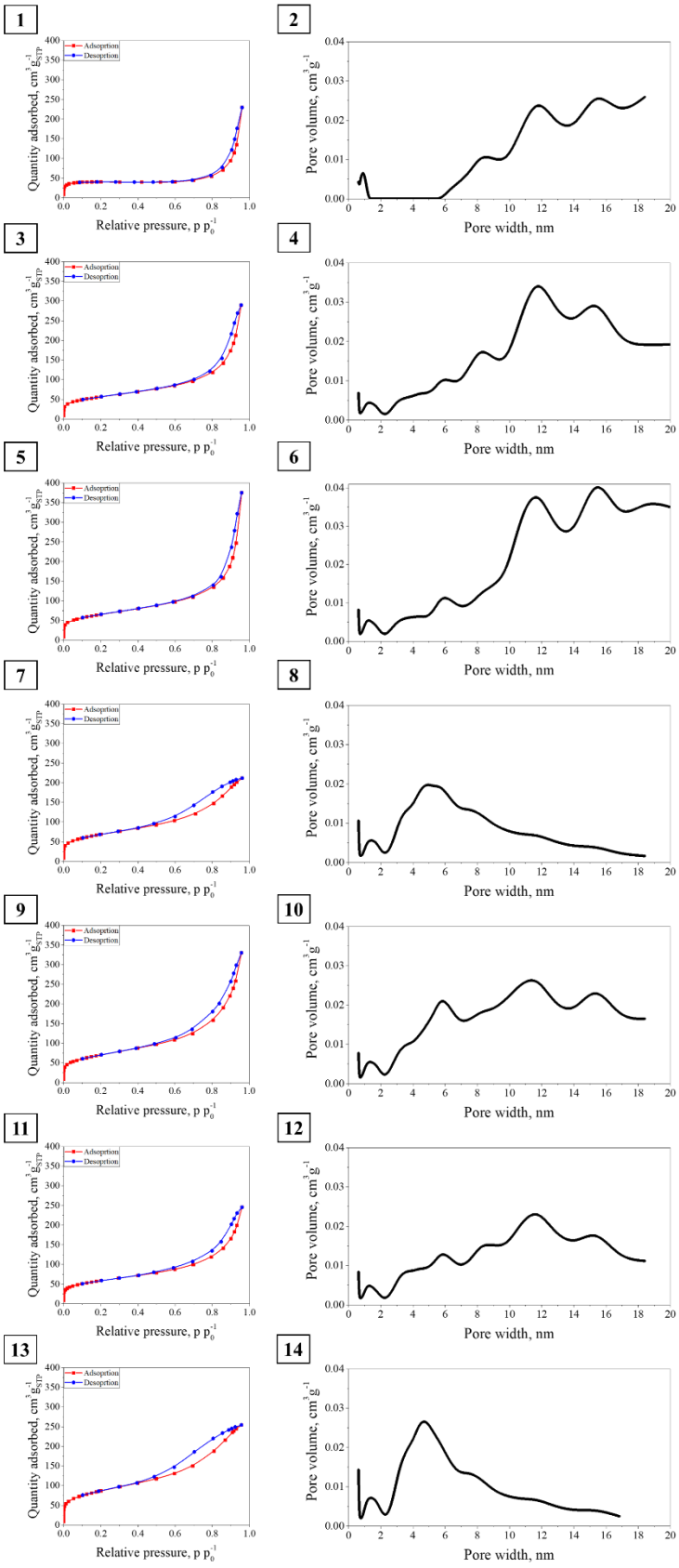

Fig. 20. The N_2 adsorption/desorption isotherms and PSD of nitrogen doped via *in-situ* technique CNF synthesized on the standard catalyst via CVD process at 500°C: 1, 2 - CNF500-Am; 3, 4 - CNF500-Ac; 5, 6 - CNF500-Me; 7, 8 - CNF500-Am-Ac; 9,10 - CNF500-Am-Me; 11, 12 - CNF500-Ac-Me; 13, 14 - CNF500-Am-Ac-Me.

Although, the hydrothermal treatment also introduces nitrogen and oxygen containing functional groups, it has led to the decrease of specific surface area to 99 m^2g^{-1} and total pore volume to 0.265 cm^3g^{-1} in comparison to the CNF500. The observed reduction of porosity can occur due to restructuring of the carbon framework, which may lead to the collapse or blockage of pores. Similar degradation of porosity of carbon materials, due to the hydrothermal treatment with ammonia, has been previously reported by Moyseowicz *et al.* [213].

Tab. 17. Influence of *ex-situ* modifications on the parameters of porous structure of CNF.

Sample	**Specific surface area, S_{QSDFT} (m^2g^{-1})**	**Total pore volume, V_T (cm^3g^{-1})**	**Mesopores volume, V_{meso} (cm^3g^{-1})**	**V_{meso}/V_T**
CNF500-OX	135	0.375	0.342	0.91
CNF500-OX-Am-ex2	155	0.377	0.336	0.89
CNF500/HT-N25/180	99	0.265	0.244	0.92

The share of mesoporosity in all of the analyzed samples has slightly increased after the *ex-situ* treatment, which is visible in the rise in the values of V_{meso}/V_T ratio in the Tab. 17, as compared to 0.88 noted for CNF500. The dominant mesoporosity is also noticeable in the type IV of N_2 adsorption/desorption isotherms at 77 K according to the IUPAC methodology as presented in the Fig. 21 [195]. Additionally, for CNF500-OX, CNF500-OX-Am-ex2, and CNF500/HT-N25/180 pores with the largest volumes have the diameters of 10 nm and above, according to the PSD graphs in the Fig. 21, which furtherly proves the dominant mesoporous nature of materials after *ex-situ* modifications.

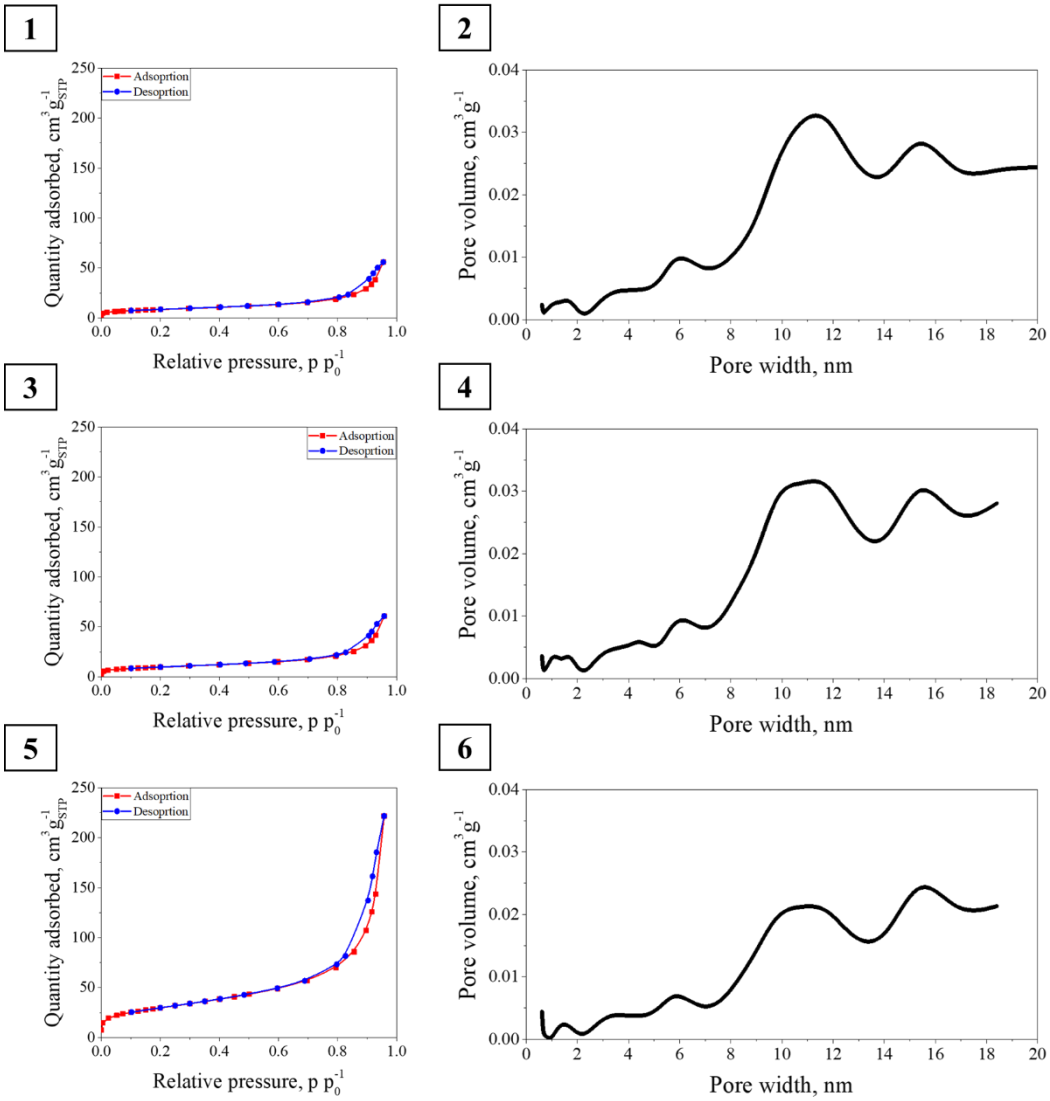

Fig. 21. The N_2 adsorption/desorption isotherms and PSD graphs of CNF after *ex-situ* modifications: 1, 2 - CNF500-OX; 3, 4 - CNF500-OX-Am-ex2; 5, 6 - CNF500/Hydro-N25/180.

Key parameters of carbon structure of selected CNF after *in-situ* and *ex-situ* modification are summarized in the Tab. 18. For all of the analyzed CNF, the growth in the level of disorder, defined by the value I_D/I_G ratio, of carbon structure is observed. The lowest increase in the level of disorder is observed for the carbon nanofibers after *in-situ* functionalization, from 1.34 for CNF500 to 1.35 for CNF500-Am-Me. The observed small increase of level of disorder for CNF500-Am-Me can be attributed to the beneficial effects of the addition of ammonia to the feeding stream on the organization of created carbon nanofibers [200]. In the case of carbon nanofibers that have undergone the *ex-situ* treatment, the disruption of the graphitic lattice is more evident, leading to higher values of I_D/I_G ratio of 1.55, 1.59, and 1.50 for CNF500-OX, CNF500-OX-Am-ex2, and CNF500/HT-N25/180, respectively. The described increased level of disorder for CNF after surface functionalization is related to the introduction of nitrogen and oxygen functional groups into the sp^2 carbon structure. The incorporation

of functional groups introduces defects and distortions in the graphitic domains of carbon nanofibers, effectively increasing their disorder level.

Tab. 18. Comparison of key parameters of Raman spectra of selected carbon nanofibers after functionalization.

Sample	**D-band peak position, cm^{-1}**	**G-band peak position, cm^{-1}**	**I_D/I_G ratio**
CNF500-Am-Me	1 339	1 583	1.35
CNF500-OX	1 336	1 579	1.55
CNF500-OX-Am-ex2	1 343	1 583	1.59
CNF500/HT-N25/180	1 336	1 579	1.50

Apart from the increase in the level of disorder, slight changes in the position of peaks for D-band and G-band are noticeable for carbon nanofibers after surface functionalization. The discussed shifts in peaks position are not as significant to be visible in the spectra in the Fig. 22, but are visible in the results presented in the Tab. 18 and their nature can be attributed to the introduction of nitrogen and oxygen functional groups. The observed slight shift of peaks position towards lower wavenumber (red shift) for both D-band and G-band peaks is related to the increased number of structural defects and increased electron density, suggesting the charge transfer from dopants to the CNF (n-doping) [177, 214].

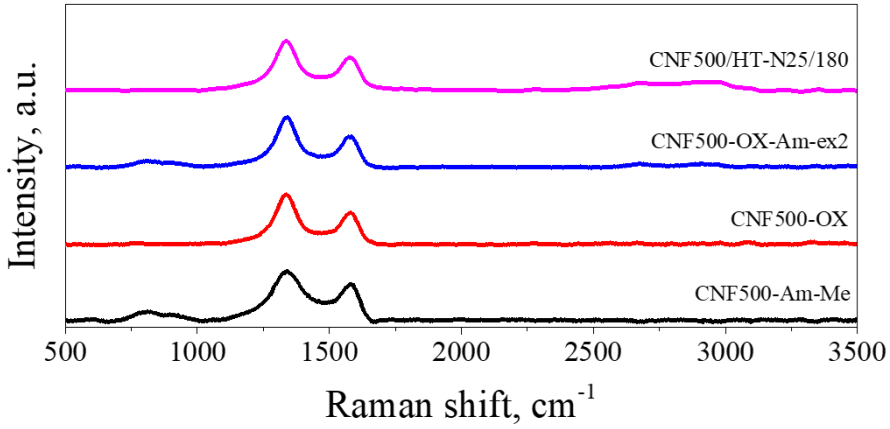

Fig. 22. Raman spectra of selected carbon nanofibers after functionalization.

6.2.3. Performance of Li-O_2 cells

For the selected carbon nanofibers, electrochemical measurements have been carried out to investigate the influence of the surface modifications of cathode materials, by *in-situ* and *ex-situ* methods, on the performance of lithium-oxygen batteries. The summary of the performance together with the galvanostatic curves for the first discharge-charge cycle are presented in the Tab. 19 and Fig. 23.

In comparison to the CNF500, serving as a reference point for the modified carbon nanofibers, all of the samples after surface functionalization enabled achieving higher first discharge capacities in the first cycle. The lowest increase by 2% amongst modified samples has been observed for CNF500-Am-Me and CNF500-Am-Ac-Me.

The mild increase by 10% has been reported for CNF500-OX. While the *ex-situ* N-doping has led to the largest increase of the first cycle discharge capacity by 14% and 20% for CNF500-OX-Am-ex2 and CNF500/HT-N25/180, respectively. The most significant changes are observed in terms of the increase of the first cycle reversibility. For materials after *in-situ* functionalization the reversibility has improved from 56% reported for CNF500, up to 92% and 95% noted for CNF500-Am-Ac-Me and CNF500-Am-Me, respectively. In the case of N-doping via *ex-situ* techniques, the observed increase in reversibility, to 95% and 96% for CNF500-OX-Am-ex2 and CNF500/HT-N25/180, is even higher than for materials after *in-situ* modifications. The only decline in the first cycle reversibility to 14% is observed for CNF500-OX.

Tab. 19. Summary of electrochemical performance of Li-O_2 batteries with CNF after surface functionalization as cathode materials during the first discharge-charge cycle

Sample	**1st cycle discharge capacity, mAh g^{-1}**	**1st cycle charge capacity, mAh g^{-1}**	**1st cycle reversibility**
CNF500-Am-Me	832	795	95%
CNF500-Am-Ac-Me	834	769	92%
CNF500-OX	899	130	14%
CNF500-OX-Am-ex2	927	885	95%
CNF500/HT-N25/180	976	932	96%

Apart from the significant increase in the reversibility of the first cycle, the slight decrease in the charge overpotential for the *in-situ* functionalized materials can be noticed. As compared to CNF500, for which the charging plateau is located at around 4.4 V, the beginning of charging plateaus for CNF500-Am-Me and CNF500-Am-Ac-Me can be assigned at around 3.75 V and 4.25 V, respectively – in these cases the plateau is defined as a moment, when the increase of potential during charging significantly slows down, due to the fact that a "conventional plateau" (region where the potential remains relatively stable for an extended period) can not be clearly defined. As a result, the charge overpotential for the discussed samples decreases to 0.75 V and 1.25 V, correspondingly. For the carbon nanofibers after *ex-situ* doping, charging plateaus at similar potentials are observed – at 3.80 V for CNF500-OX-Am-ex2 and 4.00 V for CNF500/HT-N25/180, which corresponds to charging overpotential of 0.80 V and 1.00 V, respectively. In the case of CNF500-OX, charging plateau, as described above, could not be determined.

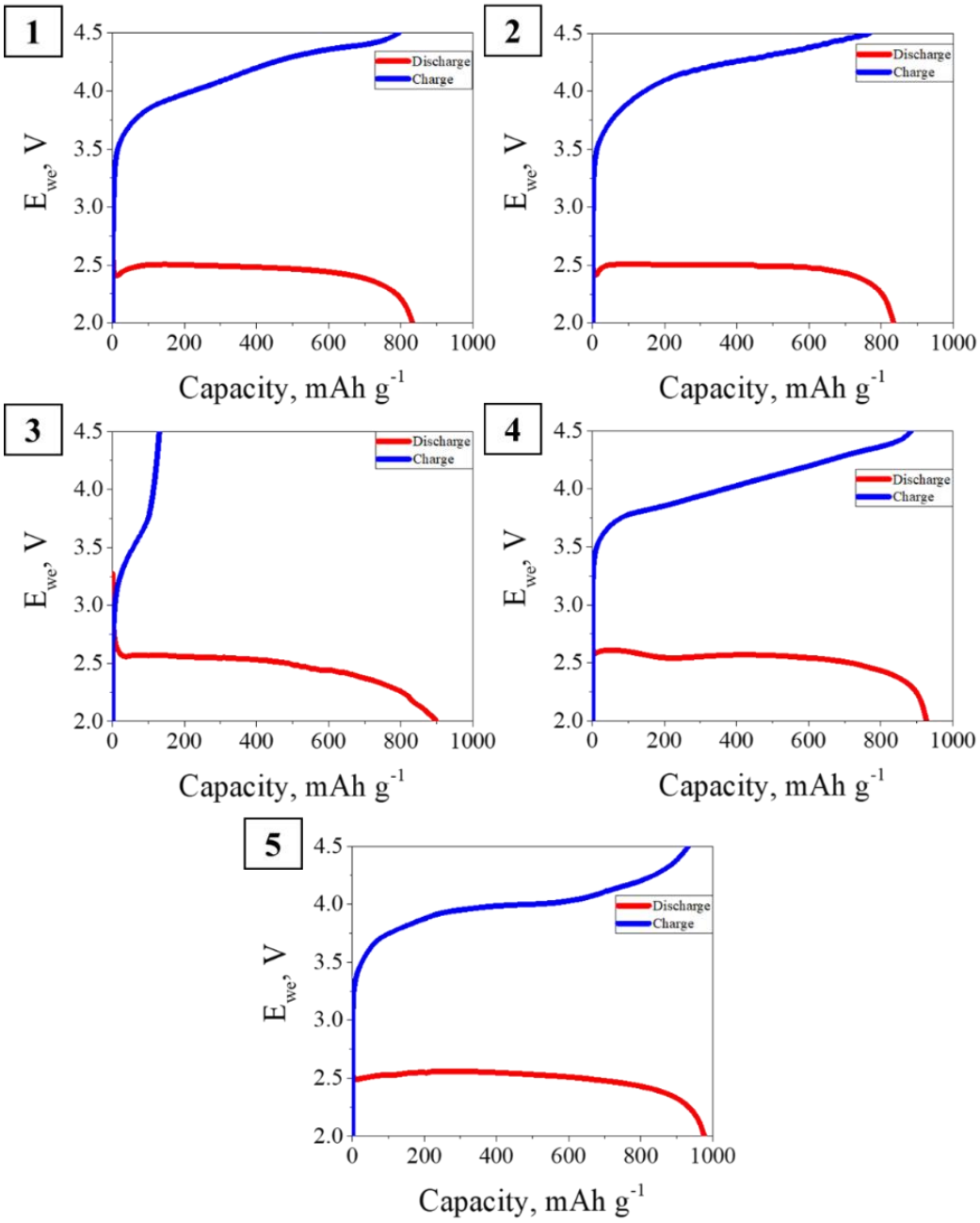

Fig. 23. Comparison of GCPL measurements for the first discharge-charge cycle conducted at current density of 0.4 mA cm^{-2} with CNF after surface functionalization as a cathode materials: 1 - CNF500-Am-Me; 2 - CNF500-Am-Ac-Me; 3 – CNF500-OX; 4 - CNF500-OX-Am-ex2; 5 - CNF500/HT-N25/180.

One of the most notable improvements in the performance after the N-doping of cathode materials have been observed for the cyclability performance, as presented in the Fig. 24. While for CNF500 the discharge capacity drops below 50 mAh g^{-1} after the initial 4 cycles, for the N-doped CNF the discharge capacities remain above this threshold for at least 12 cycles. Amongst compared materials after surface functionalization, the best performance across all 50 cycles is displayed by CNF500-Am-Ac-Me, with high capacities above 100 mAh g^{-1} retained for 11 cycles and subsequent gradual decline from around 50 mAh g^{-1} at 16th cycle to around 30 mAh g^{-1} at 50th cycle. For the other sample after *in-situ* doping (CNF500-Am-Me),

the discharge capacities gradually decline from around 120 mAh g^{-1} at the 2nd cycle to around 15 mAh g^{-1} at the 50th cycle. In the case of CNF500/HT-N25/180, high discharge capacities around 250 mAh g^{-1} are retained for the initial 6 cycles, but the steep drop to almost 0 mAh g^{-1} at 20th cycle is observed. Somewhat similar behavior to CNF500/HT-N25/180 is observed for the CNF500-OX-Am-ex2 sample, but high discharge capacity of around 250 mAh g^{-1} is remained only for 3 cycles, after which the gradual decline to only few mAh g^{-1} at 30th cycle occurs. Out of all of the compared CNF after surface modifications, arguably the worst cyclability performance is displayed by CNF500-OX. For the CNF after surface oxidation, discharge capacity drops below 50 mAh g^{-1} threshold after the 3rd cycle and is retained at relatively stable level for the next 6 cycles. Subsequent gradual decline occurs and the discharge capacity drops below 5 mAh g^{-1} after 30th cycle.

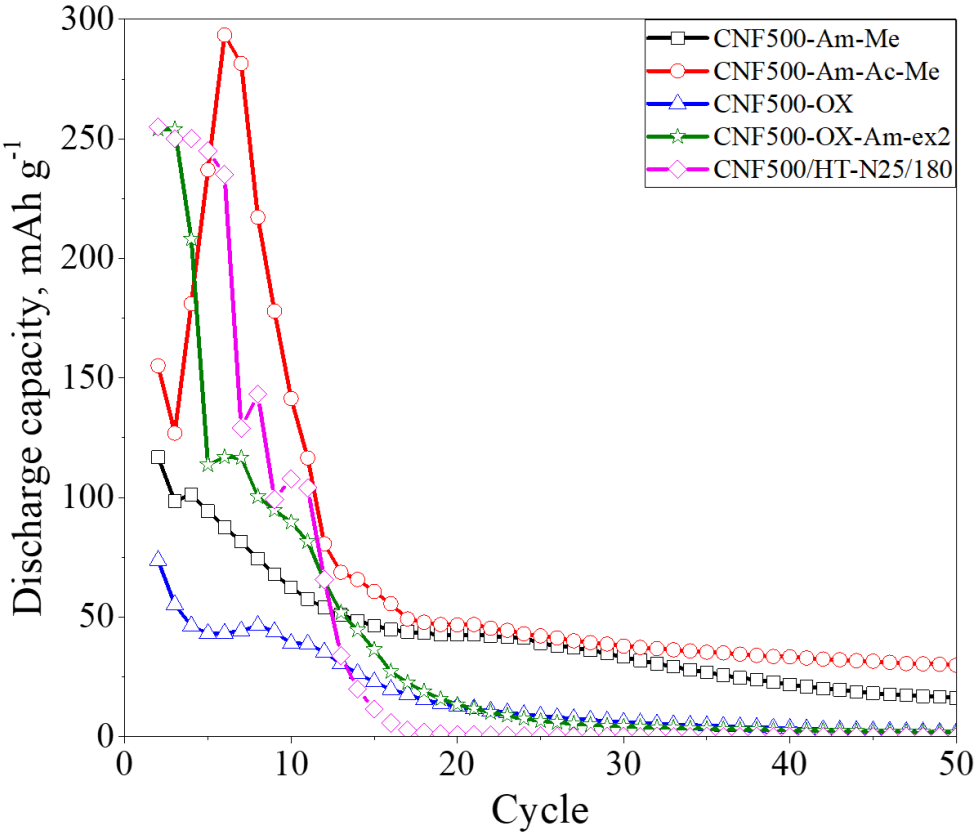

Fig. 24. Comparison of cyclability performance of CNF after surface functionalization as cathode materials during the GCPL measurements at 0.4 mA cm^{-2}, the first discharge cycle is excluded.

The growth of specific surface area and total pore volume of CNF after nitrogen doping contribute to the increase of discharge capacities of the first cycle as compared to the pristine CNF500. Additionally, presented functionalization techniques increase the number of structural defects, as can be observed in the increase of I_D/I_G ratio, which furtherly contributes to the enhancement of discharge capacity. The presented electrochemical performance of CNF after nitrogen doping is consistent with the previous reports [153, 173]. Similarly, the improvements of reversibility and cyclability

of N-doped carbon nanofibers is attributed to the surface functionalization. The incorporation of nitrogen atoms into the carbon structure is a proven strategy to increase electric conductivity and catalytic activity of cathode materials in the ORR/OER, which leads to the decrease of charge overpotential and increase of reversibility.

However, the influence of incorporation of oxygen functional groups into the structure of carbon nanofibers on the electrochemical performance requires more attention. As have been stated in previous reports, introduction of oxygen atoms can lead to the increase of the first discharge capacity, but it may result in the decrease of reversibility and overall cyclability [171, 172]. The increase of the first cycle discharge capacity for CNF500-OX originates from similar factors as in nitrogen doping – increase of SSA, V_T, and level of disorder. However, the incorporation of oxygen functional groups can also promote side reactions occurring during discharge and charge, resulting in electrolyte decomposition, creation of side products, and degradation of other cell components, like separators or current collectors. Hence the overall electrochemical properties of material are heavily impacted, which is visible in lower reversibility of the first discharge/charge cycle and poorer cyclability for CNF500-OX in comparison to the CNF500 [153].

Additionally, rapid fade of discharge capacity during cyclability measurements for *ex-situ* modified materials, as compared to the materials after *in-situ* functionalization, can also be related to higher oxygen content in these samples. This effect is especially noticeable in the case of CNF500/HT-N25/180 sample, for which the surface nitrogen content is the highest among N-doped materials, but so is the oxygen content. Thus, the discharge capacity rapidly declines after just few cycles. Even though, CNF500-OX-Am-ex2 has lower surface oxygen content than CNF500-Am-Me and CNF500-Am-Ac-Me, its surface nitrogen content is also lower leading to the decline of electrochemical performance. Moreover, CNF with the lowest surface oxygen content (2.70 at. % for CNF500-Am-Ac-Me) show the highest discharge capacity across larger number of cycles – this further proves that higher oxygen content leads to poorer cyclability performance.

The observed influence of nitrogen doping on the electrochemical performance of lithium-oxygen batteries is quite consistent with the literature reports, especially for samples after *ex-situ* functionalization, for which the reported improvements have been the most significant. The incorporation of nitrogen atoms into the structure of cathode materials, at the similar levels as the N content reported in this research, in the works by Ionescu *et al.* and Zhang *et al.* has led to the comparable increase in the first cycle discharge capacities [177, 180]. The introduction of 4.0 at. % and 2.98 at. % of nitrogen, in the mentioned works, has led to the increase of the first cycle discharge capacity by 18% and 22%, respectively, which is similar to the 20% improvement observed for CNF500/HT-N25/180. Small growth of the first cycle discharge capacity for the samples after *in-situ* functionalization is concerning, but the overall improvement of cyclability performance is achieved and can be assessed as satisfactory.

6.3. Influence of process temperature on the properties of CNF synthesized on the nickel oxalate-based catalyst

6.3.1. Synthesis

In order to confirm the composition of the prepared catalyst, XRD spectroscopy measurements have been carried out. Although the data regarding the crystallographic structure of nickel oxalate is limited, comprehensive analysis has been conducted by Koleżyński *et al.*, which will be used as the reference [215]. In the mentioned study, peaks located at 18.7°, 22.7°, 30.3°, 35.6°, and 40.9° have been highlighted as characteristic for nickel oxalate. In the XRD spectrum of prepared the catalyst in the Fig. 25, peaks located at similar positions can be observed. The consistency between the XRD spectra reported in the literature and those obtained for this sample, confirms the successful synthesis of nickel oxalate using method proposed in this work.

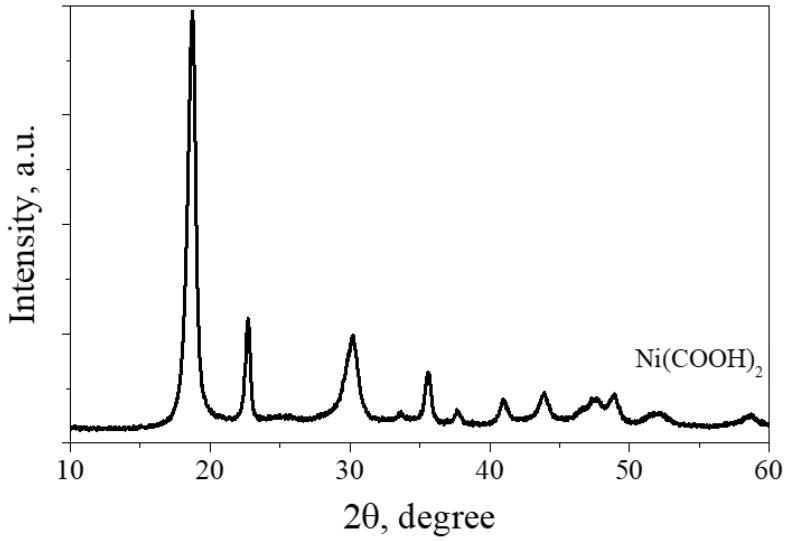

Fig. 25. XRD spectrum of prepared catalyst.

Yields of synthesis of CNF on pristine nickel oxalate are presented in the Tab. 20. When pristine $Ni(COOH)_2$ has been utilized as the catalyst, yields of all processes have reached around 1 $g_{CNF}g_{cat}^{-1}$ with small variations between each temperature. The lowest synthesis yield of 0.9 $g_{CNF}g_{cat}^{-1}$ has been achieved for the process conducted at 450°C. After increasing synthesis temperature to 500°C, yield has risen up to 1.5 $g_{CNF}g_{cat}^{-1}$. However, further growth of temperature has resulted in decrease of yields of processes carried out at 550°C and 600°C to 1.0 and 1.1 $g_{CNF}g_{cat}^{-1}$, respectively.

As have been already explained in the section 6.1.1, the growth of synthesis yield with the increase of temperature from 450°C to 500°C can be attributed to more efficient decomposition of propane. Aggregation processes of catalyst's grains are more noticeable at higher temperatures leading to the formation of larger agglomerates that promote the growth of CNF less efficiently. Moreover, achieved yields for synthesis conducted on pristine nickel oxalate-based catalyst are notably lower in comparison to synthesis carried out on the reference catalyst, see Tab. 6. This could indicate that

without appropriate catalyst support, during the thermal decomposition of nickel oxalate, grains are agglomerating into larger aggregates that are less active in the formation of CNF.

Tab. 20. Yields of synthesis of CNF on pristine nickel oxalate-based catalyst via CVD process at different temperatures.

Sample	**Synthesis yield, Y ($g_{CNF}g_{cat}^{-1}$)**	**Synthesis yield, Y_{Ni} ($g_{CNF}g_{Ni}^{-1}$)**
CNF450-NiOx	0.9	2.2
CNF500-NiOx	1.5	3.9
CNF550-NiOx	1.0	2.6
CNF600-NiOx	1.1	2.9

As illustrated in Fig. 26.1, 26.2, and 26.3, nickel oxalate forms agglomerates composed of cubic-shaped crystallites. While the size of agglomerates varies, the edges of the cubic crystallites typically measure less than 200 nm. Following the reduction in hydrogen and nitrogen atmosphere (1:1 v/v), individual agglomerates remain visible, but the edges appear significantly smoother, and the cubic shape of crystallites is no longer observable. Although the thermal decomposition of nickel oxalate in an inert atmosphere is known to yield Ni and CO_2, it cannot be definitively concluded that the images in Fig. 26.4-6 show pure nickel [216]. This uncertainty arises due to oxidation processes (caused by exposure to air) occurring during the removal of the reduced nickel oxalate sample from the furnace and storage of sample.

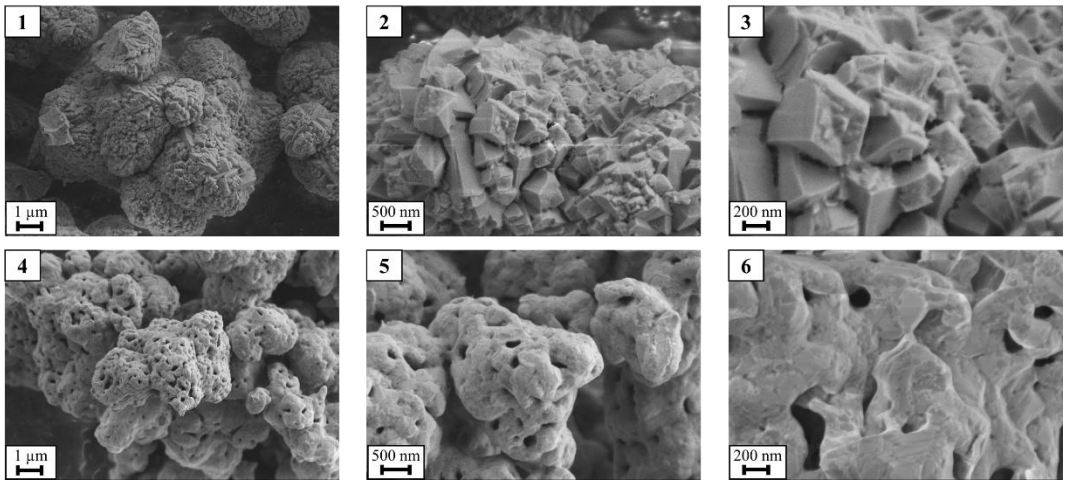

Fig. 26. SEM images of: 1, 2, 3 – pristine nickel oxalate; 4, 5, 6 - nickel oxalate after reduction in nitrogen and hydrogen atmosphere (1:1 v/v) for 1 h at 500°C.

6.3.2. Materials characterization

The morphology of carbon nanofibers synthesized on the pristine nickel oxalate is presented in SEM images in the Fig. 27. CNF450-NiOx display compact structure with the individual nanofibers being short and visibly agglomerated. Low yield of process conducted at 450°C is reflected in relatively thin coverage of catalyst nanoparticles. Increase of temperature of synthesis leads to the gradual change of morphology of obtained materials. At 500°C, created nanofibers are longer and thinner.

Moreover, their distribution is more uniform with fewer agglomerates visible. For CNF550-NiOx, the increase in length of carbon nanofibers is continued and additional fibers with significantly thinner diameters are noted. The appearance of those thinner fibers is even more evident in CNF600-NiOx, where they interlace the thick carbon nanofibers creating entangled and dense structure. Additionally, carbon nanofibers obtained at 600°C are longer and their surface is less rough in comparison to the CNF synthesized at lower temperatures.

The origin or the mechanism of growth of these thinner (diameters of a dozen nanometers) and longer fibers observed in CNF550-NiOx and CNF600-NiOx is unclear. Their diameters are notably smaller than sizes of crystallites of nickel oxalate or reduced nickel oxalate, as compared with SEM images in the Fig. 26, which would exclude their potential growth on the catalyst seeds. Perhaps, the thermal decomposition of nickel oxalate at higher temperatures leads to the creation of small nickel nanoparticles, due to breaking of the larger grains. Later, during the synthesis the smaller Ni nanoparticles remain their catalytic activity and promote the growth of these thin carbon nanofibers.

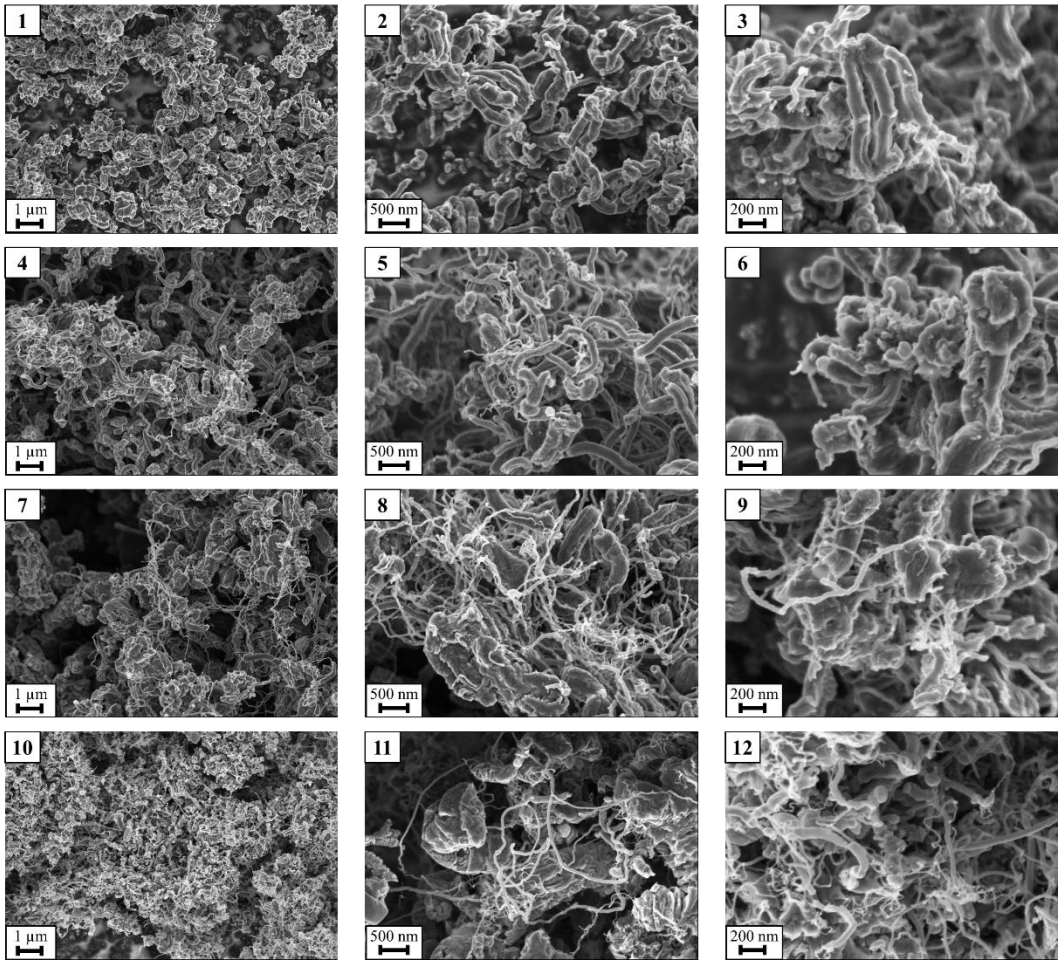

Fig. 27. SEM images of CNF synthesized on the nickel oxalate based catalyst via CVD process at different temperatures: 1, 2, 3 - CNF450-NiOx; 4, 5, 6 - CNF500-NiOx; 7, 8, 9 - CNF550-NiOx; 10, 11, 12 - CNF600-NiOx.

Specific surface area and total pore volume of all of carbon nanofibers prepared on the pristine oxalate catalyst are relatively low, see Tab. 21. With the growth of temperature of synthesis the porosity of obtained materials is developing, which is noticeable in the rise of SSA and V_T, from 58 m^2g^{-1} to 64 m^2g^{-1} and from 0.049 cm^3g^{-1} to 0.058 cm^3g^{-1}, when the temperature has been increased from 450°C to 500°C. The highest values of 77 m^2g^{-1} for SSA and 0.117 cm^3g^{-1} for V_T are observed for CNF600-NiOx. The only exception from the described trend are CNF obtained at 550°C, for which values of both parameters have dropped to 50 m^2g^{-1} and 0.031 cm^3g^{-1}.

Tab. 21. Parameters of the porous structure of CNF synthesized on the nickel oxalate based catalyst via CVD process.

Sample	**Specific surface area, S_{QSDFT} (m^2g^{-1})**	**Total pore volume, V_T (cm^3g^{-1})**	**Mesopores volume, V_{meso} (cm^3g^{-1})**	**V_{meso}/V_T**
CNF450-NiOx	58	0.049	0.026	0.54
CNF500-NiOx	64	0.058	0.032	0.56
CNF550-NiOx	54	0.050	0.031	0.61
CNF600-NiOx	77	0.117	0.091	0.78

The trend observed across all samples is the increasing share of mesoporosity with the increasing temperature of synthesis. The V_{meso}/V_T ratio has grown from 0.54 to 0.78 for CNF450-NiOx and CNF600-NiOx, respectively, with moderate values of 0.56 and 0.61 noted for CNF500-NiOx and CNF550-NiOx, accordingly. The progressing development of mesoporosity in samples is also noticeable in the N_2 adsorption/desorption isotherms at 77 K presented in the Fig. 28. All of the displayed isotherms can be classified as the type IV of isotherms according to the IUPAC terminology, with slight hysteresis loop for CNF450-NiOx and more evident hysteresis loops observed in the rest of shown isotherms, see Fig. 28. 3, 28. 5, and 28. 7. The PSD graphs also indicate the dominant share of mesoporosity in the analyzed CNF, which is reflected in the increasing volume of pores with width larger than 2 nm for materials prepared at higher temperatures.

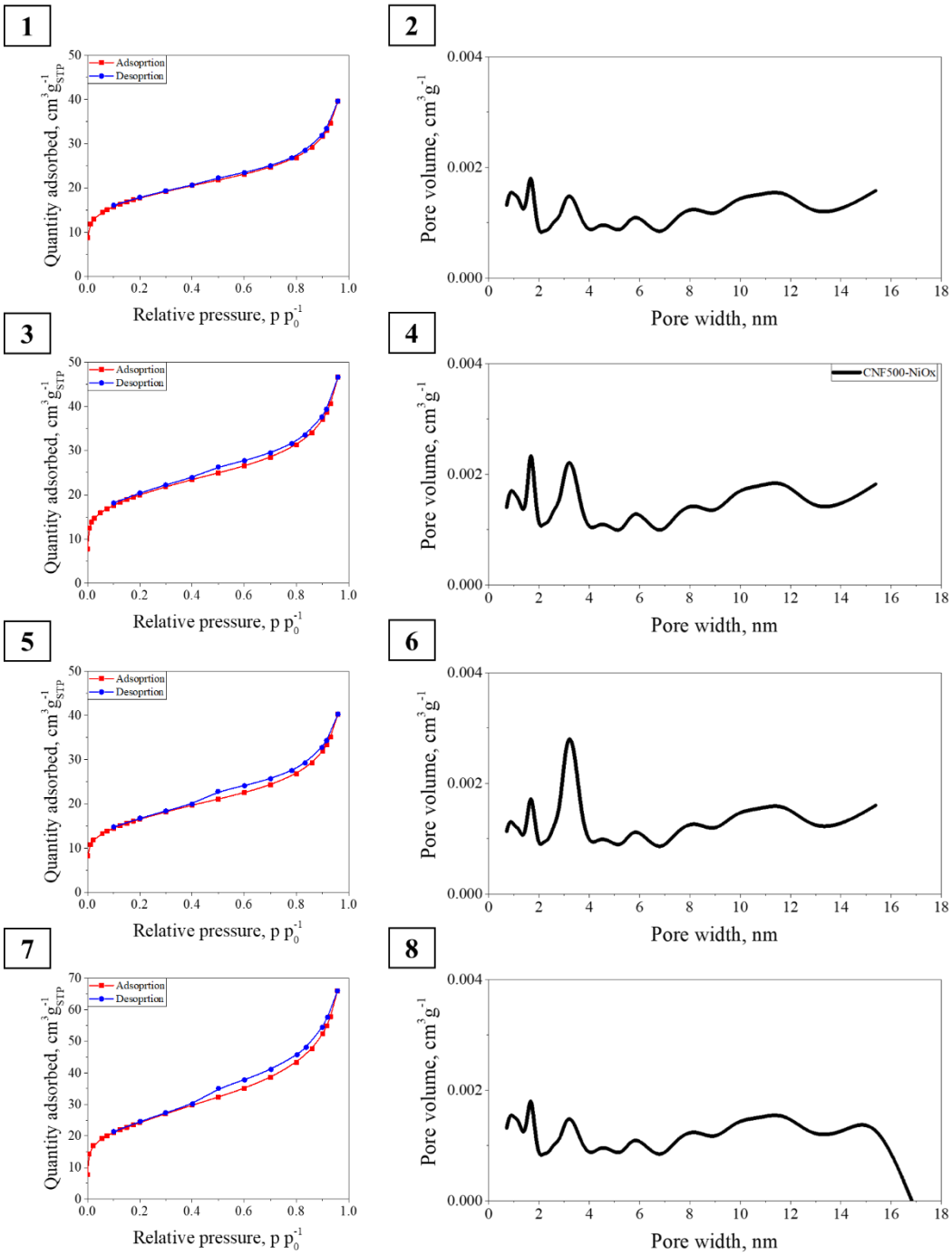

Fig. 28. The N_2 adsorption/desorption isotherms and PSD of the CNF synthesized on the nickel oxalate based catalyst via CVD process: 1, 2 - CNF450; 3, 4 - CNF500-NiOx; 5, 6 - CNF550-NiOx; 7, 8 - CNF600-NiOx.

Further investigation via Raman spectroscopy has provided valuable insight into the structure of obtained carbon nanofibers. Apart from the characteristic for carbon nanomaterials peaks located at ~1 300 cm^{-1} for the D-band and at ~1 600 cm^{-1} for the G-band, in the Raman spectra in the Fig. 29 additional peaks localized at ~1 100 cm^{-1} is observed for CNF450-NiOx, CNF550-NiOx, and CNF600-NiOx. The signal of this peak is related to the NiO created by the laser induced oxidation of nickel nanoparticles occurring during the measurement [217, 218]. For CNF450-NiOx, the intensity of

NiO-related peak in the Raman spectrum is even higher than for D-band and G-band peaks, which implies that due to the low synthesis yield, the nickel nanoparticles have not been entirely covered by the CNF. Thus, the exposed nickel nanoparticles are easily prone to the oxidation via laser during the Raman spectroscopy measurements. In the case of carbon nanofibers obtained at higher temperatures of 550°C and 600°C, synthesis yields are sufficiently high, so that the nickel nanoparticles should be completely covered. However, as have been previously stated, it is expected that the decomposition of nickel oxalates at these higher temperatures occurs more rapidly, which leads to the creation of small seeds of nickel nanoparticles – that later serve as catalysts for the formation of thin nanofibers. These smaller grains of nickel nanoparticles are more exposed and could be potentially oxidized during measurements. On the other hand, for the Raman spectrum of CNF500-NiOx no NiO-related peaks are observed, which would indicate, that the temperature of 500°C provides the optimal conditions for the uniform coverage of nickel nanoparticles.

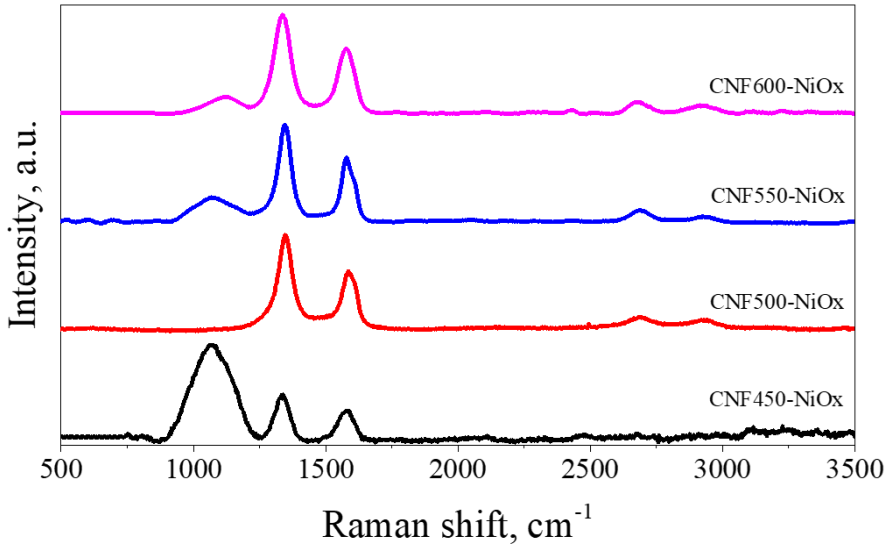

Fig. 29. Raman spectra of the CNF synthesized on the nickel oxalate based catalyst via CVD process.

The detail parameters of carbon structure from Raman spectra of CNF obtained on the nickel oxalate-based catalyst are presented in the Tab. 22. Small shifts of positions of D-band and G-band peaks are observed in the ranges from 1 336 to 1 346 cm^{-1} and from 1 579 to 1 586 cm^{-1}, respectively. Carbon nanofibers obtained on the nickel oxalate-based catalyst are characterized by relatively high levels of structural disorder visible in high values I_D/I_G ratio, from 1.46 to 1.57. However, this stands in the contrast to high crystallinity indicated by narrow peaks. Such discrepancy can be attributed to the presence of nickel and NiO nanoparticles – this phase can locally influence the electronic density increasing the I_D/I_G ratio [219].

Tab. 22. Comparison of key parameters of Raman spectra of carbon nanofibers synthesized on the nickel oxalate-based catalyst via CVD at different temperatures.

Sample	D-band peak position, cm^{-1}	G-band peak position, cm^{-1}	I_D/I_G ratio
CNF450-NiOx	1 339	1 583	1.46
CNF500-NiOx	1 346	1 586	1.57
CNF550-NiOx	1 346	1 580	1.49
CNF600-NiOx	1 336	1 579	1.51

6.3.3. Performance of Li-O_2 cells

Summary of the electrochemical performance of CNF synthesized on $Ni(COOH)_2$-based catalyst as cathode materials in lithium-oxygen batteries is presented in the Tab. 23. The initial rise in the synthesis temperature from 450°C to 500°C has led to the improvement of electrochemical performance. The first discharge capacity has grown from 331 mAh g^{-1} to 339 mAh g^{-1} and reversibility has increased from 47% to 80% for CNF450-NiOx and CNF500-NiOx, respectively. However, subsequent rise in temperature of synthesis leads to the decrease in the first discharge capacity for CNF550-NiOx and CNF600-NiOx to 246 mAh g^{-1} and 207 mAh g^{-1}, accordingly. In terms of reversibility, the decline is also observed, but it is not as linear. The reversibility has fallen to 17% for CNF550-NiOx, but small rebound is observed for CNF600-NiOx with reversibility reaching 37%.

Tab. 23. Summary of electrochemical performance of Li-O_2 batteries with CNF synthesized on the nickel oxalate-based catalyst as cathode materials during the first discharge-charge cycle.

Sample	1st cycle discharge capacity, mAh g^{-1}	1st cycle charge capacity, mAh g^{-1}	1st cycle reversibility
CNF450-NiOx	331	155	47%
CNF500-NiOx	339	271	80%
CNF550-NiOx	246	43	17%
CNF600-NiOx	207	77	37%

In terms of GCPL graphs for the first discharge-charge cycle presented in the Fig. 30, all of the compared carbon nanofibers display similar discharge plateau at around 2.6 V. However, for the phase of charging only CNF450-NiOx and CNF500-NiOx show short, but distinct, charging plateaus, as can be seen in the Fig. 30.1 and 30.2. For CNF450-NiOx, the charge plateau is localized at higher potential in comparison to the position of the charge plateau for CNF500-NiOx, 4.6 V vs 3.7 V respectively. This variation directly corresponds to the difference in the measured charge overpotentials. The significantly higher OER-overpotential of 1.6 V is attributed to CNF450-NiOx. On the other hand, the relatively low charge overpotential of 0.7 V is in line with the highest reversibility of this sample, suggesting the superiority of electrochemical properties of CNF500-NiOx among other carbon nanofibers prepared on the standalone $Ni(COOH)_2$.

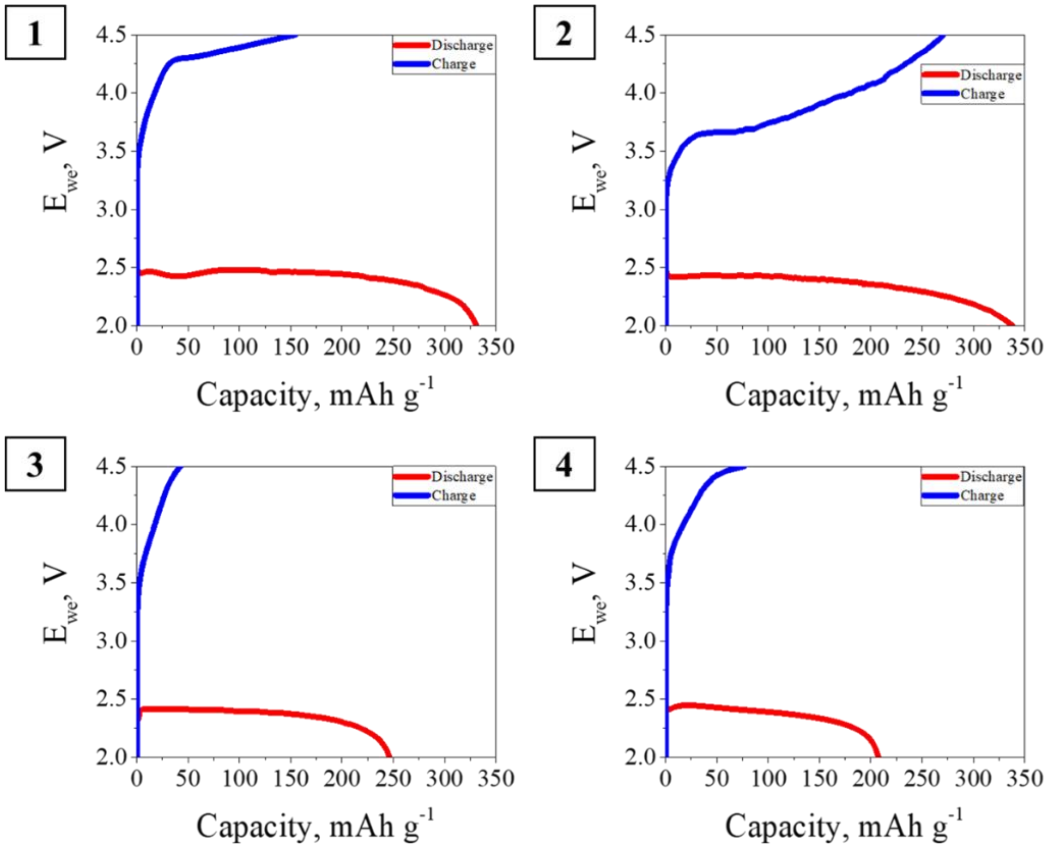

Fig. 30. Comparison of GCPL measurements for the first discharge-charge cycle conducted at current density of 0.4 mA cm^{-2} with CNF synthesized on the nickel oxalate-based catalyst via CVD process as a cathode materials: 1 - CNF450-NiOx; 2 - CNF500-NiOx; 3 - CNF550-NiOx; 4 - CNF600-NiOx.

The superiority of CNF500-NiOx in comparison to other CNF synthesized on the nickel oxalate-based catalyst is also noticeable across large number of discharge-charge cycles, as presented in the Fig. 31. After the first cycle, CNF500-NiOx show the highest retention of capacity and it gradually decreases from almost 80 mAh g^{-1} at the second cycle to around 20 mAh g^{-1} at the 6^{th} cycle. Later, the capacity of around 20 mAh g^{-1} is remained up to 50^{th} cycle. Similar behavior is displayed by CNF450-NiOx, but the observed capacity is lower and it ranges from around 45 mAh g^{-1} at the 2^{nd} cycle to around 20 mAh g^{-1} at the 6^{th} cycle. In the case of CNF550-NiOx and CNF600-NiOx, the behavior of both samples across larger number of cycle is almost identical – the discharge capacity steadily decreases to reach 10 mAh g^{-1} at approximately 10^{th} cycle and it continues to decline to reach 5 mAh g^{-1} at around 50^{th} cycle.

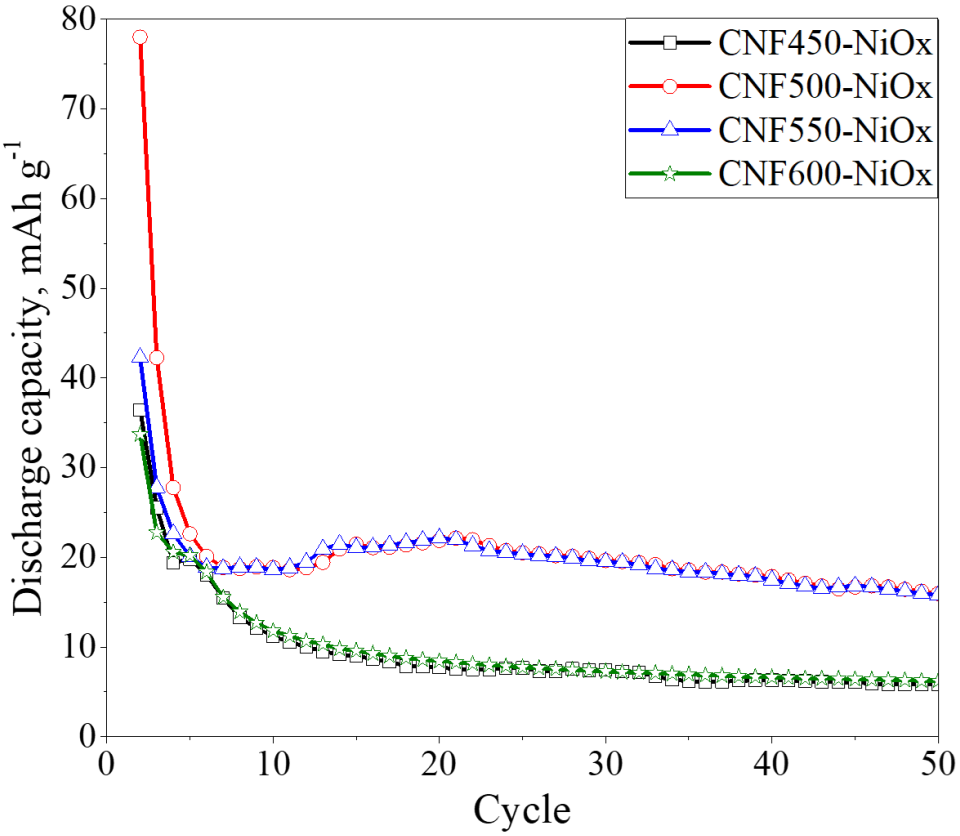

Fig. 31. Comparison of cyclability performance of CNF synthesized on the nickel oxalate-based catalyst via CVD process as cathode materials during the GCPL measurements at 0.4 mA cm^{-2}, the first discharge cycle is excluded.

Presented electrochemical performance of CNF synthesized on the standalone nickel oxalate catalyst closely resemble results obtained for CNF prepared on the standard catalyst – not necessarily value-wise, but the trend-wise. For both groups of materials, no direct correlation between structure or porosity and electrochemical performance can be drawn, at least based on the conducted measurements. Such repeating observation would indicate that there is an additional characteristic of materials, not investigated in this work, that could have the crucial influence on the performance of lithium-oxygen battery and, at the same time, it would be dependent on the temperature of synthesis.

Due to the fact that for both groups of carbon nanofibers, the same stream of raw materials and the same catalytic nanoparticles (Ni nanoparticles) have been employed, the type of CNF (fishbone, platelet, or tubular) could be the missing variable. As have been stated before, the type of CNF strongly depend on the temperature of synthesis and it impacts electric conductivity, which is also important property of cathode materials.

6.4. Comparison of activated carbons with different porosity as a cathode materials in Li-O_2 cells

6.4.1. Synthesis

Yields of all of the activation processes have been calculated according to the formula expressed in the equation (13) and are summarized in the Tab. 24. The loss of mass during the activation with KOH of CP520 in mass ratio of 3:1 has reached 30%, which is higher than 18%, that has been achieved during analogical procedure, but with CP600 as the raw material. After increasing the excess of potassium hydroxide and reaching the mass ratio of 4:1, the loss of mass during the preparation of AC/CP600/4KOH has increased to 31%. During the activation with mass ratio of 3:1, CP520 is more susceptible to higher degradation of structure, as compared to more stable CP600. To reach similar level of structure degradation for CP600, harsher environment is required and after rising the content of potassium hydroxide in the starting mixture to 80 wt. %, almost identical loss of mass is achieved.

Tab. 24. Summary of loss mass during the preparation of coke pitches and activated carbons.

Sample	**Loss of mass, Y_{AC}**
AC/CP520/3KOH	30%
AC/CP600/3KOH	18%
AC/CP600/4KOH	31%
AC/H_3PO_4	56%

The relatively high loss of mass of 56% observed during the activation with phosphoric acid results from the nature of raw materials mixture used in the process. Wood shavings contain large amounts of volatile compounds, moisture, and organic matter that are decomposed during the activation and exit the reactor. Moreover, during the heating of biomass and H_3PO_4 mixture, carbonization and activation processes are taking place simultaneously, which furtherly increases the overall loss of mass. However, the 18% loss of mass observed during the reduction of AC/H_3PO_4 is not related to the additional activation of surface, but to the decomposition of oxygen containing functional groups leading to the decrease of mass of product.

6.4.2. Materials characterization

Comparison of SEM images of CP520 and AC/CP520/3KOH, see Fig. 32, allows to observe and analyze key changes in morphology taking place during chemical activation of highly carbonaceous material with potassium hydroxide. Changes in texture of surface can be observed with CP520 having relatively smooth and more compact structure, as opposed to more degraded and irregular structure of AC/CP520/3KOH, which would indicate the activation of raw material's surface and its structural breakdown. However, similarities between both materials can be noticed, which imply partial structural retention after activation – including structural consistency indicating their primarily carbonaceous composition and fragmentation suggesting the brittle nature of presented structures.

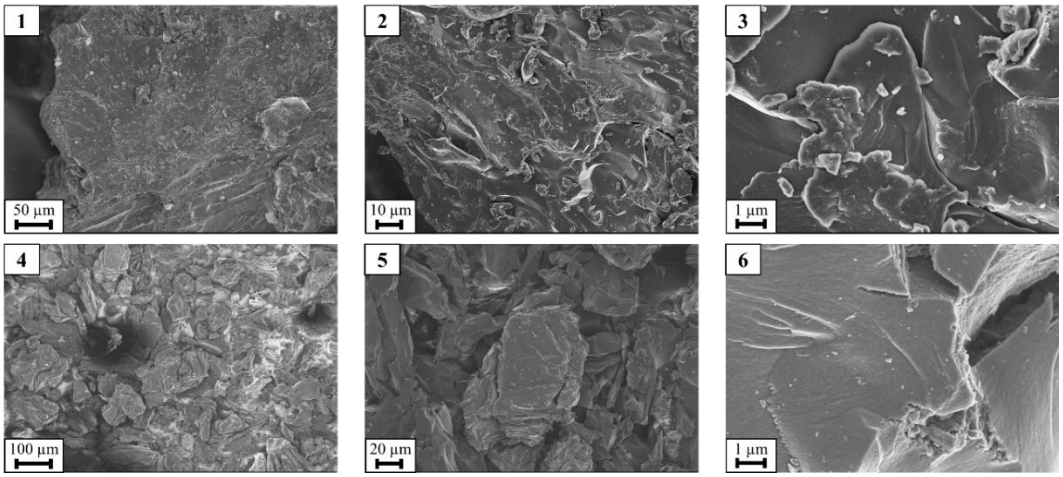

Fig. 32. SEM images of pitch coke prepared at 520°C and activated carbon obtained via chemical activation with potassium hydroxide: 1, 2, 3 - CP520; 4, 5, 6 - AC/CP520/3KOH.

The morphology of CP600 displayed in the SEM images, see Fig. 33, is similar to the morphology of CP520 with both materials having fragmented and irregular structure. However, the surface of CP600 shows rougher edges, combined with slightly higher number of cracks, which is especially visible while comparing images in the Fig. 32.6 and Fig. 33.1. These minor differences in morphology are caused by higher temperature of carbonization of CP600, which leads to the release of compounds during heating and subsequent cracking of material.

More notable difference in morphology can be observed between CP600 and products of its chemical activation with potassium hydroxide, AC/CP600/3KOH and AC/CP600/4KOH. Both of the mentioned activated carbons present more irregular structure with sharper edges and larger number of cracks in comparison to CP600. Moreover, process conducted with higher content of KOH leads to more exhaustive activation of initial material, which is especially noticeable during the comparison of images in the Fig. 33.6 and Fig. 33.9. Higher fragmentation and deeper cracks resulting in finer particles are observed for AC/CP600/4KOH, while the sample AC/CP600/3KOH seems to more closely resemble initial material.

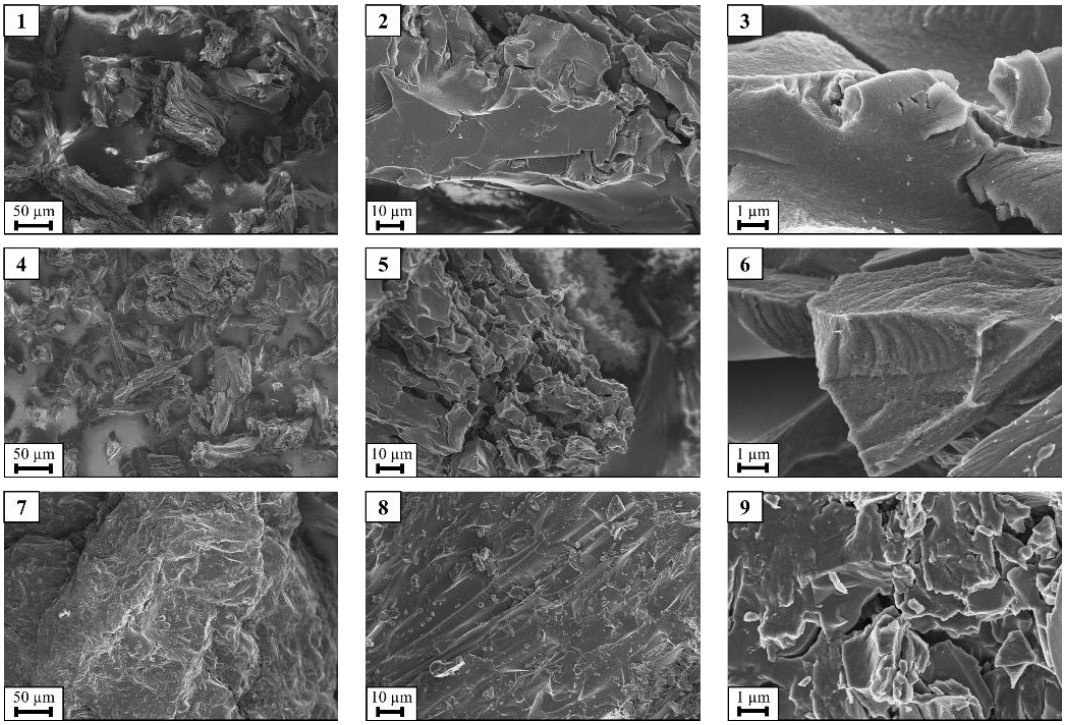

Fig. 33. SEM images of coke pitch prepared 600°C and activated carbons obtained via chemical activation with potassium hydroxide: 1, 2, 3 - CP600; 4, 5, 6 - AC/CP600/3KOH; 7, 8, 9 - AC/CP600/4KOH.

As opposed to highly carbonaceous raw materials used in the activation with KOH, considerably different morphology is presented by wood shavings utilized in the chemical activation with phosphoric acid, see Fig. 34. The fibrous and layered structure, observed in SEM images in the Fig. 34.1-34.3, is characteristic for natural wood structures. Additionally, some longitudinal cracks indicate the prone-to-breaking nature of biomass, which is reflected in the obtained activated carbon. In the images of AC/H_3PO_4, grains ranging in size from couple of µm to over 100 µm are observed. The variety of morphology of grains of AC/H_3PO_4 results from the breakage of wood shavings, caused by effective activation with phosphoric acid. AC/H_3PO_4 grains display rather sharp edges, which is changed after the reduction process. The morphology of grains of AC/H_3PO_4/RED is more compact, with less cracks than in the initial AC.

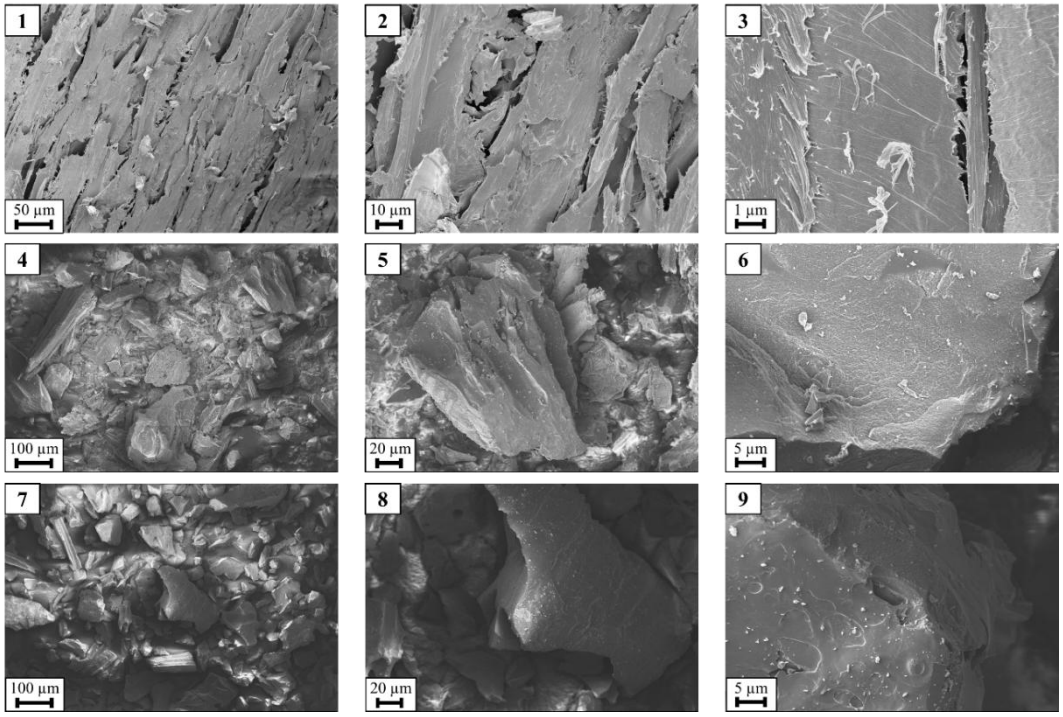

Fig. 34. SEM images of raw material and activated carbons obtained via chemical activation with phosphoric acid: 1, 2, 3 - wood shavings; 4, 5, 6 - AC/H_3PO_4; 7, 8, 9 - AC/H_3PO_4/RED.

In terms of specific surface area and porosity, significant development is observable for all products of activation processes, see Tab. 25. The activation of CP520 with potassium hydroxide in the mass ratio of 3:1 (KOH:CP520) has led to the preparation of highly porous materials with SSA of 1 799 m^2g^{-1} and the total pore volume of 0.871 cm^3g^{-1}. In the case of activation with CP600 as the raw material, both processes have led to the development of active surface, but the mass ratio of 4:1 has resulted in higher growth of SSA and porosity than the mass ratio of 3:1 – the specific surface area and total pore volume for AC/CP600/3KOH and AC/CP600/4KOH have increased to 1 106 and 1 782 m^2g^{-1} and to 0.601 and 0.971 cm^3g^{-1}, respectively. The noticeably larger development of porosity of CP520 compared with CP600, after the activation with KOH in mass ratio of 3:1 indicates, that pitch coke carbonized at 520°C is more prone-to-activation than CP600. To achieve similar level of porosity development for CP600, larger excess of KOH needs to be applied and the mass ratio of 4:1 has led to the preparation of activated carbon with well-developed active surface.

During the activation of wood shavings with phosphoric acid, activated carbon with well-developed SSA and V_T of 1 293 m^2g^{-1} and to 1.170 cm^3g^{-1} is obtained. The total pore volume of AC/H_3PO_4 is the largest amongst all of compared activated carbons. After the reduction of AC/H_3PO_4 the degradation of porosity occurs and the SSA drops to 537 m^2g^{-1} and V_T decreases to 0.552 cm^3g^{-1}. These results strongly indicate that the chosen biomass is susceptible to the activation with phosphoric acid resulting in the preparation of highly porous activated carbon.

Tab. 25. Comparison of parameters of porosity of raw materials and obtained activated carbons.

Sample	**Specific surface area, S_{QSDFT} (m^2g^{-1})**	**Total pore volume, V_T (cm^3g^{-1})**	**Mesopores volume, V_{meso} (cm^3g^{-1})**	**V_{meso}/V_T**
AC/CP520/3KOH	1799	0.871	0.026	0.03
AC/CP600/3KOH	1106	0.601	0.082	0.14
AC/CP600/4KOH	1782	0.971	0.118	0.12
AC/H_3PO_4	1293	1.170	0.714	0.61
AC/H_3PO_4/RED	537	0.552	0.395	0.72

Although the effectiveness of KOH and H_3PO_4 as activation agents has been proven, the nature of obtained activated carbons is fundamentally different. Activation with potassium hydroxide leads to the synthesis of highly microporous activated carbon, which is visible in the minimal share of mesoporosity, ranging from 0.03 to 0.14. Additionally, all of the KOH-activated materials display type I of N_2 adsorption/desorption isotherms at 77 K according to IUPAC classification characteristic to microporous materials, see Fig. 35 [195]. Moreover, adsorption and desorption isotherms of AC/CP520/3KOH, AC/CP600/3KOH, and AC/CP600/4KOH do not converge together at low range of p p_0^{-1}, which suggests that the dominant share of narrow micropores prevents full nitrogen desorption. QSDFT calculation of pore size distribution shows that indeed majority of pores in these ACs have width below 2 nm, and furtherly that high share of micropores have diameters below 0.5 nm.

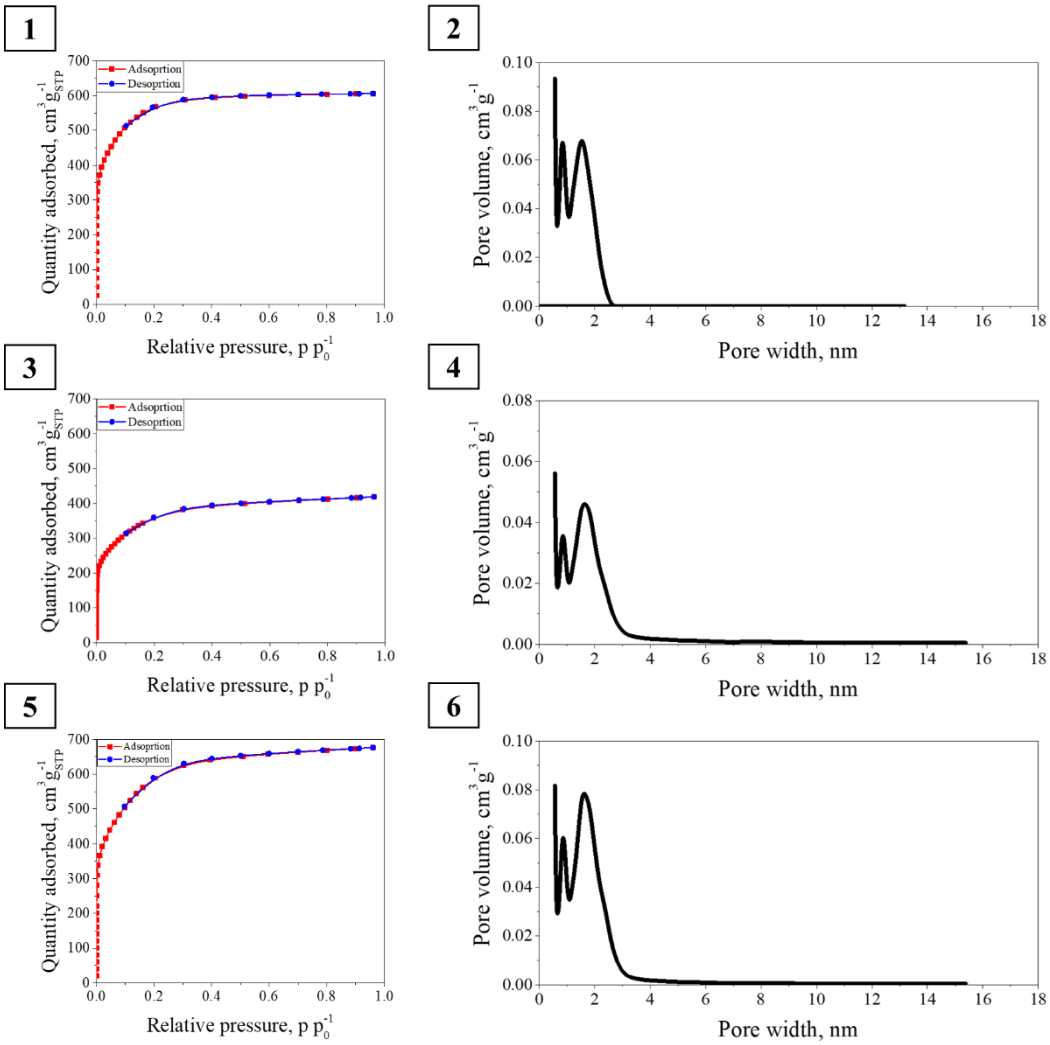

Fig. 35. The N_2 adsorption/desorption isotherms and PSD of activated carbons prepared via chemical activation with potassium hydroxide: 1, 2 - AC/CP520/3KOH; 3, 4 - AC/CP600/3KOH; 5, 6 - AC/CP600/4KOH.

On the contrary to the microporosity created by KOH, phosphoric acid used as the activation agent has led to the formation of dominant mesoporous characteristics, which is visible in the large share of V_{meso} in total pore volume of 0.61 for AC/H_3PO_4. The characteristic for mesoporous materials isotherm of N_2 adsorption/desorption at 77 K with distinct hysteresis loop corresponding to type IV, according to the IUPAC terminology [195], confirms the mesoporous nature of AC/H_3PO_4, see Fig. 36. Even though, the decrease in total pore volume and specific surface area has been observed, the mesoporous nature of AC/H_3PO_4/RED is maintained after the reduction. Relatively high value of V_{meso}/V_T ratio of 0.72, combined with the type IV isotherm with even more evident hysteresis loop than in unreduced AC, imply that the mesoporosity of initial activated carbon has been increased. In PSD graphs for AC/H_3PO_4 and AC/H_3PO_4/RED, rather proportional drop of volumes across all widths of pores is shown, but the highest degradation is observed for micropores. The removal of oxygen functional groups has disrupted the carbon structure of material, which results in micropores collapsing.

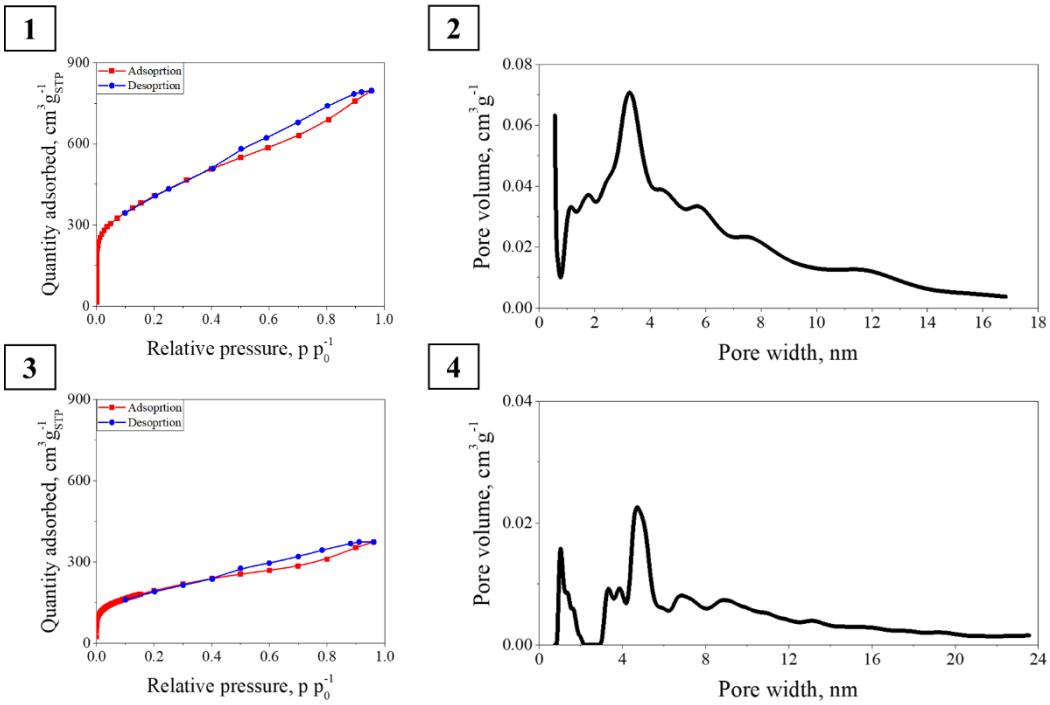

Fig. 36. The N_2 adsorption/desorption isotherms and PSD of activated carbons prepared via chemical activation with phosphoric acid: 1, 2 - AC/H_3PO_4; 3, 4 - AC/H_3PO_4/RED.

Further investigation on the influence of the type of raw material, mass ratio of KOH, and type of activation agent on the carbon structure of obtained activated carbon have been conducted using the Raman spectroscopy, key parameters of each spectra are summarized in the Tab. 26. The decrease of disorder level after the increase of carbonization temperature of coke pitch is noticeable in the Raman spectra of CP520 and CP600 presented in the Fig. 37 and Fig. 38, respectively. The I_D/I_G ratio declines from 1.01 for CP520 to 0.86 for CP600, which, in combination with narrower peaks of D-band and G-band, indicate the decrease of disorder and the increase of crystallinity levels, together with fewer defects for the material prepared in 600°C. The rise of order level in CP600 is caused by the additional removal of impurities and subsequent solidification and crosslinking processes occurring at higher temperature.

Tab. 26. Comparison of key parameters of Raman spectra of raw materials for activation and prepared activated carbons.

Sample	**D-band peak position, cm^{-1}**	**G-band peak position, cm^{-1}**	**I_D/I_G ratio**
CP520	1 354	1 565	1.01
CP600	1 343	1 590	0.86
AC/CP520/3KOH	1 347	1 568	1.04
AC/CP600/3KOH	1 343	1 583	0.93
AC/CP600/4KOH	1 366	1 561	1.01
AC/H_3PO_4	1 332	1 590	0.97
AC/H_3PO_4/RED	1 332	1 579	1.05

The disorder level and number of defects is increased after the activation with potassium hydroxide. For the AC/CP520/3KOH rise in disorder is relatively minor with the rise of I_D/I_G ratio to 1.04, as compared to 1.01 for CP520, but the slight broadening of D-band and G-band peaks can be observed. Additionally, the shift of peaks' position from 1 354 cm^{-1} to 1 347 cm^{-1} for D-band and from 1 565 cm^{-1} to 1 568 cm^{-1} for G-band is observed for CP520 and AC/CP520/3KOH, respectively.

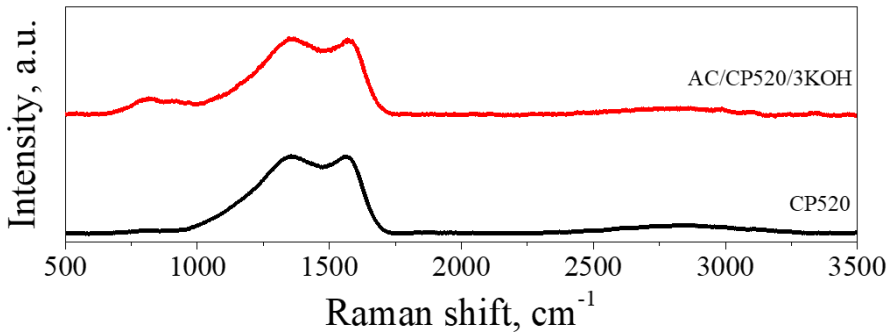

Fig. 37. Comparison of Raman spectra of CP520 before and after activation process with potassium hydroxide.

However, more evident changes in carbon structure after chemical activation are observed for CP600 than for CP520. After the activation, the disorder level gradually increases from 0.86 for CP600 to 0.93 and 1.01 for AC/CP600/3KOH and AC/CP600/4KOH, respectively. Moreover, the shape of D-band and G-band peaks become broader for AC/CP600/3KOH and both peaks are less separated than for the raw material. Widening and merging of peaks in Raman spectra is even more distinct AC/CP600/4KOH. The described changes in Raman spectra between CP600 and prepared ACs are aligned with the observation from the analysis of porosity and specific surface area – KOH effectively activate the structure of carbonaceous material leading to the development of porosity. Moreover, exhausting activation of coke pitch with mass ratio of 4:1 leads to higher deterioration of carbon structure, which corresponds to better development of active surface of AC/CP600/4KOH as compared to AC/CP600/3KOH.

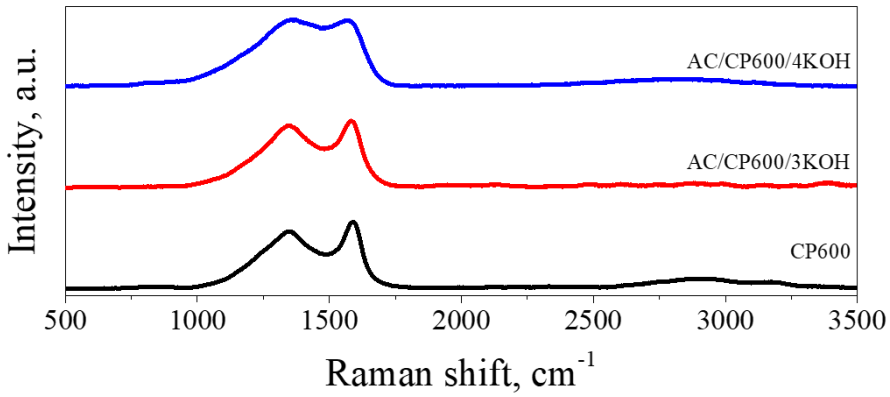

Fig. 38. Comparison of Raman spectra of CP600 before and after activation process with potassium hydroxide at different mass ratio.

For the activated carbons derived from wood shavings, similarities between their Raman spectra can be observed. Both of the spectra presented in the Fig. 39 display similar shape with relatively narrow G-band peak and broader peak for D-band. In terms of position, the D-band peaks are at 1 332 cm^{-1} for both samples, and small shift of position from 1 590 cm^{-1} to 1 579 cm^{-1} is noticed for AC/H_3PO_4 and AC/H_3PO_4/RED, respectively. The slight increase of disorder level after the reduction is noticed, based on the rise of I_D/I_G from 0.97 to 1.05. The increase of disorder level combined with the shift of the G-band peak position would suggest that during the reduction mainly the graphitic structure of AC/H_3PO_4 has been altered during the reduction process. The degradation of oxygen containing functional groups occurring during the reduction has led to the collapse of micropores, which has resulted in the growth of mainly edge-related defects in carbon structure, but has not risen the SSA and V_T as described before.

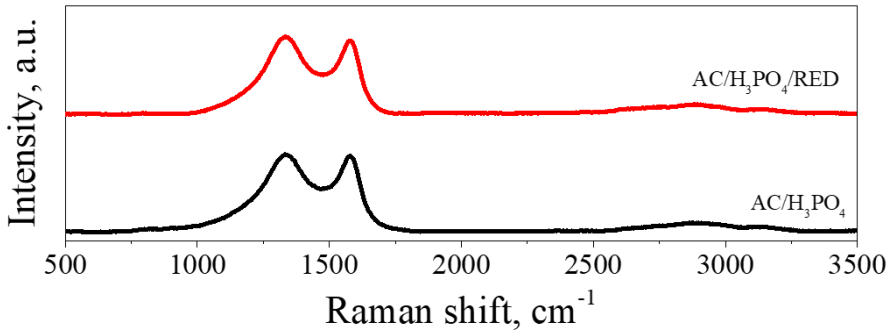

Fig. 39. Comparison of Raman spectra of activated carbon prepared via chemical activation with phosphoric acid with and without subsequent reduction.

6.4.3. Performance of Li-O_2 cells

Key parameters of electrochemical measurements for the first discharge-charge cycle of lithium-oxygen batteries utilizing activated carbons as cathode materials are listed in the Tab. 27. The highest first cycle discharge capacity of 446 mA g^{-1}, with satisfactory reversibility of 57%, has been recorded for AC/H_3PO_4. However, the performance of reduced AC/H_3PO_4 are notably worse with the first discharge cycle capacity and reversibility dropping to 249 mAh g^{-1} and 42%, respectively. In the case of materials derived from coke pitches, AC/CP600/4KOH displays the highest first discharge capacity of 377 mAh g^{-1} and exceptionally high reversibility of 99%. Comparably high reversibility of 98% is observed for AC/CP600/3KOH, but the discharge capacity is noticeably lower at 175 mAh g^{-1}. On the other hand, the lowest reversibility out of all AC of only 36% and relatively low discharge capacity for the first cycle of 250 mAh g^{-1} are presented by AC/CP520/3KOH.

Tab. 27. Summary of electrochemical performance of Li-O_2 batteries with activated carbons as cathode materials during the first discharge-charge cycle.

Sample	**1st cycle discharge capacity, mAh g^{-1}**	**1st cycle charge capacity, mAh g^{-1}**	**1st cycle reversibility**
AC/CP520/3KOH	250	91	36%
AC/CP600/3KOH	175	172	98%
AC/CP600/4KOH	377	373	99%
AC/H_3PO_4	446	256	57%
AC/H_3PO_4/RED	249	105	42%

In the case of galvanostatic curves for the first discharge-charge cycle presented in the Fig. 40, significant differences between tested activated carbons can be noticed. For two samples, AC/CP520/3KOH and AC/H_3PO_4/RED, no charge plateaus can be distinct suggesting poor energy efficiency, which is also reflected in the mentioned low reversibility of the first cycle for these two samples. For AC/H_3PO_4, the charge curve in the Fig. 40.4 is less steep and small plateau can be noticed at around 3.9-4.0 V, which would equal to charge overpotential at around 0.9-1.0 V.

The most interesting behavior is recorded for the first cycle GCPL graphs for AC/CP600/3KOH and AC/CP600/4KOH, see Fig. 40.2 and Fig. 40.3, respectively. For these samples, two charge plateaus can be distinguished. In the case of AC/CP600/3KOH, first and larger charge plateau is located at around 3.3 V and the second, considerably shorter, is located at around 4.45 V. For AC/CP600/4KOH, the first discharge plateau is located at 3.5 V, resulting in a slightly higher overpotential of 0.5 V vs 0.3 V for AC/CP600/3KOH, and the second plateau is at around 4.4 V and it is larger than the one observed for AC/CP600/3KOH. Origins of this unusual occurrence of two plateaus during charging is not well understood as it is not observed for any other samples in this study. Based on the previous reports, such behavior could be attributed to the high share of side reactions in the processes occurring during the operation of the cell, combined with pore blockage leading to the limitation of charge and oxygen transport, forcing the transitions in reactions pathways [220–222].

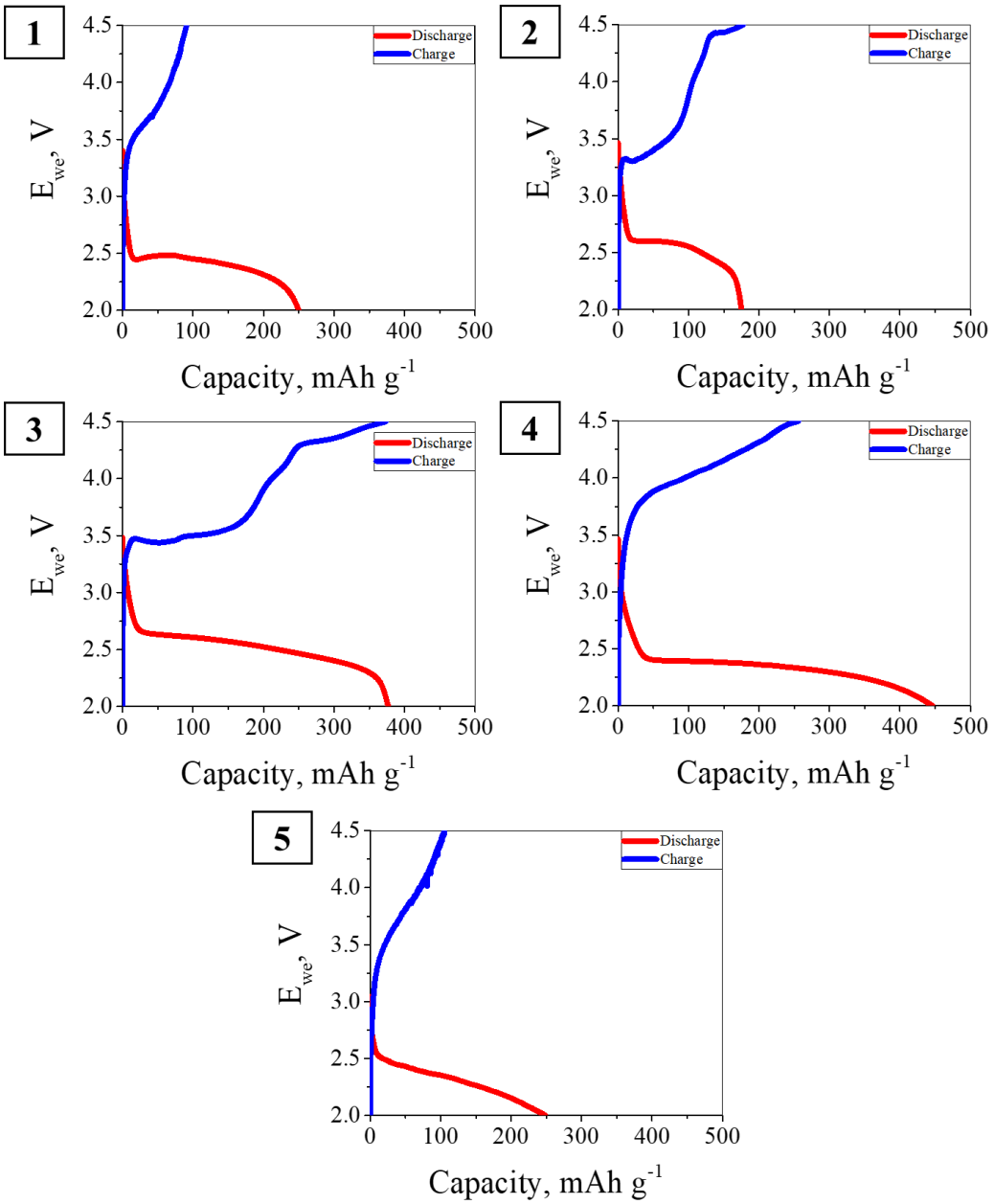

Fig. 40. Comparison of GCPL measurements for the first discharge-charge cycle conducted at current density of 0.4 mA cm^{-2} with activated carbons as a cathode materials: 1 - AC/CP520/3KOH; 2 - AC/CP600/3KOH; 3 - AC/CP600/4KOH; 4 - AC/H_3PO_4; 5 - AC/H_3PO_4/RED.

The cyclability performance of all of the activated carbons is presented in the Fig. 41. The best performance is displayed by AC/CP600/4KOH sample, for which the discharge capacity gradually decreases across 50 cycles, but for the first 6 cycles it is retained at relatively high value of over 100 mAh g^{-1}. After the 6th cycle, the decrease in discharge capacity is more steep and after 30th cycle it stabilizes at around 20 mAh g^{-1}. Similar behavior is presented by the lithium-oxygen battery with AC/CP600/3KOH as cathode material, but the absolute values of discharge capacities are lower in comparison to AC/CP600/4KOH – for the first 9 cycles the discharge capacities have been retained above 50 mAh g^{-1} and the relatively stable capacity of around 20 mAh g^{-1}

has been achieved for 22nd cycle and onwards. In the case of AC/CP520/3KOH, after the first cycle significant drop of discharge capacity below 50 mAh g^{-1} is observed, but later increase of capacity above 50 mAh g^{-1} is recorded for 5 cycles. However, after that rise, the gradual decline in discharge capacity occurs and values close to 0 mAh g^{-1} are reached at around 45th cycle. For AC/H_3PO_4, the discharge capacities rapidly fall below 50 mAh g^{-1} within the first three cycles, followed by a continuous decline, ultimately reaching nearly 0 mAh g^{-1} after approximately 30 cycles. The cyclability is slightly improved for the Li-O_2 battery utilizing AC/H_3PO_4/RED and the discharge capacities are retained above 20 mAh g^{-1} up to 30th cycle and after that gradual decrease to 5 mAh g^{-1} for the 50th cycle occurs.

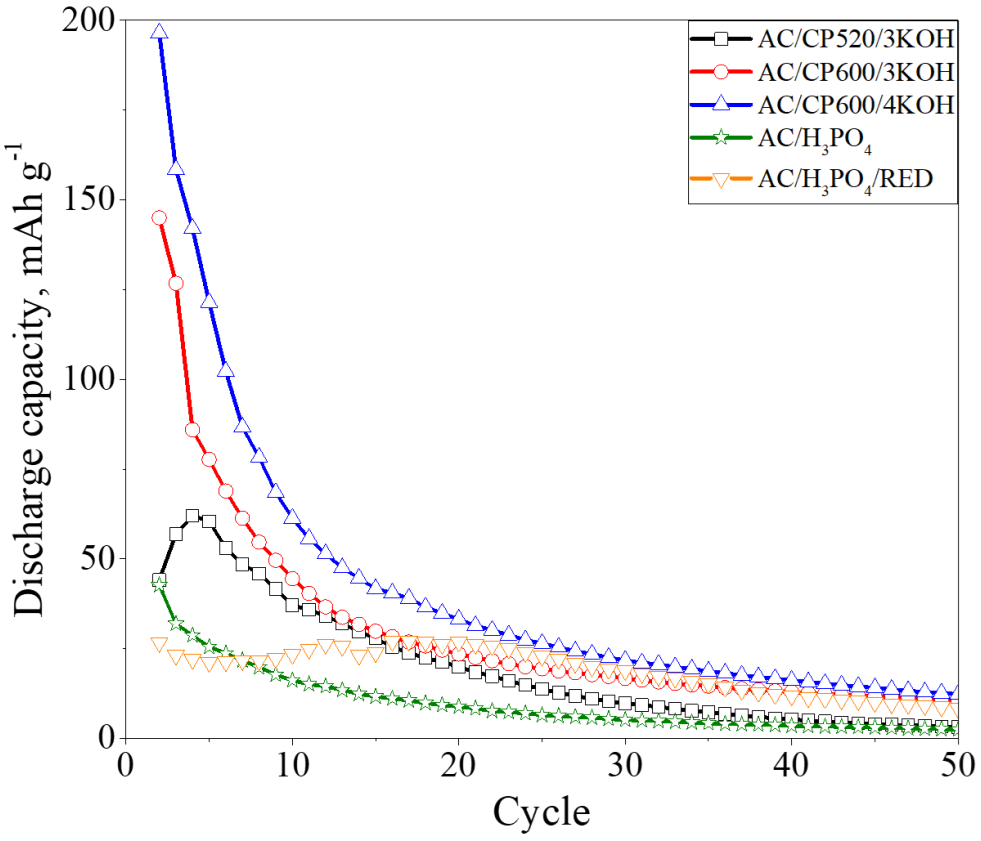

Fig. 41. Comparison of cyclability performance of activated carbons as cathode materials during the GCPL measurements at 0.4 mA cm^{-2}, the first discharge cycle is excluded.

Based on the obtained research results, several correlations can be identified regarding the influence of the porous structure on the electrochemical performance of lithium-oxygen batteries. Given that the differences in carbon structure, as indicated by Raman spectra, are considerably less pronounced than the variations in porosity, it can be implied that the porosity plays a dominant role in determining electrochemical performance.

Firstly, among activated carbons with comparable mesopore content (V_{meso}/V_T of 0.14 and 0.12 for AC/CP600/3KOH and AC/CP600/4KOH), the material with

a larger SSA enables a higher discharge capacity for the first cycle. Furthermore, this trend extends to cyclability across 50 cycles – AC/CP600/4KOH maintains a higher discharge capacity than AC/CP600/3KOH, particularly up to approximately 35th cycle. Secondly, for materials with comparable specific surface areas (1799 m^2g^{-1} for AC/CP520/3KOH and 1782 m^2g^{-1} for AC/CP600/4KOH), a larger mesopore volume and a higher share of mesoporosity contribute to achieving a higher initial discharge capacity. Higher share of mesoporosity also improves cycling stability, which is displayed in higher discharge capacities for AC/CP600/4KOH than AC/CP520/3KOH over larger number of cycles.

Furtherly, electrochemical performance of AC/H_3PO_4 indicates that SSA is not the primary factor influencing battery capacity, but rather V_T and share of mesoporosity. Despite having a specific surface area approximately 30% lower than AC/CP520/3KOH and AC/CP600/4KOH, AC/H_3PO_4 exhibits a higher first-cycle discharge capacity. This can be attributed to its greater total pore volume and significantly higher share of mesopore as compared to activated carbons derived from pitch coke. However, the poor cyclability of AC/H_3PO_4 is likely due to its relatively high content of oxygen functional groups, as supported by a comparison between unmodified and reduced carbon derived from wood shavings. Although the reduction in SSA and V_T leads to a lower initial discharge capacity, the removal of oxygen functional groups improves cycling stability, demonstrating the complex interplay between porosity and surface chemistry in determining electrochemical performance.

6.5. The development of CNF/AC composite material for the application as a cathode material in the Li-O_2 cells

As have been presented above, to maximize the performance of lithium-oxygen battery, cathode material with sufficient catalytic activity and optimal porosity is required. Based on the already presented results, the combination of carbon nanofibers and activated carbons has been proposed to achieve these requirements towards cathode material. The composites based on the carbon nanofibers synthesized directly on the activated carbon-based catalyst have been proposed.

Due to the facile, one step approach to the synthesis of CNF, nickel oxalate has been chosen as the catalyst. However, to improve the synthesis of CNF, additional phase of catalyst support in the form of activated carbon has also been incorporated in the catalyst composition. Due to its properties, such as dominant mesoporosity, relatively high SSA, and satisfactory electrochemical performance for the first discharge-charge cycle, AC/H_3PO_4 has been chosen from all of the tested ACs. In terms of selecting the temperature for the preparation of composites, 500°C has been chosen, as the CNF obtained at this temperature displayed superior electrochemical performance – nevertheless if the synthesis process has been conducted on the nickel oxalate or the standard catalyst.

6.5.1. Synthesis

Before analyzing results of synthesis conducted on the catalysts composed of AC/H_3PO_4 and different content of $Ni(COOH)_2$, it is worth to recall the synthesis yield

of process conducted on the pristine nickel oxalate at 500°C, which equals to 1.55 $g_{CNF}g_{cat}^{-1}$, as it will serve as a reference point in further discussion in this section.

For catalysts composed of nickel oxalate mixed with activated carbon, yields of synthesis have increased with increasing nickel content. However, when catalysts with low nickel content (10 and 20 wt. %) have been utilized in the synthesis, the yields have reached only 0.72 and 1.22 $g_{CNF}g_{cat}^{-1}$, respectively. This decrease in yield for AC-based catalysts is likely due to the lower surface concentration of nickel nanoparticles formed during the thermal decomposition of $Ni(COOH)_2$. In contrast, the preparation of CNF500/AC/H_3PO_4/50 has led to a substantial increase in synthesis yield, reaching 2.34 $g_{CNF}g_{cat}^{-1}$. The ratio of AC to $Ni(COOH)_2$ in AC/H_3PO_4/50 catalyst ensures both a high concentration and uniform distribution of nickel nanoparticles under synthesis conditions, enhancing their exposure to propane and improving catalytic efficiency, which is reflected in high yield.

Interesting correlation emerges when synthesis yield is recalculated and normalized to express the mass of obtained CNF per nickel mass (Y_{Ni}), rather than total catalyst mass, see Tab. 28. The AC/H_3PO_4/10 catalyst, containing the lowest nickel content, achieves the highest Y_{Ni} of 18.28 $g_{CNF}g_{Ni}^{-1}$, while for catalysts with higher nickel content Y_{Ni} decreases to 15.47 $g_{CNF}g_{Ni}^{-1}$ (AC/H_3PO_4/20) and 11.87 $g_{CNF}g_{Ni}^{-1}$ (AC/H_3PO_4/50). This reverse trend, where Y_{Ni} increases as nickel content decreases, suggests that the non-nickel phase remains inactive during CNF formation.

The achieved synthesis yields are slightly lower than those typically reported for CNF synthesis using nickel-based catalysts, where yields of few $g_{CNF}g_{cat}^{-1}$ are often observed [191]. However, the presented approach offers two essential advantages over conventional methods. Firstly, unlike traditional methods that require multi-step impregnation, calcination, and reduction, this approach involves a straightforward, one-step physical mixing of nickel oxalate with activated carbon, significantly simplifying catalyst preparation. Secondly, in contrast to commonly used inorganic supports such as hydroxyapatite or aluminum oxides, activated carbon serves not only as a catalyst support, promoting uniform nickel nanoparticle distribution, but also as an active component in the cathode material. Such approach eliminates the need for post-synthesis leaching with corrosive chemicals, such as concentrated hydrofluoric acid, reducing environmental impact and simplifying processing.

Tab. 28. Yields of synthesis of CNF on catalysts composed of AC/H_3PO_4 and different content of $Ni(COOH)_2$ via CVD process at 500°C.

Sample	**Synthesis yield, Y ($g_{CNF}g_{cat}^{-1}$)**	**Synthesis yield, Y_{Ni} ($g_{CNF}g_{Ni}^{-1}$)**
CNF500/AC/H_3PO_4/10	0.72	18.28
CNF500/AC/H_3PO_4/20	1.22	15.47
CNF500/AC/H_3PO_4/50	2.34	11.87

SEM images of catalysts composed of biomass-derived activated carbon with varying nickel oxalate content are presented in the Fig. 42. In the lower-magnification

images (Fig. 42.1, 42.4, and 42.7), the distinct structural features of AC/H_3PO_4 and Ni(COOH)$_2$ are visible – the activated carbon particles display irregular sizes and sharp edges, while nickel oxalate appears as crystalline aggregates dispersed throughout the material.

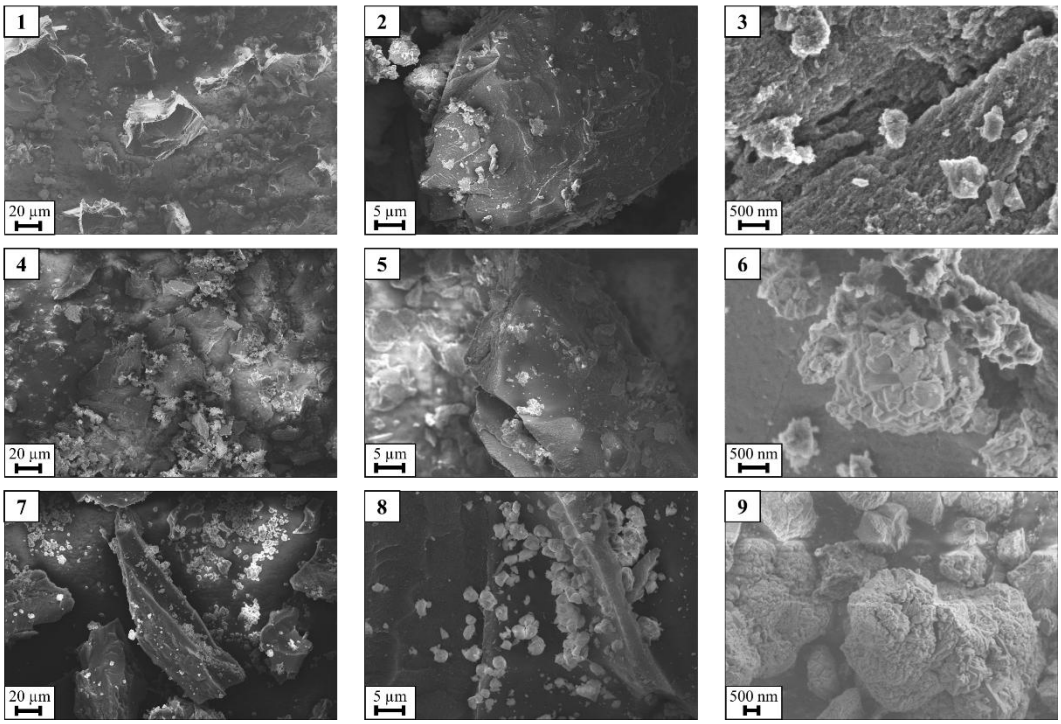

Fig. 42. SEM images of catalysts composed of AC/H_3PO_4 and different content of NI(COOH)$_2$: 1, 2, 3 - AC/H_3PO_4/10; 4, 5, 6 - AC/H_3PO_4/20; 7, 8, 9 - AC/H_3PO_4/50.

During catalyst preparation, the grinding process enables the distribution of nickel oxalate aggregates across the external surface of activated carbon. As could be expected, the number of visible nickel oxalate aggregates increases with higher nickel concentration in the catalyst. The fewest crystallite agglomerates are observed in the AC/H_3PO_4/10 sample, while the highest density of aggregated nickel oxalate is present in AC/H_3PO_4/50, reflecting the increasing nickel content in the formulation.

6.5.2. Materials characterization

Comparison of SEM images of CNF/AC composite is presented in the Fig. 43. The most dense morphology of synthesized carbon nanofibers is observed for CNF500/AC/H_3PO_4/50, for which nanofibers form clusters that wrap around grains of activated carbon. Moreover, carbon nanofibers shown in the Fig. 43.7 and 43.8 are relatively long with average length over 1 µm. On the other hand, CNF synthesized on catalysts containing 10 and 20 wt. % Ni display notably different morphologies – for both samples, the density of created nanofibers is significantly lower, and the activated carbon grains remain partially exposed. The SEM images of CNF500/AC/H_3PO_4/10 and CNF500/AC/H_3PO_4/20 do not reveal a distinct nanofiber structure, but instead, only small aggregates of carbon nanostructures are visible.

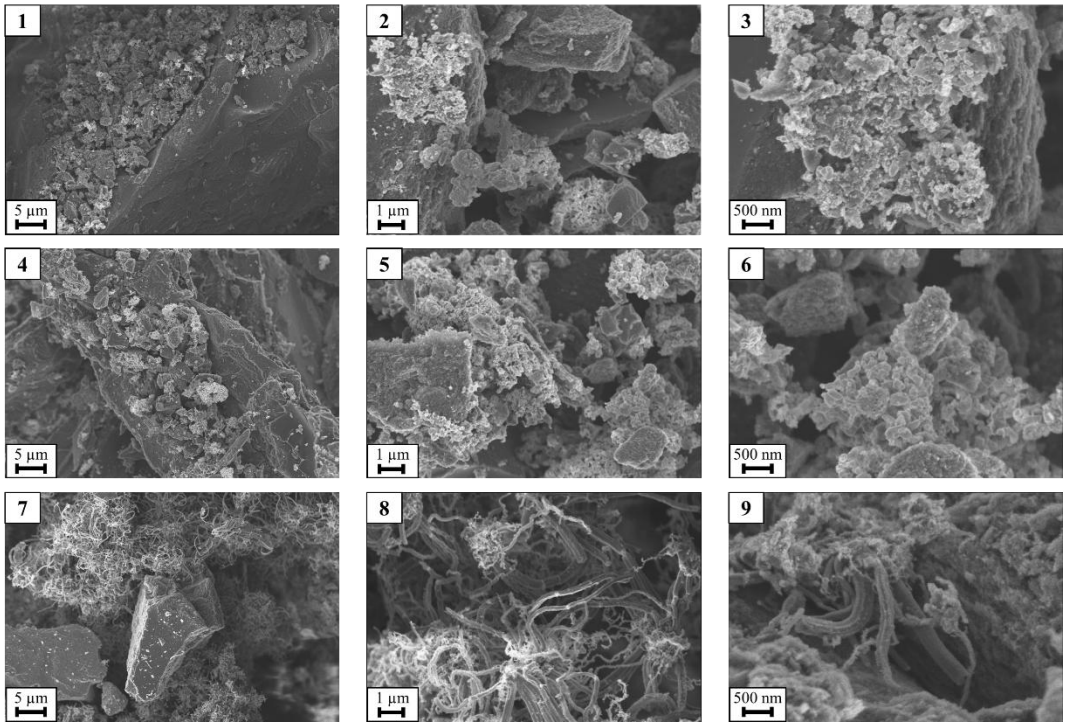

Fig. 43. SEM images of CNF synthesized on $Ni(COOH)_2$ and AC/H_3PO_4 based catalysts at 500C: 1, 2, 3 - $CNF500/AC/H_3PO_4/10$; 4, 5, 6 - $CNF500/AC/H_3PO_4/20$; 7, 8, 9 - $CNF500/AC/H_3PO_4/50$.

The summary of key parameters of porous structure of obtained CNF/AC composites and the reference sample is presented in the Tab. 29, alongside N_2 adsorption/desorption isotherms at 77 K and PSD graphs being presented in the Fig. 44. All of composites have displayed significantly higher V_T and SSA than CNF prepared on the pristine nickel oxalate. Moreover, values of both parameters have increased with the increasing content of nickel in the initial catalyst, with $CNF500/AC/H_3PO_4/10$ and $CNF500/AC/H_3PO_4/20$ having the SSA of 722 and 1 111 m^2g^{-1} and V_T of 0.627 and 1.116 cm^3g^{-1}, respectively. In the case of the both of the mentioned samples, the porosity have deteriorated in comparison to the AC/H_3PO_4. However, for $CNF500/AC/H_3PO_4/50$ the highest values of specific surface area and total pore volume of 1 783 m^2g^{-1} and 1.839 cm^3g^{-1} have been reported. The largest reduction of porosity has been observed for the reference sample, $CNF500/AC/H_3PO_4/MIX$, for which the SSA of only 601 m^2g^{-1} and V_T of 0.572 cm^3g^{-1} is noted.

Tab. 29. Parameters of the porous structure of CNF synthesized on $Ni(COOH)_2$ and AC/H_3PO_4 based catalyst via CVD process and the reference sample.

Sample	**Specific surface area, S_{QSDFT} (m^2g^{-1})**	**Total pore volume, V_T (cm^3g^{-1})**	**Mesopores volume, V_{meso} (cm^3g^{-1})**	**V_{meso}/V_T**
$CNF500/AC/H_3PO_4/10$	722	0.627	0.356	0.57
$CNF500/AC/H_3PO_4/20$	1 111	1.116	0.722	0.65
$CNF500/AC/H_3PO_4/50$	1 783	1.839	1.211	0.66
$CNF500/AC/H_3PO_4/MIX$	601	0.572	0.358	0.63

The dominant mesoporous character originating from carbon nanofibers prepared on the pristine nickel oxalate and the activated carbon obtained from biomass via activation with phosphoric acid is retained in the CNF/AC composites and the reference sample. The dominant share of mesoporosity is observed in the type IV of N_2 adsorption/desorption isotherms at 77 K according to the IUPAC terminology, with slight hysteresis loops visible in the Fig. 44 [195]. Additionally, for most of the compared CNF and AC-containing samples have displayed similar share of mesoporosity with the ratio of V_{meso}/V_T in the range from 0.63 to 0.66, with only CNF500/AC/H_3PO_4/10 having displayed slightly lower V_{meso}/V_T ratio of 0.57. Moreover, similarly to CNF500-NiOx and AC/H_3PO_4, based on the PSD graphs presented in the Fig. 44 pores with the largest share of volume have diameters between 3 and 4 nm.

For composites synthesized on catalysts with lower nickel oxalate concentrations (CNF500/AC/H_3PO_4/10 and CNF500/AC/H_3PO_4/20), as well as the reference sample (CNF500/AC/H_3PO_4/MIX), a partial loss of porosity is observed. In these samples, the lower specific surface area and total pore volume compared to the original activated carbon suggest that during catalyst preparation, the porous structure of AC/H_3PO_4 may have been damaged or blocked by nickel oxalate crystallites and have not been fully restored during CNF synthesis. In contrast, CNF500/AC/H_3PO_4/50 exhibits a significant improvement in porosity and it demonstrates the highest SSA and V_T among CNF and AC-containing materials, indicating that a higher concentration of nickel oxalate in the activated carbon-based catalyst promotes better dispersion of Ni crystallites. This enhanced distribution facilitates porosity recovery through CNF formation during CVD synthesis. The observed porosity characteristics, particularly the dominant mesoporosity, suggest that these materials are well-suited for application as cathode materials in lithium-oxygen batteries.

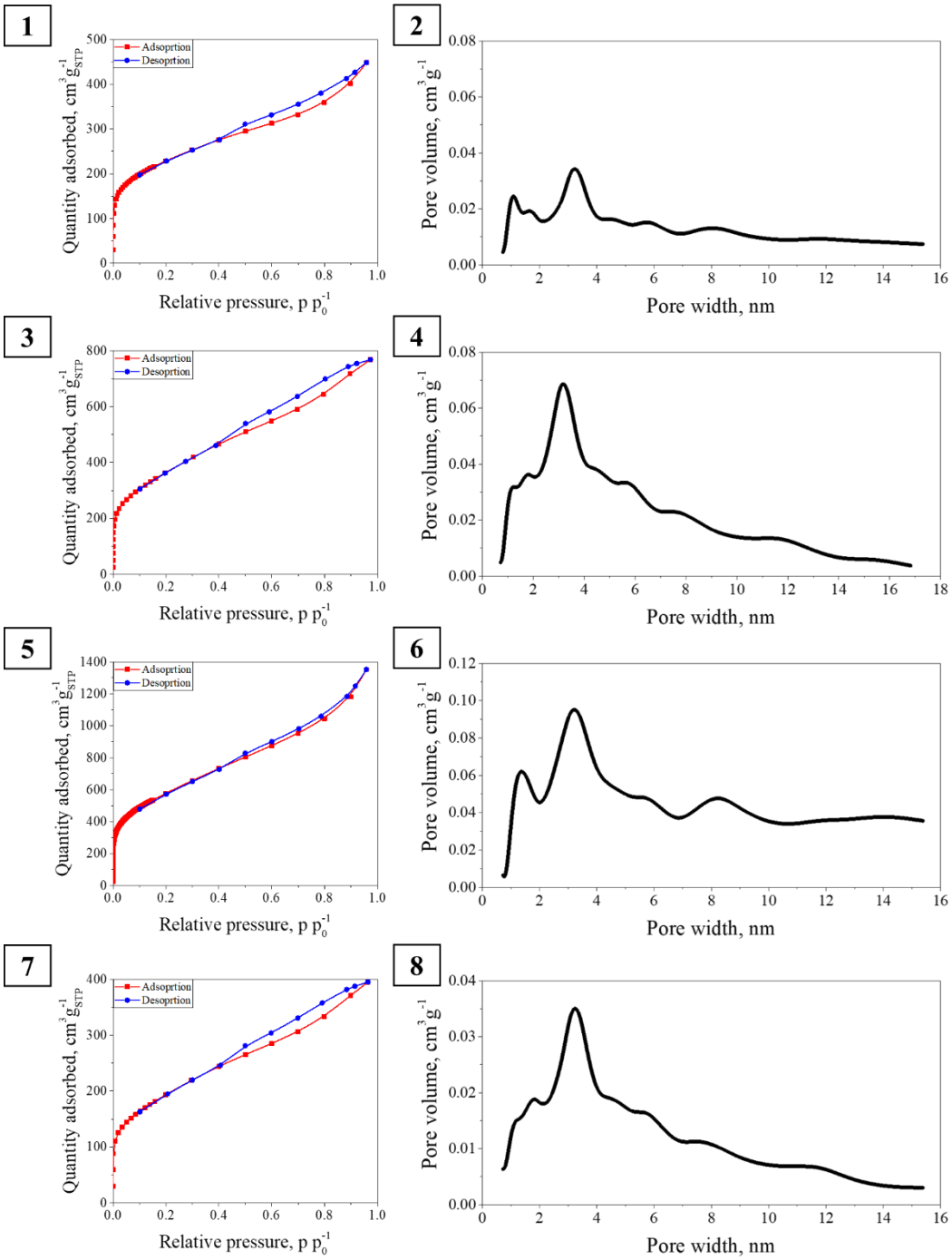

Fig. 44. The N_2 adsorption/desorption isotherms and PSD of CNF/AC composites: 1, 2 - CNF500/AC/H_3PO_4/10; 3, 4 - CNF500/AC/H_3PO_4/20; 5, 6 - CNF500/AC/H_3PO_4/50; 7, 8 - CNF500/AC/H_3PO_4/MIX.

The summary of key parameters of Raman spectra for CNF/AC composites is presented in the Tab. 30. There are no major shifts in the position of peaks for the D-band and G-band, with the maximum of D-band peaks localized at the range from 1 321 to 1 336 cm^{-1} and G-band peaks being even more closely positioned at the range of 1 579 – 1 583 cm^{-1}. However, values of I_D/I_G ratio increase with the increasing Ni content in the initial catalyst with values of 0.98, 1.12, and 1.18 noted for

CNF500/AC/H_3PO_4/10, CNF500/AC/H_3PO_4/20, and CNF500/AC/H_3PO_4/50 being reported accordingly.

Tab. 30. Comparison of key parameters of Raman spectra of CNF/AC-based composites.

Sample	**D-band peak position, cm^{-1}**	**G-band peak position, cm^{-1}**	**I_D/I_G ratio**
CNF500/AC/H_3PO_4/10	1 321	1 579	0.98
CNF500/AC/H_3PO_4/20	1 336	1 583	1.12
CNF500/AC/H_3PO_4/50	1 336	1 579	1.18

In terms of shape of D-band and G-band peaks in Raman spectra in the Fig. 45, with the increasing content of nickel in the initial catalyst peaks start to more closely resemble Raman spectrum of CNF500-NiOx – narrower and more separated peaks. The changes observed in peak shape, along with the increasing I_D/I_G, support the SEM observations, indicating that a higher nickel content in the initial catalyst leads to an increased CNF content in the resulting composite.

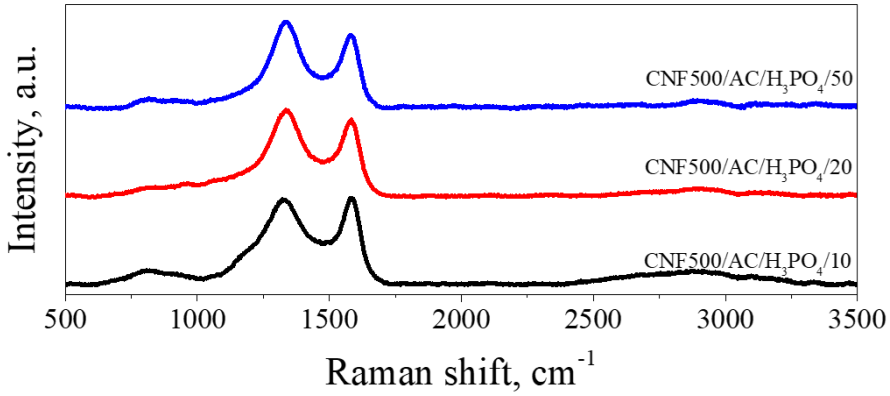

Fig. 45. Raman spectra of CNF/AC composites.

To furtherly analyze and compare the structure of obtained composites with the structure of CNF500-NiOx and AC/H_3PO_4 the XRD and Raman spectra measurements have been conducted. According to the XRD spectra of CNF500/AC/H_3PO_4/50, CNF500-NiOx, and AC/H_3PO_4 presented in the Fig. 46, two main similarities associated to the carbon nature of samples are visible. Firstly, at the range of 24-26° the peak related to the (002) plane, which is related with the interlayer spacing of graphitic carbon planes, is clearly noticeable. For CNF500/AC/H_3PO_4/50 and CNF500-NiOx, the mentioned peak is located almost precisely at 26° indicating high degree of carbonization and higher crystallinity level as compared to the AC/H_3PO_4, for which the shift in peak position towards 24° is visible. Moreover, the (002)-related peak for CNF500-NiOx is narrower in comparison to CNF500/AC/H_3PO_4/50 and AC/H_3PO_4, furtherly implying higher degree of graphitization for this sample [196]. Secondly, the small peak located at around 43° and associated with (001) plane is noticeable in each XRD spectra in the Fig. 46. Although, the intensity of this peak is significantly lower than (002)-related peak, it is related with the in-plane atomic arrangements within

individual layers in carbon materials [223]. Additional two peaks located at around 45° and 52° in XRD spectra of CNF500/AC/H_3PO_4/50 and CNF500-NiOx correspond to the signals from NiO, as has been described in section 6.4.2 [215]. Moreover, the considerable amount of amorphous carbon in CNF500/AC/H_3PO_4/50 and AC/H_3PO_4 can be noticed due to similar increase of baseline noise observed at lower range of 2Θ.

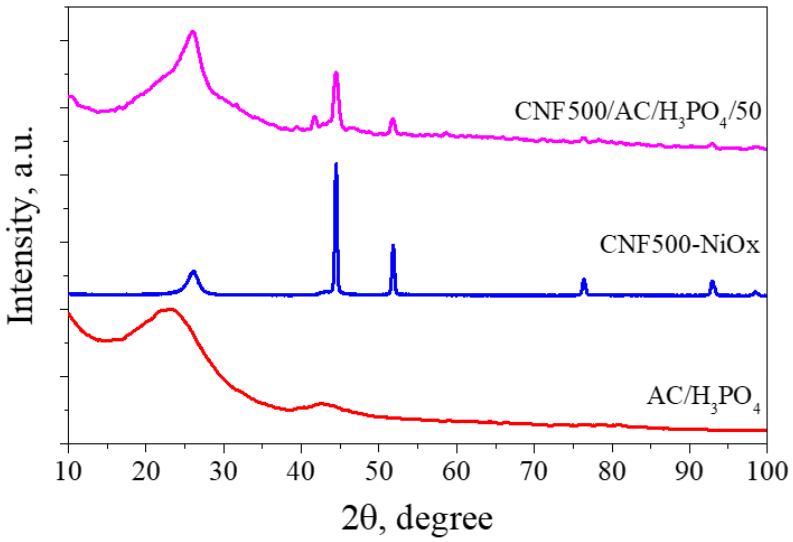

Fig. 46. XRD spectra of AC/H_3PO_4, CNF500-NiOx, and CNF500/AC/H_3PO_4/50.

The seemingly contradicting results of XRD and Raman spectra measurements can be explained with the more in-depth analysis and understanding of both techniques. The significantly higher I_D/I_G ratio for CNF500-NiOx compared to AC/H_3PO_4 and CNF500/AC/H_3PO_4/50 suggests that pristine carbon nanofibers exhibit a lower degree of graphitization. However, this observation contradicts the findings from XRD analysis. This discrepancy arises from the different structural insights provided by each analytical technique—XRD spectra reflect the bulk average structure, whereas Raman spectroscopy primarily captures surface characteristics, probing to a depth of approximately 10 nm [224].

6.5.3. Performance of Li-O_2 cells

The summary of electrochemical performance across the first discharge-charge cycle for CNF/AC composites is presented in the Tab. 31. Based on the obtained results, clear correlation is observed, that with the increasing Ni content in initial catalyst, and as a result higher share of CNF in the composition of synthesized composite, the electrochemical performance of the Li-O_2 battery improves. It is noticeable in the growth of the discharge capacity from 639 mAh g^{-1} for CNF500/AC/H_3PO_4/10 to 1 271 mAh g^{-1} for CNF500/AC/H_3PO_4/50, with moderate value of 723 mAh g^{-1} for CNF500/AC/H_3PO_4/20. In the case of reversibility of the first cycle, two composites obtained on the catalyst with lower Ni content of 10 and 20 wt. %, have reached similar reversibility of 69% and 67%, respectively. The highest reversibility of the first discharge-charge cycle at 87% has been achieved for CNF500/AC/H_3PO_4/50.

Tab. 31. Summary of electrochemical performance of Li-O_2 batteries with CNF/AC composites as cathode materials during the first discharge-charge cycle.

Sample	**1st cycle discharge capacity, mAh g^{-1}**	**1st cycle charge capacity, mAh g^{-1}**	**1st cycle reversibility**
CNF500/AC/H_3PO_4/10	639	439	69%
CNF500/AC/H_3PO_4/20	723	482	67%
CNF500/AC/H_3PO_4/50	1271	1108	87%
CNF500/AC/H_3PO_4/MIX	395	153	39%

All of the CNF/AC composites and the reference sample display discharge plateau at comparable potential of around 2.5 V, as presented in galvanostatic curves in the Fig. 47. However, only CNF500/AC/H_3PO_4/50 shows distinct and stable charge plateau at 3.75 V, which corresponds to relatively low charging overpotential of around 0.75 V.

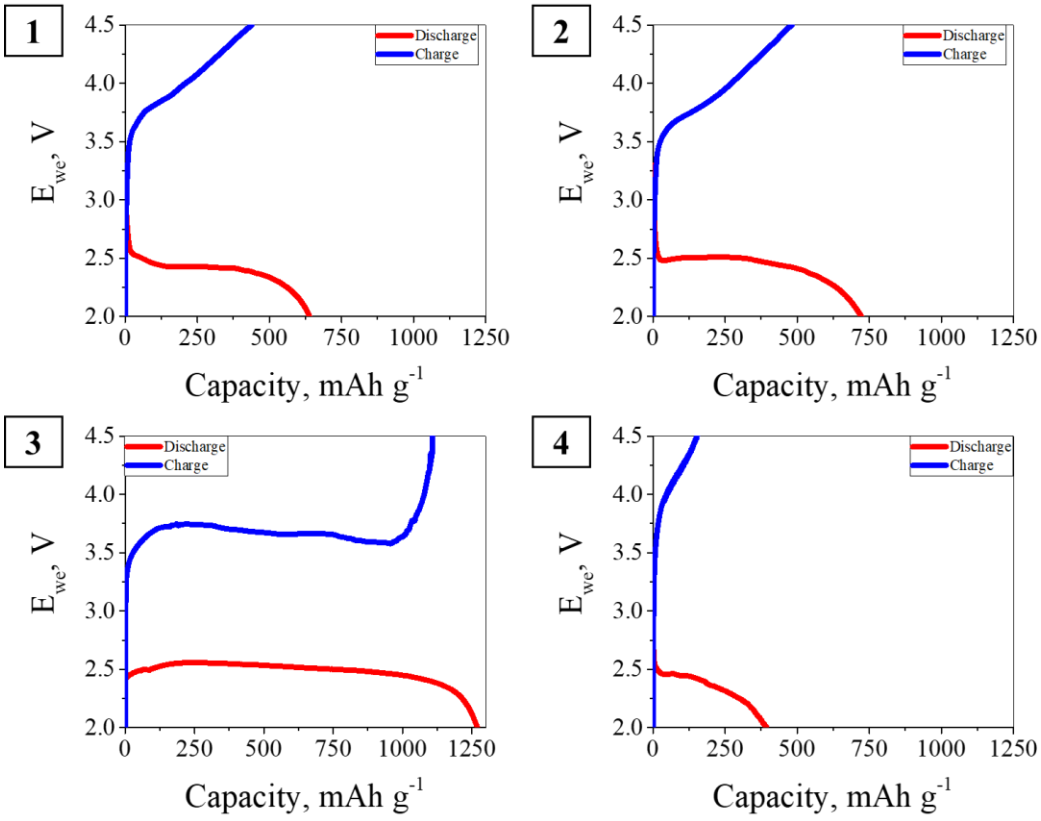

Fig. 47. Comparison of GCPL measurements for the first discharge-charge cycle conducted at current density of 0.4 mA cm^{-2} with CNF/AC composites as a cathode materials: 1 - CNF500/AC/H_3PO_4/10; 2 - CNF500/AC/H_3PO_4/20; 3 - CNF500/AC/H_3PO_4/50; 4 - CNF500/AC/H_3PO_4/MIX.

The cyclability performance of CNF and AC based materials is presented in the Fig. 48. For CNF500/AC/H_3PO_4/10 a gradual decline in discharge capacity from around 80 mAh g^{-1} in the 2nd cycle to approximately 30 mAh g^{-1} by the 30th cycle is observed, followed by a sharp drop to nearly 0 mAh g^{-1} after 40 cycles. CNF500/AC/H_3PO_4/20 maintains discharge capacity over 75 mAh g^{-1} for the first 5 cycles and later it gradually

decreases to around 50 mAh g^{-1} at the 15th cycle with a steady decline until the 50th cycle. CNF500/AC/H_3PO_4/50 demonstrates the highest stability, maintaining around 50 mAh g^{-1} across all 50 cycles. The enhanced performance of CNF/AC composites originate from the synergistic combination of high surface area and porosity from activated carbon with the strong catalytic activity of carbon nanofibers.

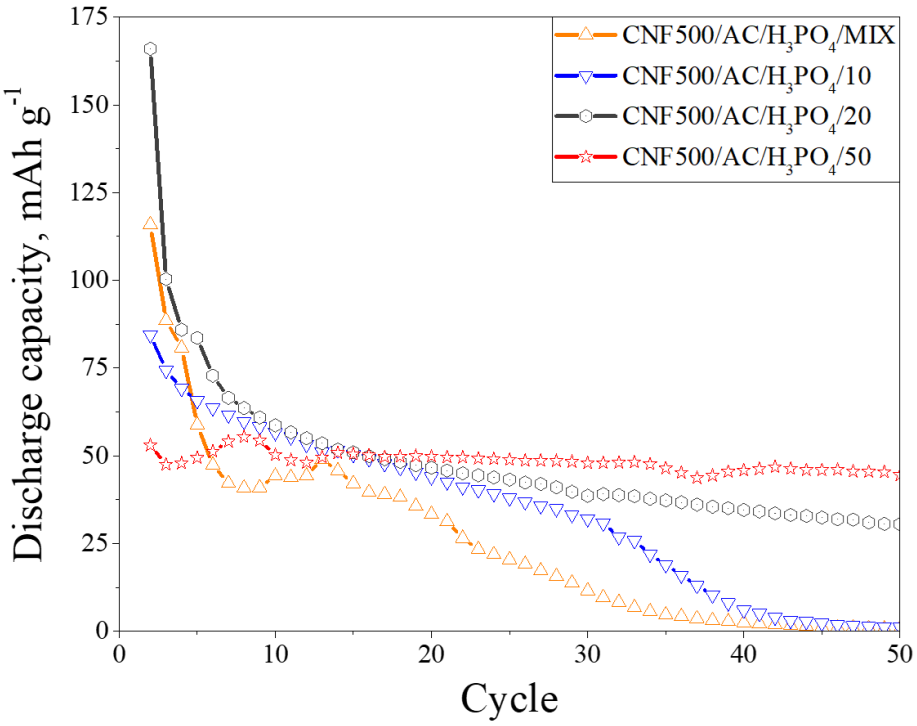

Fig. 48. Comparison of cyclability performance of CNF/AC composites as cathode materials during the GCPL measurements at 0.4 mA cm^{-2}, the first discharge cycle is excluded.

In terms of the electrochemical performance across the first cycle, all of composites have enabled achieving higher discharge capacity than the AC/H_3PO_4, CNF500-NiOx, and the reference sample (CNF500/AC/H_3PO_4/MIX). In the first cycle, the Li-O_2 battery with CNF500/AC/H_3PO_4/MIX as cathode achieves a discharge capacity of 395 mAh g^{-1}, higher than CNF500-NiOx, but lower than all of CNF/AC composites. Additionally, its reversibility of the first cycle is the lowest among all of compared samples, reaching only 39%. Over 50 cycles, its capacity remains around 50 mAh g^{-1} until the 15th cycle, after which it declines rapidly to around 0 mAh g^{-1} by the 35th cycle. These results suggest that *in-situ* synthesis of CNF/AC composites is more effective in preserving the beneficial characteristics of both activated carbon and CNF, compared to simply physically mixing two materials. The observed synergistic effect enhances the overall performance of lithium-oxygen batteries, whereas a simple physical mixture does not yield the same improvements.

Correlation between porosity and discharge capacity can be observed based on the obtained data – higher SSA, V_T, and V_{meso} generally lead to greater discharge capacities [137, 153]. However, electrochemical performance of lithium-oxygen batteries is not exclusively dependent on the porosity, which can be noticed during the

comparison of AC/H_3PO_4 and CNF500/AC/H_3PO_4/20. Both samples exhibit similar specific surface area, total pore volume, and mesopores volume, with differences between values of those parameters reaching couple of percents. Although, the porous structure is similar, significantly different electrochemical behavior is observed. The superior performance of the composite can be explained by its higher I_D/I_G ratio, indicating greater structural disorder. As have been reported previously in the literature, higher I_D/I_G ratio in cathode materials beneficially impact battery operation due to three main factors [225]. Firstly, increasing surface activity of defected structures can create better sites for nucleation and growth of lithium peroxide. Secondly, structural defects create more active sites for adsorption of oxygen, which can promote ORR and OER. Thirdly, the overpotential of ORR and OER can be reduced by enhanced charge transport facilitated by improved reaction pathways caused by defective sites and disorder structures. In contrast, reversibility and cycling stability are more dependent on the intrinsic catalytic properties of the cathode than on porosity. This explains the higher reversibility of CNF500-NiOx over AC/H_3PO_4 and the improved cyclability with increasing CNF content in composite samples.

The influence of current density on the first cycle discharge capacity is presented in the Fig. 49, and clear correlation can be observed, where increasing current density leads to decreasing discharge capacity. The highest capacity of 2 196 mAh g^{-1} is recorded at 0.1 mA cm^{-2}, dropping to 1 890 mAh g^{-1} at 0.2 mA cm^{-2}. Further increases of current densities to 0.4 and 0.6 mA cm^{-2} result in gradual declines of discharge capacity to 1 271 and 1 186 mAh g^{-1}, followed by a sharp drop to 304 mAh g^{-1} at 0.8 mA cm^{-2}. In contrast, first cycle reversibility fluctuates for different current densities. The highest values of 90% and 87% are observed at 0.2 and 0.4 mA cm^{-2}, while at 0.1, 0.6, and 0.8 mA cm^{-2}, reversibility drops significantly to 28%, 21%, and 6%, respectively.

The consumption rate of lithium ions and oxygen during ORR is proportional to current density, which corresponds to decreases in discharge capacities for higher current density, such trend is consistent with other reports [226]. Additionally, high discharge overpotential can furtherly constrain oxygen and lithium ions transportation and increasing current density leads to the rise in discharge overpotential, which is visible in the decline of discharge plateau potential. The position of discharge plateau have declined from around 2.66 V at 0.1 mA cm^{-2} by approximately 0.3 V to around 2.36 V at 0.8 mA cm^{-2}. Similarly, the reversibility of the first cycle is limited by increasing charge overpotential, which also increases with higher current density. The already sluggish kinetics of OER is furtherly impacted at higher current densities by insufficient oxygen transfer, which results in low charge capacities. However, low reversibility is also registered at the lowest of tested current density, which can results from inhibited charge transfer and high polarization of cathode surface owing to the formation of thick layer of insulating discharge products.

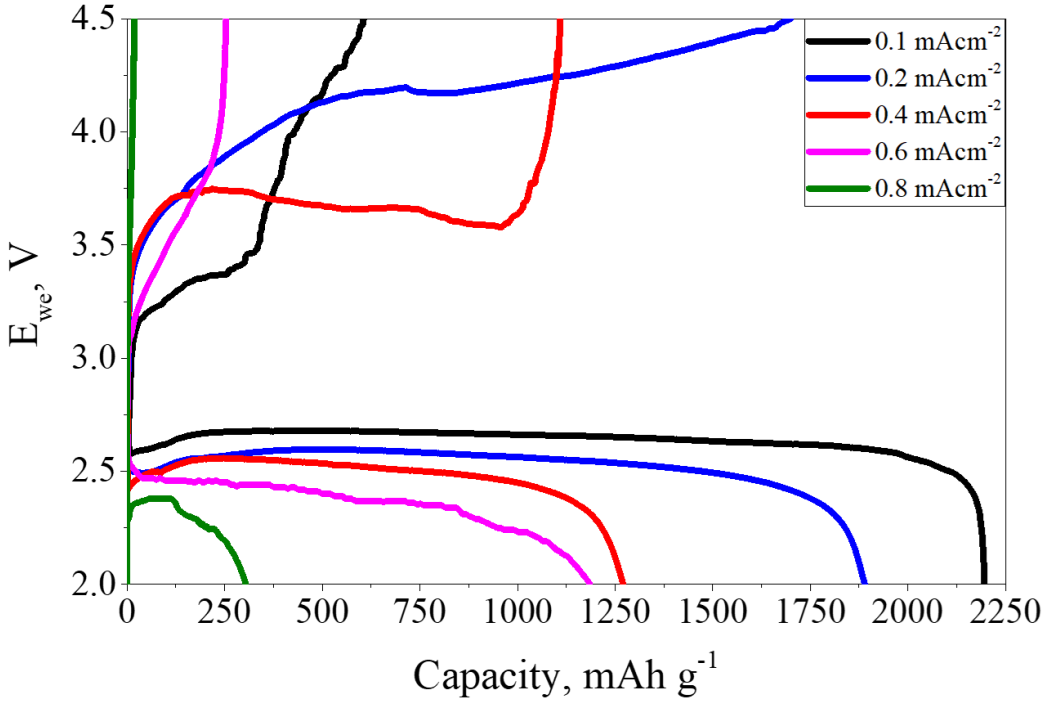

Fig. 49. Comparison of electrochemical performance of Li-O_2 battery in the first discharge charge cycle of GCPL measurements conducted at different current densities with CNF500/AC/H_3PO_4/50 as cathode material.

Due to the significant decrease of discharge capacity after couple of cycles, electrochemical measurements with limited discharge capacity have been conducted to investigate full potential of lithium-oxygen batteries. The discharge capacities of 100 and 250 mAh g^{-1} have been chosen as benchmarks and the number of cycles with 100% reversibility have been recorded. Additionally, wide range of current densities have been selected to carry out tests and results are presented in the Fig. 50.

When the discharge capacity is limited to 250 mAh g^{-1}, higher current densities appear to slightly enhance cyclability. At 0.1 and 0.2 mA cm^{-2}, the number of cycles with 100% reversibility reaches 3 and 4, respectively. Increasing the current density to 0.4 mA cm^{-2} extends the cycle life to 6 cycles, but a further rise to 0.6 mA cm^{-2} reduces it to 5 cycles. However, a different trend is observed when the discharge capacity is limited to 100 mAh g^{-1}. The lowest cycle life with 100% reversibility (5 cycles) occurs at 0.1 and 0.6 mA cm^{-2}, while a slightly higher value of 7 cycles is recorded at 0.4 mA cm^{-2}. A notable increase in cyclability is observed at 0.2 mA cm^{-2}, where the battery achieves 12 fully reversible cycles.

The observed cyclability results highlight the delicate balance required for optimal lithium-oxygen battery operation, emphasizing the need for optimization of current density and discharge capacity for improved performance. At high current density (0.6 mA cm^{-2}), increased contribution of side reactions leading to electrolyte and cathode degradation, rising overpotential and reducing battery efficiency is observed. On the other hand, at low current density (0.1 mA cm^{-2}), the formation of dense and compact layers of discharge product is favored, which limits their

decomposition during the charge cycle, thus negatively impacting cyclability. This effect is also evident in measurements without discharge capacity limitations. While low current densities reduce overpotential and promote slower kinetics, prolonged reaction times may accelerate side reactions, further degrading cathode components.

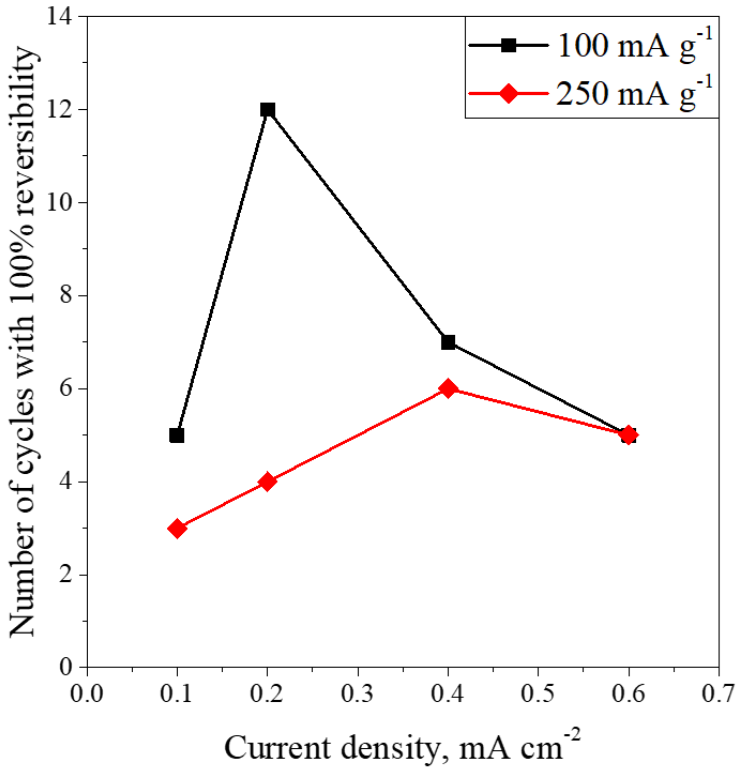

Fig. 50. Comparison of number of discharge-charge cycles with limited discharge capacity measured with 100% reversibility of Li-O_2 battery with CNF500/AC/H_3PO_4/50 as cathode materials at different current densities.

In contrast, moderate current densities (0.2 and 0.4 mA cm^{-2}) seem to enable achieving the balance between efficient ORR and OER kinetics, limiting the impact of side reactions while promoting a formation of a more easy-to-decompose layers of discharge products, which support prevention of excessive overpotential and cathode polarization. Additionally, discharge capacity limitation significantly influences battery cyclability. A lower discharge capacity (100 mAh g^{-1}) minimizes cathode stress and reduces overpotential by limiting discharge product accumulation, whereas a higher capacity (250 mAh g^{-1}) promotes more extensive discharge product growth, increasing the risk of cathode passivation and performance loss.

6.6. Carbon aerogels as free-standing cathodes in Li-O_2 cells

6.6.1. Synthesis

As shown in the Fig. 51, the proposed method enables the formation of CNT aerogels with a stable three-dimensional structure. All of synthesized aerogels exhibit a similar cylindrical shape, with heights ranging from around 1.50 to 2.00 cm and diameters of 1.00 cm. Based on the presented dimensions and the mass of CNT used in

the preparation, the density of the obtained aerogels falls within the range from 10.2 to 25.5 mg cm^{-3}.

The preparation of CNT aerogels is achieved with the minimal addition of 0.1 mmol of TETA as a cross-linking agent. In contrast, most CNT-based aerogel synthesis methods reported in the literature involve either significantly larger quantities of cross-linking agents (e.g., PVA, surfactants [227, 228]) or prior functionalization of CNT [229]. In this study, the proposed mechanism for gelation and aerogel formation is attributed to electrostatic interactions between CNT, combined with interactions between hydrogen atoms within the CNT structure and the amine groups of TETA.

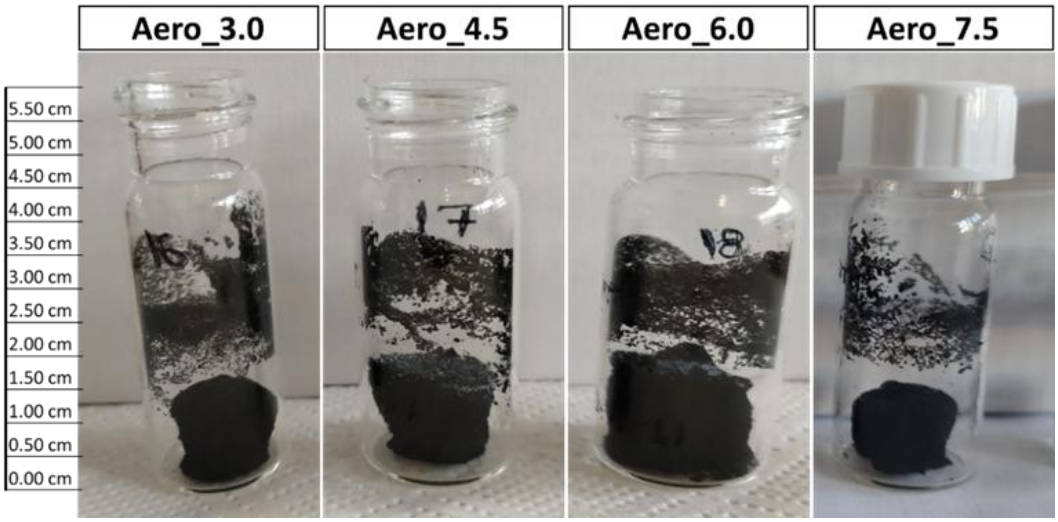

Fig. 51. Pictures of the obtained CNT based aerogels after freeze-drying.

The mechanical properties of aerogels are schematically illustrated in the Fig. 52. When a load exceeding 130 times the mass of the Aero_7.5 sample has been applied, the aerogel has compressed, and its height has been reduced from the initial 7 mm to 4 mm. However, upon removal of the load, the aerogel immediately regained part of its original dimensions, reaching a post-compression height of 5 mm. The ability to withstand significant mechanical stress while maintaining structural integrity, along with the partial recovery of its height, demonstrates the favorable mechanical properties of CNT aerogels.

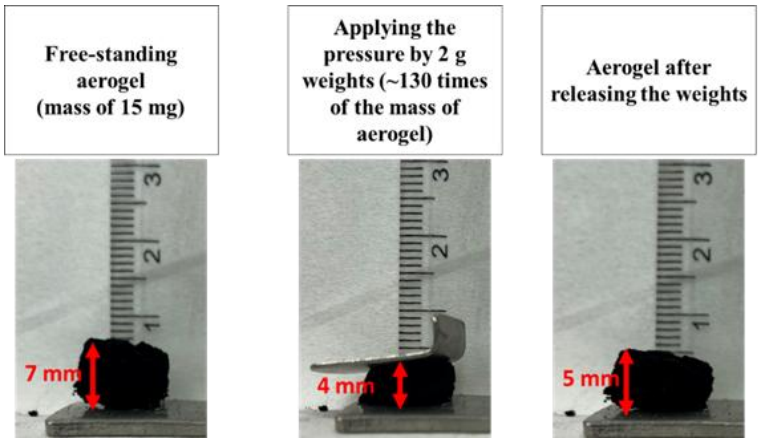

Fig. 52. Sample of Aero_7.5 aerogel during the compression test with the mass significantly larger than the mass of the sample.

6.6.2. Materials characterization

The structure of carbon nanotubes used in the preparation of carbon aerogels is presented in SEM images in the Fig. 53. The nanotubes aggregate into fiber-like structures with diameters of approximately 2-3 µm (see Fig. 53.2 and Fig. 53.3), which furtherly assemble into macroscopic seed-like clusters measuring around 30–50 µm in diameter (Fig. 53.1). Higher-magnification images (see Fig. 53.4-53.6) reveal a highly entangled CNT network, a characteristic commonly observed in commercially available nanotubes that have not undergone any untangling treatment [230]. Based on the presented images, the estimated diameter of individual nanotubes is below 10 nm, aligning with the supplier's specifications (declared diameter in the range of 6–9 nm).

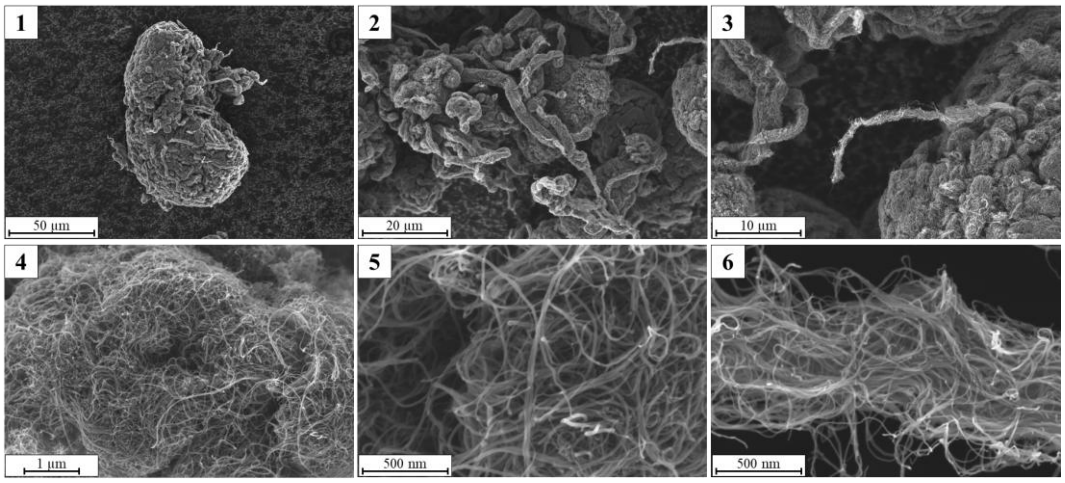

Fig. 53. SEM images of CNT used in the preparation of carbon aerogels.

For all aerogel samples, a similar macroscopic structure is observed in the SEM images presented in the Fig. 54. At lower magnification (Fig. 54.1, 54.3, 54.5, and 54.7), all samples display a sponge-like morphology composed of entangled fiber-like structures and hollow macropores formed during the aerogel synthesis process.

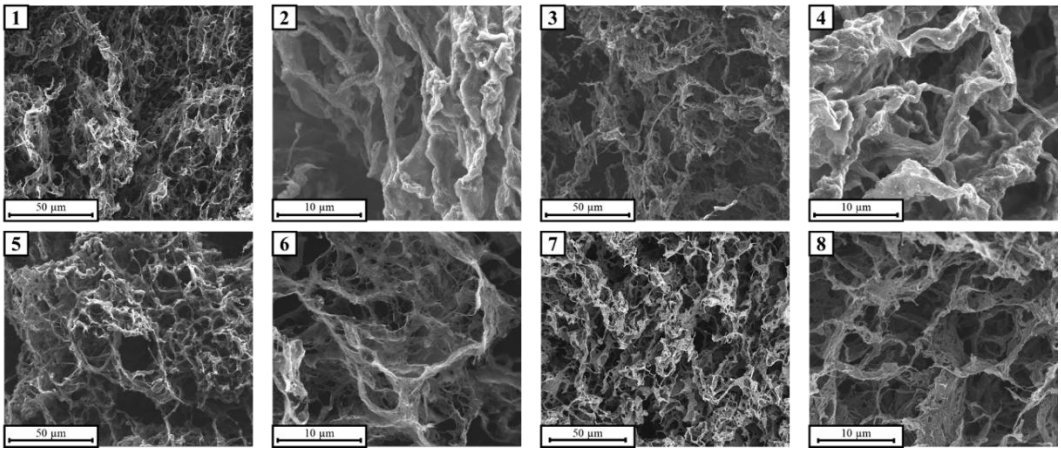

Fig. 54. SEM images of prepared CNT-based aerogels: 1, 2 - Aero_3.0; 3, 4 - Aero_4.5; 5, 6 - Aero_6.0; 7, 8 - Aero_7.5.

Higher-magnification images in the Fig. 55 reveal the presence of individual nanotubes with diameters below 10 nm, consistent with pristine CNT. These observations indicate that the nanostructure is not deteriorated during cross-linking and freeze-drying, and that only the macroscopic organization of CNT is changing during the formation of aerogels. Additionally, SEM images at the micrometer scale in the Fig. 54.2, 54.4, 54.6, and 54.8 show no significant differences in the overall morphology among obtained aerogels.

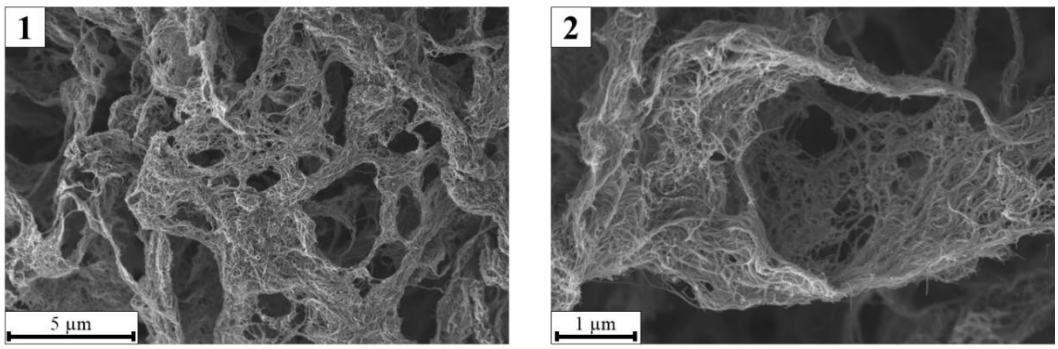

Fig. 55. SEM images of Aero_7.5 with high magnification.

The N_2 adsorption/desorption isotherms for CNT and all of analyzed cathodes are presented in the Fig. 56. Key parameters of the porous structure for CNT and aerogels are summarized in the Tab. 32. The so-called “standard cathode” is based on the CNT and PTFE slurry pressed onto the nickel foam and is referred to as CNT@Ni-foam – for the standard cathode, reported values are normalized to the mass of the non-metallic components (CNT + binder).

All of the displayed isotherms correspond to type IV of isotherms according to IUPAC classification [195] – typical for mesoporous materials. A slight hysteresis loop is observed in all curves, furtherly indicating the mesoporous nature of samples. Pristine CNT exhibit a relatively high SSA of 213 m^2g^{-1} and V_T of 0.451 cm^3g^{-1}. However, after aerogel formation, the porous structure undergoes significant deterioration, leading to a reduction in specific surface area and pore volume. Among the aerogels, Aero_4.5

maintains the highest SSA of 88 m^2g^{-1}, followed by Aero_6.0 (70 m^2g^{-1}), Aero_3.0 (66 m^2g^{-1}), and Aero_7.5 (56 m^2g^{-1}). The observed decline in porosity can be attributed to the increased entanglement of CNT during cross-linking and freeze-drying, where individual nanotubes intertwine and form denser, more compact structures, resulting in reduction of available SSA and V_T. A similar trend is observed for total pore volume, where Aero_4.5 and Aero_6.0 exhibit the highest values of 0.261 and 0.182 cm^3g^{-1}, respectively, followed by Aero_3.0 (0.154 cm^3g^{-1}) and Aero_7.5 (0.163 cm^3g^{-1}). Similar decrease in surface area after aerogel formation from CNT has been reported by Shen *et al.* [228].

Tab. 32. Comparison of parameters of porosity of CNT, standard cathode and prepared CNT-based aerogels.

Sample	**Specific surface area, S_{QSDFT} (m^2g^{-1})**	**Total pore volume, V_T (cm^3g^{-1})**	**Mesopores volume, V_{meso} (cm^3g^{-1})**	**V_{meso}/V_T**
CNT	213	0.451	0.404	0.90
CNT@Ni-foam	50	0.118	0.099	0.84
Aero_3.0	66	0.154	0.131	0.85
Aero_4.5	88	0.261	0.238	0.91
Aero_6.0	70	0.182	0.157	0.86
Aero_7.5	56	0.163	0.150	0.92

Another key parameters in evaluating the suitability of a material as a cathode for Li-O_2 battery are the mesopore volume and the share of mesoporosity in total porosity, typically expressed as the ratio of V_{meso}/V_T. All of analyzed samples, including pristine CNT, exhibit a predominantly mesoporous structure, as indicated by high V_{meso}/V_T ratio and the shape of isotherms. The mesopore volume of pristine CNT (0.404 cm^3g^{-1}) decreases after aerogel formation, with values ranging from 0.238 cm^3g^{-1} for Aero_4.5 to 0.131 cm^3/g for Aero_3.0. Comparable values are recorded for Aero_6.0 (0.157 cm^3g^{-1}) and Aero_7.5 (0.150 cm^3g^{-1}). However, the V_{meso}/V_T ratio remains relatively stable across all aerogels, ranging from 0.85 to 0.92, closely matching the value of 0.90 for CNT.

For the CNT@Ni-foam cathode, the reduction in porosity is even more noticeable. The SSA decreases to 50 m^2g^{-1}, while the V_T is reduced to 0.118 cm^3g^{-1}. Despite this substantial loss in porosity compared to pristine CNT, the sample retains a dominant mesoporous character, with a mesopore volume of 0.099 cm^3g^{-1}, which corresponds to V_{meso}/V_T ratio of 0.84.

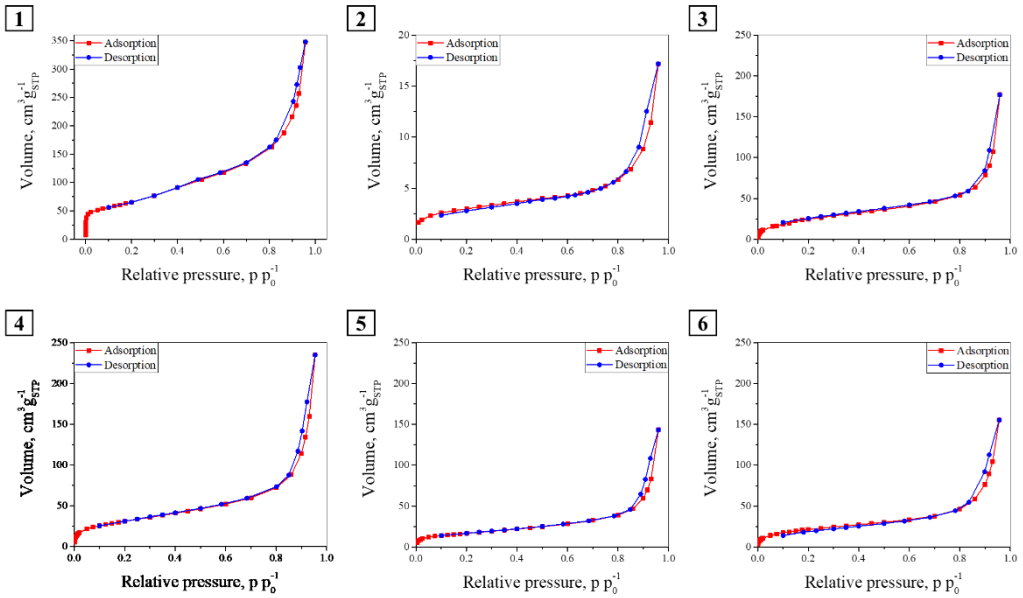

Fig. 56. The N_2 adsorption/desorption isotherms at 77 K of: 1 - CNT; 2 - CNT@Ni-foam electrode; 3 - Aero_3.0; 4 - Aero_4.5; 5 - Aero_6.0; 6 - Aero_7.5.

In terms of pore size distribution presented in the Fig. 57, CNT show a wide range of PSD between 0.7 and 20 nm with a considerable share of large mesopores (above approximately 11-12 nm). On the other hand, the PSD graphs of all of aerogels are similar, with the reduced volumes of pore ranging in diameters from 0.7 to 9 nm as compared to the pristine CNT. The observed decline can be attributed to the blockage of smaller pores during the preparation of aerogels.

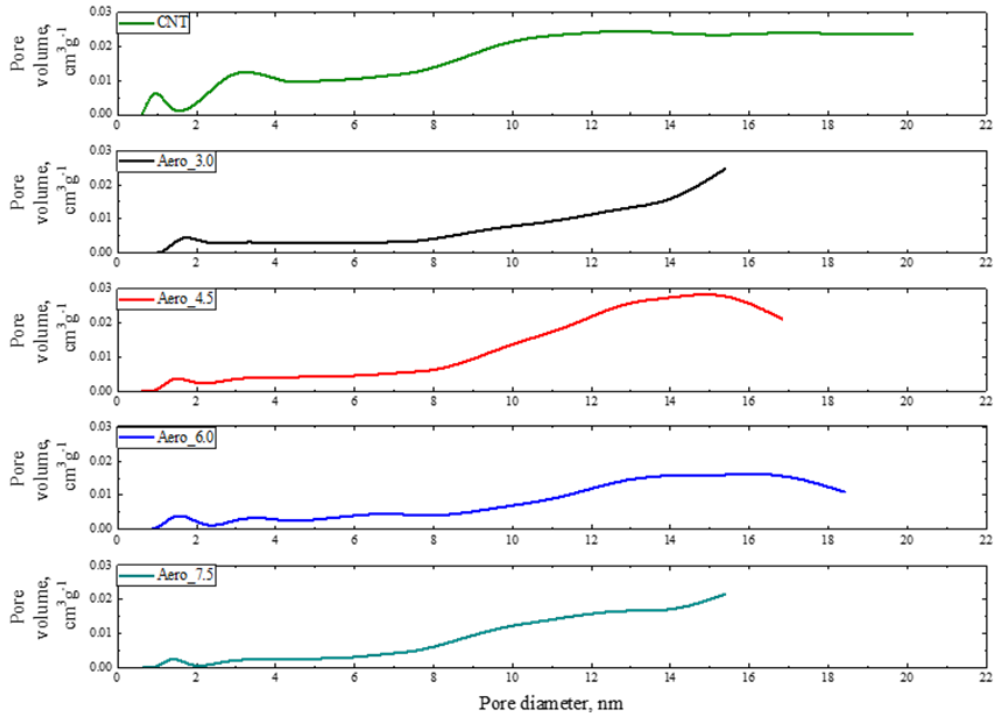

Fig. 57. PSD graphs of CNT and CNT-based aerogels.

From the presented data, the non-linear correlation between the concentration of CNT dispersion in water and V_T, V_{meso}, and SSA can be noticed. Increasing the CNT concentration in water from 3.0 mg ml^{-1} to 4.5 mg ml^{-1} leads to the increase of all key porosity parameters. However, above this values, a further increase in concentration of CNT in water results in the collapse of the porous structure, as visible in the decline of V_T, V_{meso}, and SSA. Thus, a CNT dispersion concentration of 4.5 mg ml^{-1} appears to provide an optimal balance between agglomeration tendencies and dispersion stability, ensuring a more homogeneous distribution of CNT in water. However, exceeding the critical concentration of 4.5 mg ml^{-1} increase the probability of CNT agglomeration, which can disrupt uniform distribution and hinder the formation of interconnected porous network.

A similar decline in aerogel porosity with increasing precursor concentration has been reported in the literature [231, 232]. Kondratowicz *et al.* [56] have observed a reduction in specific surface area and pore volume for graphene oxide-based aerogels as the graphene oxide concentration increased, regardless of variations in acidity, basicity, or gelation methods [231]. Similarly, Shen *et al.* reported a comparable trend in aerogels synthesized from graphene oxide and CNT mixtures, furtherly supporting the observed porosity degradation at higher CNT concentrations [232].

6.6.3. Performance of Li-O_2 cells

Electrochemical performance of carbon aerogels and standard cathode across the first discharge-charge cycle is summarized in the Tab. 33. In comparison to carbon aerogels, the Li-O_2 cell with CNT@Ni-foam cathode displays a relatively low discharge capacity of 470 mAh g^{-1} for the first cycle. Compared to the CNT@Ni-foam cathode, all aerogel samples show a substantial increase in the first cycle discharge capacity. The lowest, but still more than two-fold, growth of discharge capacity is observed for Aero_3.0, reaching 1 056 mAh g^{-1}. On the other hand, Aero_4.5 demonstrates the highest capacity of 3 967 mAh g^{-1}, which corresponds to over eightfold increase. Aero_6.0 and Aero_7.5 achieve similar discharge capacities of 2 470 mAh g^{-1} and 2 203 mAh g^{-1}, respectively.

Tab. 33. Summary of electrochemical performance of Li-O_2 battery with CNT@Ni-foam and CNT-based aerogels as a cathodes during the first discharge-charge cycle.

Sample	**1st cycle discharge capacity, mAh g^{-1}**	**1st cycle charge capacity, mAh g^{-1}**	**1st cycle reversibility**	**Volume of deposited Li_2O_2 during 1st discharge, cm^3 g^{-1}**
CNT@Ni-foam	475	470	98.9%	0.175
Aero_3.0	1 056	159	15.1%	0.389
Aero_4.5	3 967	2 540	64.0%	1.461
Aero_6.0	2 470	796	32.2%	0.910

High discharge capacity observed in the first cycle is directly related to the substantial volume of lithium peroxide formed. The calculated Li_2O_2 volumes generated during discharge are included in the Tab. 33, with the corresponding calculations

detailed below. For all samples, the calculated volume of Li_2O_2 deposited during discharge exceeds the total pore volume measured by N_2 adsorption – pores with diameters below 50 nm. Therefore, the available micropore and mesopore volumes become fully blocked, forcing the storage of excess Li_2O_2 within macropores.

The superior discharge capacity of aerogels, compared to the nickel foam-based cathode, can be attributed to their unique sponge-like structure. As shown in the SEM images (Fig. 54), all aerogels contain network of macropores with diameters of several micrometers, which provide additional space for Li_2O_2 accumulation, leading to the growth of discharge capacities. In contrast, the nickel foam cathode lacks macropores within a comparable size range. As presented in the Fig. 58, Ni-foam structure is characterized by large, electrochemically inactive pores (>200 μm), which do not contribute effectively to Li_2O_2 storage. Additionally, the total pore volume of CNT in the nickel foam cathode is furtherly reduced by the presence of the PTFE binder, leading to inferior electrochemical performance compared to the aerogel-based cathodes.

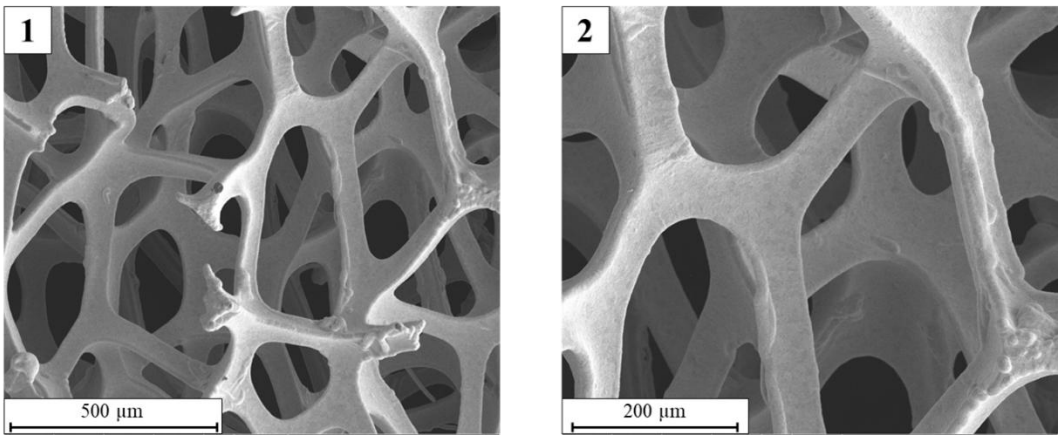

Fig. 58. SEM images of the nickel foam utilized as the support material in the CNT@Ni-foam cathode.

The step by step calculations of the mass and volume of deposited lithium peroxide during the first discharge cycle are presented below. All of the resultant values are related to 1 g of electrode active mass. In the presented case, the influence of side and parasitic reactions on created discharge products is neglected.

Firstly, by using the stoichiometric of the reaction of lithium peroxide creation, defined be equation (6), the theoretical capacity of Li_2O_2 is determined. The Li_2O_2 formation reaction presents that two moles of Li^+ are required in the formation of one mole of lithium peroxide. Considering that the charge of one mole of electrons is defined by Faraday's constant (F), approximately 96 485.3 C mol^{-1}, and that the molar mass of Li_2O_2 equals to 45.881 g mol^{-1}, its theoretical formation capacity of lithium peroxide ($C_{Theoretical}$) can be determined using the following equation:

$$C_{Theoretical} = \frac{2 \cdot F}{M_{Li_2O_2}} = \frac{2 \cdot 96\,485.3\ C\ mol^{-1}}{45.881\ g\ mol^{-1}} \approx 4\,211.42\ C\ g^{-1} \qquad (15)$$

Accounting to the fact that 1 C ≈ 0.28 mAh g^{-1}, the $C_{Theoretical}$ can be recalculated and expressed in mAh g^{-1}:

$$C_{Theoretical} = 4\,211.42\ C\ g^{-1} \cdot 0.28\ mAh\ C^{-1} \approx 1\,175.4\ mAh\ g^{-1} \quad (16)$$

Using the theoretical capacity of lithium peroxide, the mass of Li_2O_2 deposited during discharge ($m_{Li_2O_2\ deposited}$) can be determined under the assumption that the entire capacity originates from reaction described by equation (6). Subsequently, based on the calculated mass and the density of Li_2O_2 ($\rho_{Li_2O_2\ deposited}$ of 2.31 g cm^{-3}), the volume of deposited Li_2O_2 per gram of electrode (active mass) can be estimated ($V_{Li_2O_2\ deposited}$). A representative calculation for the Aero_4.5 sample is provided below.

$$m_{Li_2O_2\ deposited}^{Aero\_4.5} = \frac{1^{st}\ discharge\ capacity_{Aero_{4.5}}}{C_{Theoretical}} = \frac{3\,967\ mAh\ g^{-1}}{1\,175.4\ mAh\ g^{-1}} \approx 3.375\ g\ g^{-1} \quad (17)$$

$$V_{Li_2O_2\ deposited}^{Aero\_4.5} = \frac{m_{Li_2O_2\ deposited}^{Aero\_4.5}}{C_{Theoretical}} = \frac{3.375\ g\ g^{-1}}{2.31\ g\ cm^{-3}} \approx 1.461\ cm^3 g^{-1} \quad (18)$$

The highest first-cycle reversibility is observed for the Li–O_2 cell with the CNT@Ni-foam cathode, achieving 98.9% capacity recovery after the first discharge. None of the aerogel-based cathodes have reached such high reversibility. Among the aerogels, Aero_4.5 exhibits the highest reversibility at 64.0%, whereas Aero_3.0, Aero_6.0, and Aero_7.5 display significantly lower values of 15.1%, 32.2%, and 1.9%, respectively.

Charging plateaus around 3.6 V are observed for CNT@Ni-foam (Fig. 59.1) and Aero_6.0 (Fig. 59.4), while Aero_4.5 exhibits a plateau at approximately 4.0 V. In contrast, Aero_3.0 and Aero_7.5 do not display distinct charging plateaus. These plateaus correspond to specific redox reactions occurring during the charge process. Given that the theoretical potential of ORR/OER is 2.96 V, the overpotential for OER equals approximately 0.7 V for CNT@Ni-foam and Aero_6.0, while for Aero_4.5, it is 1.0 V.

Differences in OER plateau positions and reversibility among the samples can be attributed to variations in porous structure and cathode morphology. Surprisingly, the high reversibility of CNT@Ni-foam can be attributed its lower discharge capacity, which results in the deposition of a thinner Li_2O_2 layer. This leads to less pore blockage and to a formation of a thinner insulating film on the cathode. In contrast, aerogels exhibit much higher discharge capacities, resulting in the formation of thicker Li_2O_2 layers, which may contribute to lower reversibility and shifts in the OER plateau position.

The low reversibility of aerogel-based cathodes is primarily attributed to the irreversible deposition of lithium peroxide within their porous network, leading to pore blockage and only partial decomposition of the surface layer of Li_2O_2. Differences in overpotential between the aerogels likely originate from differences in the thickness and resistivity of the Li_2O_2 layer – thicker insulating layer requires a higher potential for decomposition. In the case of Aero_7.5, nearly all of its discharge capacity is lost during

the first charge, suggesting that complete pore blockage occurs during Li_2O_2 formation, preventing efficient decomposition and hindering the catalytic activity of CNT.

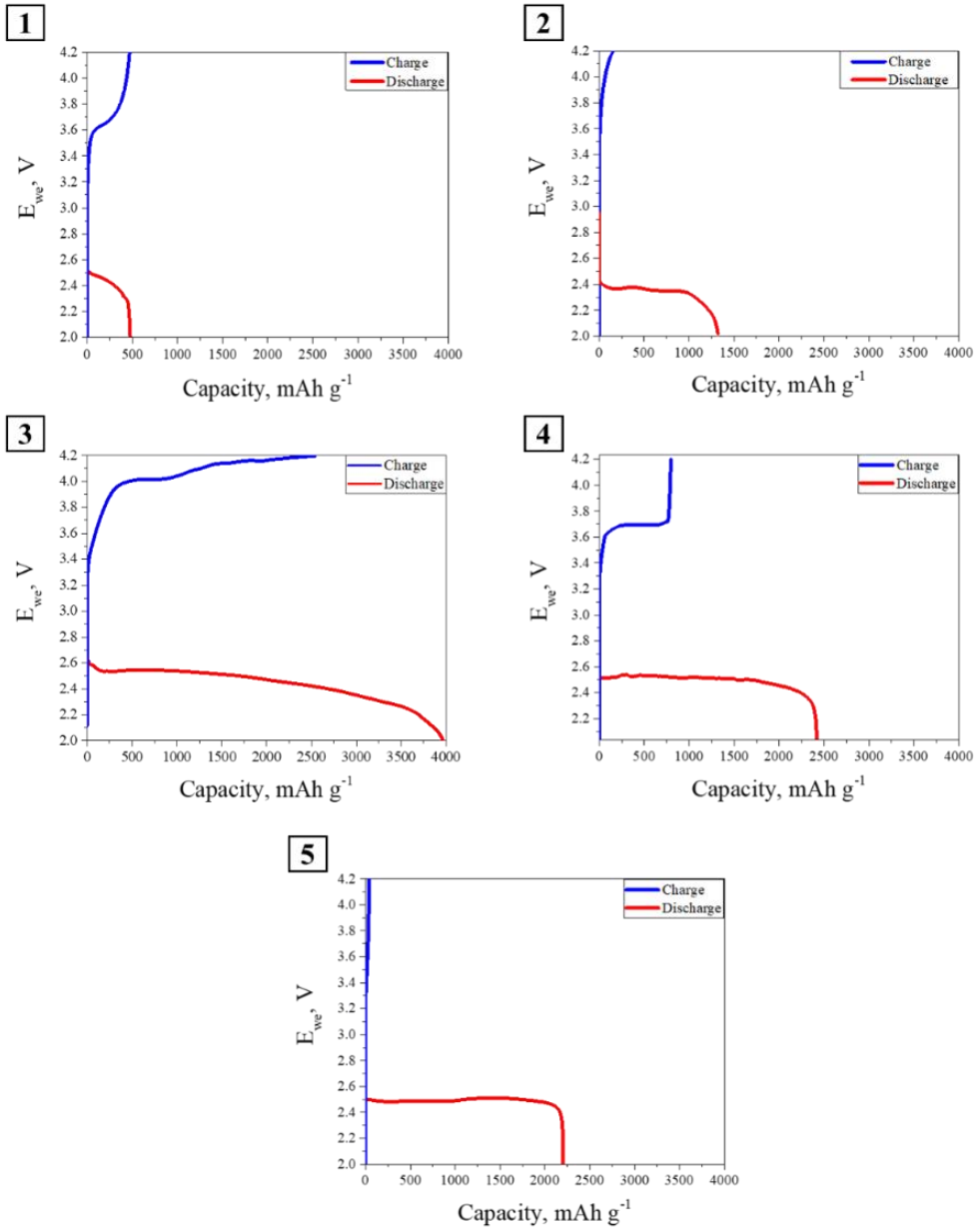

Fig. 59. Comparison of GCPL measurements for the first discharge-charge cycle conducted at current density of 0.4 mA cm^{-2} with CNT@Ni-foam and CNT-based aerogels as cathodes: 1 – CNT@Ni-foam; 2 – Aero_3.0; 3 -Aero_4.5; 4 -Aero_6.0; 5 – Aero_7.5.

To investigate the cathode surface after discharge, *ex-situ* characterization has been performed using SEM. As observed in SEM images in the Fig. 60, after discharge cathode surface becomes densely covered with a compact layer of discharge products. This deposited layer closely follows the morphology of the aerogel, completely covering the original 3D structure of CNT network and resulting in a smoother, more rounded surface appearance.

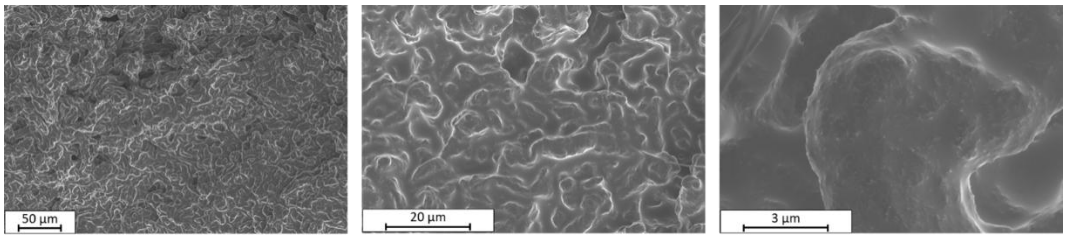

Fig. 60. The SEM images of the discharged cathode composed of Aero_4.5 from Li-O_2 battery that has been discharged one time from the open circuit voltage to 2.0 V.

To further examine the changes occurring during battery operation, Electrochemical Impedance Spectroscopy measurements have been conducted on the pristine, discharged, and recharged cells, with the corresponding Nyquist plots presented in the Fig. 61. The wide semicircles observed in the spectra, associated with charge transfer resistance (R_{ct}) indicate sluggish redox processes at the electrode/electrolyte interface. Upon discharge, semicircle significantly increases as compared to the pristine cell, reflecting the slower reaction kinetics. After recharging, R_{ct} decreases from approximately 2 900 Ω to 1 800 Ω, yet remains higher than its initial value, suggesting that the thick layer of discharge products formed during the first discharge undergoes only partial decomposition upon charging.

Additionally, fluctuations in the electric resistance (R_e) furtherly support this interpretation. Initially, R_e is around 109 Ω but rises to 149 Ω after the first discharge, before slightly decreasing to 136 Ω upon recharging. Since R_e primarily accounts for the resistance of the electrolyte, wiring, and aerogel-to-current collector contact, this increase suggests that the accumulation of non-conductive discharge products progressively hinders electrical contact, effectively isolating the aerogel from the current collector. These combined effects contribute to the overall performance degradation of the cell.

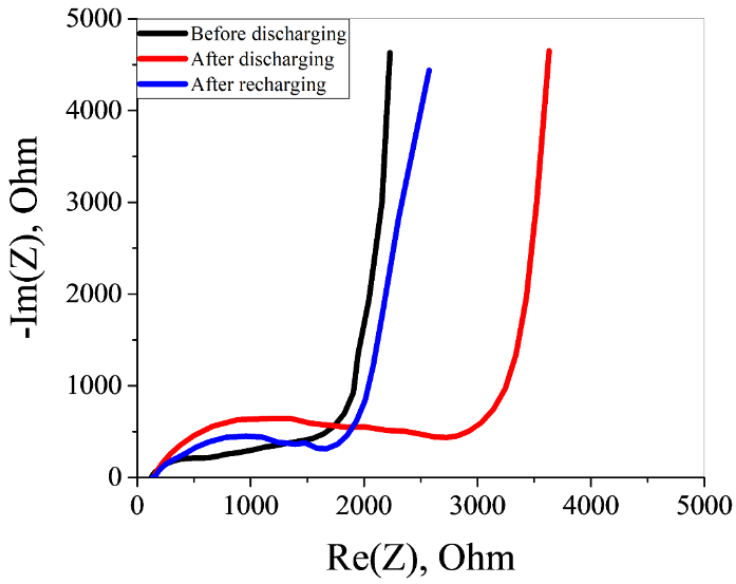

Fig. 61. The Nyquist plots obtained for the Li-O_2 battery with Aero_4.5 cathode.

Presented results align with previous literature reports regarding the relationship between discharge capacity and mesopore volume in cathode materials. As reported by Xiao *et al.* [233] and Kuboki *et al.* [234], dominant share of mesoporosity is essential for achieving high discharge capacities. Since micropores and small mesopores are quickly blocked by excess of electrolyte and products deposited at the early stage of discharge, their contribution to the Li-O_2 battery operation remains limited. Instead, a large mesopore volume facilitates efficient discharge product storage, while the presence of larger pores enhances oxygen and lithium-ion transport, further improving cathode performance.

7. Summary and conclusions

In the presented study, extensive research regarding the influence of parameters of synthesis on structures and properties of materials has been conducted. Moreover, the correlation between properties of materials and their potential application as the cathode material in lithium-oxygen batteries has been investigated by carrying out electrochemical measurements. The obtained results have enabled determination of optimal synthesis parameters in order to achieve the most promising performance of Li-O_2 batteries.

In the synthesis of carbon nanofibers using a standard catalyst composed of nickel nanoparticles supported on Al_2O_3, a relationship between synthesis temperature and material properties has been established. The specific surface area of the CNF has increased with higher CVD temperatures. Meanwhile, the total pore volume and mesopore volume have risen between 450°C and 550°C, followed by a decline at higher temperature. Despite notable variations in SSA and V_T, all samples present dominant mesoporosity (V_{meso}/V_T ranging from 0.82 to 0.88) and comparable morphology and structure, as confirmed by SEM and Raman spectroscopy. However, these differences in physical properties did not clearly translate into variations in electrochemical performance. No direct correlation has been found between the measured parameters and the Li-O_2 battery performance, indicating that further structural investigation is needed to better understand how CNF characteristics influence battery performance. Among all samples, CNF500 has exhibited the highest first cycle discharge capacity, satisfactory reversibility, and relatively stable cycling behavior. Therefore, 500°C has been selected as the optimal synthesis temperature for studies on nitrogen doping of carbon nanofibers.

All of the proposed nitrogen doping methods have resulted in the incorporation of nitrogen atoms into the carbon structure of CNF, as confirmed by elemental analysis and XPS measurements. The influence of various experimental parameters – including the type of nitrogen source, temperature, reaction time, and pH – has been thoroughly investigated in relation to the amount of nitrogen incorporated into the structure of carbon nanofiber. Nitrogen doping has substantially improved the performance of lithium-oxygen batteries, as reflected in increased first cycle discharge capacity, higher reversibility, and enhanced cyclability of the N-doped cathode materials. During *in-situ* functionalization, the utilization of two or three nitrogen sources has enabled

incorporation of higher amounts of bulk nitrogen compared to the use of a single donor. In particular, the combination of gaseous ammonia and melamine (CNF500-Am-Me) has led to the highest bulk nitrogen content among all tested samples. However, the *ex-situ* hydrothermal functionalization has introduced the highest concentration of surface nitrogen species (CNF500/HT-N25/180).

As an alternative to the standard catalyst (Ni nanoparticles deposited on Al_2O_3), catalyst based on free-standing nickel oxalate has been developed and successfully applied in the CVD synthesis of carbon nanofibers. Although all CVD processes conducted at temperatures between 450°C and 600°C have yielded carbon nanofibers, the synthesis yields obtained using the nickel oxalate-based catalyst have been significantly lower than those achieved with the standard catalyst. Carbon nanofibers synthesized using both catalysts have exhibited a similar degree of structural disorder. However, samples produced on $Ni(COOH)_2$ have shown inferior porosity – namely lower SSA, V_T, and share of mesoporosity. As with carbon nanofibers synthesized using the standard catalyst, no clear correlation has been observed between the material properties and the electrochemical performance in lithium–oxygen batteries. Consistent with earlier findings, the CNF500-NiOx sample has demonstrated the most favorable battery performance, and therefore, a synthesis temperature of 500°C has been selected for the development of composite materials.

To investigate the influence of porosity type on electrochemical performance, five activated carbons have been prepared. Highly microporous materials have been obtained via chemical activation with potassium hydroxide, while predominantly mesoporous activated carbon has been synthesized through activation with phosphoric acid. The positive effect of mesoporosity on lithium-oxygen battery performance has been demonstrated, with particular emphasis on its critical role in increasing the first discharge capacity. Although the cyclability of AC/H_3PO_4 has been found to be worse than that of the other activated carbons, this material has been selected for the development of CNF/AC-based composites, as it has enabled the highest first-cycle discharge capacity – identified as a key parameter in the search for suitable support material for composite cathodes.

Physical mixing of nickel oxalate with activated carbon in different proportions has been proposed as a preparation method for catalysts enabling the synthesis of CNF/AC composites via the CVD process. All of the tested nickel contents in the initial catalysts have successfully enabled the formation of composite materials, in which carbon nanofibers grow on nickel nanoparticles distributed across the activated carbon surface. Increasing the nickel content from 10 wt. % to 50 wt. % has led to the formation of a denser layer of carbon nanofibers, which has translated into higher SSA, and V_T in the resulting composites. The synergistic combination of properties from both components – activated carbon and carbon nanofibers – has been particularly visible in the enhanced performance of Li-O_2 batteries using these composites as cathode materials. All of the prepared composites have demonstrated higher first cycle discharge capacity, improved reversibility, and superior cyclability compared to either CNF or AC alone. Moreover, their electrochemical performance has surpassed that of the reference

sample composed of a simple physical mixture of CNF and AC, further emphasizing the advantages of the proposed synthesis approach. The extensive electrochemical research regarding the operation of Li-O_2 battery under various conditions, such as different current densities and limited discharge capacities, has highlighted the delicate balance in the operation of lithium-oxygen batteries and the requirement to optimize all measurement parameters in order to achieve the best performance of the battery.

The proposed synthesis method, based on homogenization, freeze-drying, and lyophilization of aqueous dispersion of CNT, has enabled the synthesis of carbon aerogels in relatively straightforward approach, without the need of excessive amounts of cross-linkers or prior functionalization of carbon material. The influence of the concentration of CNT in the initial water dispersion on the properties of the final aerogel has been investigated. Concentration of CNT at 4.5 mg ml^{-1} has been determined as the optimal for the preparation of the free-standing carbon aerogel-based cathode and achieving the best performance of the Li-O_2 battery across the first cycle. Moreover, the post-mortem study of the surface of cathode and EIS measurements have been carried out to enable more in-depth characterization of reaction occurring during the operation of the battery.

To summarize, extensive research has been conducted on the preparation and characterization of various cathode material groups. Multiple strategies to enhance the performance of Li-O_2 batteries have been proposed, including nitrogen doping, composite formation, and the development of free-standing cathodes. Among the tested materials, carbon aerogels have achieved the highest first-cycle discharge capacities, while the composites have demonstrated the most promising cyclability. Additionally, nitrogen doping has significantly improved the first-cycle discharge capacity, reversibility, and long-term cycling performance of carbon nanofibers, highlighting the potential of this functionalization technique to enhance cathode behavior. At the same time, this work has emphasized the need to optimize synthesis parameters across all material groups in parallel with advancing lithium-oxygen battery operation. Carbon nanomaterials have shown substantial potential in improving Li-O_2 battery performance, yet further investigation into strategies for enhancing long-term cyclability remains necessary.

8. References

1. Gür, T.M.: Review of electrical energy storage technologies, materials and systems: challenges and prospects for large-scale grid storage. Energy Environ Sci. 11, 2696–2767 (2018). https://doi.org/10.1039/C8EE01419A

2. Scrosati, B.: History of lithium batteries. Journal of Solid State Electrochemistry. 15, 1623–1630 (2011). https://doi.org/10.1007/S10008-011-1386-8/TABLES/3

3. Kao, W.H.: Substrate materials for bipolar lead/acid batteries. J Power Sources. 70, 8–15 (1998). https://doi.org/10.1016/S0378-7753(97)02605-0

4. Lopes, P.P., Stamenkovic, V.R.: Past, present, and future of lead–acid batteries. Science (1979). 369, 923–924 (2020). https://doi.org/10.1126/SCIENCE.ABD3352

5. Etacheri, V., Marom, R., Elazari, R., Salitra, G., Aurbach, D.: Challenges in the development of advanced Li-ion batteries: A review. Energy Environ Sci. 4, 3243–3262 (2011). https://doi.org/10.1039/C1EE01598B

6. Mizushima, K., Jones, P.C., Wiseman, P.J., Goodenough, J.B.: LixCoO2 (0 < x ∼< 1): A NEW CATHODE MATERIAL FOR BATTERIES OF HIGH ENERGY DENSITY. North-Holland Publishing Company (1981)

7. Armstrong, A.R., Bruce, P.G.: Synthesis of layered LiMnO2 as an electrode for rechargeable lithium batteries. Nature. 381, 499–500 (1996). https://doi.org/10.1038/381499a0

8. Severson, K.A., Attia, P.M., Jin, N., Perkins, N., Jiang, B., Yang, Z., Chen, M.H., Aykol, M., Herring, P.K., Fraggedakis, D., Bazant, M.Z., Harris, S.J., Chueh, W.C., Braatz, R.D.: Data-driven prediction of battery cycle life before capacity degradation. Nature Energy 2019 4:5. 4, 383–391 (2019). https://doi.org/10.1038/s41560-019-0356-8

9. Bloom, I., Jones, S.A., Battaglia, V.S., Henriksen, G.L., Christophersen, J.P., Wright, R.B., Ho, C.D., Belt, J.R., Motloch, C.G.: Effect of cathode composition on capacity fade, impedance rise and power fade in high-power, lithium-ion cells. J Power Sources. 124, 538–550 (2003). https://doi.org/10.1016/S0378-7753(03)00806-1

10. Yabuuchi, N., Ohzuku, T.: Novel lithium insertion material of LiCo1/3Ni1/3Mn1/3O2 for advanced lithium-ion batteries. J Power Sources. 119–121, 171–174 (2003). https://doi.org/10.1016/S0378-7753(03)00173-3

11. Chen, C.H., Liu, J., Stoll, M.E., Henriksen, G., Vissers, D.R., Amine, K.: Aluminum-doped lithium nickel cobalt oxide electrodes for high-power lithium-ion batteries. J Power Sources. 128, 278–285 (2004). https://doi.org/10.1016/J.JPOWSOUR.2003.10.009

12. Tarascon, J.M., Armand, M.: Issues and challenges facing rechargeable lithium batteries. Nature. 414, 359–367 (2001). https://doi.org/10.1038/35104644

13. Goodenough, J.B., Park, K.S.: The Li-ion rechargeable battery: A perspective. J Am Chem Soc. 135, 1167–1176 (2013). https://doi.org/10.1021/JA3091438/ASSET/IMAGES/MEDIUM/JA-2012-091438_0009.GIF

14. Li, J., Zhang, K., Wang, B., Peng, H.: Light-Assisted Metal–Air Batteries: Progress, Challenges, and Perspectives. Angewandte Chemie International Edition. 61, e202213026 (2022). https://doi.org/10.1002/ANIE.202213026

15. Timofeeva, E. V., Segre, C.U., Pour, G.S., Vazquez, M., Patawah, B.L.: Aqueous air cathodes and catalysts for metal–air batteries. Curr Opin Electrochem. 38, 101246 (2023). https://doi.org/10.1016/J.COELEC.2023.101246

16. Zhang, D., Li, R., Huang, T., Yu, A.: Novel composite polymer electrolyte for lithium air batteries. J Power Sources. 195, 1202–1206 (2010). https://doi.org/10.1016/J.JPOWSOUR.2009.08.063

17. Wang, G., Huang, L., Liu, S., Xie, J., Zhang, S., Zhu, P., Cao, G., Zhao, X.: Understanding Moisture and Carbon Dioxide Involved Interfacial Reactions on Electrochemical Performance of Lithium-Air Batteries Catalyzed by Gold/Manganese-Dioxide. ACS Appl Mater Interfaces. 7, 23876–23884 (2015). https://doi.org/10.1021/ACSAMI.5B05250/SUPPL_FILE/AM5B05250_SI_001.PDF

18. Wang, J., Ke, Y., Chen, X., Jia, Z.: Preparation of Waterproof and Air-Permeable Membrane by Water Surface Spreading Method for Metal-Air Battery. ACS Sustain Chem Eng. 10, 2903–2913 (2022). https://doi.org/10.1021/ACSSUSCHEMENG.1C07526/SUPPL_FILE/SC1C07526_SI_001.PDF

19. Caramia, V., Bozzini, B.: Materials science aspects of zinc-air batteries: A review. Mater Renew Sustain Energy. 3, 1–12 (2014). https://doi.org/10.1007/S40243-014-0028-3/FIGURES/12

20. Olabi, A.G., Sayed, E.T., Wilberforce, T., Jamal, A., Alami, A.H., Elsaid, K., Rahman, S.M.A., Shah, S.K., Abdelkareem, M.A.: Metal-air batteries—a review, (2021)

21. Khan, Z., Vagin, M., Crispin, X.: Can Hybrid Na–Air Batteries Outperform Nonaqueous Na–O2 Batteries?, (2020)

22. CRC Handbook of Chemistry and Physics. CRC Press (2016)

23. Zu, C.X., Li, H.: Thermodynamic analysis on energy densities of batteries. Energy Environ Sci. 4, 2614–2624 (2011). https://doi.org/10.1039/C0EE00777C

24. Sun, Q., Yang, Y., Fu, Z.W.: Electrochemical properties of room temperature sodium–air batteries with non-aqueous electrolyte. Electrochem commun. 16, 22–25 (2012). https://doi.org/10.1016/J.ELECOM.2011.12.019

25. Liang, F., Watanabe, T., Hayashi, K., Yao, Y., Ma, W., Bin Yang, Dai, Y.: Liquid exfoliation graphene sheets as catalysts for hybrid sodium-air cells. Mater Lett. 187, 32–35 (2017). https://doi.org/10.1016/J.MATLET.2016.10.054

26. Zhang, S., Wen, Z., Rui, K., Shen, C., Lu, Y., Yang, J.: Graphene nanosheets loaded with Pt nanoparticles with enhanced electrochemical performance for sodium–oxygen batteries. J Mater Chem A Mater. 3, 2568–2571 (2015). https://doi.org/10.1039/C4TA05427J

27. Jian, Z., Chen, Y., Li, F., Zhang, T., Liu, C., Zhou, H.: High capacity Na–O2 batteries with carbon nanotube paper as binder-free air cathode. J Power Sources. 251, 466–469 (2014). https://doi.org/10.1016/J.JPOWSOUR.2013.11.091

28. Hashimoto, T., Hayashi, K.: Aqueous and Nonaqueous Sodium-Air Cells with Nanoporous Gold Cathode. Electrochim Acta. 182, 809–814 (2015). https://doi.org/10.1016/J.ELECTACTA.2015.09.153

29. Kang, Y., Su, F., Zhang, Q., Liang, F., Adair, K.R., Chen, K., Xue, D., Hayashi, K., Cao, S.C., Yadegari, H., Sun, X.: Novel High-Energy-Density Rechargeable Hybrid Sodium-Air Cell with Acidic Electrolyte. ACS Appl Mater Interfaces. 10, 23748–23756 (2018). https://doi.org/10.1021/ACSAMI.8B04278/SUPPL_FILE/AM8B04278_SI_001.PDF

30. Khan, Z., Park, S., Hwang, S.M., Yang, J., Lee, Y., Song, H.K., Kim, Y., Ko, H.: Hierarchical urchin-shaped α-MnO2 on graphene-coated carbon microfibers: a binder-free electrode for rechargeable aqueous Na–air battery. NPG Asia Mater. 8, e294–e294 (2016). https://doi.org/10.1038/am.2016.104

31. Liu, W.M., Yin, W.W., Ding, F., Sang, L., Fu, Z.W.: NiCo2O4 nanosheets supported on Ni foam for rechargeable nonaqueous sodium–air batteries. Electrochem commun. 45, 87–90 (2014). https://doi.org/10.1016/J.ELECOM.2014.05.021

32. Bi, X., Wang, R., Yuan, Y., Zhang, D., Zhang, T., Ma, L., Wu, T., Shahbazian-Yassar, R., Amine, K., Lu, J.: From Sodium-Oxygen to Sodium-Air Battery: Enabled by Sodium Peroxide Dihydrate. Nano Lett. 20, 4681–4686 (2020). https://doi.org/10.1021/ACS.NANOLETT.0C01670/SUPPL_FILE/NL0C01670_SI_001.PDF

33. Hartmann, P., Bender, C.L., Vračar, M., Dürr, A.K., Garsuch, A., Janek, J., Adelhelm, P.: A rechargeable room-temperature sodium superoxide (NaO2) battery. Nature Materials 2012 12:3. 12, 228–232 (2012). https://doi.org/10.1038/nmat3486

34. Wu, Y., Qiu, X., Liang, F., Zhang, Q., Koo, A., Dai, Y., Lei, Y., Sun, X.: A metal-organic framework-derived bifunctional catalyst for hybrid sodium-air batteries. Appl Catal B. 241, 407–414 (2019). https://doi.org/10.1016/J.APCATB.2018.09.063

35. Mir, S., Vij, S., Dhawan, N.: Evaluation of end-of-life zinc-air hearing aid batteries for zinc recovery. Miner Eng. 198, 108082 (2023). https://doi.org/10.1016/J.MINENG.2023.108082

36. Rahman, Md.A., Wang, X., Wen, C.: High Energy Density Metal-Air Batteries: A Review. J Electrochem Soc. 160, A1759–A1771 (2013). https://doi.org/10.1149/2.062310JES/META

37. Liu, X., Yuan, Y., Liu, J., Liu, B., Chen, X., Ding, J., Han, X., Deng, Y., Zhong, C., Hu, W.: Utilizing solar energy to improve the oxygen evolution reaction kinetics in zinc–air battery. Nat Commun. 10, (2019). https://doi.org/10.1038/s41467-019-12627-2

38. Gu, P., Zheng, M., Zhao, Q., Xiao, X., Xue, H., Pang, H.: Rechargeable zinc–air batteries: a promising way to green energy. J Mater Chem A Mater. 5, 7651–7666 (2017). https://doi.org/10.1039/C7TA01693J

39. Chen, Z., Yu, A., Higgins, D., Li, H., Wang, H., Chen, Z.: Highly active and durable core-corona structured bifunctional catalyst for rechargeable metal-air battery application. Nano Lett. 12, 1946–1952 (2012). https://doi.org/10.1021/NL2044327/SUPPL_FILE/NL2044327_SI_001.PDF

40. Müller, S., Holzer, F., Haas, O.: Optimized zinc electrode for the rechargeable zinc-air battery. J Appl Electrochem. 28, 895–898 (1998). https://doi.org/10.1023/A:1003464011815/METRICS

41. Devyatkina, T.I., Gun'ko, Y.L., Mikhalenko, M.G.: Development of ways to diminish corrosion of zinc electrode. Russian Journal of Applied Chemistry. 74, 1122–1125 (2001). https://doi.org/10.1023/A:1013058615990/METRICS

42. Kim, K., Cho, Y.H., Eom, S.W., Kim, H.S., Yeum, J.H.: Anions of organic acids as gas suppressants in zinc–air batteries. Mater Res Bull. 45, 262–264 (2010). https://doi.org/10.1016/J.MATERRESBULL.2009.06.020

43. Xu, J.J., Ye, H., Huang, J.: Novel zinc ion conducting polymer gel electrolytes based on ionic liquids. Electrochem commun. 7, 1309–1317 (2005). https://doi.org/10.1016/J.ELECOM.2005.09.011

44. Wang, X., Sebastian, P.J., Smit, M.A., Yang, H., Gamboa, S.A.: Studies on the oxygen reduction catalyst for zinc–air battery electrode. J Power Sources. 124, 278–284 (2003). https://doi.org/10.1016/S0378-7753(03)00737-7

45. Meng, H., Shen, P.K.: Novel Pt-free catalyst for oxygen electroreduction. Electrochem commun. 8, 588–594 (2006). https://doi.org/10.1016/J.ELECOM.2006.01.020

46. Gupta, N., Toh, T., Fatt, M.W., Mhaisalkar, S., Srinivasan, M.: Paper like free-standing hybrid single-walled carbon nanotubes air electrodes for zinc-air batteries. Journal of Solid State Electrochemistry. 16, 1585–1593 (2012). https://doi.org/10.1007/S10008-011-1559-5/FIGURES/11

47. Goel, P., Dobhal, D., Sharma, R.C.: Aluminum–air batteries: A viability review. J Energy Storage. 28, 101287 (2020). https://doi.org/10.1016/J.EST.2020.101287

48. Lameche-Djeghaba, S., Benchettara, A., Kellou, F., Ji, V.: Electrochemical Behaviour of Pure Aluminium and Al-5%Zn Alloy in 3% NaCl Solution. Arab J Sci Eng. 39, 113–122 (2014). https://doi.org/10.1007/S13369-013-0876-7/METRICS

49. Ma, J., Wen, J., Gao, J., Li, Q.: Performance of Al−1Mg−1Zn−0.1Ga−0.1Sn as anode for Al-air battery. Electrochim Acta. 129, 69–75 (2014). https://doi.org/10.1016/J.ELECTACTA.2014.02.080

50. Park, I.J., Choi, S.R., Kim, J.G.: Aluminum anode for aluminum-air battery – Part II: Influence of In addition on the electrochemical characteristics of Al-Zn alloy in alkaline solution. J Power Sources. 357, 47–55 (2017). https://doi.org/10.1016/J.JPOWSOUR.2017.04.097

51. Iwai, T., Nguyen, D.T., Taguchi, K.: Study of Activated Carbon Sheets Used for Air-Cathodes of Portable Quasi-Solid Aluminum-Air Batteries. IEEJ Transactions on Electrical and Electronic Engineering. 16, 653–655 (2021). https://doi.org/10.1002/TEE.23343

52. Namwong, N., Kruehong, C.: Chain-like carbon nano-onions from candle flame combustion as a high-performance cathode for aluminum-air batteries. Diam Relat Mater. 129, 109396 (2022). https://doi.org/10.1016/J.DIAMOND.2022.109396

53. Guo, M., Zhang, X., Yang, T., Dang, Q., Li, X., Wang, Y., Zhang, G.: Binary FeCo-N-doped carbon/carbon nanotube composites for efficient oxygen reduction and high-performance aluminum-air battery. J Power Sources. 456, 227933 (2020). https://doi.org/10.1016/J.JPOWSOUR.2020.227933

54. Luo, Z., Yin, L., Xiang, L., Liu, T.X., Song, Z., Li, Y., Zhou, L., Luo, K., Wu, K., Jiang, J.: AuPt Nanoparticles/ Multi-Walled carbon nanotubes catalyst as high active and stable oxygen reduction catalyst for Al-Air batteries. Appl Surf Sci. 564, 150474 (2021). https://doi.org/10.1016/J.APSUSC.2021.150474

55. Wang, M., Ma, J., Yang, H., Lu, G., Yang, S., Chang, Z.: Nitrogen and Cobalt Co-Coped Carbon Materials Derived from Biomass Chitin as High-Performance Electrocatalyst for Aluminum-Air Batteries. Catalysts 2019, Vol. 9, Page 954. 9, 954 (2019). https://doi.org/10.3390/CATAL9110954

56. Mokhtar, M., Talib, M.Z.M., Majlan, E.H., Tasirin, S.M., Ramli, W.M.F.W., Daud, W.R.W., Sahari, J.: Recent developments in materials for aluminum–air batteries: A review. Journal of Industrial and Engineering Chemistry. 32, 1–20 (2015). https://doi.org/10.1016/J.JIEC.2015.08.004

57. Rota, M., Comninellis, C., Moller, S., Holzer, F., Haas, O.: Bipolar Al/02 battery with planar electrodes in alkaline and acidic electrolytes. J Appl Electrochem. 25, 114–121 (1995). https://doi.org/10.1007/BF00248167/METRICS

58. Gaele, M.F., Migliardini, F., Di Palma, T.M.: Dual solid electrolytes for aluminium-air batteries based on polyvinyl alcohol acidic membranes and neutral hydrogels. Journal of Solid State Electrochemistry. 25, 1207–1216 (2021). https://doi.org/10.1007/S10008-021-04900-6/FIGURES/10

59. Wang, D.P., Zhang, D.Q., Lee, K.Y., Gao, L.X.: Performance of AA5052 alloy anode in alkaline ethylene glycol electrolyte with dicarboxylic acids additives for

aluminium-air batteries. J Power Sources. 297, 464–471 (2015). https://doi.org/10.1016/J.JPOWSOUR.2015.08.033

60. Deyab, M.A.: 1-Allyl-3-methylimidazolium bis(trifluoromethylsulfonyl)imide as an effective organic additive in aluminum-air battery. Electrochim Acta. 244, 178–183 (2017). https://doi.org/10.1016/J.ELECTACTA.2017.05.116

61. Wang, D., Li, H., Liu, J., Zhang, D., Gao, L., Tong, L.: Evaluation of AA5052 alloy anode in alkaline electrolyte with organic rare-earth complex additives for aluminium-air batteries. J Power Sources. 293, 484–491 (2015). https://doi.org/10.1016/J.JPOWSOUR.2015.05.104

62. Zhu, C., Yang, H., Wu, A., Zhang, D., Gao, L., Lin, T.: Modified alkaline electrolyte with 8-hydroxyquinoline and ZnO complex additives to improve Al-air battery. J Power Sources. 432, 55–64 (2019). https://doi.org/10.1016/J.JPOWSOUR.2019.05.077

63. Bruce, P.G., Freunberger, S.A., Hardwick, L.J., Tarascon, J.M.: Li–O2 and Li–S batteries with high energy storage. Nature Materials 2011 11:1. 11, 19–29 (2011). https://doi.org/10.1038/nmat3191

64. Girishkumar, G., McCloskey, B., Luntz, A.C., Swanson, S., Wilcke, W.: Lithium-air battery: Promise and challenges. Journal of Physical Chemistry Letters. 1, 2193–2203 (2010). https://doi.org/10.1021/JZ1005384/ASSET/IMAGES/LARGE/JZ-2010-005384_0005.JPEG

65. Kang, J.H., Lee, J., Jung, J.W., Park, J., Jang, T., Kim, H.S., Nam, J.S., Lim, H., Yoon, K.R., Ryu, W.H., Kim, I.D., Byon, H.R.: Lithium-air batteries: Air-breathing challenges and perspective, (2020)

66. Gao, J., Cai, X., Wang, J., Hou, M., Lai, L., Zhang, L.: Recent progress in hierarchically structured O2-cathodes for Li-O2 batteries. Chemical Engineering Journal. 352, 972–995 (2018). https://doi.org/10.1016/J.CEJ.2018.06.014

67. Elia, G.A., Park, J.B., Sun, Y.K., Scrosati, B., Hassoun, J.: Role of the Lithium Salt in the Performance of Lithium–Oxygen Batteries: A Comparative Study. ChemElectroChem. 1, 47–50 (2014). https://doi.org/10.1002/CELC.201300160

68. Oloniyo, O., Kumar, S., Scott, K.: Performance of MnO 2 crystallographic phases in rechargeable lithium-air oxygen cathode. J Electron Mater. 41, 921–927 (2012). https://doi.org/10.1007/S11664-012-2046-1/METRICS

69. Lu, Y.-C., Gasteiger, H.A., Crumlin, E., McGuire, R., Shao-Horn, Y.: Electrocatalytic Activity Studies of Select Metal Surfaces and Implications in Li-Air Batteries. J Electrochem Soc. 157, A1016 (2010). https://doi.org/10.1149/1.3462981/XML

70. Xu, W., Hu, J., Engelhard, M.H., Towne, S.A., Hardy, J.S., Xiao, J., Feng, J., Hu, M.Y., Zhang, J., Ding, F., Gross, M.E., Zhang, J.G.: The stability of organic

solvents and carbon electrode in nonaqueous Li-O2 batteries. J Power Sources. 215, 240–247 (2012). https://doi.org/10.1016/J.JPOWSOUR.2012.05.021

71. Li, F., Zhang, T., Zhou, H.: Challenges of non-aqueous Li–O 2 batteries: electrolytes, catalysts, and anodes. Energy Environ Sci. 6, 1125–1141 (2013). https://doi.org/10.1039/C3EE00053B

72. Cecchetto, L., Salomon, M., Scrosati, B., Croce, F.: Study of a Li–air battery having an electrolyte solution formed by a mixture of an ether-based aprotic solvent and an ionic liquid. J Power Sources. 213, 233–238 (2012). https://doi.org/10.1016/J.JPOWSOUR.2012.04.038

73. Hassoun, J., Croce, F., Armand, M., Scrosati, B.: Investigation of the O2 electrochemistry in a polymer electrolyte solid-state cell. Angewandte Chemie - International Edition. 50, 2999–3002 (2011). https://doi.org/10.1002/ANIE.201006264

74. McCloskey, B.D., Bethune, D.S., Shelby, R.M., Girishkumar, G., Luntz, A.C.: Solvents critical role in nonaqueous Lithium-Oxygen battery electrochemistry. Journal of Physical Chemistry Letters. 2, 1161–1166 (2011). https://doi.org/10.1021/JZ200352V/SUPPL_FILE/JZ200352V_SI_001.PDF

75. McCloskey, B.D., Speidel, A., Scheffler, R., Miller, D.C., Viswanathan, V., Hummelshøj, J.S., Nørskov, J.K., Luntz, A.C.: Twin problems of interfacial carbonate formation in nonaqueous Li-O 2 batteries. Journal of Physical Chemistry Letters. 3, 997–1001 (2012). https://doi.org/10.1021/JZ300243R/SUPPL_FILE/JZ300243R_SI_001.PDF

76. Ottakam Thotiyl, M.M., Freunberger, S.A., Peng, Z., Bruce, P.G.: The carbon electrode in nonaqueous Li-O2 cells. J Am Chem Soc. 135, 494–500 (2013). https://doi.org/10.1021/JA310258X/SUPPL_FILE/JA310258X_SI_001.PDF

77. Mccloskey, B.D., Valery, A., Luntz, A.C., Gowda, S.R., Wallraff, G.M., Garcia, J.M., Mori, T., Krupp, L.E.: Combining accurate O2 and Li2O2 assays to separate discharge and charge stability limitations in nonaqueous Li-O 2 Batteries. Journal of Physical Chemistry Letters. 4, 2989–2993 (2013). https://doi.org/10.1021/JZ401659F/SUPPL_FILE/JZ401659F_SI_001.PDF

78. Mahne, N., Schafzahl, B., Leypold, C., Leypold, M., Grumm, S., Leitgeb, A., Strohmeier, G.A., Wilkening, M., Fontaine, O., Kramer, D., Slugovc, C., Borisov, S.M., Freunberger, S.A.: Singlet oxygen generation as a major cause for parasitic reactions during cycling of aprotic lithium–oxygen batteries. Nature Energy 2017 2:5. 2, 1–9 (2017). https://doi.org/10.1038/nenergy.2017.36

79. Zhang, T., Imanishi, N., Hirano, A., Takeda, Y., Yamamoto, O.: Stability of Li/polymer electrolyte-ionic liquid composite/lithium conducting glass ceramics in an aqueous electrolyte. Electrochemical and Solid-State Letters. 14, A45 (2011). https://doi.org/10.1149/1.3545964/XML

80. Akhtar, N., Akhtar, W.: Prospects, challenges, and latest developments in lithium–air batteries. Int J Energy Res. 39, 303–316 (2015). https://doi.org/10.1002/ER.3230

81. Manthiram, A., Li, L.: Hybrid and Aqueous Lithium-Air Batteries. Adv Energy Mater. 5, 1401302 (2015). https://doi.org/10.1002/AENM.201401302

82. Stevens, P., Toussaint, G., Caillon, G., Viaud, P., Vinatier, P., Cantau, C., Fichet, O., Sarrazin, C., Mallouki, M.: Development of a Lithium Air Rechargeable Battery. ECS Trans. 28, 1–12 (2010). https://doi.org/10.1149/1.3507922/XML

83. Knauth, P.: Inorganic solid Li ion conductors: An overview. Solid State Ion. 180, 911–916 (2009). https://doi.org/10.1016/J.SSI.2009.03.022

84. Goodenough, J.B., Hong, H.Y.P., Kafalas, J.A.: Fast Na+-ion transport in skeleton structures. Mater Res Bull. 11, 203–220 (1976). https://doi.org/10.1016/0025-5408(76)90077-5

85. Jian, Z., Hu, Y.-S., Ji, X., Chen, W., Jian, Z., Chen, W., Ji, X., Hu, Y.-S.: NASICON-Structured Materials for Energy Storage. Advanced Materials. 29, 1601925 (2017). https://doi.org/10.1002/ADMA.201601925

86. Lei, B., Liu, A., Koudakan, A., Kim, H., Kim, M.-J., Sun, Y.-K., Wang, Y., Zhu, X., Qin, J., Han, Y., Zhang, X., Lu, B., Li, Y., Shao, C., Guo, Q., Zhang□, Z.: Recent advances in solid state lithium–oxygen batteries: electrolytes and multi-functions. Nano Futures. 4, 032005 (2020). https://doi.org/10.1088/2399-1984/ABACD3

87. Stevens, P., Toussaint, G., Caillon, G., Viaud, P., Vinatier, P., Cantau, C., Fichet, O., Sarrazin, C., Mallouki, M.: Development of a Lithium Air Rechargeable Battery. ECS Trans. 28, 1–12 (2010). https://doi.org/10.1149/1.3507922/XML

88. Inaguma, Y., Nakashima, M.: A rechargeable lithium–air battery using a lithium ion-conducting lanthanum lithium titanate ceramics as an electrolyte separator. J Power Sources. 228, 250–255 (2013). https://doi.org/10.1016/J.JPOWSOUR.2012.11.098

89. Rhee, C.K., Chun, Y.B., Kang, S.H., Kim, W.W., Cao, G.: LITHIUM-ION CONDUCTIVE FILM MEMBRANE OF Li0.3La0.57TiO2 PEROVSKITE STRUCTURE AND ITS APPLICATION IN Li-AIR BATTERIES. Archives of Metallurgy and Materials. 68, 191–194 (2023). https://doi.org/10.24425/AMM.2023.141493

90. Liu, Y., He, P., Zhou, H.: Rechargeable Solid-State Li–Air and Li–S Batteries: Materials, Construction, and Challenges. Adv Energy Mater. 8, 1701602 (2018). https://doi.org/10.1002/AENM.201701602

91. Inaguma, Y., Nakashima, M.: A rechargeable lithium–air battery using a lithium ion-conducting lanthanum lithium titanate ceramics as an electrolyte separator. J Power Sources. 228, 250–255 (2013). https://doi.org/10.1016/J.JPOWSOUR.2012.11.098

92. Wolfenstine, J.: Stability predictions of solid Li-ion conducting membranes in aqueous solutions. J Mater Sci. 45, 3954–3956 (2010). https://doi.org/10.1007/S10853-010-4522-4/FIGURES/2

93. Yang, H., Tay, K., Xu, Y., Rajbanshi, B., Kasani, S., Bright, J., Boryczka, J., Wang, C., Bai, P., Wu, N.: Nitrogen-Doped Lithium Lanthanum Titanate Nanofiber-Polymer Composite Electrolytes for All-Solid-State Lithium Batteries. J Electrochem Soc. 168, 110507 (2021). https://doi.org/10.1149/1945-7111/AC30AD

94. Li, Y., Han, J.T., Wang, C.A., Xie, H., Goodenough, J.B.: Optimizing Li+ conductivity in a garnet framework. J Mater Chem. 22, 15357–15361 (2012). https://doi.org/10.1039/C2JM31413D

95. Murugan, R., Thangadurai, V., Weppner, W.: Fast Lithium Ion Conduction in Garnet-Type Li7La3Zr2O12. Angewandte Chemie International Edition. 46, 7778–7781 (2007). https://doi.org/10.1002/ANIE.200701144

96. Huang, J., Liang, F., Hou, M., Zhang, Y., Chen, K., Xue, D.: Garnet-type solid-state electrolytes and interfaces in all-solid-state lithium batteries: progress and perspective. Appl Mater Today. 20, 100750 (2020). https://doi.org/10.1016/J.APMT.2020.100750

97. Balaish, M., Peled, E., Golodnitsky, D., Ein-Eli, Y.: Liquid-Free Lithium–Oxygen Batteries. Angewandte Chemie. 127, 446–450 (2015). https://doi.org/10.1002/ANGE.201408008

98. Liu, T., Chang, Z., Yin, Y., Chen, K., Zhang, Y., Zhang, X.: The PVDF-HFP gel polymer electrolyte for Li-O2 battery. Solid State Ion. 318, 88–94 (2018). https://doi.org/10.1016/J.SSI.2017.08.001

99. Abraham, K.M., Jiang, Z.: A Polymer Electrolyte-Based Rechargeable Lithium/Oxygen Battery. J Electrochem Soc. 143, 1–5 (1996). https://doi.org/10.1149/1.1836378/XML

100. Shui, J., Du, F., Xue, C., Li, Q., Dai, L.: Vertically aligned N-doped coral-like carbon fiber arrays as efficient air electrodes for high-performance nonaqueous Li-O2 batteries. ACS Nano. 8, 3015–3022 (2014). https://doi.org/10.1021/NN500327P/SUPPL_FILE/NN500327P_SI_001.PDF

101. Luo, G.-S., 罗广生, Huang, S.-T., 黄诗 婷, Zhao, N., 赵宁, Cui, Z.-H., 崔忠 慧, Guo, X.-X., 郭向 欣: A superhigh discharge capacity induced by a synergetic effect between high-surface-area carbons and a carbon paper current collector in a lithium–oxygen battery*. Chinese Physics B. 24, 088102 (2015). https://doi.org/10.1088/1674-1056/24/8/088102

102. Hayashi, M., Sakamoto, S., Nohara, M., Iwata, M., Komatsu, T.: Electrochemical Properties of Large-Discharge-Capacity Air Electrodes with Nickel Foam Sheet Support for Lithium Air Secondary Batteries. Electrochemistry. 86, 333–338 (2018). https://doi.org/10.5796/ELECTROCHEMISTRY.18-00045

103. Heine, J., Rodehorst, U., Badillo, J.P., Winter, M., Bieker, P.: Chemical Stability Investigations of Polyisobutylene as New Binder for Application in Lithium Air-Batteries. Electrochim Acta. 155, 110–115 (2015). https://doi.org/10.1016/J.ELECTACTA.2015.01.001

104. Kichambare, P., Kumar, J., Rodrigues, S., Kumar, B.: Electrochemical performance of highly mesoporous nitrogen doped carbon cathode in lithium–oxygen batteries. J Power Sources. 196, 3310–3316 (2011). https://doi.org/10.1016/J.JPOWSOUR.2010.11.112

105. Zhang, P., Zhao, Y., Zhang, X.: Functional and stability orientation synthesis of materials and structures in aprotic Li–O2 batteries. Chem Soc Rev. 47, 2921–3004 (2018). https://doi.org/10.1039/C8CS00009C

106. Khodabakhshi, S., Fulvio, P.F., Andreoli, E.: Carbon black reborn: Structure and chemistry for renewable energy harnessing. (2020). https://doi.org/10.1016/j.carbon.2020.02.058

107. Wang, M.-J., Gray, C.A., Reznek, S.A., Mahmud, K., Kutsovsky, Y.: Carbon Black. Kirk-Othmer Encyclopedia of Chemical Technology. (2003). https://doi.org/10.1002/0471238961.0301180204011414.A01.PUB2

108. Pawlyta, M., Rouzaud, J.-N., Duber, S.: Raman microspectroscopy characterization of carbon blacks: Spectral analysis and structural information. (2014). https://doi.org/10.1016/j.carbon.2014.12.030

109. Liu, C.-C., Walters, A.B., Vanmce~, M.A.: MEASUREMENT OF ELECTRICAL PROPERTIES OF A CARBON BLACK. Carbon N Y. 33, 1699–1708 (1995)

110. Sánchez-González, J., Macías-García, A., Alexandre-Franco, M.F., Gó Mez-Serrano, V.: Electrical conductivity of carbon blacks under compression. (2004). https://doi.org/10.1016/j.carbon.2004.10.045

111. Wang, J., Yin, G., Shao, Y., Zhang, S., Wang, Z., Gao, Y.: Effect of carbon black support corrosion on the durability of Pt/C catalyst. J Power Sources. 171, 331–339 (2007). https://doi.org/10.1016/J.JPOWSOUR.2007.06.084

112. Kierzek, K., Gryglewicz, G.: Activated Carbons and Their Evaluation in Electric Double Layer Capacitors. Molecules 2020, Vol. 25, Page 4255. 25, 4255 (2020). https://doi.org/10.3390/MOLECULES25184255

113. Jordá-Beneyto, M., Suárez-García, F., Lozano-Castelló, D., Cazorla-Amorós, D., Linares-Solano, A.: Hydrogen storage on chemically activated carbons and carbon nanomaterials at high pressures. Carbon N Y. 45, 293–303 (2007). https://doi.org/10.1016/J.CARBON.2006.09.022

114. Heidarinejad, Z., Dehghani, M.H., Heidari, M., Javedan, G., Ali, I., Sillanpää, M.: Methods for preparation and activation of activated carbon: a review. Environmental Chemistry Letters 2020 18:2. 18, 393–415 (2020). https://doi.org/10.1007/S10311-019-00955-0

115. Miriyala, N., Ouyang, D., Perrie, Y., Lowry, D., Kirby, D.J.: Activated carbon as a carrier for amorphous drug delivery: Effect of drug characteristics and carrier wettability. European Journal of Pharmaceutics and Biopharmaceutics. 115, 197–205 (2017). https://doi.org/10.1016/J.EJPB.2017.03.002

116. Salleh, Z., Islam, M.M., Yusop, M.Y.M., Idrus, M.A.M.M.: Mechanical Properties of Activated Carbon (AC) Coconut Shell Reinforced Polypropylene Composites Encapsulated with Epoxy Resin. APCBEE Procedia. 9, 92–96 (2014). https://doi.org/10.1016/J.APCBEE.2014.01.017

117. Gonsalvesh, L., Marinov, S.P., Gryglewicz, G., Carleer, R., Yperman, J.: Preparation, characterization and application of polystyrene based activated carbons for Ni(II) removal from aqueous solution. Fuel Processing Technology. 149, 75–85 (2016). https://doi.org/10.1016/J.FUPROC.2016.03.024

118. Bratek, W., Świątkowski, A., Pakuła, M., Biniak, S., Bystrzejewski, M., Szmigielski, R.: Characteristics of activated carbon prepared from waste PET by carbon dioxide activation. J Anal Appl Pyrolysis. 100, 192–198 (2013). https://doi.org/10.1016/J.JAAP.2012.12.021

119. Hu, W., Cheng, S., Xia, H., Zhang, L., Jiang, X., Zhang, Q., Chen, Q.: Waste phenolic resin derived activated carbon by microwave-assisted KOH activation and application to dye wastewater treatment. Green Processing and Synthesis. 8, 408–415 (2019). https://doi.org/10.1515/GPS-2019-0008/MACHINEREADABLECITATION/RIS

120. Yadav, D., Amini, F., Ehrmann, A.: Recent advances in carbon nanofibers and their applications – A review. Eur Polym J. 138, 109963 (2020). https://doi.org/10.1016/J.EURPOLYMJ.2020.109963

121. Ruiz-Cornejo, J.C., Sebastián, D., Lázaro, M.J.: Synthesis and applications of carbon nanofibers: A review. Reviews in Chemical Engineering. 36, 493–511 (2020). https://doi.org/10.1515/REVCE-2018-0021/ASSET/GRAPHIC/J_REVCE-2018-0021_FIG_004.JPG

122. Rahaman, M.S.A., Ismail, A.F., Mustafa, A.: A review of heat treatment on polyacrylonitrile fiber. Polym Degrad Stab. 92, 1421–1432 (2007). https://doi.org/10.1016/J.POLYMDEGRADSTAB.2007.03.023

123. Megelski, S., Stephens, J.S., Bruce Chase, D., Rabolt, J.F.: Micro- and Nanostructured Surface Morphology on Electrospun Polymer Fibers. Macromolecules. 35, 8456–8466 (2002). https://doi.org/10.1021/MA020444A

124. Ashok, J., Reema, S., Anjaneyulu, C., Subrahmanyam, M., Venugopal, A.: Methane decomposition catalysts for CO x-free hydrogen production. Reviews in Chemical Engineering. 26, 29–39 (2010). https://doi.org/10.1515/REVCE.2010.002/MACHINEREADABLECITATION/RIS

125. Lobo, L.S.: Nucleation and growth of carbon nanotubes and nanofibers: Mechanism and catalytic geometry control. Carbon N Y. 114, 411–417 (2017). https://doi.org/10.1016/J.CARBON.2016.12.005

126. Gryglewicz, S., Śliwak, A., Ćwikła, J., Gryglewicz, G.: Performance of carbon nanofiber and activated carbon supported nickel catalysts for liquid-phase hydrogenation of cinnamaldehyde into hydrocinnamaldehyde. Catal Letters. 144, 62–69 (2014). https://doi.org/10.1007/S10562-013-1146-8/TABLES/3

127. Lin, J.F., Mohl, M., Nelo, M., Toth, G., Kukovecz, Á., Kónya, Z., Sridhar, S., Vajtai, R., Ajayan, P.M., Su, W.F., Jantunen, H., Kordas, K.: Facile synthesis of nanostructured carbon materials over RANEY® nickel catalyst films printed on Al2O3 and SiO2 substrates. J Mater Chem C Mater. 3, 1823–1829 (2015). https://doi.org/10.1039/C4TC02442G

128. Lu, W., He, T., Xu, B., He, X., Adidharma, H., Radosz, M., Gasem, K., Fan, M.: Progress in catalytic synthesis of advanced carbon nanofibers. J Mater Chem A Mater. 5, 13863–13881 (2017). https://doi.org/10.1039/C7TA02007D

129. Collins, P.G., Avouris, P.: Nanotubes for electronics. Sci Am. 283, 62–69 (2000). https://doi.org/10.1038/SCIENTIFICAMERICAN1200-62

130. Yu, M.F., Lourie, O., Dyer, M.J., Moloni, K., Kelly, T.F., Ruoff, R.S.: Strength and breaking mechanism of multiwalled carbon nanotubes under tensile load. Science. 287, 637–640 (2000). https://doi.org/10.1126/SCIENCE.287.5453.637

131. Geng, H., Peng, Y., Qu, L., Zhang, H., Wu, M.: Structure Design and Composition Engineering of Carbon-Based Nanomaterials for Lithium Energy Storage. Adv Energy Mater. 10, 1903030 (2020). https://doi.org/10.1002/AENM.201903030

132. Frackowiak, E., Lota, G., Cacciaguerra, T., Béguin, F.: Carbon nanotubes with Pt–Ru catalyst for methanol fuel cell. Electrochem commun. 8, 129–132 (2006). https://doi.org/10.1016/J.ELECOM.2005.10.015

133. Portet, C., Taberna, P.L., Simon, P., Flahaut, E.: Influence of carbon nanotubes addition on carbon–carbon supercapacitor performances in organic electrolyte. J Power Sources. 139, 371–378 (2005). https://doi.org/10.1016/J.JPOWSOUR.2004.07.015

134. Yu, W.J., Liu, C., Hou, P.X., Zhang, L., Shan, X.Y., Li, F., Cheng, H.M.: Lithiation of silicon nanoparticles confined in carbon nanotubes. ACS Nano. 9, 5063–5071 (2015). https://doi.org/10.1021/ACSNANO.5B00157/SUPPL_FILE/NN5B00157_SI_004.AVI

135. Gupta, N., Gupta, S.M., Sharma, S.K.: Carbon nanotubes: synthesis, properties and engineering applications. Carbon Letters. 29, 419–447 (2019). https://doi.org/10.1007/S42823-019-00068-2/FIGURES/14

136. Scott, C.D., Arepalli, S., Nikolaev, P., Smalley, R.E.: Growth mechanisms for single-wall carbon nanotubes in a laser-ablation process. Appl Phys A Mater Sci Process. 72, 573–580 (2001). https://doi.org/10.1007/S003390100761/METRICS

137. Kopiec, D., Wrobel, P.S., Szeluga, U., Kierzek, K.: Facile method of preparation of carbon nanotubes based aerogels as cathodes for lithium-oxygen cells. J Power Sources. 604, 234501 (2024). https://doi.org/10.1016/J.JPOWSOUR.2024.234501

138. Fischer, U., Saliger, R., Bock, V., Petricevic, R., Fricke, J.: Carbon Aerogels as Electrode Material in Supercapacitors. Journal of Porous Materials. 4, 281–285 (1997). https://doi.org/10.1023/A:1009629423578/METRICS

139. Hao, P., Zhao, Z., Leng, Y., Tian, J., Sang, Y., Boughton, R.I., Wong, C.P., Liu, H., Yang, B.: Graphene-based nitrogen self-doped hierarchical porous carbon aerogels derived from chitosan for high performance supercapacitors. Nano Energy. 15, 9–23 (2015). https://doi.org/10.1016/J.NANOEN.2015.02.035

140. Yang, B.S., Kang, K.Y., Jeong, M.J.: Preparation of lignin-based carbon aerogels as biomaterials for nano-supercapacitor. Journal of the Korean Physical Society. 71, 478–482 (2017). https://doi.org/10.3938/JKPS.71.478/METRICS

141. Xu, L., Xiao, G., Chen, C., Li, R., Mai, Y., Sun, G., Yan, D.: Superhydrophobic and superoleophilic graphene aerogel prepared by facile chemical reduction. J Mater Chem A Mater. 3, 7498–7504 (2015). https://doi.org/10.1039/c5ta00383k

142. Lv, X., Zheng, P., Wu, Z., Yu, J., Ge, D., Yang, L.: Self-assembly of Fe2O3 nanorods in carbon nanotube network as a 3D aerogel architecture for lithium ion batteries. Ceram Int. 45, 5796–5800 (2019). https://doi.org/10.1016/J.CERAMINT.2018.12.047

143. Hao, F., Zhang, Z., Yin, L.: Co3O4/carbon aerogel hybrids as anode materials for lithium-ion batteries with enhanced electrochemical properties. ACS Appl Mater Interfaces. 5, 8337–8344 (2013). https://doi.org/10.1021/AM400952J/SUPPL_FILE/AM400952J_SI_001.PDF

144. Xiong, Q.Q., Ji, Z.G.: Controllable growth of MoS2/C flower-like microspheres with enhanced electrochemical performance for lithium ion batteries. J Alloys Compd. 673, 215–219 (2016). https://doi.org/10.1016/J.JALLCOM.2016.02.253

145. Li, D., Chang, G., Zong, L., Xue, P., Wang, Y., Xia, Y., Lai, C., Yang, D.: From double-helix structured seaweed to S-doped carbon aerogel with ultra-high surface area for energy storage. Energy Storage Mater. 17, 22–30 (2019). https://doi.org/10.1016/J.ENSM.2018.08.004

146. Kim, C.H.J., Varanasi, C. V., Liu, J.: Synergy of polypyrrole and carbon x-aerogel in lithium–oxygen batteries. Nanoscale. 10, 3753–3758 (2018). https://doi.org/10.1039/C7NR08494C

147. Wang, F., Xu, Y.H., Luo, Z.K., Pang, Y., Wu, Q.X., Liang, C.S., Chen, J., Liu, D., Zhang, X.H.: A dual pore carbon aerogel based air cathode for a highly

rechargeable lithium-air battery. J Power Sources. 272, 1061–1071 (2014). https://doi.org/10.1016/J.JPOWSOUR.2014.08.126

148. Ma, L., Yu, T., Tzoganakis, E., Amine, K., Wu, T., Chen, Z., Lu, J.: Fundamental Understanding and Material Challenges in Rechargeable Nonaqueous Li–O2 Batteries: Recent Progress and Perspective. Adv Energy Mater. 8, 1800348 (2018). https://doi.org/10.1002/AENM.201800348

149. Wei, Z.H., Tan, P., An, L., Zhao, T.S.: A non-carbon cathode electrode for lithium–oxygen batteries. Appl Energy. 130, 134–138 (2014). https://doi.org/10.1016/J.APENERGY.2014.05.029

150. Peng, Z., Freunberger, S.A., Chen, Y., Bruce, P.G.: A reversible and higher-rate Li-O2 battery. Science (1979). 337, 563–566 (2012). https://doi.org/10.1126/SCIENCE.1223985/SUPPL_FILE/PENG.SM.PDF

151. Cui, Y., Wen, Z., Liu, Y.: A free-standing-type design for cathodes of rechargeable Li–O2 batteries. Energy Environ Sci. 4, 4727–4734 (2011). https://doi.org/10.1039/C1EE02365A

152. Zhou, Y., Guo, S.: Recent advances in cathode catalyst architecture for lithium–oxygen batteries. eScience. 3, 100123 (2023). https://doi.org/10.1016/J.ESCI.2023.100123

153. Kopiec, D., Kierzek, K.: Application of functionalized carbon nanotubes as the cathode of nonaqueous lithium-oxygen cells. Solid State Ion. 385, 116007 (2022). https://doi.org/10.1016/J.SSI.2022.116007

154. Fan, W., Guo, X., Xiao, D., Gu, L.: Influence of gold nanoparticles anchored to carbon nanotubes on formation and decomposition of Li2O2 in nonaqueous Li-O2 batteries. Journal of Physical Chemistry C. 118, 7344–7350 (2014). https://doi.org/10.1021/JP500597M/SUPPL_FILE/JP500597M_SI_001.PDF

155. Shen, Y., Sun, D., Yu, L., Zhang, W., Shang, Y., Tang, H., Wu, J., Cao, A., Huang, Y.: A high-capacity lithium–air battery with Pd modified carbon nanotube sponge cathode working in regular air. Carbon N Y. 62, 288–295 (2013). https://doi.org/10.1016/J.CARBON.2013.05.066

156. Zhang, Y., Wang, X., Yin, J., Wang, Y., Li, C., Xia, D.: Ultrafine Ru/RuO x Nanoparticles Uniformly Anchored on Carbon Nanotubes as Cathode Electrocatalyst for Lithium-Oxygen Batteries. ChemistrySelect. 4, 4593–4597 (2019). https://doi.org/10.1002/SLCT.201900023

157. Huang, X., Yu, H., Tan, H., Zhu, J., Zhang, W., Wang, C., Zhang, J., Wang, Y., Lv, Y., Zeng, Z., Liu, D., Ding, J., Zhang, Q., Srinivasan, M., Ajayan, P.M., Hng, H.H., Yan, Q.: Carbon nanotube-encapsulated noble metal nanoparticle hybrid as a cathode material for Li-oxygen batteries. Adv Funct Mater. 24, 6516–6523 (2014). https://doi.org/10.1002/ADFM.201400921

158. McCloskey, B.D., Scheffler, R., Speidel, A., Bethune, D.S., Shelby, R.M., Luntz, A.C.: On the efficacy of electrocatalysis in nonaqueous Li-O2 batteries. J Am

Chem Soc. 133, 18038–18041 (2011). https://doi.org/10.1021/JA207229N/SUPPL_FILE/JA207229N_SI_001.PDF

159. Li, J., Wang, N., Zhao, Y., Ding, Y., Guan, L.: MnO2 nanoflakes coated on multi-walled carbon nanotubes for rechargeable lithium-air batteries. Electrochem commun. 13, 698–700 (2011). https://doi.org/10.1016/J.ELECOM.2011.04.013

160. Luo, C., Sun, H., Jiang, Z., Guo, H., Gao, M., Wei, M., Jiang, Z., Zhou, H., Sun, S.G.: Electrocatalysts of Mn and Ru oxides loaded on MWCNTS with 3D structure and synergistic effect for rechargeable Li-O2 battery. Electrochim Acta. 282, 56–63 (2018). https://doi.org/10.1016/J.ELECTACTA.2018.06.040

161. Hu, S.J., Fan, X.P., Chen, J., Peng, J.M., Wang, H.Q., Huang, Y.G., Li, Q.Y.: Carbon Nanotubes/Carbon Fiber Paper Supported MnO2 Cathode Catalyst for Li−Air Batteries. ChemElectroChem. 4, 2997–3003 (2017). https://doi.org/10.1002/CELC.201700582

162. Liu, Y., Liu, Y., Cheng, S.H.S., Yu, S., Nan, B., Bian, H., Md, K., Wang, M., Chung, C.Y., Lu, Z.G.: Conformal Coating of Heterogeneous CoO/Co Nanocomposites on Carbon Nanotubes as Efficient Bifunctional Electrocatalyst for Li-Air Batteries. Electrochim Acta. 219, 560–567 (2016). https://doi.org/10.1016/J.ELECTACTA.2016.10.064

163. Huang, Y. guo, Chen, J., Zhang, X. hui, Zan, Y. hui, Wu, X. ming, He, Z. qiang, Wang, H. qiang, Li, Q. yu: Three-dimensional Co3O4/CNTs/CFP composite as binder-free cathode for rechargeable Li-O2 batteries. Chemical Engineering Journal. 296, 28–34 (2016). https://doi.org/10.1016/J.CEJ.2016.03.081

164. Peng, S.H., Chen, T.H., Lee, C.H., Lu, H.C., Lue, S.J.: Optimal cobalt oxide (Co3O4): Graphene (GR) ratio in Co3O4/GR as air cathode catalyst for air-breathing hybrid electrolyte lithium-air battery. J Power Sources. 471, 228373 (2020). https://doi.org/10.1016/J.JPOWSOUR.2020.228373

165. Yang, J., Ma, D., Li, Y., Zhang, P., Mi, H., Deng, L., Sun, L., Ren, X.: Atomic layer deposition of amorphous oxygen-deficient TiO2-x on carbon nanotubes as cathode materials for lithium-air batteries. J Power Sources. 360, 215–220 (2017). https://doi.org/10.1016/J.JPOWSOUR.2017.05.094

166. Wu, M.C., Zhao, T.S., Tan, P., Jiang, H.R., Zhu, X.B.: Cost-effective carbon supported Fe2O3 nanoparticles as an efficient catalyst for non-aqueous lithium-oxygen batteries. Electrochim Acta. 211, 545–551 (2016). https://doi.org/10.1016/J.ELECTACTA.2016.05.147

167. Jung, J.W., Jang, J.S., Yun, T.G., Yoon, K.R., Kim, I.D.: Three-Dimensional Nanofibrous Air Electrode Assembled with Carbon Nanotubes-Bridged Hollow Fe2O3 Nanoparticles for High-Performance Lithium-Oxygen Batteries. ACS Appl Mater Interfaces. 10, 6531–6540 (2018).

https://doi.org/10.1021/ACSAMI.7B15421/SUPPL_FILE/AM7B15421_SI_002.AVI

168. Kavakli, C., Meini, S., Harzer, G., Tsiouvaras, N., Piana, M., Siebel, A., Garsuch, A., Gasteiger, H.A., Herranz, J.: Nanosized Carbon-Supported Manganese Oxide Phases as Lithium–Oxygen Battery Cathode Catalysts. ChemCatChem. 5, 3358–3373 (2013). https://doi.org/10.1002/CCTC.201300331

169. Osgood, H., Devaguptapu, S. V., Xu, H., Cho, J., Wu, G.: Transition metal (Fe, Co, Ni, and Mn) oxides for oxygen reduction and evolution bifunctional catalysts in alkaline media. Nano Today. 11, 601–625 (2016). https://doi.org/10.1016/J.NANTOD.2016.09.001

170. Cai, Y., Hou, Y., Lu, Y., Chen, J.: Recent Progress on Catalysts for the Positive Electrode of Aprotic Lithium-Oxygen Batteries †. Inorganics 2019, Vol. 7, Page 69. 7, 69 (2019). https://doi.org/10.3390/INORGANICS7060069

171. Qian, Z., Sun, B., Du, L., Lou, S., Du, C., Zuo, P., Ma, Y., Cheng, X., Gao, Y.Z., Yin, G.: Insights into the role of oxygen functional groups and defects in the rechargeable nonaqueous Li–O2 batteries. Electrochim Acta. 292, 838–845 (2018). https://doi.org/10.1016/J.ELECTACTA.2018.09.202

172. Huang, S., Fan, W., Guo, X., Meng, F., Liu, X.: Positive role of surface defects on carbon nanotube cathodes in overpotential and capacity retention of rechargeable lithium-oxygen batteries. ACS Appl Mater Interfaces. 6, 21567–21575 (2014). https://doi.org/10.1021/AM506564N/SUPPL_FILE/AM506564N_SI_001.PDF

173. Majeed, S., Zhao, J., Zhang, L., Anjum, S., Liu, Z., Xu, G.: Synthesis and electrochemical applications of nitrogen-doped carbon nanomaterials. Nanotechnol Rev. 2, 615–635 (2013). https://doi.org/10.1515/NTREV-2013-0007/ASSET/GRAPHIC/NTREV-2013-0007_CV6.JPG

174. Li, Y., Wang, J., Li, X., Geng, D., Banis, M.N., Li, R., Sun, X.: Nitrogen-doped graphene nanosheets as cathode materials with excellent electrocatalytic activity for high capacity lithium-oxygen batteries. Electrochem commun. 18, 12–15 (2012). https://doi.org/10.1016/J.ELECOM.2012.01.023

175. Shui, J.L., Karan, N.K., Balasubramanian, M., Li, S.Y., Liu, D.J.: Fe/N/C composite in Li-O 2 battery: Studies of catalytic structure and activity toward oxygen evolution reaction. J Am Chem Soc. 134, 16654–16661 (2012). https://doi.org/10.1021/JA3042993/SUPPL_FILE/JA3042993_SI_001.PDF

176. Wu, G., MacK, N.H., Gao, W., Ma, S., Zhong, R., Han, J., Baldwin, J.K., Zelenay, P.: Nitrogen-doped graphene-rich catalysts derived from heteroatom polymers for oxygen reduction in nonaqueous lithium-O2 battery cathodes. ACS Nano. 6, 9764–9776 (2012). https://doi.org/10.1021/NN303275D/SUPPL_FILE/NN303275D_SI_001.PDF

177. Ionescu, M.I., Laforgue, A.: Synthesis of nitrogen-doped carbon nanotubes directly on metallic foams as cathode material with high mass load for lithium-air batteries. Thin Solid Films. 709, 138211 (2020). https://doi.org/10.1016/J.TSF.2020.138211

178. Mi, R., Li, S., Liu, X., Liu, L., Li, Y., Mei, J., Chen, Y., Liu, H., Wang, H., Yan, H., Lau, W.M.: Electrochemical performance of binder-free carbon nanotubes with different nitrogen amounts grown on the nickel foam as cathodes in Li–O2 batteries. J Mater Chem A Mater. 2, 18746–18753 (2014). https://doi.org/10.1039/C4TA03457K

179. Lin, X., Lu, X., Huang, T., Liu, Z., Yu, A.: Binder-free nitrogen-doped carbon nanotubes electrodes for lithium-oxygen batteries. J Power Sources. 242, 855–859 (2013). https://doi.org/10.1016/J.JPOWSOUR.2013.05.100

180. Zhang, Z., Peng, B., Chen, W., Lai, Y., Li, J.: Nitrogen-doped carbon nanotubes with hydrazine treatment as cathode materials for lithium-oxygen batteries. Journal of Solid State Electrochemistry. 19, 195–200 (2015). https://doi.org/10.1007/S10008-014-2591-Z/METRICS

181. Luo, W. Bin, Chou, S.L., Wang, J.Z., Liu, H.K.: A B4C nanowire and carbon nanotube composite as a novel bifunctional electrocatalyst for high energy lithium oxygen batteries. J Mater Chem A Mater. 3, 18395–18399 (2015). https://doi.org/10.1039/C5TA04374C

182. Lin, Q., Cui, Z., Sun, J., Huo, H., Chen, C., Guo, X.: Formation of Nanosized Defective Lithium Peroxides through Si-Coated Carbon Nanotube Cathodes for High Energy Efficiency Li-O2 Batteries. ACS Appl Mater Interfaces. 10, 18754–18760 (2018). https://doi.org/10.1021/ACSAMI.8B04419/ASSET/IMAGES/LARGE/AM-2018-04419Y_0005.JPEG

183. Dong, L., Hu, C., Huang, X., Chen, N., Qu, L.: One-pot Synthesis of Nitrogen and Phosphorus Co-doped Graphene and Its Use as High-performance Electrocatalyst for Oxygen Reduction Reaction. Chem Asian J. 10, 2609–2614 (2015). https://doi.org/10.1002/ASIA.201500707

184. Zhang, P., Wang, Z., Wang, P., Hui, X., Zhao, D., Zhang, Z., Yin, L.: Heteroatom Doping-Induced Defected Co3O4Electrode for High-Performance Lithium Oxygen Battery. ACS Appl Energy Mater. 5, 3359–3368 (2022). https://doi.org/10.1021/ACSAEM.1C03984/ASSET/IMAGES/LARGE/AE1C03984_0006.JPEG

185. Series 4560 Mini Reactors, 100-600 mL - Parr Instrument Company, https://www.parrinst.com/products/stirred-reactors/series-4560-100-600-ml-mini-reactors/

186. Shirley, D.A.: High-Resolution X-Ray Photoemission Spectrum of the Valence Bands of Gold. Phys Rev B. 5, 4709 (1972). https://doi.org/10.1103/PhysRevB.5.4709

187. High Resolution XPS of Organic Polymers: The Scienta ESCA300 Database (Beamson, G.; Briggs, D.). J Chem Educ. 70, A25 (1993). https://doi.org/10.1021/ED070PA25.5

188. Rouxhet, P.G., Genet, M.J.: XPS analysis of bio-organic systems. Surface and Interface Analysis. 43, 1453–1470 (2011). https://doi.org/10.1002/SIA.3831

189. Wagner, A.D., Naumkin, A. V., Kraut-Vass, A., Allison, J.W., Powell, C.J., Rumble, J.R.J.: NIST Standard Reference Database 20

190. Biesinger, M.C., Payne, B.P., Grosvenor, A.P., Lau, L.W.M., Gerson, A.R., Smart, R.S.C.: Resolving surface chemical states in XPS analysis of first row transition metals, oxides and hydroxides: Cr, Mn, Fe, Co and Ni. Appl Surf Sci. 257, 2717–2730 (2011). https://doi.org/10.1016/J.APSUSC.2010.10.051

191. Miniach, E., Śliwak, A., Moyseowicz, A., Gryglewicz, G.: Growth of carbon nanofibers from methane on a hydroxyapatite-supported nickel catalyst. J Mater Sci. 51, 5367–5376 (2016). https://doi.org/10.1007/S10853-016-9839-1/FIGURES/9

192. Śliwak, A., Grzyb, B., Ćwikła, J., Gryglewicz, G.: Influence of wet oxidation of herringbone carbon nanofibers on the pseudocapacitance effect. Carbon N Y. 64, 324–333 (2013). https://doi.org/10.1016/J.CARBON.2013.07.082

193. Ci, L., Wei, J., Wei, B., Liang, J., Xu, C., Wu, D.: Carbon nanofibers and single-walled carbon nanotubes prepared by the floating catalyst method. Carbon N Y. 39, 329–335 (2001). https://doi.org/10.1016/S0008-6223(00)00126-3

194. Melechko, A. V., Merkulov, V.I., McKnight, T.E., Guillorn, M.A., Klein, K.L., Lowndes, D.H., Simpson, M.L.: Vertically aligned carbon nanofibers and related structures: Controlled synthesis and directed assembly. J Appl Phys. 97, (2005). https://doi.org/10.1063/1.1857591/914738

195. Sing, K.S.W.: Physisorption of gases by carbon blacks. Carbon N Y. 32, 1311–1317 (1994). https://doi.org/10.1016/0008-6223(94)90117-1

196. Song, M.J., Shin, M.W.: Fabrication and characterization of carbon nanofiber@mesoporous carbon core-shell composite for the Li-air battery. Appl Surf Sci. 320, 435–440 (2014). https://doi.org/10.1016/J.APSUSC.2014.09.100

197. Moyseowicz, A., Śliwak, A., Gryglewicz, G.: Influence of structural and textural parameters of carbon nanofibers on their capacitive behavior. J Mater Sci. 51, 3431–3439 (2016). https://doi.org/10.1007/S10853-015-9660-2/FIGURES/6

198. De Jong, K.P., Geus, J.W.: Carbon Nanofibers: Catalytic Synthesis and Applications. Catalysis Reviews. 42, 481–510 (2000). https://doi.org/10.1081/CR-100101954

199. Jang, Y.T., Ahn, J.H., Lee, Y.H., Ju, B.K.: Effect of NH3 and thickness of catalyst on growth of carbon nanotubes using thermal chemical vapor deposition. Chem Phys Lett. 372, 745–749 (2003). https://doi.org/10.1016/S0009-2614(03)00501-3

200. Karwa, A.N., Davis, V.A., Tatarchuk, B.J.: Carbon Nanofiber Synthesis within 3-Dimensional Sintered Nickel Microfibrous Matrices: Optimization of Synthesis Conditions. J Nanotechnol. 2012, 396269 (2012). https://doi.org/10.1155/2012/396269

201. Wan, L., Deng, C., Zhao, Z.Y., Chen, H., Wang, Y.Z.: Flame Retardation of Natural Rubber: Strategy and Recent Progress. Polymers 2020, Vol. 12, Page 429. 12, 429 (2020). https://doi.org/10.3390/POLYM12020429

202. Britt, P.F.: Pyrolysis and Combustion of Acetonitrile. , Oak Ridge, TN (United States) (2002)

203. Zhang, H., Kuila, T., Kim, N.H., Yu, D.S., Lee, J.H.: Simultaneous reduction, exfoliation, and nitrogen doping of graphene oxide via a hydrothermal reaction for energy storage electrode materials. Carbon N Y. 69, 66–78 (2014). https://doi.org/10.1016/J.CARBON.2013.11.059

204. Sun, L., Wang, L., Tian, C., Tan, T., Xie, Y., Shi, K., Li, M., Fu, H.: Nitrogen-doped graphene with high nitrogen level via a one-step hydrothermal reaction of graphene oxide with urea for superior capacitive energy storage. RSC Adv. 2, 4498–4506 (2012). https://doi.org/10.1039/C2RA01367C

205. Li, X., Wang, H., Robinson, J.T., Sanchez, H., Diankov, G., Dai, H.: Simultaneous Nitrogen-Doping and Reduction of Graphene Oxide. J Am Chem Soc. 131, 15939–15944 (2009). https://doi.org/10.1021/ja907098f

206. Keru, G., Ndungu, P.G., Nyamori, V.O.: Nitrogen-Doped Carbon Nanotubes Synthesised by Pyrolysis of (4-{[(pyridine-4-yl)methylidene]amino}phenyl)ferrocene. J Nanomater. 2013, 750318 (2013). https://doi.org/10.1155/2013/750318

207. Liu, X., Hao, J., Gaan, S.: Recent studies on the decomposition and strategies of smoke and toxicity suppression for polyurethane based materials. RSC Adv. 6, 74742–74756 (2016). https://doi.org/10.1039/C6RA14345H

208. Sheng, Z.H., Shao, L., Chen, J.J., Bao, W.J., Wang, F. Bin, Xia, X.H.: Catalyst-free synthesis of nitrogen-doped graphene via thermal annealing graphite oxide with melamine and its excellent electrocatalysis. ACS Nano. 5, 4350–4358 (2011). https://doi.org/10.1021/NN103584T/SUPPL_FILE/NN103584T_SI_001.PDF

209. Mombeshora, E.T., Jarvis, A.L.L., Ndungu, P.G., Doyle, B.P., Carleschi, E., Nyamori, V.O.: Some perspectives on nitrogen-doped carbon nanotube synthesis from acetonitrile and N,N′-dimethylformamide mixtures. Mater Chem Phys. 199, 435–453 (2017). https://doi.org/10.1016/J.MATCHEMPHYS.2017.07.044

210. Jerigová, M., Odziomek, M., López-Salas, N.: “We Are Here!” Oxygen Functional Groups in Carbons for Electrochemical Applications. ACS Omega. 7, 11544–11554 (2022). https://doi.org/10.1021/ACSOMEGA.2C00639/ASSET/IMAGES/LARGE/AO2C00639_0005.JPEG

211. Li, L., Yao, X., Li, H., Liu, Z., Ma, W., Liang, X.: Thermal Stability of Oxygen-Containing Functional Groups on Activated Carbon Surfaces in a Thermal Oxidative Environment. JOURNAL OF CHEMICAL ENGINEERING OF JAPAN. 47, 21–27 (2014). https://doi.org/10.1252/JCEJ.13WE193

212. Fedoseeva, Y. V., Lobiak, E. V., Shlyakhova, E. V., Kovalenko, K.A., Kuznetsova, V.R., Vorfolomeeva, A.A., Grebenkina, M.A., Nishchakova, A.D., Makarova, A.A., Bulusheva, L.G., Okotrub, A. V.: Hydrothermal Activation of Porous Nitrogen-Doped Carbon Materials for Electrochemical Capacitors and Sodium-Ion Batteries. Nanomaterials. 10, 2163 (2020). https://doi.org/10.3390/NANO10112163

213. Moyseowicz, A., González, Z., Melendi-Espina, S., Acevedo, B., Predeanu, G., Axinte, S.M., Fernández, J.J., Granda, M., Minta, D., Moyseowicz, A., Gryglewicz, G.: Hydrothermal nitrogen doping of anthracene oil-derived activated carbons for wide voltage asymmetric capacitors. J Energy Storage. 60, 106704 (2023). https://doi.org/10.1016/J.EST.2023.106704

214. Maldonado, S., Stevenson, K.J.: Influence of Nitrogen Doping on Oxygen Reduction Electrocatalysis at Carbon Nanofiber Electrodes. Journal of Physical Chemistry B. 109, 4707–4716 (2005). https://doi.org/10.1021/JP044442Z

215. Koleżyński, A., Handke, B., Drozdz-Cieå la, E.: Crystal structure, electronic structure, and bonding properties of anhydrous nickel oxalate. J Therm Anal Calorim. 113, 319–328 (2013). https://doi.org/10.1007/S10973-012-2844-Y/TABLES/6

216. Małecka, B., Małecki, A., Drozdz-Cieśla, E., Tortet, L., Llewellyn, P., Rouquerol, F.: Some aspects of thermal decomposition of NiC2O4·2H2O. Thermochim Acta. 466, 57–62 (2007). https://doi.org/10.1016/J.TCA.2007.10.010

217. Mironova-Ulmane, N., Kuzmin, A., Steins, I., Grabis, J., Sildos, I., Pärs, M.: Raman scattering in nanosized nickel oxide NiO. J Phys Conf Ser. 93, 012039 (2007). https://doi.org/10.1088/1742-6596/93/1/012039

218. Galaburda, M., Kovalska, E., Hogan, B.T., Baldycheva, A., Nikolenko, A., Dovbeshko, G.I., Oranska, O.I., Bogatyrov, V.M.: Mechanochemical synthesis of carbon-stabilized Cu/C, Co/C and Ni/C nanocomposites with prolonged resistance to oxidation. Scientific Reports 2019 9:1. 9, 1–10 (2019). https://doi.org/10.1038/s41598-019-54007-2

219. Coelho, M.C., Titus, E., Cabral, G., Neto, V., Madaleno, J.C., Fan, Q.H., Sousa, A.C.M., Grácio, J.: Hydrogen adsorption onto nickel modified carbon nanotubes. J Nanosci Nanotechnol. 8, 4023–4028 (2008). https://doi.org/10.1166/JNN.2008.AN25

220. Zhang, Z., Xiao, X., Yan, A., Sun, K., Yu, J., Tan, P.: Breaking the capacity bottleneck of lithium-oxygen batteries through reconceptualizing transport and nucleation kinetics. Nature Communications 2024 15:1. 15, 1–11 (2024). https://doi.org/10.1038/s41467-024-54366-z

221. Xia, C., Kwok, C.Y., Nazar, L.F.: A high-energy-density lithium-oxygen battery based on a reversible four-electron conversion to lithium oxide. Science (1979). 361, 777–781 (2018). https://doi.org/10.1126/SCIENCE.AAS9343/SUPPL_FILE/AAS9343-XIA-SM.PDF

222. Prehal, C., Mondal, S., Lovicar, L., Freunberger, S.A.: Exclusive Solution Discharge in Li-O2Batteries? ACS Energy Lett. 7, 3112–3119 (2022). https://doi.org/10.1021/ACSENERGYLETT.2C01711/ASSET/IMAGES/MEDIUM/NZ2C01711_M025.GIF

223. He, X., Xu, X., Bo, G., Yan, Y.: Studies on the effects of different multiwalled carbon nanotube functionalization techniques on the properties of bio-based hybrid non-isocyanate polyurethane. RSC Adv. 10, 2180–2190 (2020). https://doi.org/10.1039/C9RA08695A

224. Kim, C., Yang, K.S., Kojima, M., Yoshida, K., Kim, Y.J., Kim, Y.A., Endo, M.: Fabrication of Electrospinning-Derived Carbon Nanofiber Webs for the Anode Material of Lithium-Ion Secondary Batteries. Adv Funct Mater. 16, 2393–2397 (2006). https://doi.org/10.1002/ADFM.200500911

225. Li, Y., Wang, J., Li, X., Liu, J., Geng, D., Yang, J., Li, R., Sun, X.: Nitrogen-doped carbon nanotubes as cathode for lithium–air batteries. Electrochem commun. 13, 668–672 (2011). https://doi.org/10.1016/J.ELECOM.2011.04.004

226. Mohazabrad, F., Wang, F., Li, X.: Experimental Studies of Salt Concentration in Electrolyte on the Performance of Li-O 2 Batteries at Various Current Densities . J Electrochem Soc. 163, A2623–A2627 (2016). https://doi.org/10.1149/2.0711613JES/XML

227. Zheng, Q., Javadi, A., Sabo, R., Cai, Z., Gong, S.: Polyvinyl alcohol (PVA)–cellulose nanofibril (CNF)–multiwalled carbon nanotube (MWCNT) hybrid organic aerogels with superior mechanical properties. RSC Adv. 3, 20816–20823 (2013). https://doi.org/10.1039/C3RA42321B

228. Shen, Y., Du, A., Wu, X.L., Li, X.G., Shen, J., Zhou, B.: Low-cost carbon nanotube aerogels with varying and controllable density. J Solgel Sci Technol. 79, 76–82 (2016). https://doi.org/10.1007/S10971-016-4002-7/METRICS

229. Gromov, A. V., Kulur, A., Gibson, J.A.A., Mangano, E., Brandani, S., Campbell, E.E.B.: Carbon nanotube/PVA aerogels impregnated with PEI: solid adsorbents for CO 2 capture. Sustain Energy Fuels. 2, 1630–1640 (2018). https://doi.org/10.1039/C8SE00089A

230. White, C.M., Banks, R., Hamerton, I., Watts, J.F.: Characterisation of commercially CVD grown multi-walled carbon nanotubes for paint applications. Prog Org Coat. 90, 44–53 (2016). https://doi.org/10.1016/J.PORGCOAT.2015.09.020

231. Kondratowicz, I., Żelechowska, K., Nadolska, M., Jażdżewska, A., Gazda, M.: Comprehensive study on graphene hydrogels and aerogels synthesis and their ability of gold nanoparticles adsorption. Colloids Surf A Physicochem Eng Asp. 528, 65–73 (2017). https://doi.org/10.1016/J.COLSURFA.2017.05.063

232. Shen, Y., Zhu, X., Zhu, L., Chen, B.: Synergistic effects of 2D graphene oxide nanosheets and 1D carbon nanotubes in the constructed 3D carbon aerogel for high performance pollutant removal. Chemical Engineering Journal. 314, 336–346 (2017). https://doi.org/10.1016/J.CEJ.2016.11.132

233. Xiao, J., Wang, D., Xu, W., Wang, D., Williford, R.E., Liu, J., Zhang, J.-G.: Optimization of Air Electrode for Li/Air Batteries. J Electrochem Soc. 157, A487 (2010). https://doi.org/10.1149/1.3314375/XML

234. Kuboki, T., Okuyama, T., Ohsaki, T., Takami, N.: Lithium-air batteries using hydrophobic room temperature ionic liquid electrolyte. J Power Sources. 146, 766–769 (2005). https://doi.org/10.1016/J.JPOWSOUR.2005.03.082